Graphene - Nonlinear Optical Properties and Modelocking Capabilities

A dissertation submitted to the University of Dublin
for the degree of Doctor of Philosophy

Aidan A. Baker-Murray
Trinity College Dublin, January 2020

School of Physics
University of Dublin
Trinity College

Declaration

I declare that this thesis has not been submitted as an exercise for a degree at this or any other university and it is entirely my own work.

I agree to deposit this thesis in the University's open access institutional repository or allow the library to do so on my behalf, subject to Irish Copyright Legislation and Trinity College Library conditions of use and acknowledgement.

Name: Aidan Baker-Murray

Signature:  **Date:** 27/01/2020

Summary

In this thesis, graphene saturable absorber mirror's (SAM) potential for mode-locking ultrafast lasers has been demonstrated, in particular at 2 μm. The saturable absorption of graphene thin films (prepared via drop-casting) was demonstrated at 1 μm 1.2 μm and 2 μm, utilising the Z-scan technique. The graphene also reacted favourably with the two different laser systems used, and in particular the different repetition rates (80 MHz, 25 kHz and 100 kHz). The response at 1.2 μm was more pronounced than at 2 μm. The successful demonstration of saturable absorption in graphene at 2 μm allowed the group to move on to the development of mode-locking devices for ultrafast pulsed lasers operating at the same wavelength.

Graphene SAMs were prepared via drop-casting and vacuum filtration of liquid-phase exfoliated (LPE) graphene, and by transfer of CVD prepared graphene, on silver mirrors. The nonlinear optical properties were examined with the I-scan technique at 2 μm. These were compared with a commercial semiconductor saturable absorber mirror (SESAM) from BATOP, and the graphene SAMs were proven to have similar characteristics.

The vacuum-filtrated graphene SAM and the SESAM had very similar values for linear reflectance (63.6% to 64.6%), non-saturable losses (25% each) and modulation depth ($\sim$11% each). However, the graphene SAM needed a higher laser intensity to be saturated than the SESAM, according to the larger saturated intensity (I_S). An advantage of ultrafast lasers are their high intensity, the larger I_S is possibly acceptable in most practical applications. Stable mode-locking

was achieved, with pulse generation at 1.5μm with a repetition rate of around 17MHz.

To Vanessa,
whose smile is brighter than all the lasers in the world

"Well, science is what scientists do, Sarah. You know, nobody's got any idea. We're just, poking at things with sticks"
- Cosima Niehaus

Acknowledgements

To start, I have to sincerely thank Professor Werner J. Blau, for his direction throughout my research and his invaluable help.

I am thankful to the entire ISLA consortium, for giving me the opportunity to tackle this project, for the financing, and for interesting conversations during the meetings.

I have to acknowledge my group in general for the camaraderie. An honest thank you to Astrid Wachauer, Beata Szydłowska, Gaozhong Wang, John James Magan, Kangpeng Wang, Pinar Arpaçay, Sevilay Akca, and Dr. Yong Zhang, for all the chats and fun times.

I would like to thank Professor Jean-Michel Mnard, for allowing me to build a z-scan system in his laboratory at the University of Ottawa and welcoming me into his group. Speaking of which, I want to extend appreciate to the help of Samantha Scarfe, Nicolas Couture, Alexei Halpin, Zyad Shehata and the rest of Prof. Mnard's expanding group for their assistance and embrace.

Finally, I'd like to show my appreciation to my family and friends. I'm thankful to Anthony Murray, Christina Murray, Stephen S. Farrell, and Walter Jenkins for the fun times that were invaluable in helping me get through the past few years. And of course, last but not least, I have to express my gratitude to my wonderful, talented, patient, amazing and beautiful wife and partner, Vanessa Baker-Murray.

List of Publications

1. Wang, G., **Baker-Murray, A. A.**, & Blau, W. J.
   "Saturable Absorption in 2D Nanomaterials and Related Photonic Devices.",
   Laser Photonics Reviews, 13, 1800282 (2019)

2. Wang, G., **Baker-Murray, A. A.**, Zhang, X., Bennett, D., Wang, J. J., Wang, J., Wang, K., & Blau, W. J.
   "Broadband saturable absorption and exciton-exciton annihilation in MoSe2 composite thin films",
   Optical Materials Express, Vol. 9, Issue 2, pp. 483-496 (2019)

3. Wang, G., Liang, G., **Baker-Murray, A. A.**, Wang, K., Wang, J. J., Zhang, X., Bennett, D., Luo, J. T., Wang, J., Fan, P., & Blau, W. J.
   "Nonlinear optical performance of few-layer molybdenum diselenide as a slow-saturable absorber",
   Photonics Research, Vol. 6, Issue 7, pp. 674-680 (2018)

4. Roelen, Z., Bustamante, J. A., Carlsen, A., **Baker-Murray, A. A.**, & Tabard-Cossa, V.
   "Instrumentation for low noise nanopore-based ionic current recording under laser illumination",
   Review of Scientific Instruments, 89, 015007 (2018)

5. Wang, G., Wang, K., Szydowska, B. M., **Baker-Murray, A. A.**, Wang, J. J., Feng, Y., Zhang, X., Wang, J., & Blau, W. J.
   "Ultrafast Nonlinear Optical Properties of a Graphene Saturable Mirror in the 2 μm Wavelength Region",

Laser Photonics Reviews, Vol. 11, Issue 11, 1800282 (2017) (Wang *et al.*, 2017a)

6. **Murray, A. A.**, & Blau, W. J.
"Nonlinear Properties of Graphene Dispersions and Thin Films at a Wavelength of 1.2μm",
Proceedings of the 3rd International Workshop on Nanocarbon Photonics and Optoelectronics
Journal of Nanoelectronics and Optoelectronics, vol. 8, pp. 23-27 (2013)

Contents

List of Figures

List of Tables

Glossary

α Absorption Coefficient. 6

γ Surface Tension. 7

ω Frequency. 30

β Nonlinear Absorption Cofficient. 91, 227

λ Wavelength. 231

$\chi^{(1)}$ First-Order Optical Susceptibility. 28

$\chi^{(3)}$ Third-Order Optical Susceptibility. 30, 95

A_c Coherence Area. 20

E Electric Field. 28

I_S Saturated Intensity. 199, 226

L_c Coherence Length. 20

MoS_2 Molybdenum Disulphide. 103, 187, 227

P Dielectric Polarisation. 28

$P(t)$ Polarisation Density. 28

R_0 Linear Reflectance. 195

R_{max} Maximum Reflectance. 195

Z_0 Rayleigh Length. 92

c Concentration. 6

n_2 Nonlinear Refractive Index. 91

v Viscosity. 8

v_F Fermi Velocity. 13

A Absorbance. 6

A-FPSA Antiresonant Fabry-Perot Saturable Absorber. 42

AFM Atomic Force Microscopy. 4, 7

BN Boron Nitride. 103, 187, 227, 235

CA Closed-Aperture. 92

CMA Centre for Microscopy and Analysis. 107

CVD Chemical Vapour Deposition. 9, 27, 103, 113, 124, 221, 226

CW Continuous Wave. 26, 220

D-SAM Dispersive Saturable Absorber Mirror. 43

DMF Dimethylformamyde. 6, 8, 105

DOS Density of States. 10

EDFL Erbium Doped Fibre Laser. 27

FWHM Full-Width at Half Max. 194

G-SAM Graphene Saturable Absorber Mirror. 112, 194, 217, 226

GBL γ-Butyrolactone. 6, 8, 105

GO Graphene Oxide. 27

GSA Graphene Saturable Absorber. 27

GSAM Graphene Satruable Absorber Mirror. 189, 190, 192

GVD Group Velocity Dispersion. 40, 41

HOPG Highly Orientated Pyrolytic Graphite. 2

ISLA Integrated disruptive componentS for 2μm LAsers. 103, 215, 231

KLM Kerr Lens Mode-locking. 40

LPE Liquid Phase Exfoliation. 5, 8, 9, 27, 103, 125, 150, 153, 181, 235

MOPA Master Oscillator Power Amplifier. 218

NLO Non-Linear Optical. 126, 197, 227

NLS Nonlinear Scattering. 32

NMP N-Methylpyrrolidone. 6, 8, 105, 159, 225

OA Open-Aperture. 92

OAS Optical Absorption Spectroscopy. 6

OPA Optical Parametric Amplifier. 179

ORC Optoelectronics Research Centre. 219, 220, 235

PCF Photonic Crystal Fibres. 27

PMMA Poly(Methly Methacrylate). 107, 112, 159, 176

RGO Reduced Graphene Oxide. 27

RSA Reverse Saturable Absorption. 32

RT Room Temperature. 8

SA Saturable Absorption. 27, 31, 34, 125, 166

SAM Saturable Absorber Mirror. 97, 118, 125, 181, 189, 194, 197, 225

SC Sodium Cholate. 6, 8

SDBS Sodium Dodecylbenzene Sulfonate. 6

SDC Sodium Deoxycholate. 8

SEM Scanning Electron Microscopy. 114, 120

SESAM Semiconductor Saturable Absorber Mirror. 27, 37, 42, 189, 190, 199, 204, 220, 226

SLG Single Layer Graphene. 5, 7, 9

SPM Self-Phase Modulation. 40, 41

SSL Solid State Laser. 37

SWNT Single Wall Nanotube. 27

TEM Transmission Electron Microscopy. 7, 105

TGA Thermogravimetric Analysis. 6

THF Tetrahydrofuran. 105

TMDC Transition Metal Dichalcogenides. 235

UV-VIS Ultra Violet-Visible. 105

1 Introduction

1.1 Graphene

The term *graphene* is a portmanteau of "graphite" with the suffix "-ene", which was coined by Hanns-Peter Boehm in 1962 to describe single-layer carbon foils. As displayed in Figure 1.1, graphene is a single atomic-layer of carbon, with said carbon atoms in a hexagonal pattern, often likened to "chicken wire".

Graphene has a host of novel qualities such as high mobility, optical transparency, mechanical strength, flexibility and environmental stability. Due to these qualities, graphene has had a colossal impact on fundamental science (Du *et al.*, 2009; Geim & Novoselov, 2007; Zhang *et al.*, 2005). These properties also make graphene-centric materials a potential platform for composites, sensors, spintronics, electronics, photonics and optoelectronics (Barone *et al.*, 2006; Bonaccorso *et al.*, 2010). There is a wide-range of promising possible uses including solar cells (Wang *et al.*, 2008), light-emitting devices (Meyer *et al.*, 2007), spin valves (Hill *et al.*, 2006), photodetectors (Xia *et al.*, 2009), touch screens (Bae *et al.*, 2010), high frequency electronics (Lin *et al.*, 2010) and even ultrafast lasers (Bao *et al.*, 2009, 2011; Chen *et al.*, 2012; Song *et al.*, 2010a), as well as many more being explored.

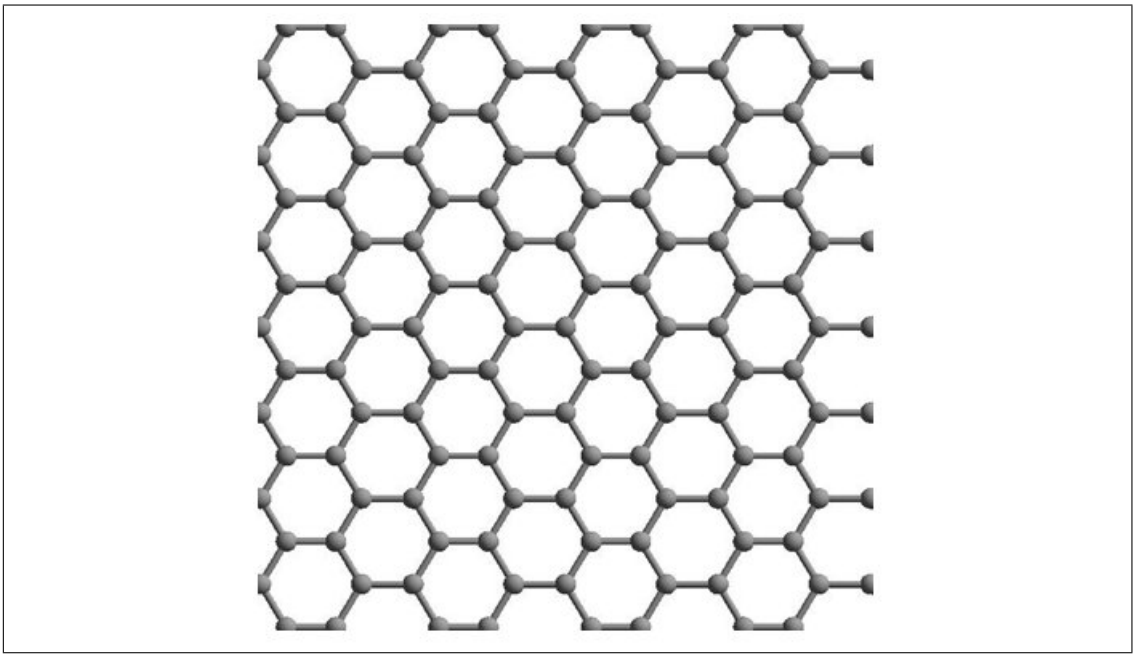

Figure 1.1: Hexagonal structure of carbon atoms, which is referred to as graphene.

We are in what is sometimes referred to as the second phase of graphene research, following the awarding of the Nobel Prize in Physics to graphene pioneers Konstontin Novoselov and Andre Geim in 2010. During this phase, aside from efforts to deepen understandings of the fundamental aspects of graphene, there also needs to be a push to tap into the applications and manufacturing process, and to broaden the research into other two-dimensional (2D) materials and hybrid systems.

Development of graphene has the potential to impact products in several industries, from high performance computing and spintronics, to flexible, wearable and transparent electronics. The integration of such new materials should bring a fresh dimension to future technologies in a time where thinner, stronger, faster, flexible and broadband devices are needed. To achieve this goal, cost-efficient, large-scale production methods are necessary, with an aim of striking a balance between quality of material and ease of fabrication.

1.1.1 Graphene Production

Though theoretically hypothesised much earlier, graphene was first produced a little over a decade ago. Geim and Novoselov initially produced graphene by exploiting mechanical cleavage with the deceptively simple method of peeling Scotch tape off bulk Highly Orientated Pyrolytic Graphite (HOPG). Since then, methods of graphene production have advanced at an extraordinary rate. Today, there are several main methods of production, each with their own distinct advantages and disadvantages. The most common methods are summarised in Figure 1.2, and in Table 1.1.

Table 1.1: Comparison of different production methods graphene.

Production Method	Dimension	Number of Layers (#)	Mobility $cm^2/(V.s)$	Substrate (nm)	References
Exfoliated HOPG	∼tens of μm	Mono-, bi- & multilayer	∼10,000 (300K)	SiO_2/Si (+transfer)	Novoselov *et al.* (2004a)
Epitaxial Method	∼cm	Mono- to tens of layers	∼10,000 (300K)	C face of SiC	Berger *et al.* (2006)
CVD	∼cm	Mono- to <10 layers	∼3,700 (low)	SiO_2/Si (+transfer)	Kim *et al.* (2009)
Reduced GO	∼tens μm	Monolayer+	∼400 (300K)	Arbitrary	Wang *et al.* (2009a)
LPE graphite	∼1μm	Monolayer+	∼400 (300K)	Arbitrary	Shih *et al.* (2011)

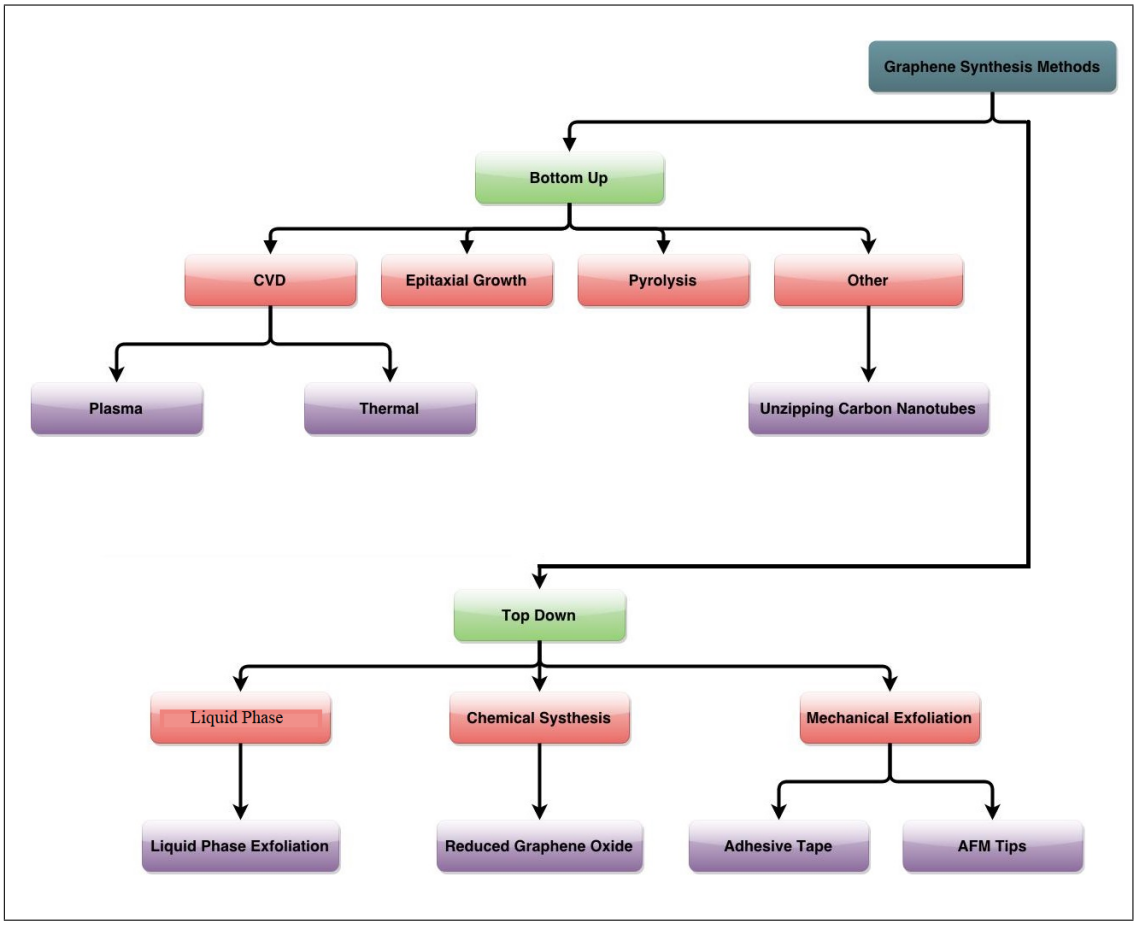

Figure 1.2: Graphene production methods.

1.1.1.1 Mechanical Exfoliation

Mechanical exfoliation is considered the first method of graphene production, which is a top-down technique in nanotechnology. The first method employed a longitudinal or transverse stress on the surface of the layered material using Scotch tape. An alternative method uses an Atomic Force Microscopy (AFM) tip to slice a single layer or several layers from the material onto a chosen substrate.

Graphite is formed when monatomic graphene layers are stacked together, and are attached by weak van der Waals forces. The interlayer bond energy and the interlayer distance are $2eV/nm^2$ and $3.34\mathring{A}$, respectively. For mechanical cleaving, an external force of roughly $300nN/\mu m^2$ is necessary to separate one monatomic layer from graphite (Zhang *et al.*, 2005).

Lu *et al.* (1999) first proposed the mechanical exfoliation technique using plasma-etched, pillared Highly Orientated Pyrolytic Graphite (HOPG), using AFM tips to fabricate graphene. With this method, thin, multilayered graphite was fabricated with the lowest thickness of around 200nm, which equates to between 500 to 600 layers of monolayer graphene.

Then in 2004, Novoselov et al. utilised adhesive tape to manufacture single layers of graphene by employing a mechanical cleaving technique from 1 millimetre thick HOPG. Initially, they employed dry etching, using oxygen plasma, to prepare few millimetres thick graphite mesas on the graphite platelets. These graphite platelets were then compressed against a 1 millimetres thick, wet photoresist over a glass substrate, which was then baked, to firmly attach the HOPG mesas to the photoresist. Next, using the famous Scotch tape, they progressively peeled off the graphite flakes, then released the flakes into acetone. Novoselov et al. used a silicon wafer, comprised of n-doped Si with an SiO_2, and transferred the graphene (single layer and few layer) from the acetone to the Si substrate, which was then cleaned with water and propanol.

Thin graphene flakes, with a thickness under 10 nanometres, adhered to the surface of the wafer. The adhesive force between the graphene and the Si substrate was explained by van der Waals and/or capillary forces.

1.1.1.2 Liquid-Phase Exfoliation

Graphite can be exfoliated in a liquid environment if ultrasounds are exploited to extract the individual layers. The Liquid Phase Exfoliation (LPE) process generally involves three steps:

1. dispersion of graphite in a solvent
2. exfoliation
3. purification

The third step is required to separate the exfoliated flakes from the unexfoliated flakes, and is generally carried out via ultracentrifugation.

The LPE yield can often be described in several ways. The yield by weight ($Y_W[\%]$) is also defined by the ratio between the weight of dispersed graphitic material and that of the starting graphite flakes (Hernandez *et al.*, 2008a). The yield by Single Layer Graphene (SLG) percentage ($Y_M[\%]$) is defined by the ratio between the number of SLG and the total number of graphitic flakes in the dispersion (Hernandez *et al.*, 2008a). The yield by SLG weight ($Y_{WM}[\%]$) is defined as the ratio between the total mass of dispersed SLG and the total mass of all dispersed flakes. Y_M does not give any information on the number of SLG, but only on the amount of graphitic material. $Y_M[\%]$ and $Y_{WM}[\%]$ are more suitable to quantify the amount of dispersed SLG.

To determine Y_W it is necessary to calculate the concentration (c $[gL^{-1}]$) of dispersed graphitic material, c is often determined via Optical Absorption Spectroscopy (OAS), making use of the Beer-Lambert Law:

$$A = \alpha c l \tag{1.1}$$

where A is the Absorbance (A), α $[Lg^{-1}m^{-1}]$ is the Absorption Coefficient (α), and l [m] is the length of the optical path.

A can be determined experimentally by filtering a known volume of the dispersion, for example, via vacuum filtration, onto a filter of known mass, and the measure the resulting mass using a microbalance (Hernandez *et al.*, 2008a,b; Khan *et al.*, 2010; Lotya *et al.*, 2009, 2010; Valles *et al.*, 2008). The filtered material is made up of graphitic flakes, surfactants or solvents and residual from the filter. Thermogravimetric Analysis (TGA) is used to determine the weight percentage of graphitic material in it, this enabling the measurement of c (Kim & Drzal, 2009; Sun *et al.*, 2010a,d; Valles *et al.*, 2008).

Though different values for α have been determined for both aqueous-based (Lotya *et al.*, 2009) and non-aqueous-based (Hernandez *et al.*, 2008b) dispersions by different groups, α was determined to be $2,460$ $L.g^{-1}.m^{-1}$ for several solvents: N-Methylpyrrolidone (NMP), Dimethylformamyde (DMF), Benzyl Benzoate, γ-Butyrolactone (GBL), etc. by Hernandez *et al.* (2008b), whereas Khan *et al.* (2010) later reported $\alpha \sim 3,620$ $L.g^{-1}.m^{-1}$ for these same solvents. As for aqueous, $\alpha \sim$

$1,390\ L.g^{-1}.m^{-1}$ was reported by Lotya *et al.* (2009) for Sodium Dodecylbenzene Sulfonate (SDBS), while they later stated a high value of $\alpha \sim 6,600\ L.g^{-1}.m^{-1}$ (Lotya *et al.*, 2010), also for an aqueous solution, this time Sodium Cholate (SC) was used as a surfactant. The group attribute this change to the difference in Concentration (c) in the two dispersions. However, α must not be dependent on c, and so more work is required to confirm the value.

Y_M is generally determined by utilising Transmission Electron Microscopy (TEM) and atomic force microscopy (AFM). In TEM, N can be counted by either analysing the edges of the flakes or by using electron diffraction patterns. AFM enables the estimation of N by measuring the height of the deposited flakes and dividing by the graphite interlayer distance. Though, the estimation of the SLG height by AFM is dependent on the substrate in question. For example, on SiO_2, a SLG can appear to have a height of $\sim$ 1nm (Novoselov *et al.*, 2005b), whereas on mica this height is $\sim$ 0.4nm (Valles *et al.*, 2008). Raman spectroscopy can be utilised to determine Y_M (Hasan *et al.*, 2010), and to confirm the result obtained via TEM and/or AFM.

$Y_{WM}[\%]$ requires the estimation of the SLGs area, other than N. Although this is more accurate with respect to Y_W and Y_M, determining this way is more time consuming. This method has reportedly only been employed once, that being when it was defined (Hernandez *et al.*, 2008b).

Graphene flakes can be obtained by exfoliaton of graphite via chemical wet dispersions followed by ultrasonication in water (Green & Hersam, 2009; Maragó *et al.*, 2010) and organic solvents (Blake *et al.*, 2008). Ultrasound-assisted exfoliation is controlled by hydrodynamic shear forces, associated with cavitation. This is the formation, growth, and collapse of bubbles or voids in liquids due to pressure fluctuations. After exfoliation, the solvent-graphene interaction needs to balance the inter-sheet attractive forces.

Solvents that minimise the interfacial tension [mN/m] between the liquid and graphene flakes (i.e., the force that minimises the area of the surface in contact) are ideal for dispersing graphene. In general, the interfacial tension plays a key role when a solid surface is immersed in a liquid medium. If the interfacial tension between the solid and the liquid is high there is a poor dispersibility of the solid in the liquid.

In the case of graphitic flakes in solution, if the interfacial tension is high, the flakes tend to adhere to each other and the work of cohesion, the energy per unit area required to separate two flat surfaces in contact, between them is high, which hinders their dispersion in the liquid. Liquids with a Surface Tension (γ) of ~ 40 mN/m work best as solvents for the dispersion of graphene, as they minimise the interfacial tension between solvent and graphene.

Most of the solvents that have such surface tension (NMP, DMF, GBL, etc.) have some disadvantages. NMP is toxic to reproductive organs, for example. These solvents also have high boiling points (>450K), which makes it difficult to remove the solvent after exfoliation. However, it is possible to use low-boiling point alternatives, such as acetone, chloroform, etc.

Water has $\gamma \sim 72$ mN/m, which is too high for dispersing graphene and graphite (Wang *et al.*, 2009b). In this case, linear chain surfactants, such as sodium dodecylbenzene sulfonate (SDBS (Lotya *et al.*, 2009)), or bile salts, such as Sodium Deoxycholate (SDC) and SC (Hasan *et al.*, 2010), can be used to stabilise against re-aggregation by Coulomb repulsion. It is even possible to stabilise using polymers such as pluronic (Seo *et al.*, 2011). However, the method chosen is dependent on the final application, as the presence of surfactants/polymers can affect the conductivity of the flakes etc.

High concentration is necessary for large scale production of composites (Hernandez *et al.*, 2008b) and inks (Torrisi *et al.*, 2012). Y_M up to 70% was achieved via mild sonication in water with SDC, followed by SBS, and Y_M of 33% was achieved with NMP (Torrisi *et al.*, 2012). This difference is due to the difference in flake lateral size. In water-surfactant flakes are on average smaller (roughly 30nm to 200nm) than in NMP (1 μm) (Hernandez *et al.*, 2008b; Torrisi *et al.*, 2012), as the Viscosity (v), at Room Temperature (RT) of NMP (1.7 mPas) is higher than in water (1 mPas). Larger flakes in the higher viscosity medium experience a higher fricitonal force, which in turn reduces their sedimentation coefficient, making it more difficult for them to sediment. Therefore Y_M decreases in NMP compared with water.

LPE is cheap and easily scalable, and does not require expensive growth substrates. Also, it is an ideal means to fabricate inks (Torrisi *et al.*, 2012), thin films (Hernandez *et al.*, 2008b) and composites (Hasan *et al.*, 2009b). The resulting

materials can be deposited on different substrates (rigid or flexible) by spin and drop casting (Wang *et al.*, 2008), rod coating, spray coating (Blake *et al.*, 2008), screen and ink-jet printing(Torrisi *et al.*, 2012), vacuum filtration (Hernandez *et al.*, 2008b), Langmuir-Boldgett (Li *et al.*, 2008) and other techniques.

Liquid-phase exfoliated flakes have limited size due to both the exfoliation process, which induces in-plane fracture, and the purification process, which separates large, unexfoliated flakes. So far, LPE-SLG have area generally below 1μm (Hernandez *et al.*, 2008b; Zhang *et al.*, 2005).

1.1.1.3 Chemical Vapour Deposition

Chemical Vapour Deposition (CVD) is a chemical process used to manufacture high quality, high performing, solid materials. This production method is commonly used in the semiconductor industry to manufacture thin films. Generally, a substrate, often a wafer, is exposed to one or more volatile precursors, which react and/or decompose on the surface of said substrate to create the wanted deposition. There is a gas flow through the reaction chamber, to remove the volatile by-products produced during the CVD process.

There are now two variations of CVD that are now considered standard in producing graphene: Thermal Chemical Vapour Deposition and Plasma-Enhanced Chemical Vapour Deposition.

In its basic sense, Thermal Chemical Vapour Deposition (CVD) is a chemical process through which a substrate is introduced to thermally decomposed precursors, after which the desired material deposits onto the surface of the substrate at a high temperature. Due to high temperature sometimes being a hindrance or unwanted in some cases, the alternative plasma-assisted decomposition and reaction can be used to lower the process temperature.

However, there are several advantages to the thermal CVD method. This process does yield a high-quality, large-scale final product with remarkably high purity, due to the general lack of defects. Through tinkering with the CVD process parameters, it is possible to exert some control over a number of aspects of the resulting product, such as morphology, crystallinity, shape, and size. By varying the precursor material, it is possible to create a large range of nanomaterials and thin films using this method.

Lang (1975) first reported the deposition of monolayer graphitic material on platinum (Pt) utilising thermal CVD. The group reported that the decomposition of ethylene onto a platinum substrate resulted in the formation of a graphitic overlayer, as well as surface rearrangement of the substrate.

Four years later, Eizenberg & Blakely (1979) published about their work involving the formation of graphitic layer formation on nickel (Ni) (111). Their method consisted of doping single-crystal Ni (111) with carbon at an increased temperature of 1200-1300 Kelvin for an extended time period - roughly a week - and finished with quenching. The group employed detailed thermodynamic analysis to determine the carbon phase condensation on the Ni (111), and discovered that the carbon phase segregation on Ni (111) is solely dependant on the quenching rate.

1.1.2 Dirac Electrons

Graphene, a honeycomb net of $p\pi$-bonded carbon atoms, supports an unusual variety of quanta and quantum fields, which in turn leads to interesting low-energy physics. Most useful for optics is the fact that the electrons in graphene act as massless Dirac particles, a phenomenon discovered by Novoselov *et al.* (2005a). It is this remarkable characteristic that allows graphene to absorb electromagnetic radiation over such a wide wavelength range.

The electronic structure of graphene is summarised in Figure 1.3, and the electronic Density of States (DOS) for metals, semiconductors and graphene is displayed in Figure 1.5.

The low-energy band structure of graphene can be described by cones located at two inequivalent corners of the Brillouin zone

$$\pm\mathbf{K} = \left(\pm \frac{4\pi}{\sqrt{3}a}, 0 \right) \tag{1.2}$$

where a is the lattice constant. These are called the K and K' points. In these cones, there is a linear relation to the two-dimensional energy dispersion. Figure 1.4 shows the K point for graphene, and a comparative version for semiconductors.

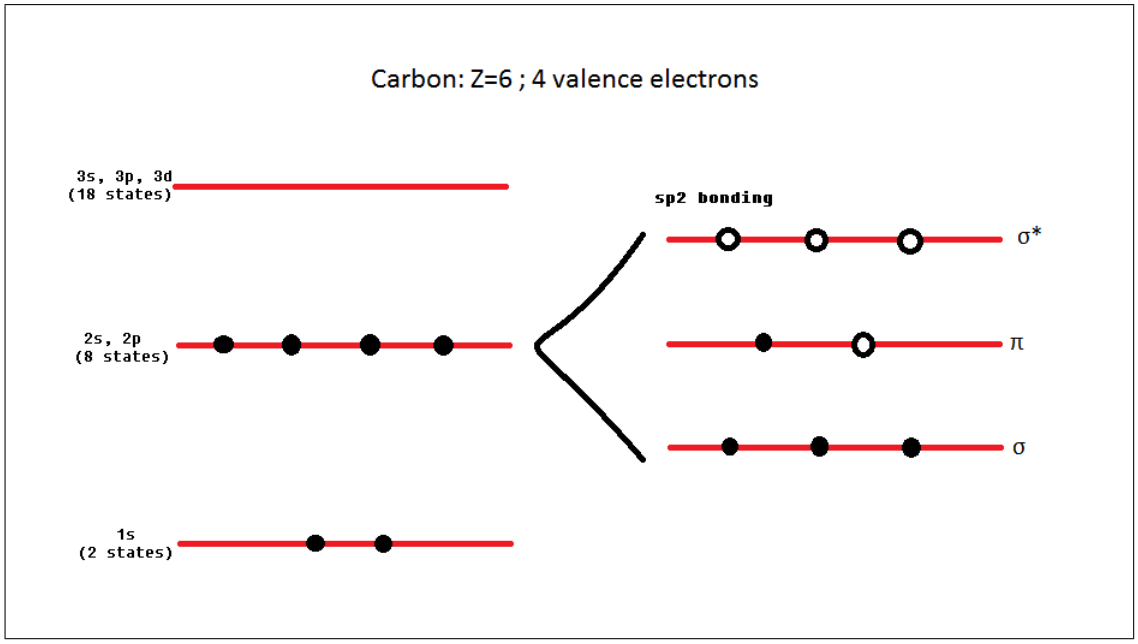

Figure 1.3: The Electronic Structure of Graphene

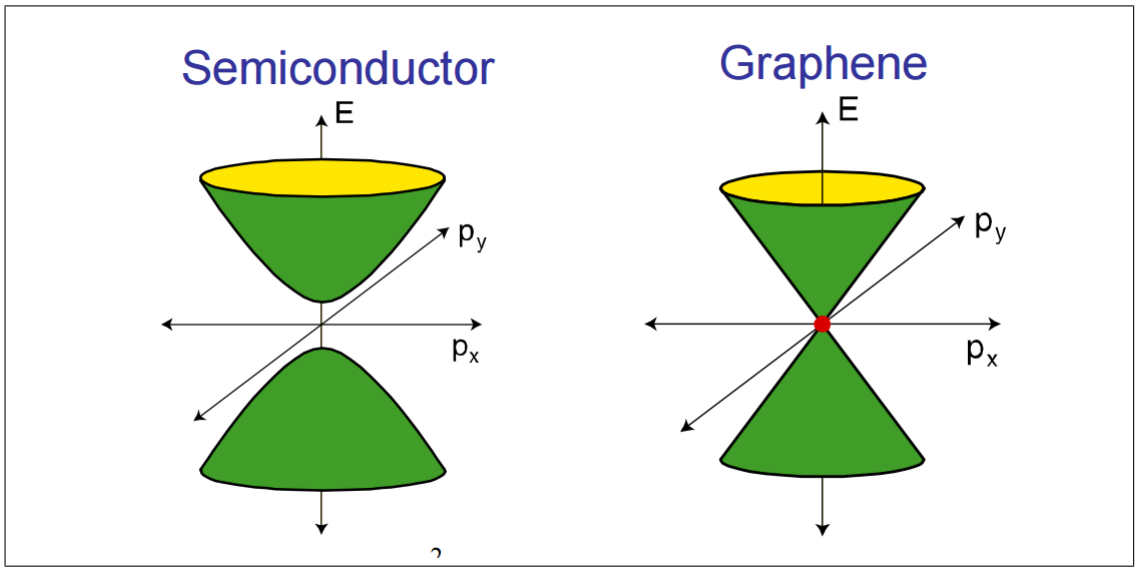

Figure 1.4: K Point for Semiconductors and Graphene

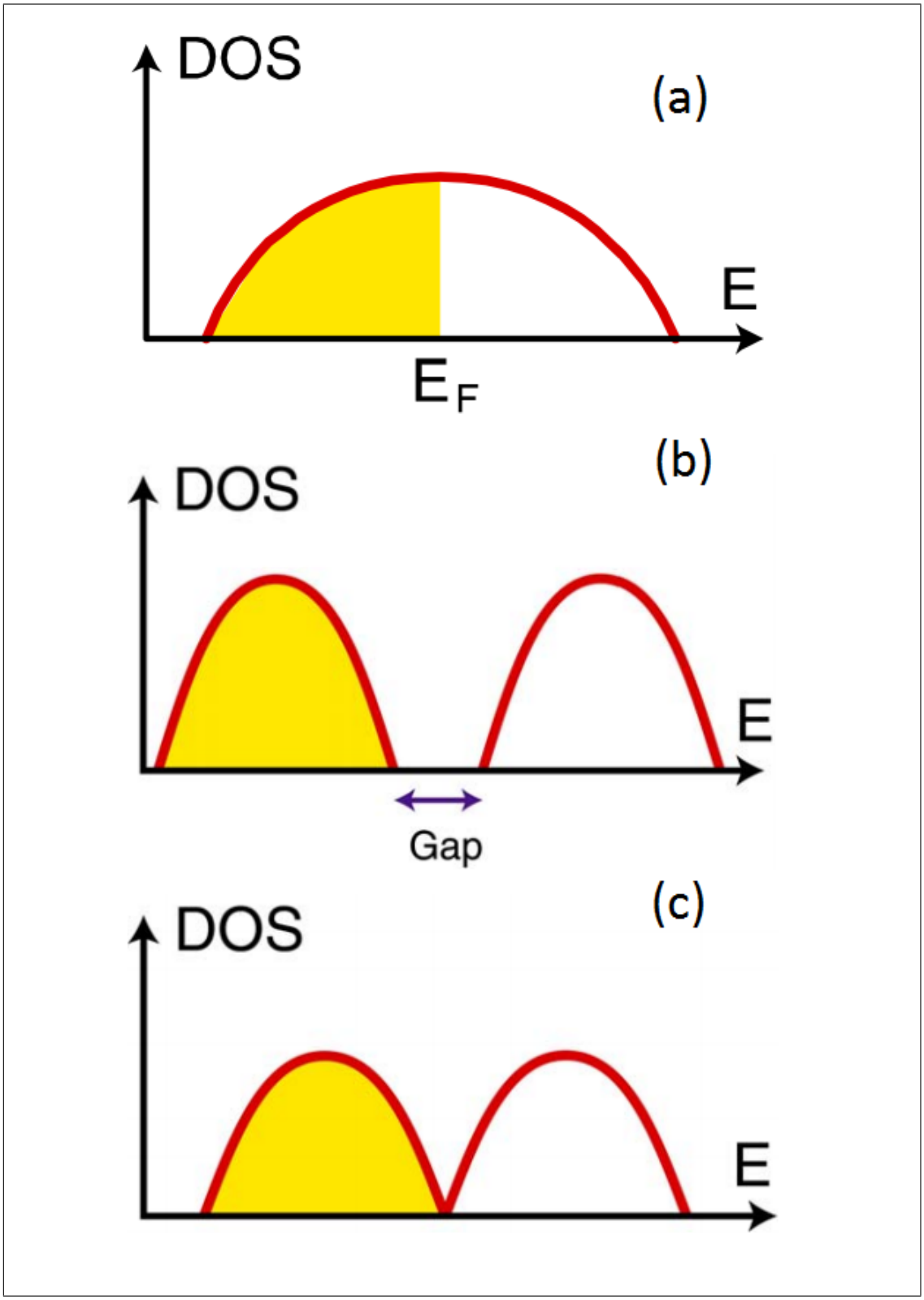

Figure 1.5: Electronic Density of States for Different Materials: (a) Metal, (b) Semiconductor, and (c) Graphene/Zero Gap Semiconductor/Zero DOS Metal

$$E_{\pm} = \hbar v_F |\mathbf{k} \mp \mathbf{K}| \tag{1.3}$$

in which $\mathbf{k} \simeq \pm\mathbf{K}$, and the Fermi Velocity (v_F) is $\approx 10^6 m/s \approx c/300$.

The electrons near the K and K' points are described well by the Dirac Hamiltonian in the Weyl representation

$$H_D^{\pm} = v_F(\pm\alpha_x p_x + \alpha_y p_y) = v_F(\pm\sigma_x p_x + \sigma_y p_y)\gamma_5 \tag{1.4}$$

$$\alpha = \begin{pmatrix} 0 & \sigma \\ \sigma & 0 \end{pmatrix} \tag{1.5}$$

$$\gamma_5 = \begin{pmatrix} 0 & 1 \\ 1 & 0 \end{pmatrix} \tag{1.6}$$

This describes a (2+1)-dimensional system, and the electrons are massless.

To reach this point, it is prudent to begin with relativity. A stationary particle (p=0) has a rest energy of

$$E = mc^2 \tag{1.7}$$

Whereas a particle in motion is described by the relativistic disperison relation:

$$E = \sqrt{(mc^2)^2 + (cp)^2} \tag{1.8}$$

and the velocity is given by:

$$v = \frac{\partial E}{\partial p} = c\frac{cp}{\sqrt{(mc^2)^2 + (cp)^2}} \tag{1.9}$$

The energy equation for a massive particle, such as an electron, is shown in Equation 1.8, for nonrelativistic limit, v<<c. This can be expressed as:

$$E \approx mc^2 + \frac{p^2}{2m} + \dots \tag{1.10}$$

Whereas for a massless particle, such as a photon, clearly when $m = 0$ the equations of 1.8 and 1.9 simplify to, respectively:

$$E = c|p| \tag{1.11}$$

$$v = c \tag{1.12}$$

Next, introducing the wave equation will show:

$$E = \hbar\omega \sim i\hbar\frac{\partial}{\partial t} \tag{1.13}$$

$$\overrightarrow{p} = \hbar k \sim -i\hbar\overrightarrow{\nabla} \tag{1.14}$$

For example, $\Psi = e^{i(k\bullet r - \omega t)}$. For non relativistic particles, Schrodinger Equation is arrived at:

$$E = \frac{p^2}{2m} \Longrightarrow i\hbar\frac{\partial\Psi}{\partial t} = -\frac{\hbar^2}{2m}\nabla^2\Psi \tag{1.15}$$

Whereas for relativistic particles, the math leads to the Klein-Gordon Equation:

$$E = c^2p^2 + m^2c^4 \Longrightarrow -\hbar^2\frac{\partial^2\Psi}{\partial t^2} = (-\hbar^2c^2\nabla^2 + m^2c^4)\Psi \tag{1.16}$$

To preserve particle conservation, quantum theory requires a wave equation that is first order in time. Dirac attempted to address this, and subsequently

developed Dirac Matrices (1.19) to solve this problem.

$$(p_x^2 + p_y^2 + m^2)\begin{pmatrix}1 & 0\\ 0 & 1\end{pmatrix} = \begin{pmatrix}m & p_x - ip_y\\ p_x + ip_y & -m\end{pmatrix}\begin{pmatrix}m & p_x - ip_y\\ p_x + ip_y & -m\end{pmatrix} \tag{1.17}$$

$$\sqrt{(p_x^2 + p_y^2 + m^2)I} = p_x\sigma_x + p_y\sigma_y + m\sigma_z \tag{1.18}$$

$$\sigma_x = \begin{pmatrix}0 & 1\\ 1 & 0\end{pmatrix}; \sigma_y = \begin{pmatrix}0 & -i\\ i & 0\end{pmatrix}; \sigma_z = \begin{pmatrix}1 & 0\\ 0 & -1\end{pmatrix} \tag{1.19}$$

This then leads to the Dirac Equation:

$$i\hbar^2\frac{\partial\Psi}{\partial t} = [-i\hbar(\sigma_x\frac{\partial}{\partial x} + \sigma_y\frac{\partial}{\partial y}) + \sigma_z m]\Psi \tag{1.20}$$

where $\Psi = \begin{pmatrix}\Psi_A\\ \Psi_B\end{pmatrix}$

1.1.3 Linear Optical Properties

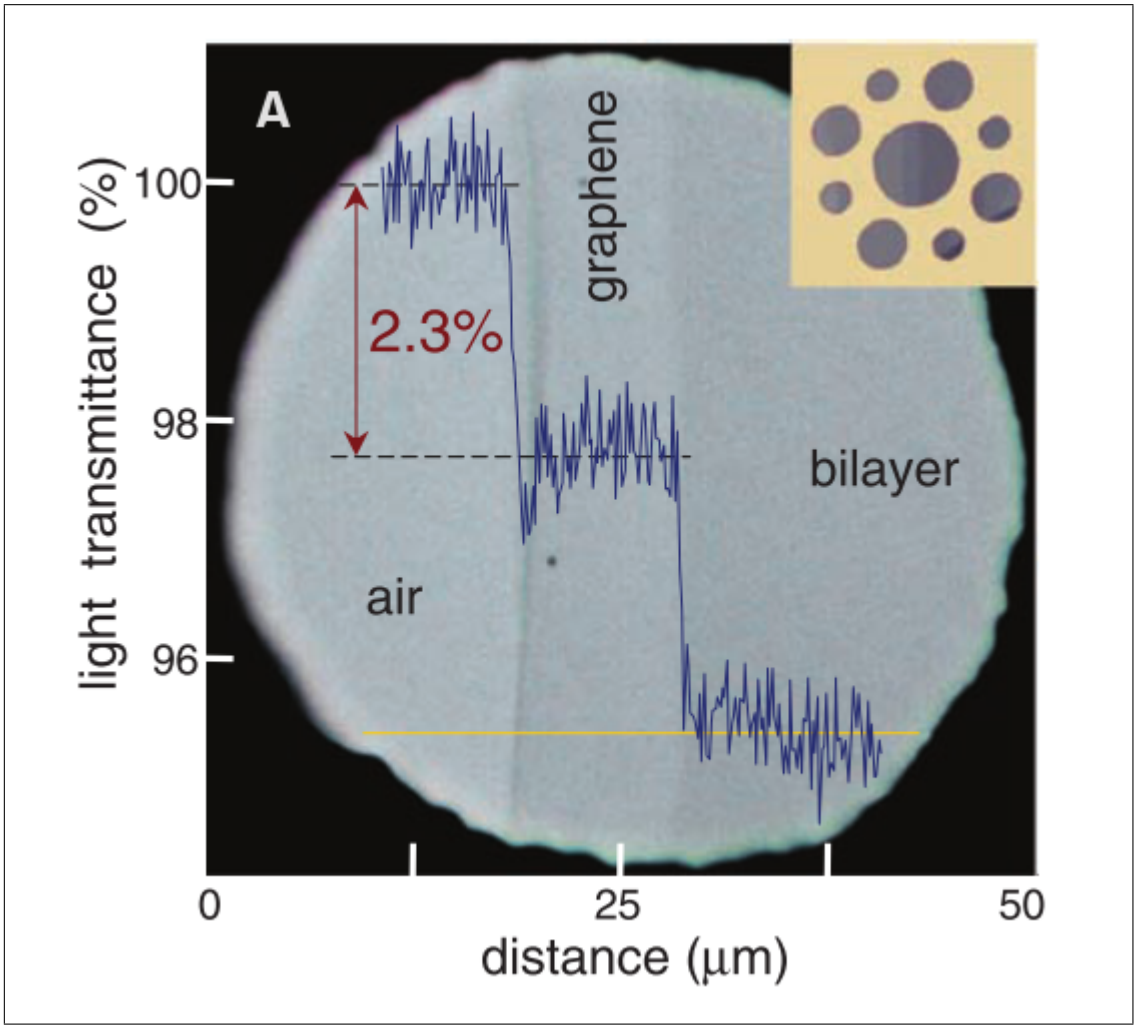

Figure 1.6: Photographof a 50-mmaperture partially covered by graphene and its bilayer. The line scan profile shows the intensity of transmitted white light along the yellow line. (Inset) The sample design used in the paper the figure is from: A 20μm thick metal support structure with several apertures (20, 30 and 50 μm in diameter), with graphene crystallites placed over them. This figure appears in Nair *et al.* (2008)

It has been shown by groups, such as Schedin *et al.* (2007), that the opacity of suspended graphene is solely defined by the fine structure constant, $\alpha = e^2/\hbar c \approx 1/137$, in which c is the speed of light. This is the parameter that relates the coupling of the relativistic electrons and light, and is generally associated with

quantum electrodynamics rather than material science. Even though graphene is just one atom thick, this material was discovered to absorb a significant percentage of incident white light ($\pi\alpha = 2.3\%$), which is an effect of the unique electronic structure of graphene. This is exhibited in Figure 1.6.

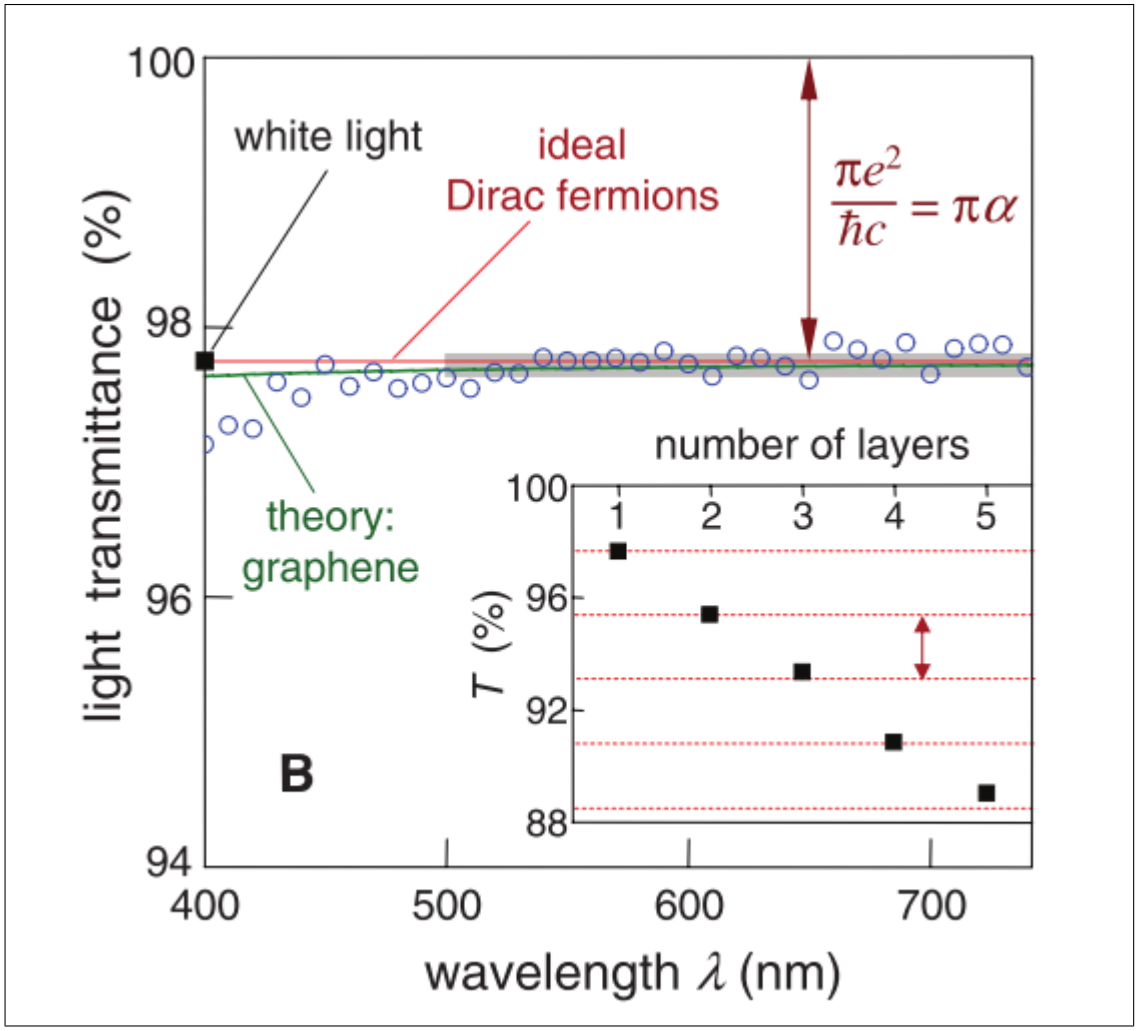

Figure 1.7: Shows the transmittance spectrum of single-layer graphene (open circles). There is slightly lower transmittance for λ <500nm, which is probably due to hydrocarbon contamination. Whereas the red line is the transmittance ($T = (1 + 0.5\pi\alpha)^{-}2$) and is expected for two-dimensional Dirac fermions, while the green curves takes into account the nonlinearity and triangular warping of the electronic spectrum of graphene. (Inset) The white light transmittance as a function of the number of graphene layers. the dashed red lines refer to the intensity reduction by $\pi\alpha$ with each added layer. This figure appears in Nair *et al.* (2008)

Other groups (Ando *et al.*, 2002; Gusynin *et al.*, 2006) have proposed that the Dirac fermions high-frequency conductivity (G) in graphene should be a universal constant which is equal to $e^2/4\hbar$ and is different from the universal dc conductivity, which is equal to $4e^2/\pi h$.

This universal G means that some observable quantities, for example the reflectance, R, and the optical transmittance, T (Kuzmenko *et al.*, 2008). For normal light incidence on the graphene, $R \equiv 0.25\pi^2\alpha^2 T$ and $T \equiv (1 + 2\pi G/c)^-2 = (1 + 0.5\pi\alpha)^-2$. This can be used to give the opacity of graphene, which is $(1 - T) \approx \pi\alpha$. Figure 1.7 shows the transmittance spectrum for graphene.

The fact that the optical properties of graphene can be expressed by the fundamental constants is due to the two-dimensional nature of the material, as well as the gapless electronic spectrum. Interestingly, it does not have any direct dependence on the chirality of the charge carriers (Nair *et al.*, 2008).

1.2 Laser

"A laser is a device that amplifies light and produces a highly directional, high-intensity beam that most often has a very pure frequency or wavelength. It comes in sizes ranging from approximately one tenth the diameter of a human hair to the size of a very large building, in powers ranging from 10^{-9} *to* 10^{20} *W, and in wavelengths ranging from the microwave to the soft-X-ray spectral regions with corresponding frequencies from* 10^{11} *to* 10^{17} *Hz. Lasers have pulse energies as high as* 10^4 *J and pulse durations as short as* 5×10^{-15} *s. They can easily drill holes in the most durable of materials and can weld detached retinas within the human eye. They are a key component of some of our most modern communication systems and are the "phonograph needle" of our compact disc players. They perform heat treatment of high-strength materials, such as the pistons of our automobile engines, and provide a special surgical knife for many types of medical procedures. They act as target designators for military weapons and provide for the rapid check-out we have come to expect at the supermarket. What a remarkable range of characteristics for a device that is in only its fifth decade of existence!"*

-Silfvast (1996)

Laser is an acronym standing for "Light Amplification by Stimulated Emission of Radiation", and the term was first published by Gordon Gould (1959) at a conference. There is still some debate over who deserves the credit for the actual theoretical invention of the laser, with both Charles Hard Townes and Gould having credible claims.

However, the first functioning laser was created by Theodore H. Maiman, and was first successfully operated on May 16th, 1960. This laser used an artificial ruby crystal as the gain medium or amplifier, and was pumped by solid-state flashlamp as the energy source (Maiman, 1960). The helical flashlamp surrounded a rod-shaped ruby crystal, while the optical cavity was formed by coating the flattened ends of the ruby rod with a high-reflecting material. The emitted radiation was red light, with $\lambda = 694nm$.

The first gas laser followed very soon after, achieved by Ali Javan, William R. Bennett and Donald Herriott at Bell Laboratories on December 12th, 1960, utilising helium and neon as the gain medium to produce a continuous-wave emission in the infrared region, with five wavelengths possible (Javan *et al.*, 1961). Also at Bell Laboratories, L. F. Johnson and K. Nassau developed the world's first neodymium laser (Geusic *et al.*, 1964).

The first laser diode was created in 1962 by Nick Holonyak, Jr., which emitted at 850nm, and was made from gallium arsenide (Holonyak Jr & Bevacqua, 1962).

Lasers can be subcategorised based on their characteristics, such as mode of operation:

- Continuous wave laser systems
- High power Q-switched systems
- Pulsed laser systems (Mode-locked)

Or by the mechanism by which population inversion is achieved:

- Three level lasers
- Four level lasers

Or based on the gain/active medium:

- Gas laser
- Semiconductor laser
- Solid state laser
  - Fibre laser
- Tunable dye laser

1.2.1 Coherence

Lasers, and more specifically the radiation produced, have several characteristics that set them apart from the light that is more common in daily life, such as sunlight and that from bulbs. The most important trait is that the laser emits light that is highly coherent. There are several types of coherence:

- Temporal coherence
- Spatial coherence
- Spectral coherence
- Polarisation coherence

Temporal and spatial coherence are the more important characteristics to consider when it comes to laser science.

Temporal coherence in the most basic sense determines whether or not the beam is monochromatic. It is the measurement of the average correlation between the value of a wave and that of the wave delayed by time, τ. The delay over which the amplitude or phase of the wave varies by a significant amount, and therefore the correlation is also lowered, and referred to as the coherence time, τ_c. When there is no delay ($\tau = 0$), the coherence is perfect, but will drop substantially

when the delay passes times equal to the coherence time ($\tau = \tau_c$). The so-called Coherence Length (L_c) is the distance that the wave travels during τ_c.

Spatial coherence comes into play when considering wave states that can extend over one or two dimensions. It refers to the interference ability of two points, x_1 and x_2, in space within the wave, when averaged over time. The spatial coherence is the cross-correlation between two points in a wave at all times. To be perfectly spatially coherent, a wave requires a single amplitude value over an infinite length. The range of separation between the two points over which there is significant interference is referred to as the Coherence Area (A_c).

1.2.2 Laser Systems

The basic idea behind laser technology is harnessing the stimulated emission of specific media, which is known as the gain medium.

Said gain medium generally can be thought of as a population of atoms, initially in their ground state. These atoms are then exposed to some form of pump energy, often other photons from a flashlamp or another laser, which causes the electrons in the atom to go to an excited quantum, or high-energy, state. Once in this excited state, emission can either be spontaneous or stimulated. In the case of the former, without any outside influence, the atom returns to its ground state, and a photon is emitted after an arbitrary time. However, particles can interact with electromagnetic radiation and either absorb or emit photons. So, when in this excited state, if another photon interacts with the atom, a photon is emitted, travelling in the same direction as the interacting one.

Population inversion is achieved when the number of atoms in the excited energy state surpasses the number of atoms in the ground state, and once this occurs the amount of stimulated emission due to light passing through is larger than the amount of photons absorbed. Hence, the light is then amplified, and this set-up is referred to as an optical amplifier.

To "complete" the laser, such an optical amplifier is placed inside resonant optical cavity, and the whole apparatus is a laser oscillator.

1.2.2.1 Three-Level and Four-Level Laser

A common approach for producing a population inversion in a laser system is to add energy to the medium in order to excite the molecules or atoms into higher energy levels. Under thermodynamic equilibrium, adding energy by thermal agitation of the medium is not sufficient to produce population inversion, because heat can only increase the average energy of the population. It does not increase the number of species in the excited state relative to that in the lower state. The ratio of the number of atoms at two energy levels (1 and 2) is given by the Equation 1.21 under thermodynamic equilibrium:

$$N_2/N_1 = e^{[-(E_2-E_1)/kT]} \tag{1.21}$$

where N_1 and N_2 are the number of atoms in level 1 and level 2, respectively, E_1 and E_2 are the energies of the two levels, T is the temperature in kelvins, and k is the Boltzmann constant. As seen in Equation 1.21, at thermodynamic equilibrium, N_2 can be greater than N_1 only if the temperature is a negative number. Before maser and laser action research was published, physicists referred to a population inversion as a negative temperature, which was indicative of the view that any condition other than thermodynamic equilibrium was not likely to be sustainable.

To achieve the necessary population inversion for laser activity, atoms or molecules must be selectively excited to specific energy levels. Light and electricity are the superior excitation mechanisms for most lasers. Either light or electrons can provide the energy required to excite atoms or molecules to the selected, higher energy levels, and the transfer of energy does not need to directly excite electrons to a specific upper level of the laser transition. One frequently used method excites an atom or molecule to a higher energy level than required, after which it drops to the upper laser level. Indirect excitation can be employed to excite atoms in a surrounding gas mixture, which then transfer their energy to the atoms or molecules responsible for producing the laser action.

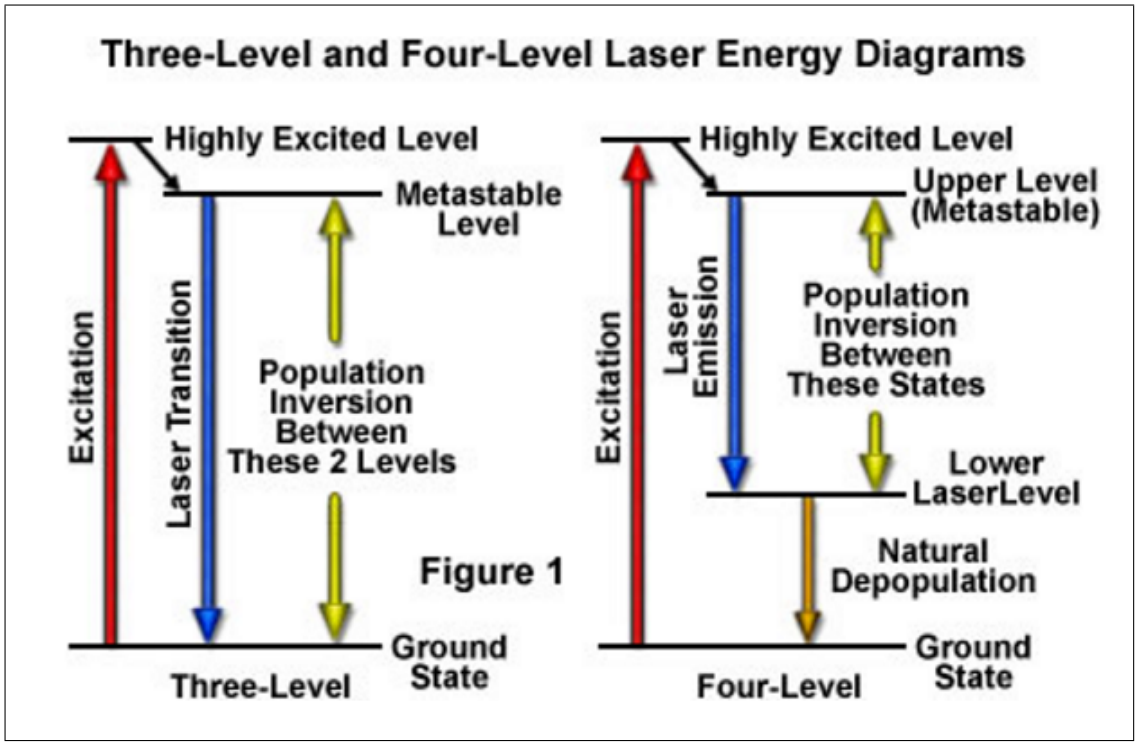

Figure 1.8: Three-Level and Four-Level Laser Energy Diagrams

The amount of time spent by an atom or molecule in an excited state is critical in determining whether it will be stimulated to emission and participate in a cascade of photons, or lose the energy through spontaneous emission. Excited states often have lifetimes of just nanoseconds before releasing their energy via spontaneous emission. Such a timescale is not long enough to consistently undergo stimulation by another photon. A critical requirement for laser action is a longer-lived state that is suitable for the upper energy level. Such states do exist for certain materials, and are referred to as metastable states, which can be seen in Figure 1.8.

The average lifetime before spontaneous emission occurs for a metastable state is on the order of a microsecond to a millisecond, a relatively long time on the atomic timescale. With lifetimes of this length, excited atoms and molecules can produce a significant amount of stimulated emission. Laser action is only possible if the population builds up faster than it decays in the upper energy level, maintaining a population larger than that of the lower level. The longer the spontaneous emission lifetime, the more suitable a molecule or atom is for laser applications.

The simplest functional energy-level structure for laser operation is the three-level system, which is illustrated in Figure 1.8. For a three-level laser, the ground state is the lower laser level, and a population inversion is created between this level and a higher-energy metastable state. Most of the atoms or molecules are initially excited to a short-lived high-energy state that is higher than the metastable level. From this state, there is a quick decay to the intermediate metastable level, which has a significantly longer lifetime than the higher energy state. This can often be 10^3 times longer. Because the time each atom resides in the metastable state is comparatively long, the population tends to increase and leads to a population inversion between the metastable state and the lower ground state, which is continuously being depopulated to the highest level. Stimulated emission results from the fact that more atoms are available in the upper excited (metastable) state than in the lower state where absorption of light would most likely occur.

Although the three-level laser system works for all practical purposes, there are a number of problems which limit the effectiveness of this approach. The main problem occurs because the lower laser level is the ground level, which is the normal state for most atoms or molecules. In order to produce the population inversion, a majority of ground state electrons must be moved to the highly excited energy level, which needs a significant external energy input. The population inversion is difficult to sustain for an appreciable time, and therefore, three-level lasers must be operated in pulsed mode rather than continuously.

Lasers which use four or more energy levels sidestep some of the problems mentioned above, and therefore are more commonly utilized. The energy level structure is similar to that in the three-level system, except that after the atoms drop from the highest level to the metastable upper state, they do not drop all the way to the ground state in a single step. The population inversion is not created between the ground state and the upper level, the number of atoms or molecules that must be elevated is dramatically reduced in this model. In a typical four-level laser system, if only one or two percent of the atoms or molecules reside in the lower laser level (which is above the ground state), then exciting only two to four percent of the total to the higher level will achieve the required population inversion.

Another benefit of separating the lower laser level from the ground level is that the lower level atoms will naturally fall to the ground state. If the lower laser level has a lifetime that is much shorter than the upper level, atoms will decay to the ground level at a rate that avoids accumulation in the lower laser level. Many of the lasers designed under these constraints can be operated in a continuous mode to produce an uninterrupted beam.

1.3 Fibre Lasers - ISLA

Industrial lasers are used in the fabrication of a huge variety of everyday items. The powerful, focussed beam of light they produce is used, for example, to slice through metal, mark serial numbers onto surfaces, etch energy producing solar panels, and quickly and accurately cut out plastic components.

ISLA was a research and development project with the key aim of challenging the boundaries of current laser material processing technology. It took current components, which operate at a wavelength of $1\mu m$ (one millionth of a meter), and developing them to operate at double this wavelength, $2\mu m$. By doing this, the power of the system can be increased by around ten times.

The project ran from October 1st, 2011 until June 30th, 2015. The ISLA project was undertaken by a consortium of top companies and research groups in Europe, including:

1. Gooch and Housego (Torquay)
2. II-VI Laser Enterprise
3. JDSU (formerly Time-Bandwidth Products)
4. Rofin-Sinar Laser
5. Vivid Components
6. ORC Southampton
7. Trinity College Dublin

Until now, materials processing applications have used the $1\mu m$ components as they had already been adopted and developed by the telecommunications industry for sending data over long distance fibre optic cables such as those used by the Internet. In order to increase to $2\mu m$, a series of inter-dependant components had to be developed, including lasers (which create the light), glass fibres (which guide the light) and Q switches/mode lockers (which split a continual light source into a series of intense pulses). ISLA took on this challenge, bringing together the best in European engineering organisations with the support of the EU Commission under the Framework 7 funding mechanism to deliver new systems over a period of four years.

Prof. Werner J. Blau's group in Trinity College Dublin researched the viability of mode-locking such a laser system with a carbon-based device.

The overall aim of the project was to make three fibre lasers (1 Continuous Wave (CW) and 2 pulsed) based on Ho-doped fibre as the gain medium, pumped by a Tm fibre laser. The three types planned were:

1. Continuous Wave Laser - Rofin-Sinar Laser

    - Expected Results: 500 W CW Ho-doped fibre laser for the cutting of selected transparent plastics (without addition of any dyes or additives). The performance will be compared directly with a similar power 1 μm reference laser.

2. Q-switched Pulsed Laser - Rofin-Sinar Laser

    - Expected Results: 20 W 10 mJ Ho-doped Q-switched fibre laser; its performance will be demonstrated in the scribing of thin film PV panels. Higher scribing speed will be demonstrated for the ISLA 2 μm fibre laser compared with a 1m reference.

3. Graphene Mode-Locked Pulsed Laser - JDSU

    - Expected Results: 100W ps Ho-doped MOPA will explore the potential for scaling short pulse fibre sources in the 2 μm wavelength regime to much higher power levels.

1.4 Ultrafast Laser Applications

The ultrafast nonlinear properties of graphene have been intensively investigated by such research groups as Bonaccorso *et al.* (2010); Breusing *et al.* (2009); Choi *et al.* (2009); Kumar *et al.* (2009a); Sun *et al.* (2009, 2010d); Winnerl *et al.* (2011).

Two relaxation time scales are generally observed. A fast one (<100 fs), typically associated with carrier-carrier intra-band collisions and phonon emission (Breusing *et al.*, 2009), and a slower one (∼ps), which corresponds with the electron inter-band relaxation and cooling of hot phonons (Lazzeri *et al.*, 2006). Graphene is an ultrafast Saturable Absorption (SA) material (Bonaccorso *et al.*, 2010). Hasan *et al.* (2009a) were the first to report a Graphene Saturable Absorber (GSA) mode-locked laser. Subsequently, a variety of lasers mode-locked by graphene have been demonstrated (Bao *et al.*, 2009, 2010, 2011; Chen *et al.*, 2012; Cunning *et al.*, 2011; Sun *et al.*, 2010c).

Graphene has been sourced in various ways, such as liquid-phase exfoliation LPE (Cunning *et al.*, 2011), chemical vapour deposition CVD (Bao *et al.*, 2009, 2010), carbon segregation (Yu *et al.*, 2010), graphene oxide Graphene Oxide (GO) (Bao *et al.*, 2010), Reduced Graphene Oxide (RGO) (Song *et al.*, 2010a) and micromechanical cleavage (Bonaccorso *et al.*, 2010). Many different approaches have been investigated for integrating GSAs into cavities, such as sandwiching, free-space coupling, placement inside Photonic Crystal Fibres (PCF), and evanescent field interaction. These mostly follow from previous approaches used for Single Wall Nanotube (SWNT) SAs. Sandwiching a GSA is currently the most common method used for GSA integration (Barone *et al.*, 2006; Cho *et al.*, 2011; Du *et al.*, 2009; Meyer *et al.*, 2007).

Compared to traditional SAs, like Semiconductor Saturable Absorber Mirror (SESAM) and SWNT-SAs, the major advantage of using graphene is the intrinsic wide-band operation. So far, GSAs have been able to produce pulses at 1 μm (Tan *et al.*, 2010), 1.25 μm (Cho *et al.*, 2011), 1.5 μm (Cunning *et al.*, 2011) and 2 μm (Liu *et al.*, 2012). Similar to SWNT-SAs, GSA have been mostly combined with Erbium Doped Fibre Laser (EDFL) (Balandin *et al.*, 2008; Zhang *et al.*, 2009b), not because GSA has any requirement for wavelength, but because EDFLs can easily produce soliton pulses in single mode fibres, and all necessary components

are economically available from the optical telecom market. Sun *et al.* (2010d) reported GSA mode-locked fibre lasers tunable in the 1,525nm to 1,559nm range, only limited by the filter used in the cavity. Zhang *et al.* (2010) report sin 240 fs tunable pulse generation using fibre lasers under different operation regimes (e.g., all-anomalous to all-normal dispersion). Stretched-pulse design was employed, generating sub-200fs pulses (Popa *et al.*, 2010). Liu *et al.* (2011a) reported 163nJ pulse generation. Whereas other groups also report pulse generation using solid-state lasers mode-locked by GSAs. 94fs tunable ($\sim$ 1.22μm to 1.27μm) pulses have been achieved with a GSA mode-locked solid state Cr: forsterite laser (Cho *et al.*, 2011). High-power ($\sim$1 W) pulses have been demonstrated with a GSA mode-locked ND:YVO_4 solid-state laser (Zhang *et al.*, 2011a).

A summary of successful incorporation of graphene as a saturable absorber for ultrafast pulse generation can be seen in Table 1.2

1.5 Nonlinear Optics

Nonlinear optics is the field that deals with the behaviour of light in a nonlinear medium, which are media in which the Dielectric Polarisation (P) responds nonlinearly to the Electric Field (E) of light. In general, most materials can be considered "nonlinear" as linear optics is essentially just an approximation, which ignores the higher order sections.

This is partially due to nonlinear optical effects requiring very high intensity light, of the order of roughly $10^{13}W/m^2$, while sunlight is only about $10^2W/m^2$ (Gates, 1966), an 11 order of magnitude difference. This difference is not usually apparent in every day life, as normal light sources are incoherent. Also, phase matching is necessary to realise nonlinearity. Therefore, laser light is required to make use of the nonlinear effects.

When the field strength is small enough, the linear approximation is quite accurate.

$$P(t) = \varepsilon_0 \chi^{(1)} E(t) \tag{1.22}$$

Table 1.2: Ultrashort pulse generation using graphene as saturable absorber.

Sample	Laser Type	Repetition Rate (MHz)	Pulse Width (ps)	Wavelength (nm)	References
CVD Graphene	Fibre Laser	1.79	0.75	1565	Bao *et al.* (2009)
Exfoliated Graphene	Fibre Laser	27.4	0.17	1550	Popa *et al.* (2010)
Exfoliated Graphene	Fibre Laser	19.9	0.46	1559	Sun *et al.* (2010b)
Exfoliated Graphene	Fibre Laser	6.22	0.88	1566	Martinez *et al.* (2011)
Exfoliated Graphene	Solid-State-Laser (SSL)	-	16	1064	Xu *et al.* (2011c)

Where Polarisation Density ($P(t)$), ε_0 is the electric permittivity of free space, First-Order Optical Susceptibility ($\chi^{(1)}$) and E is the electric field. The susceptibility is a dimensionless proportionality constant that indicates the degree of polarisation of a dielectric material in response to an applied electric field (Young *et al.*, 2007).

$$\chi^{(1)} = \varepsilon_r - 1 \tag{1.23}$$

Where ε_r is the relative permittivity.

However, for very high field strength, the polarisation response is no longer linear, and can be decomposed into a Taylor series. This gives the nonlinear response as the sum of the quadratic response, third-power response and so forth.

$$P(E) = P^{(1)} + P^{(2)} + P^{(3)} + \cdots \tag{1.24}$$

$$\overrightarrow{P} = \varepsilon_0(\chi^{(1)}\overrightarrow{E} + \chi^{(2)}\overrightarrow{E}^2 + \chi^{(3)}\overrightarrow{E}^3 + \cdots) \tag{1.25}$$

In this work, the Third-Order Optical Susceptibility ($\chi^{(3)}$) was primarily of interest, which is related to the nonlinear refractive index, or Kerr nonlinearity, $n_2 \propto Real(\chi^{(3)})$, and the nonlinear absorption coefficient, $\beta \propto Imaginary(\chi^{(3)})$ (Weinberger, 2008).

$$Im(\chi^{(3)}) = \frac{n_0^2 \varepsilon_0 c^2 \beta}{\omega} \tag{1.26}$$

Where c is the speed of light in a vacuum, Frequency (ω) and $n_0 = Re(\sqrt{1+\chi^{(1)}})$ and is the dispersion, frequency is dependent on speed of propagation.

$$n^2 = 1 + \chi_{eff} = 1 + \chi^{(1)} + \frac{3\chi^{(3)}}{4}E_0^2 \tag{1.27}$$

But

$$I = \frac{1}{2}\sqrt{\frac{\varepsilon}{\mu_0}}E_0^2 \tag{1.28}$$

$$n = n_0 + n_2 I \tag{1.29}$$

$$n_2 = \frac{3\chi^{(3)}}{4n_0}\sqrt{\frac{\mu_o}{\varepsilon_r \varepsilon_0}} = \frac{3\chi^{(3)}}{4n_0^2}\sqrt{\frac{\mu_o}{\varepsilon_0}} \tag{1.30}$$

The Kerr effect is the change in the refractive index of a material in response to an applied electric field (Coelho, 2012).

In these regimes, the uses of the nonlinear material can be broadly determined to be one of two, either saturable absorption or optical limiting.

For mode-locking a material with saturable absorption SA is desired. Saturable absorption is a property of a material in which the absorption of the material decreases as the light intensity increases as more and more light is transmitted at higher and higher intensities. Therefore SA is useful in letting random high intensity fluctuations through, while absorbing the lower intensity light. It requires very high intensities of light to manifest. It occurs due to the sufficiently high intensities of light striking the material, and the atoms in the ground state becoming excited into an upper energy state at a such a high rate that there is not enough time for the electrons to decay back to the ground state before it has become depleted, and therefore the absorption saturates.

This can be attributed to Pauli Blocking, which is a consequence of the Pauli Exclusion Principle. The Pauli Exclusion Principle states that, in an atom or molecule, no two electrons can have the same four electronic quantum numbers, essentially stating that only one electron can occupy a particular state at one time. A consequence that an orbital can contain two electrons at most, the two electrons must have opposite spins. This means if one is assigned an up-spin (+1/2), the other must therefore have down-spin (-1/2).

Electrons that are in the same orbital have the same first three quantum numbers. Which are, for example, $n = 1$, $l = 0$, $m_l = 0$ for the 1s subshell. Only two electrons can have these numbers, so that their spin moments must be either $m_s = 1/2$ or $m_s = +1/2$. Whereas, if the 1s orbital has just one electron, there is one m_s value and the electron configuration is written as 1s1, which corresponds

to hydrogen. However, when it is fully occupied, there are two m_s values, with an electron configuration of 1s2, which corresponds to helium.

Therefore, Pauli blocking will occur when the last transition states are filled, so incoming electrons can not complete this transition. Which, again, is a direct consequence of the Pauli exclusion principle. So, if there is sufficient intensity of photons on the material, the absorption saturates, and photons arriving after transmit through the material with little loss.

The other use is optical limiting, which is important for laser safety applications (Harter *et al.*, 1984). The nonlinear optical properties that are harnessed for this purpose are Reverse Saturable Absorption (RSA) and Nonlinear Scattering (NLS). Both achieve the same goal, but via different methods. In the case of RSA, the absorption of the material increases as the light intensity increases. Similarly, nonlinear scattering increases as in the intensity of light increases. The result of both is a decrease of transmission as light intensity increases.

Nonlinear scattering can often occur when the absorbent is in a matrix or solution. The absorbent releases some of the laser power absorbed into the surrounding media as thermal energy, and depending on the properties of said surrounding media, either plasma or microbubbles (solution) can form. These act as scattering centres, the number of which increases with increasing intensity, and as such, the scattered light increases also.

1.6 Mode-locking

Mode-locking is arguably the most popular method to achieve ultrashort pulses lasers. Lasers with multi-gigahertz repetition rates have become very important in modern times for many applications. They are a mainstay in high-capacity telecommunication systems, photonics switching devices and optical interconnections, among many other fields. A brief history of mode-lock laser technology is shown in Figure 1.9 (Keller, 2003).

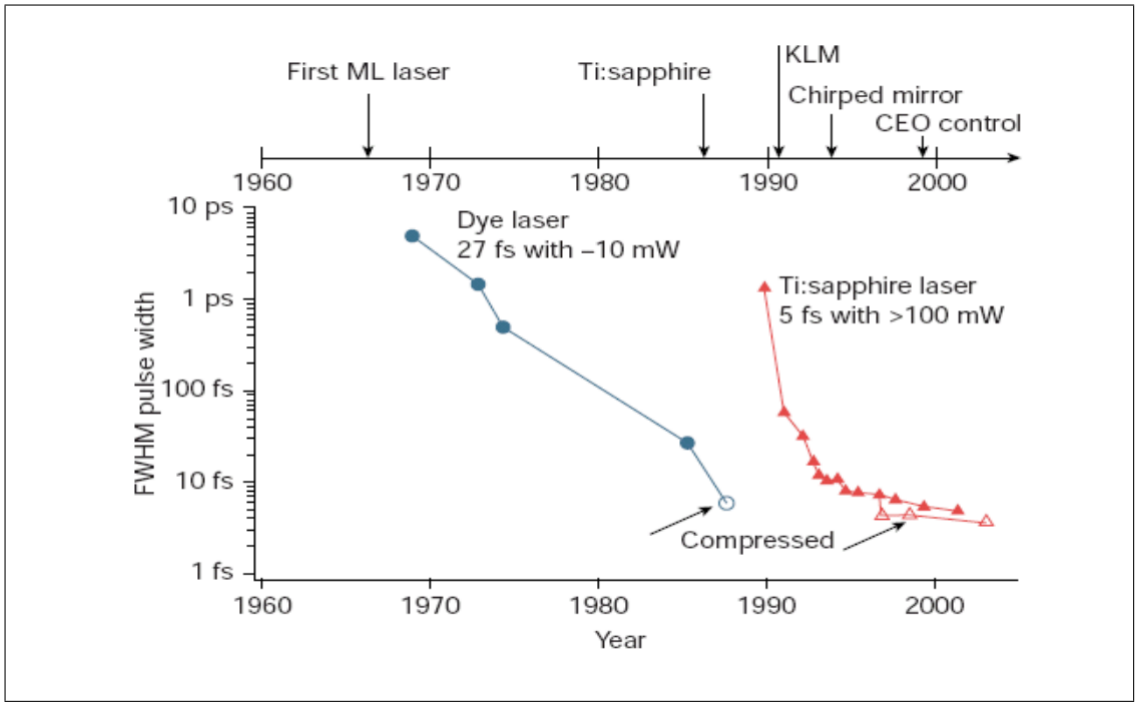

Figure 1.9: History of mode-locked pulsed laser technology (Keller, 2003)

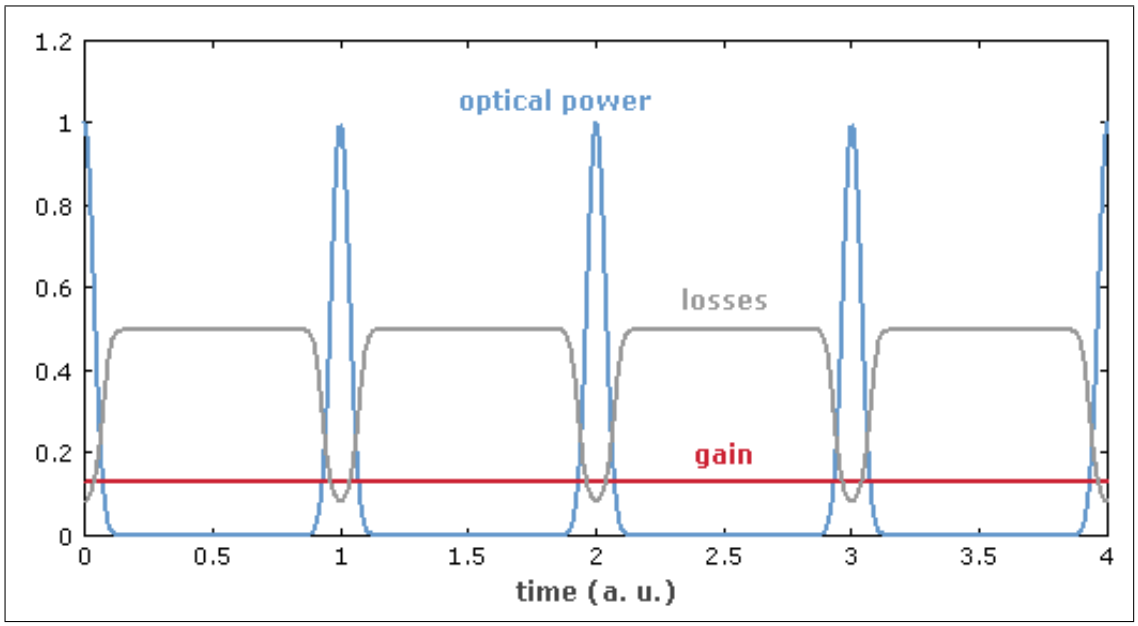

Figure 1.10: Pulses formed via mode-locking

Mode-locking is a method of creating a laser that has the ability to produce a

pulsed output beam of very short duration, usually either in the order of femtoseconds ($10^{-15}s$) or picoseconds ($10^{-12}s$) (Hönninger *et al.*, 1999). Mode-locking was chosen over other methods, such as Q-switching because an ultra-fast pulse was desired. Q-switching generally creates much lower pulse repetition rates, but compensates with far longer pulse durations and higher pulse energies.

This technique hinges upon inducing a fixed phase relationship between the modes of the resonant cavity of the laser. Such a laser is then said to be mode-locked or phase-locked. It is the interference between these modes that causes the laser light to become a train of pulses.

In basic lasers, each mode oscillates independently without a fixed relationship between one another, somewhat like a set of separate lasers each emitting light at slightly different frequencies. Each mode does not have a fixed phase, and can vary randomly.

If the laser has only a few oscillating modes, interference between the modes may lead to a "beating" effect in the laser output, which can cause fluctuations in intensity. Whereas in lasers with thousands and thousands of modes, these effects due to inference average out to a near constant output beam, and such lasers are referred to as continuous wave (c.w.) operation.

However, when the modes have a fixed phase between them, then the modes of the laser will all constructively interfere with one another periodically. This produces a pulse or intense burst of light, because it is mode-locked. Such pulses occur a time apart equal to $\tau \sim 2\frac{L}{c}$.

Where τ is the time taken for the light to make one round trip of the laser cavity, L is the length of the cavity, and c is the speed of light.

This time also relates to a frequency corresponding to the mode spacing of the laser, $\Delta v = \frac{1}{\tau}$

There are several techniques that can be incorporated to achieve mode-locking, though this research focused on passive mode-locking. In a basic sense, passive mode-locking methods are those that do not require an external signal to produce pulses. They incorporate materials that use the intracavity light to affect their properties, which then itself produces a change in the intracavity light. It is generally desired to play off the nonlinear optical properties of the material to make this a reality, most commonly achieved using a saturable absorber SA.

Any low-intensity, continuous-wave light will be absorbed by the saturable absorber, but any random high-intensity fluctuations will be allowed through. The light in the cavity will oscillate, and so the process repeats, which leads to the selective amplifications of the high-intensity peaks, while absorbing the low-intensity light. After many, many round trips, the result is a train of pulses and mode-locking of the laser, as shown in figure 1.10.

1.6.1 Passive Mode-locking

Passive mode-locking techniques are those that do not need an external signal to produce pulses in the laser. Instead, the main concept is that the light in the cavity itself inflicts a change in some intracavity element, which in turn illicit a change in the intracavity light. The most common material employed to achieve this is a saturable absorber.

As described in Section 1.5, saturable absorbers are materials for which the intensity of the electromagnetic radiation interacting with the SA increases, the absorption decreases and as such the transmission increases. In other words, an optical device that exhibits an intensity-dependant transmission.

The key to passive mode-locking is that the saturable absorber will selectively absorb the low-intensity light while allowing sufficiently high-intensity light through. When placed into a laser cavity, the SA attenuates the low-intensity constant wave light (pulse wings).

There will be random intensity fluctuations created in a non-mode-locked laser, and these higher intensity fluctuations are preferentially allowed through the saturable absorber. Due to the nature of the laser cavity, the light oscillates, and this process gets repeated many times, which leads to a selective amplification of the high-intensity spikes, and the low-intensity background light gets absorbed. This is what leads to a train of pulses, and mode-locking of the laser.

1.6.1.1 Methods of Passive Mode-locking

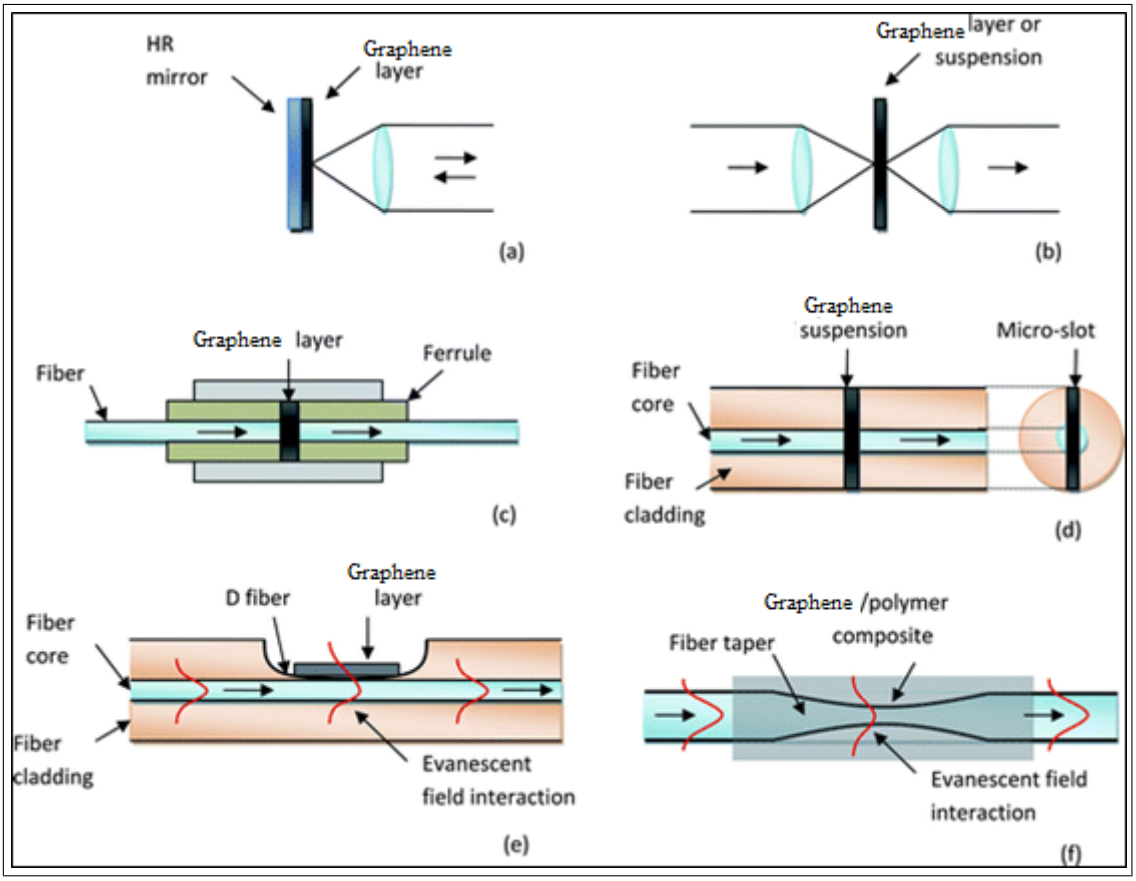

Figure 1.11: Passive mode-locking methods

There are many methods used to achieve passive mode-locking, with the basic idea being that the saturable absorber, while not necessarily in the beam path, has to somehow interact with the laser light. The simplest method is, of course, to have the SA in the path of the laser beam, which works for most types of gain medium.

However, for certain gain media, such as fibre laser, more exotic methods can be utilised. For example, coating the fibre in a specific saturable absorber so the evanescent field interacts with the SA, and in turn can lead to the mode-locking of the system. These methods are summarised in Figure 1.11.

Graphene as a suspended layer (b in Figure 1.11) was shown to be a successful candidate for mode-locking ultrafast lasers near 2 μm by the Wan *et al.* (2016) group. Their stable diode-pumped passively mode-locked Tm:YAP laser achieved

a maximum output of 256 mW at the center wavelength of 1988.5 nm from the absorbed pump power of 7.67 W. The pulse train had a repetition rate of 62.38 MHz and had the highest single pulse energy of 4.1 nJ.

Each of these techniques were considered, and many initially tested, during the course of the ISLA project, but a graphene saturable absorber mirror ((a) in Figure 1.11) appeared the most promising.

One of the most common methods to achieve mode-locking is through the use of a Semiconductor Saturable Absorber Mirror (SESAM).

1.6.1.2 SESAM

Around 1992, semiconductor saturable absorber materials were established as vital components for compact mode-locking of solid-state lasers Solid State Laser (SSL) (Keller *et al.*, 1996). The introduction of these materials opened up the possibility of pulsed solid-state laser systems, enabling Q-switching to achieve pulses in the nano- and picosecond regions, as well as mode-locked pulses in the picosecond and all the way down to the femtosecond regime.

As described in Section 1.6, a saturable absorber is essentially a material that has decreased absorption with increasing light intensity. With the aim of mode-locking there are several parameters which are important for the SA in question to possess:

- Wavelength Range - where it absorbs
- Dynamic Response - how quickly it recovers
- Saturation Intensity and Fluence - the intensity or pulse energy density at which saturation occurs

Though expensive and relatively complicated to manufacture, semiconductor materials can absorb over a broad wavelength range, from the visible to the mid-infrared. The absorption recovery time and saturation fluence (usually 1-100mJ/cm^2) can be controlled via altering the device design and growth parameters.

A SESAM is a saturable absorber which operates based on reflection, and as such the reflectivity increases with higher incoming pulse intensities. Over the last two decades, significant strides have been made toward improving the device design, fabrication processes, and long-term device reliability. There are tried and tested SESAM designs that operate at various pulsewidths from femtosecond to nanosecond, wavelengths from sub-800nm to beyond 1,600nm range, and power levels from milliwatt to hectowatts. Some companies, such as BATOP, have even begun making SESAMs in the $2\mu m$ wavelength range.

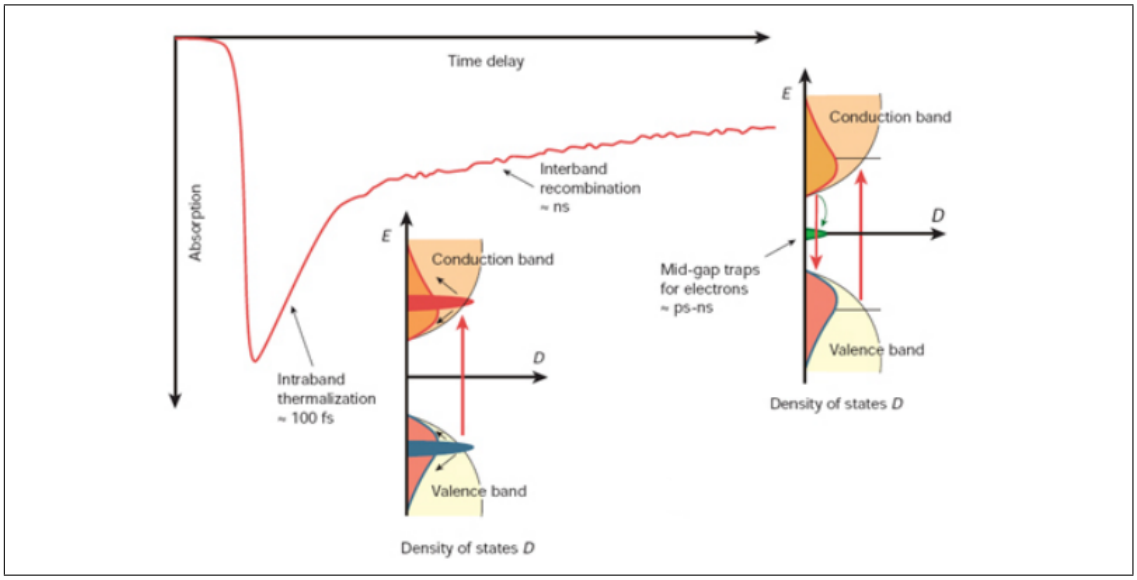

Figure 1.12: Mechanism behind semiconductor absorber (Keller *et al.*, 1996)

As shown in Figure 1.12, when the photon is of sufficient energy, the carriers from the valence band excite to the conduction band of the semiconductor material. Assuming operation under strong excitation conditions, the absorption is saturated due to possible initial states of the pump transition being depleted while the final states are partially occupied. Within 60 fs to 300 fs of excitation, the carriers in each band thermalise, which leads to the partial recovery of the absorption. Over longer time scales, picosecond to nanosecond region the carrier will be removed by recombination and trapping.

The presence of two different time scales can be useful for the process of mode-locking. The longer time constant results in a reduced saturation intensity for a

part of the absorption, which aids in self-starting mode-locking while the faster time constant is more effective at shaping sub-picosecond pulses. In this way, SESAMs facilitate achieving self-starting mode-locking (Keller *et al.*, 1996).

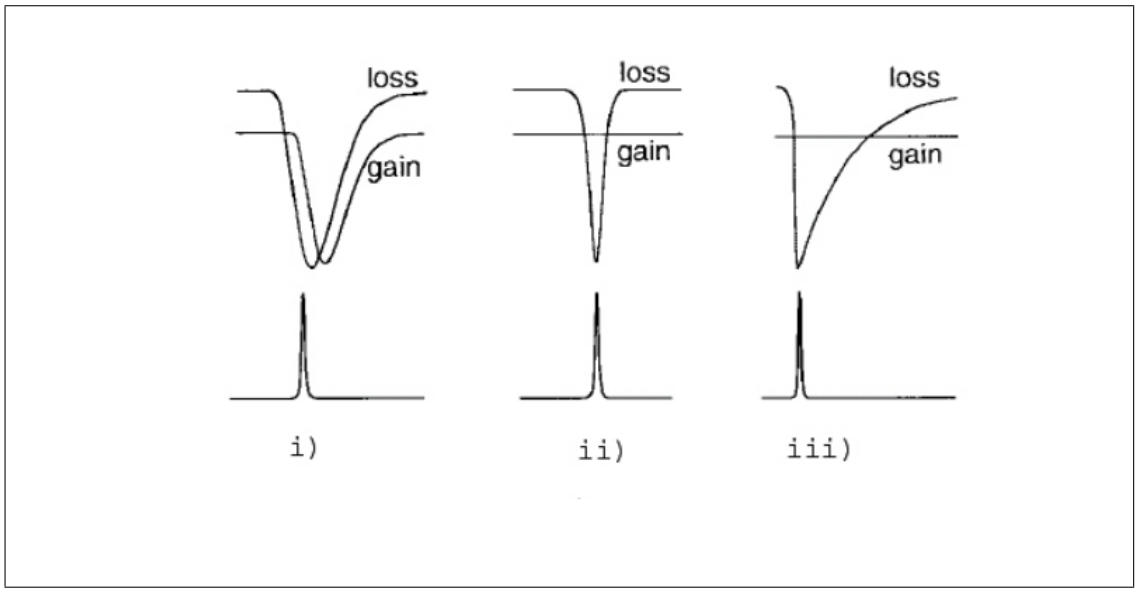

Figure 1.13: Fundamental passive mode-locking models: i) passive mode-locking with a slow saturable absorber and dynamic gain saturation, ii) fast absorber mode-locking, iii) soliton mode-locking (Keller *et al.*, 1996)

The low intensity portion of the pulse is absorbed by the saturable absorber, whereas the high intensity portion passes the material with little loss, the result being the compression of the pulse, so the pulse becomes shorter and shorter as it passes through the SESAM. Figure 1.13 demonstrates the three fundamental passive mode-locking models.

i Passive mode-locking with a slow saturable absorber and dynamic saturation (Haus *et al.*, 1975; New, 1972)

ii Fast absorber mode-locking (Haus, 1975a; Haus *et al.*, 1991)

iii Soliton mode-locking (Jung *et al.*, 1995a; Kärtner & Keller, 1995a; Kärtner *et al.*, 1996)

These three basic mode-locking models demonstrate the different pulses obtainable, when combining different gain medium and saturable absorbers.

In the first and second case, a small net-gain window forms and stabilises an ultrashort pulse. This net-gain window will also form the minimal stability requirement, meaning that the net loss just before and after the pulse will define the extent.

Whereas, in soliton modelocking, the pulse formation is dominated by the balance of Group Velocity Dispersion (GVD) and Self-Phase Modulation (SPM). Groups such as Jung *et al.* (1995a) have shown that, depending on the specific laser parameters, the net-gain window can remain open for over ten times longer than the ultrashort pulse. The slower saturable absorber only stabilises the soliton and begins the pulse formation process.

Until the end of the 1980s, dye lasers dominated the ultrashort pulse generation industry. In such systems, mode-locking was based on a balanced saturation of both gain and loss, which enabled a steady-state net gain window as short as the pulse duration, which is represented as (i) in Figure 1.13, the slow-absorber with dynamic gain saturation model (Haus *et al.*, 1975; New, 1972). It was possible to generate pulses as short as 27 fs and with an average power of 10 mW (Valdmanis & Fork, 1986). Shorter pulse durations as low as 6 fs were achieved through fibergrating pulse compression combined with additional amplification, which was compensated with a much lower repetition rate (Fork *et al.*, 1987).

The laser community was altered after development and commercialization of the Ti:sapphire laser (Moulton, 1986), which had a gain-bandwidth large enough to facilitate ultrashort pulse generation. Unfortunately, contemporary mode-locking techniques were inadequate due to the much longer upper state lifetime, as well as the smaller gain cross section of this laser. Which would result in negligible pulse-to-pulse dynamic gain saturation. It was proposed that a fast saturable absorber would be required to generate ultrashort pulses, represented as (ii) in Figure 1.13. A suitably fast saturable absorber was uncovered (Spence *et al.*, 1991), which utilised Kerr Lens Mode-locking (KLM) as the physical mechanism (Keller *et al.*, 1991; Maldonado *et al.*, 2001; Salin *et al.*, 1991). This was the strong self-focusing of the laser beam, when combined with either a hard aperture or a soft gain aperture, is harnessed to produce a self amplitude modulation, which equates to an equivalently fast saturable absorber.

Over the past several decades, significant research has been directed toward optimising KLM for shorter pulse generation, with around 8 fs (Stingl *et al.*, 1995; Xu *et al.*, 1996; Zhou *et al.*, 1994) directly from the laser being standard. Utilising broad-band intracavity SESAM devices, in addition to KLM and higher order dispersion compensation (Kärtner *et al.*, 1997; Szipöcs *et al.*, 1994), the Jung *et al.* (1997b) group have generated pulses as short as 6.5 fs directly from a Ti:sapphire laser with 200 mW average output power with a pulse repetition rate of 85 MHz. External pulse compression techniques, which use fibre-grating pulse compressors, have been used to reduce the pulse duration even more from a Ti:sapphire laser to 5 fs at a center wavelength of 800 nm (Baltuska *et al.*, 1997; Bethge *et al.*).

There are some limitations for practical ultrafast lasers. Firstly, the cavity is typically operated near the edge of its stability range, where the Kerr-lens-induced change of the beam diameter is large enough to sustain mode-locking. This results in a requirement for critical cavity alignment where mirrors and laser crystal have to be positioned to an accuracy of several hundred microns typically. Not only this, but the self-focusing required for KLM imposes limitations on the design of the cavity and can lead to strong space-time coupling of the pulses in the laser crystal that results in complex laser dynamics (Christov *et al.*, 1995; Cundiff *et al.*, 1996). Once the cavity is aligned correctly, KLM can be extremely stable and, if specific conditions are met, even self-starting (Cerullo *et al.*, 1994a,b).

As shown by groups like Kärtner *et al.* (1995), Jung *et al.* (1995a) and Haus *et al.* (1991), soliton mode-locking addresses a lot of these issues. In soliton mode-locking, pulse shaping is achieved via soliton formation only. This means that the balance of GVD and SPM is at steady state, with no additional requirements on the cavity stability regime. An additional loss mechanism, such as a saturable absorber (Haus *et al.*, 1991; Jung *et al.*, 1995a), or an acousto-optic mode-locker (Kärtner *et al.*, 1995; Kopf *et al.*, 1994), is required to initiate the mode-locking process and to stabilise the soliton.

The soliton will lose energy due to gain dispersion and losses in the cavity. Gain dispersion and losses can be treated as perturbation to the nonlinear Schrodinger equation for which a soliton is a stable solution Kärtner *et al.* (1995). This lost energy is referred to as the continuum in soliton perturbation theory (Kaup, 1990). It is initially contained in a low intensity background pulse, which experiences

slight bandwidth broadening from SPM, which increases in time due to GVD. This continuum experiences a higher gain compared to the soliton, because it only sees the gain at line center, whereas the soliton sees an effectively lower average gain due to its larger bandwidth. After a suitable build-up time, the continuum can grow until it reaches an effective lasing threshold, destabilising the soliton. It is possible to stabilise the soliton by introducing a slow saturable absorber into the cavity. Such a slow absorber adds an additional, necessary loss such that the continuum no longer reaches threshold, but with negligible increased loss for the short soliton pulse.

Providing that specific laser parameters are combined such as gain dispersion, small signal gain, and negative dispersion, a slow saturable absorber can stabilise a soliton with a response time of more than ten times longer than the steady-state soliton pulsewidth, which can be seen as (iii) in Figure 1.13. Ideal transform-limited soliton pulses over more than six orders of magnitude, even though the net gain window is open much longer than the pulse duration, has been displayed with high-dynamic range autocorrelation measurements (Jung *et al.*, 1997a; Kärtner & Keller, 1995a; Kopf *et al.*, 1995). Because of the slow saturable absorber, the soliton undergoes an efficient pulse cleaning mechanism (Jung *et al.*, 1995a). In each round-trip, the soliton is delayed with respect to the continuum, due to the front section of the soliton being absorbed.

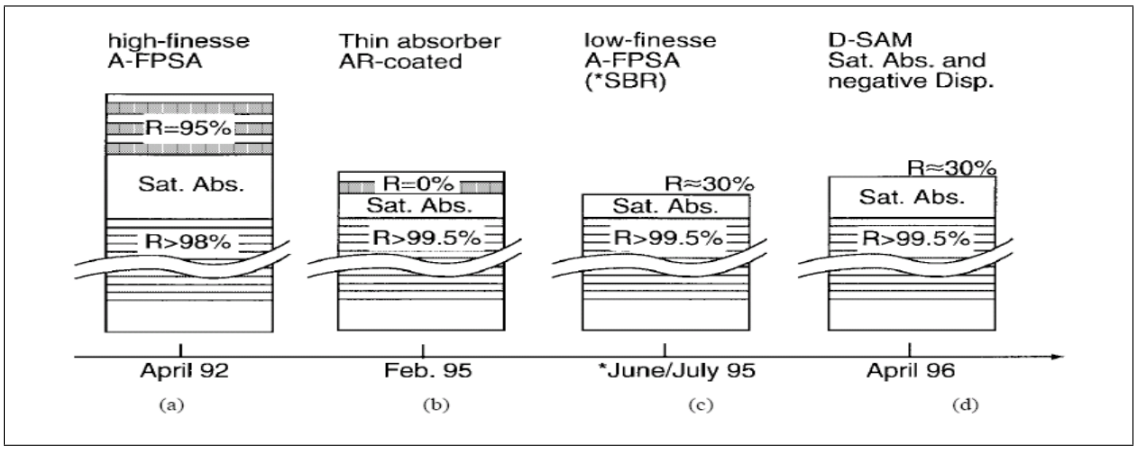

Figure 1.14: Different SESAM Devices (Keller, 2003)

A SESAM can offer a distinct range of operating parameters, which are not

possible with other methods. The Keller (1996) group utilised several SESAM designs to achieve many of the desired properties. Figure 1.14 shows several typical SESAM designs, in historical order. The initial intracavity SESAM was an Antiresonant Fabry-Perot Saturable Absorber (A-FPSA) (Keller *et al.*, 1992). This was first used in a system with a rather high top reflector, which is referred to as a high-finesse A-FPSA. The FabryPerot is usually formed by the lower semiconductor Bragg mirror with a dielectric top mirror, combined with a saturable absorber and occasionally with a transparent spacer layer between them. The thickness of the total absorber and spacer layers are altered to have the FabryPerot operate at antiresonance. Operating with antiresonance will result in a SESAM which is broad-band and has minimal group velocity dispersion. There is a bandwidth limit of the A-FPSA due to either the bandwidth of the mirrors or the free spectral range of the FabryPerot.

The intensity entering the semiconductor saturable absorber is determined by the top reflector of the A-FPSA, which is an adjustable parameter. And so in turn determines the effective saturation intensity or absorber cross section of the device. The Brovelli *et al.* (1995) group demonstrated another SESAM designs, which replaced the top mirror with an AR-coating, and is shown as (b) in Figure 1.14. It was possible to adapt the incident pulse energy density to the saturation fluence of the device by using the incident laser mode area as an adjustable parameter. It should be noted that to reduce the nonsaturable insertion loss of the device, it is often necessary to reduce the thickness of the saturable absorber layer.

A third design is referred to as a low-finesse A-FPSA (Hönninger *et al.*, 1995; Jung *et al.*, 1995b; Tsuda *et al.*, 1995), and is shown as (c) in Figure 1.14. This is possible without adding top coating, which results in a top reflector formed by the Fresnel reflection (usually around 30%) at the semiconductor/air interface.

Finally, a Dispersive Saturable Absorber Mirror (D-SAM) (Kopf *et al.*, 1996) is shown as (d) in Figure 1.14. This SESAM design incorporates both dispersion and saturable absorption into one device, and is similar to a low-finesse A-FPSA, but the D-SAM operates close to resonance.

1.7 Thesis Outline

Chapter 2: Review of the relevant Literature

Chapter 3: outlines are the experimental methods and the equipment used throughout the project.

Chapter 4: discusses materials used and the methods employed to prepare the samples.

Chapter 5: examines the nonlinear optical properties of graphene (dispersions, thin films and graphene-polymer composites) via the Z-scan technique at 1 μm, 1.2 μm and 2 μm, primarily to determine the saturable absorption nature of graphene. Antimonene, Molybdenum Diselenide, Boron nitride, molybdenum disulphide and carbon nanotubes are also briefly explored.

Chapter 6: examines the nonlinear optical properties of graphene SAMs utilising the I-scan technique, and compares our samples with commercial SESAMs. This chapter also discusses the development of the ISLA test lasers, and the use of our graphene SAMs in such a system. The graphene SAMs are utilised as mode-lockers in a pulsed laser system.

Chapter 7: reviews the results from the previous sections and suggests future work.

2
Literature Review

Wide-spectral saturable absorption (SA) has been experimentally demonstrated in two-dimensional (2D) nanomaterials with outstanding performance, such as low saturation intensity, deep modulation depth and fast recovery time of excited carriers. Hence 2D nanomaterials can be utilized as saturable absorbers for mode-locking or Q-switching to generate laser pulses with short duration and high repetition rate. In this Chapter, the SA properties of graphene, layered transition metal dichalcogenide (TMDs), Group-V elements and other 2D nanomaterials are reviewed by summarizing their slow- or fast- saturable absorption behavior using the modified Frantz-Nodvik model or the steady-state solution of Hercher's rate equations. The dependence of SA in 2D nanomaterials on excitation wavelength, linear absorption coefficient and pulse duration is explained. Finally, the applications of these 2D nanomaterials in a range of pulsed lasers are summarised.

2.1 Introduction

The intriguing light-matter interactions of two-dimensional (2D) nanomaterials has been in the spotlight of optical research due to a wide variety of applications from photovoltaics, photonics, valleytronics to optoelectronics.(Bonaccorso *et al.*,

2010) Under the irradiation of intense light, researchers have observed many novel nonlinear optical (NLO) phenomena in 2D materials such as two-photon absorption (TPA), second-harmonic generation, and staturable absorption (SA). The SA behavior is caused by Pauli-blocking, i.e., band-filling effect.(Dong *et al.*, 2017, 2018; Huang *et al.*, 2017; Keller *et al.*, 1996; Wang *et al.*, 2013a; Zhang *et al.*, 2017b) According to the Pauli exclusion principle, the same quantum state cannot be simultaneously occupied by two or more identical fermions, such as electrons. This results in limited positions for electrons in the conduction band of a semiconductor. When intense light irradiates a SA material for which the ground-state absorption is larger than that of the excited-state, electrons from the valence band are excited to fill the conduction band.

No more incoming electrons can be accepted, and the majority of the incident light is not absorbed. According to NLO theory, this SA behavior can also be understood through the total absorption coefficient (α(I)) of a saturable absorber, which is dependent on the incident intensity, I, : $\alpha(I) = \alpha_0/(1+I/I_s)$.(Boyd, 2003; Wang *et al.*, 2013a) Here α_0 represents the linear absorption coefficient and Is is the saturation intensity of the saturable absorber. The physical meaning of α(I) is that the absorption of the saturable absorber decreases with the increasing intensity, which leads to an increase in the transmission. At high intensities, absorption and stimulated emission balance out, which leads to T going to 1. In reality, there are also higher excited states which lead to excited state absorption and a decrease of ultimate transmission.

A saturable absorber is a key passive mode-locking component in a laser cavity to generate ultrashort laser pulses. Saturable absorbers can include fast- or slow-absorbers. Fast-saturable absorbers have much shorter excited carrier relaxation times than the mode-locked pulse duration, whereas slow-saturable absorbers have longer excitation carrier relaxation times.(Wang *et al.*, 2017a) The excited carrier relaxation time of a saturable absorber can be determined via time-resolved pump-probe techniques based on ultrafast lasers.(Wang *et al.*, 2017a, 2016b) Once the recovery time has been obtained, the 2D nanomaterials SA properties as either a slow- or fast- absorbers can be verified by the modified Frantz-Nodvik model or the steady-state solution of Hercher's rate equations, respectively.(Burshtein *et al.*, 1998; Pokrass *et al.*, 2012; Wang *et al.*, 2018b)

Many 2D nanomaterials have been demonstrated to possess novel SA properties, such as large modulation depth, giant NLO coefficient, low saturation intensity, large third-order NLO susceptibility. Therefore, 2D nanomaterials are promising saturable absorber candidates for mode-locking. As one of the best known 2D materials, graphene was found to possess SA properties with low saturation intensity, large modulation depth and fast relaxation time of excited carriers.(Kumar *et al.*, 2009a) Some layered TMDs were even experimentally demonstrated to have better NLO properties then graphene at some wavelengths.

Layered molybdenum disulfide (MoS_2) was reported to have stronger SA than graphene at the wavelength of 800 nm with an imaginary part of third-order nonlinear optical susceptibility of -1.56 10^{-14} esu.(Wang *et al.*, 2013a) Layered black phosphorus (BP) was found to have SA properties in a wide wavelength range from the visible to the mid-infrared due to the materials large bandgap transition.(Li *et al.*, 2016; Wang *et al.*, 2016b, 2015; Xu *et al.*, 2016) All-optical thresholding/optical modulation by SA effects have also been reported in layered black phosphorus.(Zheng *et al.*, 2017a,b) The stability of the black phosphorus is important for the practical application of SA and this issue has been solved.(Guo *et al.*, 2017; Tang *et al.*, 2017; Xing *et al.*, 2017)

Benefiting from the above outstanding NLO performance, many 2D nanomaterials have been utilized to produce SA devices such as saturable absorption mirrors (SAMs) and polymer/2D materials composite saturable absorbers. For example, our previous work utilised polyvinyl alcohol (PVA) as the host matrix to embed graphene nanosheets to study the dependence of SA properties on wavelength and laser pulse duration.(Feng *et al.*, 2015a) These results indicate that graphene/PVA composites have lower saturation intensity, larger NLO coefficient and figure of merit for nanosecond laser pulses than femtosecond pulses.

Another paper from our group detailed fabricating a graphene saturable absorption mirror (GSAM) by transferring liquid-phase-exfoliated graphene flakes onto a silver-coated mirror.(Wang *et al.*, 2017a) This set of experiments are detailed in more detail in Chapter 6. The paper compared the NLO properties of our GSAM to a commercial saturable absorption mirror (SESAM), which showed that the GSAM possessed significant advantages over the SESAM with 28% less

absorptive cross-section ratio of excited-state to ground-state and 50 times faster recovery time as a saturable absorber at the wavelength of 2 μm.

By employing these 2D nanomaterials SA devices into laser cavities, a series of laser pulses with high repetition rate, ultrashort duration from the visible to mid-infrared wavelength have been reported.(Chen *et al.*, 2016; Jin *et al.*, 2018a; Kong *et al.*, 2015; Qiaoliang Bao, 2009; Qin *et al.*, 2015; Sotor *et al.*, 2015b; Wang *et al.*, 2016c) For example, graphene was utilized as a saturable absorber in a mode-locked fiber laser to generate ultrashort laser pulses with a duration of 756 fs at the wavelength of 1565 nm.(Qiaoliang Bao, 2009)

An ytterbium-doped mode-locking fiber laser using layered MoS_2 as a saturable absorber achieved lasing with a power output of 210 mW, a repetition rate of 6.74 MHz and pulse duration of 656 ps at the center wavelength of 1042.6 nm.(Du *et al.*, 2014) Layered black phosphorus was utilized to generate ultrafast laser pulses with 272 fs pulse duration at the 1550 nm telecommunication wavelength.(Sotor *et al.*, 2015b) This is a popular telecommunication wavelength, which implies promising applications in optical communications.

Some publications have reviewed ultrafast lasers mode-locked by 2D nanomaterials such as layered black phosphorous, topological insulators, MoS_2 and other TMDs.(Dhanabalan *et al.*, 2017; Haus, 2000; Luo *et al.*, 2016; Wu *et al.*, 2018; Zhou *et al.*, 2017) These reviews gave a valuable overview and perspective on the performance of mode-locked and Q-switched fiber lasers based on the above 2D saturable absorbers. However, these reviews contain very little discussion on the saturable absorption in a range of 2D materials, which could provide an important guideline for the design of ultrafast lasers based on 2D saturable absorbers. Here, the SA properties of 2D nanomaterials and related photonic devices are reviewed with the corresponding applications in mode-locked or Q-switched pulse lasers.

Firstly, the NLO properties of 2D materials for a wide spectral region are detailed, such as the third-order NLO susceptibility, SA coefficient, and modulation depth. These materials include graphene, TMDs, antimonene, arsenene, bismuthene, back phosphorus, MXenes and topological insulators. These NLO properties are discussed via the modified Frantz-Nodvik model or the steady-state solution of Hercher's rate equations, which model the slow or fast saturable absorption performance respectively. The SA properties dependence on wavelength, linear

absorption and laser pulse duration is summarized with corresponding physical explanations.

Next, 2D SA photonic devices are introduced, including SAMs and polymer-2D nanomaterial saturable absorbers. The methods to produce these devices are outlined and the SA properties of such devices are explored. Finally, the performance of ultrafast lasers mode-locked by these 2D nanomaterials is discussed. This review offers clear insight into the NLO performance of 2D saturable absorbers with corresponding photonic applications, and serves as a reference to physicists and optical engineers developing ultrafast laser sources.

2.2 Saturable absorption

2.2.1 Pauli-Blocking in SA materials and NLO methods

As mentioned in the introduction, the saturable absorber is a significant component for passive mode-locked lasers.(Schröder *et al.*, 1980) Saturable absorption is a NLO property of materials which occurs under high intensity light, such as lasers. Saturable absorption is a phenomenon caused by the Pauli-blocking effect, where a transition state is fully occupied and can no longer accept incoming electrons.(Sheik-Bahae *et al.*, 1989a) When a ray of light interacts with the NLO material, the electrons in the valence band absorb incident photons and then are excited to the conduction band.

As shown in Figure 2.1 (a), at low incident intensity most of the photons are absorbed and this therefore results in low transmission. In contrast, for relatively high incident laser beam intensities, a large number of electrons are excited to fill the conduction band of a SA sample whose cross-section of the ground state is smaller than that of excited states, and the conduction band cannot accept any more incoming electrons. Consequently, most of the incident photons are not absorbed and transverse the material, i.e., high transmission, as seen in Figure 2.1 (b).

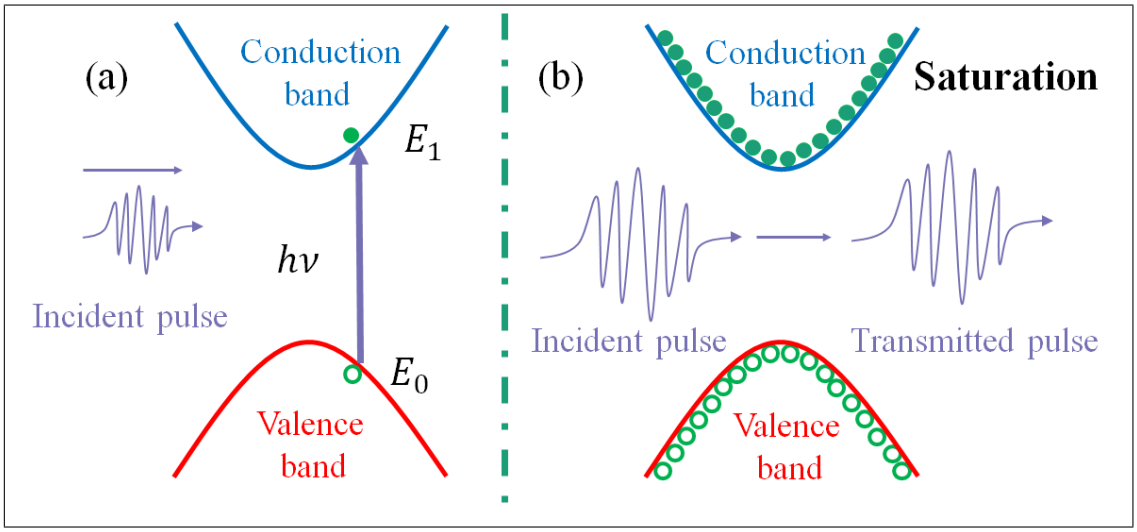

Figure 2.1: The principle of saturable absorption due to the Pauli-blocking. (a) A low-intensity incident laser beam passes through a nonlinear optical material with a low transmission, while (b) the high intensity one results in high transmission. The green solid circles stand for electrons and the open circles for holes.

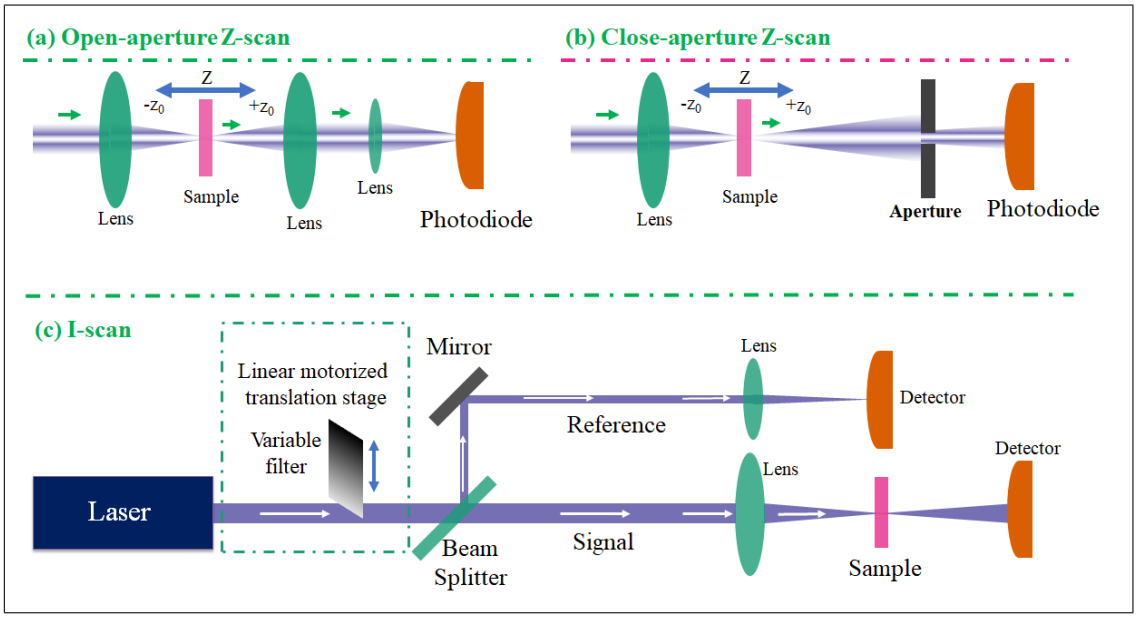

Figure 2.2: Schemes showing the principle of (a) open-aperture, (b) closed-aperture Z-scans and (c) I-scan.

Hence, the SA behavior of materials can be studied by Z-scan or I-scan techniques via the measurement of the transmitted light as a function of the incident

light. The Z-scan technique was invented by Sheik-Bahae et al. and was first reported in 1989.(Eilers *et al.*, 1992; Sheik-Bahae *et al.*, 1990) The group initially utilized the technique to measure the nonlinear refractive index, n2,(Sheik-Bahae *et al.*, 1990) This technique was later improved upon in 1990 by David J. Hagan et al to measure nonlinear absorption.(Eilers *et al.*, 1992) This methodology can be further broken down to open-aperture and closed-aperture Z-scans, which can be used to measure the third-order nonlinear susceptibility, nonlinear absorption coeffecient and nonlinear refractive index, respectively (see Figure 2.2 (a) and (b)).(Feng *et al.*, 2015a; Yang *et al.*, 2011a)

In a Z-scan measurement, a lens is used to focus the beam to achieve a continuously variable laser intensity. The sample is then placed after the lens, in the direction of travel of the laser, and is moved in the Z-direction. For open-aperture Z-scan measurements, all the transmitted signal is collected by a lens into a detector. Whereas for closed-aperture configuration, an aperture is placed in the center of the laser beam before the detector (See Figure 2.2 (b)). This ensures that only a small portion of the light from the center of the transmitted beam can arrive at the detector. For both methods, the transmission as a function of incident laser intensity can be acquired by recording the position of the sample on the Z-axis.

Open-aperture Z-scan has become a popular nonlinear optical tool which has been widely utilized to study third-order optical effects, scatterings and absorption, and is particularly useful for saturable absorption measurements.(Wang *et al.*, 2013a, 2016b) As the sample moves towards the focal point, i.e., increasing the intensity, more electrons are excited from the ground-state to the excited states. Once the incident intensity reaches a saturable threshold, the transmittance increases with the incident laser intensity, i.e., the movement of the sample toward the focus point.

To analyze the SA behavior using Z-scan measurements, NLO theories and models are needed. When the light is propagating along the z direction inside the NLO medium, the corresponding equation can be written as:(Wang *et al.*, 2013a)

$$\frac{dI}{dz} = -\alpha(I) \cdot I \tag{2.1}$$

Where I is the laser intensity, z is the propagating distance in the medium and α(I) is the total absorption which can be expressed using linear and nonlinear absorptive coefficients (α_0 and α_{NL} respectively):(Feng *et al.*, 2015a; Zheng *et al.*, 2012a)

$$\alpha(I) = \alpha_0 + \alpha_{NL} I \tag{2.2}$$

This equation indicates that the total absorption originates from both linear and nonlinear parts, of which α_0 can be measured directly under a lower incident intensity. By applying Equations 2.1 and 2.2 to fit the open-aperture Z-scan trace, the nonlinear absorption coefficient can be obtained.(Feng *et al.*, 2015b) Since α_{NL} is related to the imaginary part of the third nonlinear optical susceptibility, Im(χ(3)), one can obtain the third-order NLO susceptibility of a SA material:(Feng *et al.*, 2015a; Wang *et al.*, 2013a; Zheng *et al.*, 2012a)

$$Im(x^{(3)}) = (1.04 \times 10^{-9} c\lambda n^2/\pi^2) \cdot \alpha^{NL} \tag{2.3}$$

Where c is the light speed, λ represents the incident laser wavelength in vacuum and n is the effective refractive index of the material.

In a case where both saturable and reversible saturable absorption exist, the total absorption can be written as:(Yang *et al.*, 2011b)

$$\alpha(I) = \alpha_0/(1 + I/I_S) + \beta I \tag{2.4}$$

where Is is the saturable absorption intensity, which is defined as the intensity where the transmittance reaches half of the maximum. The first term of Equation 2.4 is utilized to describe the saturable absorptive behavior while the second term (βI) is related to the reversible saturable absorption such as TPA. By combining Equation 2.1 and 2.4, one obtains the general nonlinear propagation equation for modeling Z-scan traces:(Yang *et al.*, 2011b)

$$dI/dz = -[\alpha_0/(1 + I/I_S) + \beta I] \cdot I \tag{2.5}$$

This equation can be utilized to model the general open-aperture Z-scan results to analyze the NLO behavior of materials. If the nonlinear absorption coefficient, β, was fitted to be zero, the total absorption in Equation 2.4 can be written as $\alpha(\mathrm{I}) = \alpha_0/(1 + I/I_s)$, which is a standard SA model. I-scan is another effective method to study the SA properties of materials, particularly for solid samples. A typical I-scan set-up is shown in Figure 2.2 (c). The intensity of an initial laser beam is tuned by a variable filter which is moved via a linear motorised stage. After the variable filter, the laser beam is split into two beams: a reference and main beam. The reference beam is collected by a convex lens directly into a photodiode. To measure the transmitted (reflective) signal a second convex lens is employed to focus the main beam onto the sample which is placed at the focal point, followed by another lens guiding the beam into a photodiode. By moving the variable filter to change the incident intensity, the transmittance (reflection) as a function of the intensity can be obtained. As the laser spot is focused at a single position on the sample, I-scan has the obvious advantage of avoiding the noise created by moving the sample when compared to Z-scan technique.

2.2.2 Wide-spectral NLO response of 2D Materials

Based on the above NLO techniques, the SA properties of many 2D nanomaterials have been demonstrated in a wide wavelength region from the visible to mid-infrared range, with some published work even reaching as far as the microwave spectrum.(Feng *et al.*, 2015a; Kumar *et al.*, 2009a; Podila *et al.*, 2012; Wang *et al.*, 2017a, 2018b, 2013a, 2016b, 2015; Zhang *et al.*, 2014b,c) The wide-spectral photonic response of 2D nanomaterials is related to their interesting band structure and electronic properties, as illustrated in Figure 2.3.

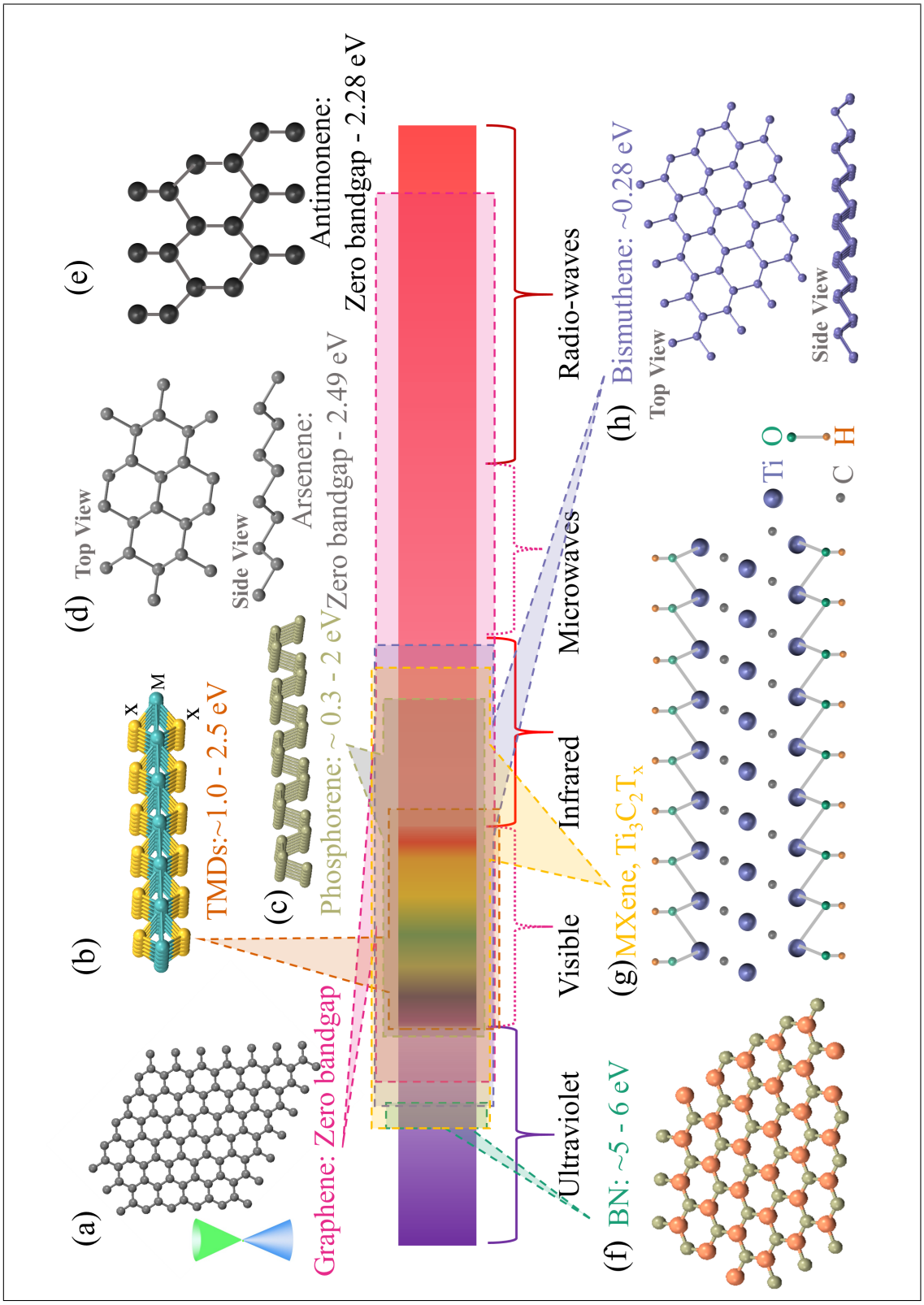

Figure 2.3: The spectral region that is covered by 2D materials. Graphene possesses broadband photonic response from ultraviolet to radio-waves region due to the zero bandgap. Monolayer TMDs are direct semiconductors with bandgap of 1.0 - 2.5 eV and optical response are mainly in visible region.(Tongay *et al.*, 2012a; Wang *et al.*, 2013a) Most of the Group-V monolayers and MXene cover the spectral regions from visible to mid-infrared. 2D BN has a bandgap of 5 - 6 eV and hence interacts with ultraviolet photons.(Mao *et al.*, 2016)

The first experimentally obtained 2D nanomaterial was graphene,(Novoselov *et al.*, 2004b) a single layer of carbon atoms with gapless and conical-shape band structure, as shown in Figure 2.3 (a). This band structure results in a wide-spectral photonic response from ultraviolet to the radio-wave regimes.(Bittner *et al.*, 2010; Feng *et al.*, 2015a; Hanlon *et al.*, 2015; Kumar *et al.*, 2009a; Qiaoliang Bao, 2009; Wang *et al.*, 2017a; Xing *et al.*, 2010; Zhang *et al.*, 2014b) Utilizing similar methods to graphene preparation, a range of graphene analogues were experimentally obtained, such as 2D transition metal dichalcogenides (TMDs), black phosphorus and boron nitride (BN).(Coleman *et al.*, 2011b; Cunningham *et al.*, 2012; Zheng *et al.*, 2012a)

Layered TMDs are a large family of 2D materials with the form of chemical composition of MX_2, where M stands for transition metal atoms such as Mo, W, Ti, Ta, Nb, etc., and X for the dichalcogenides atom like S, Se, Ru, Te, etc.(Gordon *et al.*, 2002; Tongay *et al.*, 2012a) As shown in Figure 2.3 (b), in a MX2 monolayer, the transition metal atom layer is sandwiched by two dichalcogenides atom layers.(Tongay *et al.*, 2012a; Xia *et al.*, 2014a) In the majority of these TMDs, a transition from the indirect bandgap in bulk limit to the direct bandgap in their monolayer forms was observed, hinting at possible interesting photonic properties in the visible region. For example, $MoSe_2$ and MoS_2 monolayers have direct bandgap of 1.55 eV and 1.89 eV, while the bulk counterpart was proven to be an indirect semiconductor with a bandgap of 1.1 eV and 1.54 eV, respectively.Tongay *et al.* (2012b) Hence, 2D TMDs mainly interact with light in the visible wavelength regime, see Figure 2.3 (b).(Zhang *et al.*, 2015b) Layered boron nitride has a bandgap of 5 - 6 eV and therefore exhibits a narrow optical response in the ultraviolet wavelength region, see Figure 2.3 (f).(Zhang *et al.*, 2017a)

Some group-V elements were subsequently found to possess interesting electronic properties in a transfer from bulk limit to 2D limit. Layered black phosphorus has a large bandgap transition from 0.3 eV - 2 eV and possesses broadband optical properties from the visible to mid infrared region, as shown in Figure 2.3 (c).(Wang *et al.*, 2016b) The transition from bulk to monolayer of antimony and arsenic was predicted to have a transformation from semimetals to indirect semiconductors with a bandgap of 2.49 eV and 2.28 eV, respectively (see Figure 2.3 (d) and (e)).

A first principles study showed that monolayer bismuth, i.e., bismuthene, is a quantum spin Hall state with a bandgap of 0.28 eV, resulting in a photonic response from the violet to far-infrared region. MXene are interesting 2D nanomaterials with a chemical formula of $M_{n+1}X_nT_x$, where M is an early transition metal, X represents C and/or N, T_x is the surface termination groups (=O, -OH or -F), shown in Figure 2.3 (g).(Lu *et al.*, 2017b; Lukatskaya *et al.*, 2013) For example, both $Ti_3C_2(OH)_2$ and $Ti_3C_2F_2$ monolayers are direct semiconductors with a bandgap of <0.1 eV, whereas both Ti_3C_2-based monolayers are semimetal. This grants MXene a broadband photonic response from visible up to the far-infrared region.(Lu *et al.*, 2017b)

The broadband SA properties of all the above mentioned 2D nanomaterials have been reported in a wide-spectral range. Figure 2.4 gives an overall view on saturation intensities of 2D nanomaterials versus the excited wavelength. Specifically, Z-scan results in Figure 2.5 (a) and (b) show that graphene hosted within a PVA matrix possesses obvious SA at the wavelength of 515 nm and 1030 nm, respectively.

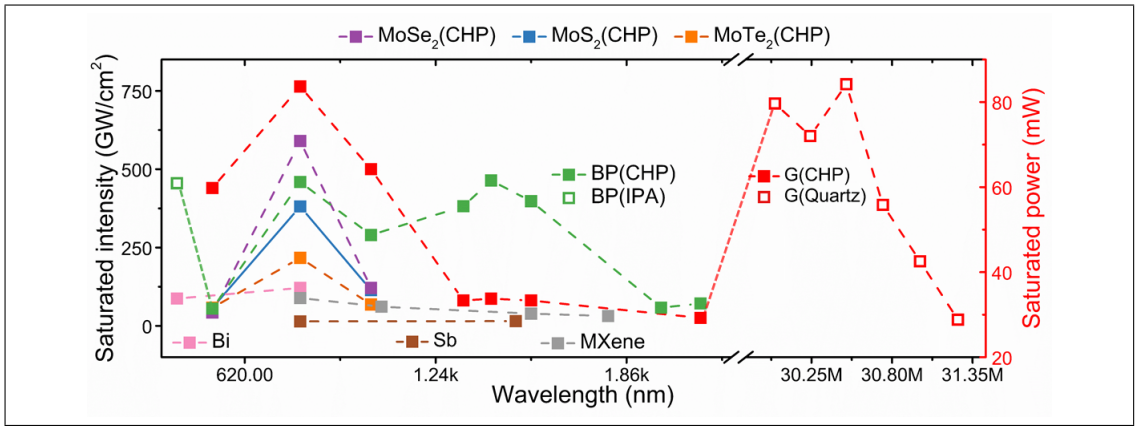

Figure 2.4: Wide-spectral SA of 2D nanomaterials. Graphene dispersed in CHP was measured to have SA response from visible to mid-infrared region, (Wang *et al.*, 2016b) and the SA of graphene deposited on quartz covered the micro-wave region. (Zhang *et al.*, 2014b) Most layered TMDs mainly show SA behavior in visible and near-infrared region (Chang *et al.*, 2010a), while semimetal WTe_2 shows response in min-infrared region.(Gao *et al.*, 2018; Song *et al.*, 2017a) The I_S for bulk WTe_2 at 1.55 μm is 64.6 W. (Chang *et al.*, 2010a) The SA of 2D Group-V elements such as BP, Bi and Sb have been experimentally obtained in a broadband wavelength range. (Lu *et al.*, 2017a, 2015; Song *et al.*, 2017b; Wang *et al.*, 2016b, 2015) The SA of MXene covered a wide-spectral range from 800 nm to 1800 nm.(Dal Conte *et al.*, 2015a,a; Dawlaty *et al.*, 2008a)

Specifically in a Z-scan measurement, this means that the transmission increased when the sample was moved toward the focus point (z=0), i.e., increased the incident intensity.(Feng *et al.*, 2015a) This optical phenomenon was also observed in few-layer $MoSe_2$ under the irradiation of 800 nm, 100 fs and 100 kHz laser pulses, see Figure 2.5 (c). For group-V elements, layered BP has been demonstrated to have SA characteristics at a wavelength range from 800 nm to 2010 nm, with nonlinear absorption coefficients of 0.0138 cm/GW - 0.1 cm/GW, see Figure 2.5 (d).(Wang *et al.*, 2016b)

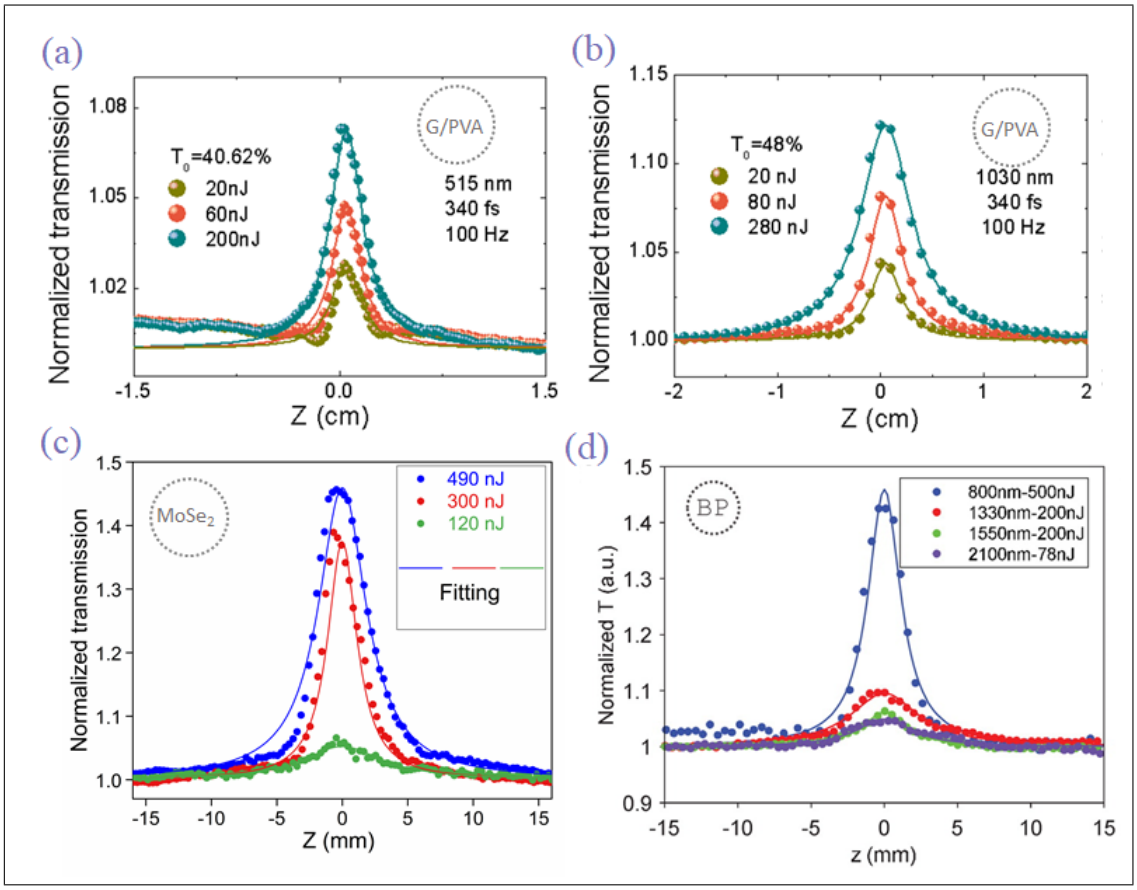

Figure 2.5: The SA behavior of graphene/PVA at the wavelength of (a) 515 nm and (b) 1030 nm. Reproduced from (Feng *et al.*, 2015a), OSA. (c) The open-aperture Z-scan data of few-layer MoSe2 in water with linear absorption coefficients of 6.51 cm^{-1} at the wavelength of 800 nm. Reproduced from (Wang *et al.*, 2018a), CLP. The SA response of layered black phosphorus in a wide wavelength range from 800 nm to 2100 nm. Reproduced from (Wang *et al.*, 2016b)

Strong SA has been experimentally observed in few-layer bismuthene with saturated intensities of 121.4 GW/cm^2 at 800 nm and 87.1 GW/cm^2 at 400 nm.(Lu *et al.*, 2017a) However, very little has been reported on the SA properties of antimonene and BN to date. The majority of 2D TMDs have been demonstrated to possess SA at the visible range, such as $MoSe_2$ at 800 nm (See Figure 2.5 (c)), and MoS_2, $MoSe_2$ and MoTe2 at 515 nm.(Wang *et al.*, 2018b, 2014a) As a new member of the 2D family, MXene has been found to have SA behavior at 800 nm, 1064 nm, 1550 nm and 1800 with saturation energy fluence of 8.4 mJ/cm^2, 8.2 mJ/cm^2, 5.7 mJ/cm^2 and 5.8 mJ/cm^2, respectively.(Shi *et al.*, 2013a) This

novel 2D nanomaterial was then utilised to mode-lock ultrafast laser pulses with a duration of 660 fs and repetition rate of 15.4 MHz at 1557 nm.(Dawlaty *et al.*, 2008a)

2.2.2.1 Slow- and fast- saturable absorber

The term saturable absorber refers to both fast- and slow- absorbers, which are related to laser pulse duration and relaxation time of excited carriers.(Wang *et al.*, 2017a) Hence, before exploiting the capabilities of either a fast- or slow- SA, it is important to know the excitation carrier lifetime, which can be obtained via time-resolved measurements. Pump-probe techniques utilising ultrafast lasers are an effective method to determine the recovery time of materials by investigating the excitation carrier dynamics. It can also be employed to identify other photophysical phenomenon that might occur along with saturable absorption like exciton formation and free carrier absorption. In a pump-probe measurement, an intense laser beam pumps the carriers into excited states, and these excited carriers are subsequently probed by a delayed and relatively low-intensity beam to obtain the differential transmission/reflection (ΔT/T or ΔR/R) of the probe beam that is defined as the relative change of the probe beam transmission/reflection with and without pump pulses.

To resolve the relaxation process of the excited carrier, the transmission/reflection is measured as a function of the pump-probe delay time. The schematic of a wavelength-degenerate and non-collinear pump-probe setup used in our previous work is shown in the inset of Figure 2.6 (d). The laser source produces ultrashort pulses with 100 fs pulse duration and a 100 kHz repetition rate at the central wavelength of 800 nm (RegA 9000, Coherent). Pump and probe beams were modulated by an optical chopper at 733 Hz and 442 Hz respectively. To eliminate the coherent spike, a polarizer and a half-wave is employed.

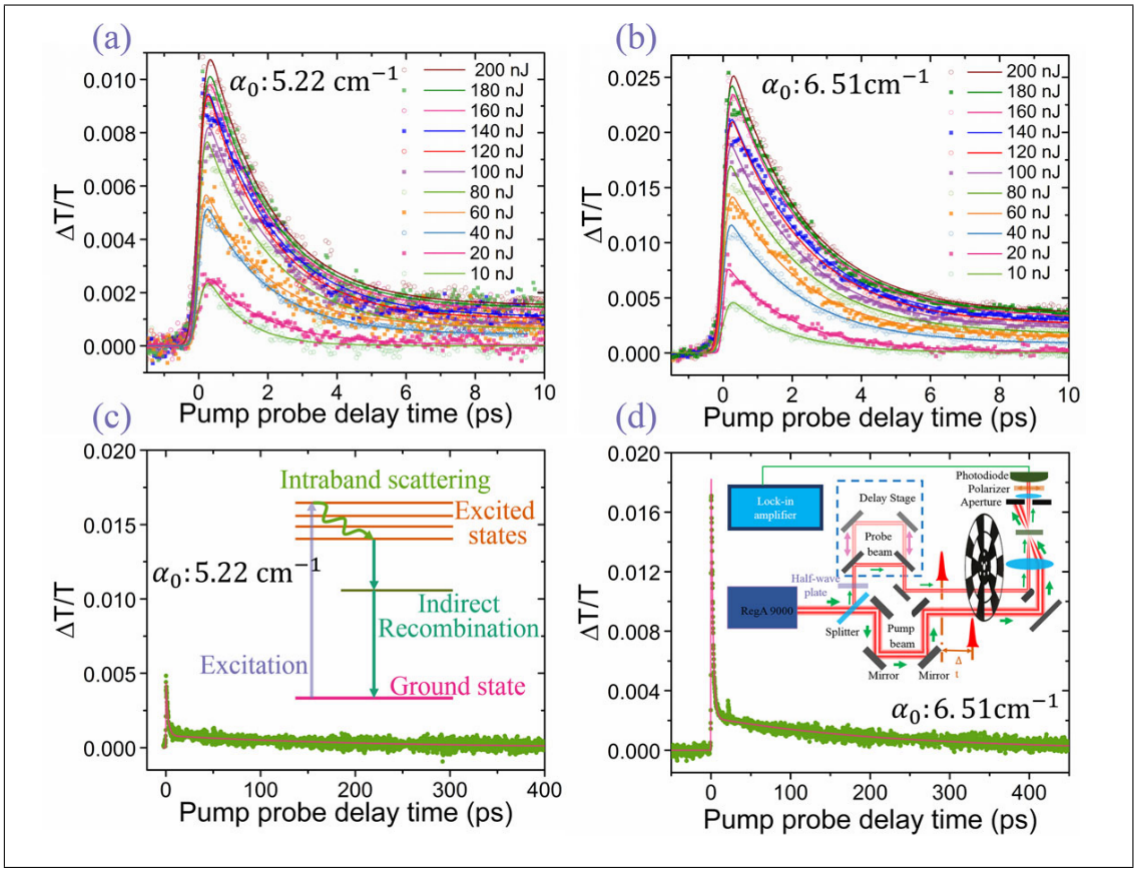

Figure 2.6: The SA excitation carrier dynamics of few-layer $MoSe_2$ obtained by a wavelength-degenerate pump-probe using 800 nm, 100 fs and 100 kHz laser pulses. The experimental (scatters) and biexponential decay fitting (solid lines) pump-probe traces of few-layer $MoSe_2$ with linear absorption coefficients of (a) 5.22 cm^{-1} and 6.51 cm^{-1} under varied pump irradiation from 10 nJ to 200 nJ. (c) and (d) are the cases at a long pump-probe decay time. The inset in (c) illustrates the indirect recombination of the excited carriers while the inset in (d) shows the diagram of the wavelength-degenerate pump-probe. The laser beam from RegA 9000 was divided by a splitter into an intense light for pumping and a relatively-low-intensity light for probing. Pump and probe beams were noncollinear and modulated by the same optical chopper at 733 Hz and 442 Hz respectively. A polarizer and a half-wave are employed for eliminating the coherent artefact. Reproduced from (Wang *et al.*, 2018a), CLP.

This time-resolved setup was employed to study the ultrafast nonlinear excitation carrier dynamics of few-layer $MoSe_2$ dispersed in deionized (DI) water. The pump-probe traces of the few-layer $MoSe_2$ dispersions with linear absorption coefficients of 5.22 cm^{-1} and 6.21 cm^{-1} are presented in Figure 2.6 (a) and (b)

respectively. The maximum of the differential transmission increased when the pump energy was increased from 10 nJ to 200 nJ. Figure 2.6 (c) and (d) are the corresponding pump-probe traces at a long pump-probe delay time from -5 ps to 400 ps. All these traces indicate that the relaxation of excited carriers in few-layer $MoSe_2$ possess a fast- and a relatively slow- exponential decay, see Figure 2.6.

Table 2.1: The NLO performance of 2D nanomaterials as slow- and fast- saturable absorbers

Material	Laser	τ_R (ps)	τ_P (ps)	SA Model	T_0 (%)	T_{max} (%)	Δ T (%)	A_{ns} (%)	I_S (GW/cm^2)	σ_e/σ_g	Ref.
Graphene (CHP)	515 nm, 1 kHz	0.4-11 0.1	0.34	Slow Fast	80.5 80.5	91 98.7	10.5 18.2	9 1.3	$\tilde{4}40$	0.43 0.06	(Dawlaty *et al.*, 2008a) (Shi *et al.*, 2013b)
	1030 nm, 1 kHz	0.4-11 0.1		Slow Fast	82.3 82.3	91.1 92.4	8.8 10.1	8.9 7.6	$\tilde{5}00$	0.48 0.41	(Dawlaty *et al.*, 2008b)
	800 nm, 10 kHz	0.481	0.08	Slow	38.66	50.5	11.84	49.5	764	0.72	(Wang *et al.*, 2016b)
	1330 nm, 50 kHz	0.481 -2.291		Slow	45.47	64.5	19.03	35.5	81 ±18	0.56	
	1420 nm, 50 kHz			Slow	56.14	83	26.86	17	86.7 ±15.8	0.34	
	1550 nm, 50 kHz			Slow	54.09	81.2	27.11	18.8	81 ±17.4	0.35	
	2100 nm, 50 kHz			Slow	60.05	78	17.95	22	25.4 ±4.82	0.45	
Graphene	1030 nm	0.1	0.34	Slow	48	64.77	16.77	35.23	88.9 ±27.3	0.59	(Feng *et al.*, 2015a)
/PVA	515 nm	0.1	0.34	Slow	40.62	54.32	13.7	45.68	309.4 ±152.7	0.68	
	1064 nm	1.3	6 ns	Fast	44.87	61.03	16.16	38.97	3.9 ±0.83	0.62	
MoS_2 (CHP)	515 nm, 1 kHz	4 -74	0.34	Slow	80.3	91	10.7	9	110	0.43	(Dawlaty *et al.*, 2008b)
	1030 nm, 1 kHz		Slow	80.3	95	14.7	5	430	0.31	-	(Dal Conte *et al.*, 2015a)
$MoSe_2$ (Water)	800 nm, 100 kHz	220	0.1	Slow Slow	47.8 34.9	55.2 55	7.4 20.1	44.8 45	39.37 234.75	0.81 0.57	(Wang *et al.*, 2018a)
BP (CHP)	515 nm, 1 kHz	0.36 -5.96 0.024	0.34	Slow Fast	79.9 79.9	94.8 98.3	14.9 18.4	5.2 1.7	55	0.24 0.077	(Yang *et al.*, 2009) (Sun *et al.*, 2008)
	1030 nm, 1 kHz	0.36 -5.96 0.024		Slow Fast	81.2 81.2	98.2 99.76	17 18.56	1.8 0.24	290	0.09 0.012	(Dawlaty *et al.*, 2008b) (Wang *et al.*, 2015)
	800 nm, 10 kHz	0.376	0.059	Slow	42.37	74.61	32.24	25.39	459	0.34	(Wang *et al.*, 2016b)
	1330 nm, 50 kHz	0.376 -1.39		Slow	46.05	87.8	41.75	12.2	382 ±60	0.2	
	1420 nm, 50 kHz			Slow	55.53	100	44.47	–	464 ±130	–	
	1550 nm, 50 kHz			Slow	58.92	68.8	9.88	31.2	398 ±163	0.71	
	1972 nm, 50 kHz			Slow	55.61	76.9	21.29	23.1	58.2 ±19.4	0.47	
	2100 nm, 50 kHz			Slow	56.72	78	21.28	22	71.3 ±28.2	0.59	

The decay of the excited carrier in many other 2D nanomaterials also follows the exponential modes according to the rate equations. For example, the excitons of suspended monolayer MoS_2 has been demonstrated to have triple exponential decay processes for the probe wavelengths of 600 nm, 665 nm, 670 nm and 690 nm.(Shi *et al.*, 2013b) The decay traces of these excitons can be well fitted by the Gaussian function convoluted with a tri-exponential function, Aexp(-t/τ_1) + Bexp(-t/$\tau_2$2) + Cexp(-t/τ_3). Here A, B and C are constants, t represents the pump-probe decay time and τ_1, τ_2 and τ_3, are the relaxation times, which were fitted to be 2.6 0.1 ps, 74 3 ps and 850 48 ps for monolayer MoS_2, respectively.(Shi *et al.*, 2013b) 7-9 layers black phosphorus has been reported to possess two exponential decay processes with a fast carrier relaxation time of 0.016 - 0.24 ps and relatively slow one of 0.36 1.36 ps.(Wang *et al.*, 2016b) More carrier lifetimes in 2D nanomaterials are summarized in Table 2.1. To make a conclusion on these different excited carrier dynamics, here a general single- or multi-exponential model with autocorrelations is presented, which can be utilized to analyze all the exponential decay cases to determine the relaxation time:

$$S(t) = \sum^{i=1,2,3..,n} D_i exp(-\frac{t}{\tau_i}) erfc(\frac{\sigma}{\sqrt{2}\tau_i} - \frac{t}{\sqrt{2}\sigma}) \tag{2.6}$$

Here S(t) represents the differential transmission/reflection, t is pump-probe delayed time, σ is the pulse duration and erfc stands for the standard error function. i = 1, 2, 3.., n is the number of the excited carrier relaxation processes, i.e., the number of the total exponential decays. D_i and τ_i represent the relative amplitudes and independent decay times, respectively. The relaxation processes of excited carriers in few-layer $MoSe_2$ have two exponential decay parts and hence, the model modified from Equation 2.6 to fit these results is a bi-exponential equation:(Wang *et al.*, 2018b)

$$\frac{\Delta T}{T} = \{D_1 exp(-\frac{t}{\tau_1}) erfc(\frac{\sigma}{\sqrt{2}\tau_1} - \frac{t}{\sqrt{2}\sigma}) + D_2 exp(-\frac{t}{\tau_2}) erfc(\frac{\sigma}{\sqrt{2}\tau} - \frac{t}{\sqrt{2}\sigma})\} \tag{2.7}$$

The biexponential fitting curves were plotted in Figure 2.6using solid lines, which are in good agreement with the experimental data for all the pump energies. The schematic of relaxation processes is plotted in the inset of Figure 2.6 (c). The pump beam interacted with the few-layer $MoSe_2$, generating electron-hole pairs, and the electrons were injected to the excited states.

Subsequently, these excited electrons relax to the low-energy-level excited states via the intraband scattering within a short time, τ_1. As few-layer $MoSe_2$ is an

indirect bandgap semiconductor, these electrons will finally relax to the ground state through the indirect recombination with a relatively long lifetime, τ_2. The fitting τ_1 and τ_2 are shown in Table 2.1.

After obtaining the recovery time of a saturable absorber, the NLO performance of 2D nanomaterials can be studied using the modified Frantz-Nodvik model or the steady-state solution of Hercher's rate equations, which are defined as the slow- or fast- SA model, respectively. The study on Cr4+ hosted by Garnet crystals provided a detailed derivation of slow- or fast- SA models based on rate equations.(Burshtein *et al.*, 1998)

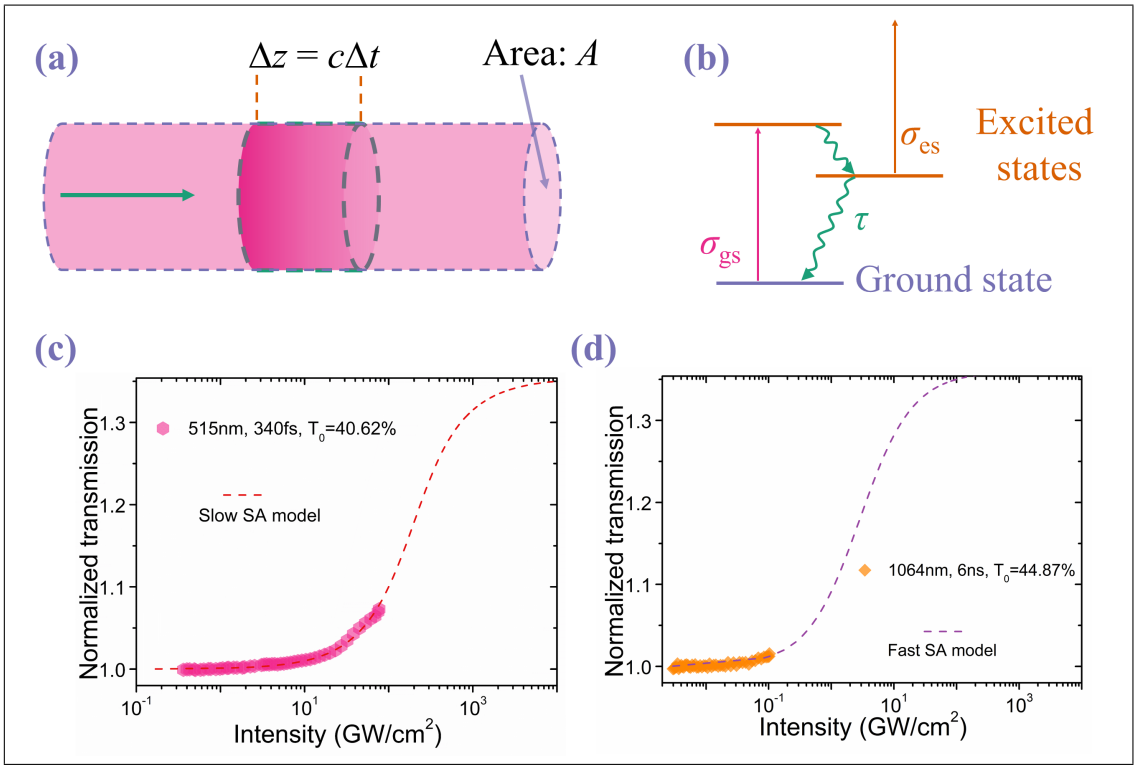

Figure 2.7: Slow- and fast- SA of 2D nanomaterials. (a) The schematic illustrating the absorption of photons by atoms. (b) The excitation and relaxation of carriers. The slow-SA of a few-graphene/PVA composite thin film analyzed by the modified Frantz-Nodvik model: (c) the transmission as a function of intensity. (d) The fast-SA of the graphene/PVA composite thin film. Adapted from (Feng *et al.*, 2015a), OSA. All the scatters stand for experimental results and the dash lines represent fitting data.

As illustrated in Figure 2.7 (a), a ray of light with a photon density of E(z, t) is propagating inside materials and partial photons are absorbed by atoms. These absorbed photons inject the electrons to excited states, as seen in Figure 2.7 (b).

As photons are absorbed by atoms both at ground- and excited- states, the rate equation can be written as:

$$[E(z,t)-E(z,t+\Delta t)]\cdot\Delta z\cdot A+\Delta z\cdot A\cdot[E(z,t)-E(z+\Delta z,t)]=(\sigma_{gs}\cdot\Delta z)\cdot N(z,t)\cdot[E(z,t)\cdot\Delta z\cdot A]$$

$$+(\sigma_{es}\cdot\cdot\Delta z)\cdot[N_T-N(z,t)]\cdot[E(z,t)\cdot\Delta z\cdot A] \quad (2.8)$$

Here c is the light speed, z is the propagation distance in the materials, $\Delta z = c\Delta t$, σ_{gs} and σ_{es} represent the absorption cross-sections of ground state and excited states, respectively. N(z,t) is the density of ground-state atoms and NT is the total of absorption atoms density. A is the area of the light and material interact. This rate equation can be simply derived as:(Burshtein *et al.*, 1998)

$$\frac{\partial}{\partial t}E(z,t)+c\frac{\partial}{\partial z}E(z,t)=-\Delta\sigma cN(z,t)E(z,t)-\sigma_{es}cN_TE(z,t) \quad (2.9)$$

Here $\Delta\sigma = \sigma_{gs} - \sigma_{es}$. Another well-known rate equation can be expressed as:(Burshtein *et al.*, 1998)

$$\frac{\partial}{\partial}N(z,t)=-\sigma_{gs}cN(z,t)+\frac{N_T-N(z,t)}{\tau} \quad (2.10)$$

Where τ is the lifetime of the excited carrier. In a slow saturable absorber where the light pulse duration is much shorter than the lifetime of excited carriers, the second term of Equation 2.9 can be neglected. For an ideal slow saturable absorber where $\sigma_{es} = 0$, an analytical solution for Equation 2.8 and 2.9 can be obtained and the energy transmission, T_{FN}, of an ideal slow saturable absorber with thickness of L can be expressed as:

$$T_{FN}\equiv\frac{E(L)}{E(0)}=ln[1+T_0(e^{\sigma g_s E(0)-1})]/[\sigma_{g_s}E(0)], T_0=e^{-\sigma gsNL} \quad (2.11)$$

This is the Frantz-Nodvik equation. T_0 is the linear transmission of the absorber. For a practical saturable absorber, σ_es $\neq 0$ and transmission obtained from the rate equations is given by:(Burshtein *et al.*, 1998; Feng *et al.*, 2015a)

$$T(F)=T_0+\frac{T^{FN}-T_0}{1-T_0}(T_{max}-T_0), F=\hbar\omega E, T_{max}=e^{-\sigma_{es}NL} \quad (2.12)$$

Here T_{max} is the maximum transmission that can be reached for an absorber

under the irradiation of very intense light. This slow-SA model can be employed to fit the NLO measurements to obtain corresponding parameters such as saturation intensity, maximum transmission, ground- and excited- states absorption cross-sections, NLO modulation depth, and non-saturable loss. It can be seen from equation 2.11 and 2.12, the thickness of the sample and the absorptive cross-sections play a significant role on both NLO losses and modulation depth.

This model was utilized to study the saturable absorption behavior of some 2D nanomaterials. The excited carriers of graphene have been demonstrated to possess a fast recovery time of 0.4- 11 ps in the visible region.(Dawlaty *et al.*, 2008b; Sun *et al.*, 2008; Wang *et al.*, 2016b; Zhang *et al.*, 2016b) For laser pulses with duration of 340 fs, graphene can be used as a slow saturable absorber and the NLO performance can be analyzed via Equation 2.11. The fitting result are shown in Figure 2.7 (c). In the near- to mid- infrared region, the excited carrier lifetime of graphene was obtained by wavelength-degenerate pump-probe experiment to be 0.481-2.291 ps, and therefore graphene can be used as slow saturable absorbers for 340 fs and 80 fs laser pulses.(Wang *et al.*, 2016b; Zhang *et al.*, 2016b)

The saturation intensity, NLO modulation depth, non-saturable loss and the absorptive cross-section ratio of excited state over ground state (four NLO parameters) of graphene in CHP in near- and mid- infrared regions obtained from slow SA-model are 25.4-86.7 GW/cm^2, 17.95%-27.11%, 17.0%-35.5% and 0.34-0.56 for 80 fs laser pulses, and 500 GW/cm^2, 8.8%, 8.9% and 0.48 for 350 laser pulses at 1030 nm, respectively.

The NLO parameters of some other 2D nanomaterials are listed in Table 2.1. As mentioned previously in the pump-probe section, the excited carrier lifetime of few-layer $MoSe_2$ were measured to be 220 ps, which is much longer than the femtosecond region. Hence it can be utilized as a slow absorber when the laser pulse is in the order of femtoseconds. The absorption cross-section ratios of excited state over ground state were fitted to be 0.81 and 0.57, with non-saturable loss of 44.8% and 45.0% for the few-layer $MoSe_2$ dispersions with the linear transmission of 47.8% and 34.9%, respectively.(Wang *et al.*, 2018b)

Layered black phosphorus is another 2D nanomaterial with a wide-spectral NLO response from visible to mid-infrared region. This group's previous work on few-layer phosphorus showed that the carrier lifetime at the wavelength region from 800 nm to 2100 nm ranged from 0.376 ps to 1.39 ps. For 50 kHz, 59 fs laser pulses, the four NLO parameters of few-layer phosphorus as a slow saturable absorber is reported to be 58.2 - 464 GW/cm^2, 9.88% - 44.47%, 12.2% - 31.2% and 0.012 - 0.71 at the wavelength range from 800 nm to 2100 nm.(Wang *et al.*, 2016b)

The slow-saturable absorption properties of layered black phosphorus were also studied by 340 fs laser pulses at 515 nm and 1030 nm. The saturation intensity

and NLO modulation depth are slightly larger at 1030 nm (290 GW/cm^2 and 17.0%) than those at 515 nm (55 GW/cm^2 and 14.9%), while the non-saturable loss and the absorptive cross-section ratio of excited state over ground state are slightly smaller for longer wavelength (1.8% and 0.09 for 1030 nm, 5.2% and 0.24 for 515 nm, respectively).(Zhang *et al.*, 2016b)

Some other 2D TMDs have been demonstrated to possess slow-SA performance using femtosecond lasers. Under the irradiation of 340 fs laser, few-layer $MoSe_2$ with linear transmission was saturated at the intensities of 110 GW/cm^2 and 430 GW/cm^2 at 515 nm and 1030 nm, respectively.(Zhang *et al.*, 2016b)

In contrast, for a fast-saturable absorber, τ needs to be accounted for in Equation 2.9, which can be expressed as follows for a constant intensity:(Burshtein *et al.*, 1998; Zhang *et al.*, 2016b)

$$\frac{\partial}{\partial t}N(z) = -\sigma_{gs}N(z)I(z) + \frac{N_T - N(z)}{\tau} = 0 \tag{2.13}$$

By substituting Equation 2.12 into Equation 2.8, one obtains the fast- SA model:

$$T[\frac{I(0)+S}{I(0)+S}]^D = T_0, S = \frac{1}{\tau\sigma_{gs}}, D = \frac{\Delta\sigma}{\sigma_{gs}} \tag{2.14}$$

Here I(0) represents the incident intensity (photons per unit area). An example of employing this fast SA model to study the NLO properties of 2D nanomaterial is shown in Figure 2.7 (d). In this study, graphene/PVA composite thin films were irradiated by laser pulses with the duration of 6 ns, much larger than the recovery time (1.3 ps) of the excited carrier in the composite thin film. The modeled curve (dash line) favorably fits the experimental data (solid scatters).

The four NLO parameters were fitted to be 3.9 GW/cm^2, 16.16%, 38.97 and 0.62 at a central wavelength of 1064 nm. 2-3 and 80 layers black phosphorus can also be utilized as fast saturable absorber for 340 fs laser pulses as they have carrier lifetimes of 24 fs and ¡100 fs respectively.(Suess *et al.*, 2015; Wang *et al.*, 2015) [14, 71] In the fast-SA model, the NLO parameters were fitted to be relatively small, e.g., absorptive cross-section ratios of excited state over ground state of 0.012 and 0.077 and 0.24% and 1.7% at the wavelength of 1030 and 515 nm, respectively.(Zhang *et al.*, 2016b)

2.2.2.2 Wavelength- and pulse duration - dependence

It can be seen in Table 2.1 that some interesting phenomena exist in the saturable absorption of 2D nanomaterials. For instance, the SA properties of some 2D

nanomaterials show certain dependences on the linear transmission, excited wavelength and pulse duration. These have also been experimentally demonstrated other published works.(Feng *et al.*, 2015a; Zhang *et al.*, 2018) Here these works are summarised with qualitative and quantitative analysis.

In Table 2.1, the modulation depth of graphene displays an upward trend as the irradiated wavelength moves from visible to mid infrared, whereas black phosphorous reaches a maximum at 1400 nm. Nonlinear optical losses are similar for both graphene and black phosphorous, reaching a peak in the near infrared and both exhibit small NLO loss in the visible and mid-infrared region. There is a decrease in the saturation intensity of graphene and layered phosphorus as the excitation wavelength changed from 800 nm to 2.1 μm. This is more obvious when plotting the saturation intensity as a function of the wavelength, shown as the solid scatters in Figure 2.8 (a)-(b).

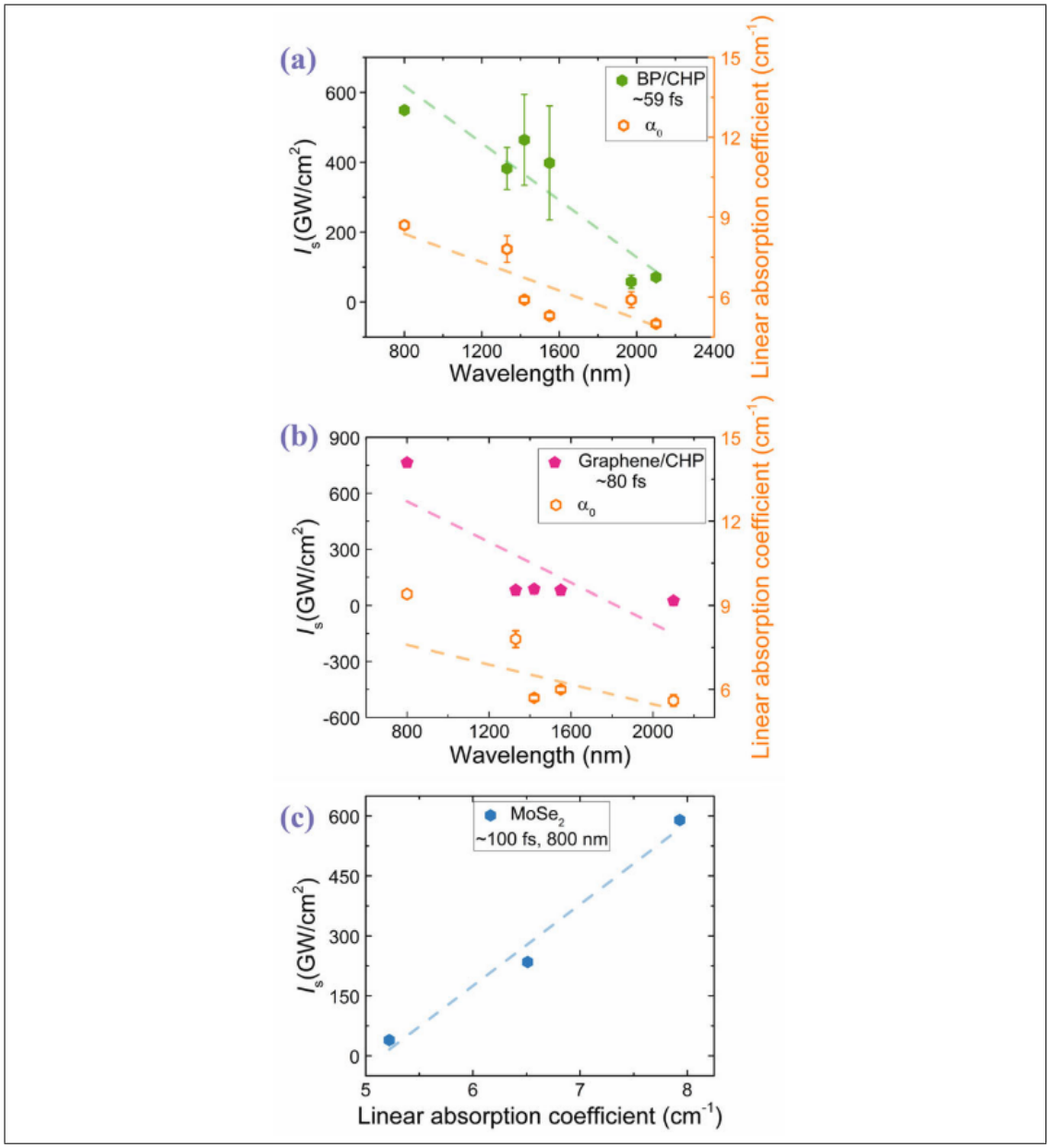

Figure 2.8: The saturation intensity and linear absorption coefficient as a function of excited laser wavelength from 800 nm to mid-infrared in (a) layered black phosphorus and (b) graphene. Reproduced from (Wang *et al.*, 2016b) (c) The saturation intensity vs linear absorption coefficient in few-layer $MoSe_2$. (Wang *et al.*, 2018a, 2014a).

This can be understood by the linear absorption coefficient at different wavelength. The linear absorption coefficient is larger at shorter wavelength for both graphene and black phosphorous (BP).(Wang *et al.*, 2016b) A larger linear absorp-

tion coefficient means more photons are required to excite the electrons, resulting in a higher saturation intensity. On the same graph, to better understand this relationship, the corresponding linear absorption coefficient is also plotted (shown as open scatters in Figure 2.8), which indicates a decreasing trend with increasing wavelength. The dependence of saturation intensity on the linear absorption coefficient has been observed in few-layer $MoSe_2$ under the irradiation of 100 fs, 800 nm laser pulses.(Wang *et al.*, 2018b, 2014a)

As seen in Figure 8 (c), the linear absorption coefficient increases from 5.22 cm^{-1}, 6.51 cm^{-1} to 7.93 cm^{-1}, and the saturation intensity increases from 39.37 GW/cm^2, 234.75 GW/cm^2 to 590 GW/cm^2, respectively. According to T=exp(-αL) and T=exp(-σNL), more photons are needed to fully fill the excited states of a sample with a larger linear coefficient, resulting in larger saturation intensity. Note that these 2D nanomaterials were studied in solution and the laser power required to reach the damage threshold is relatively high.

Another interesting SA phenomenon reported in 2D nanomaterials is the pulse-duration-dependent saturation intensity. The saturation intensity of graphene/PVA was measured to be 88.9 27.3 GW/cm^2 for 340 fs laser pulses at the wavelength of 1030 nm and 3.9 0.83 GW/cm^2 for 6n laser pulses at 1064 nm.(Feng *et al.*, 2015a) Higher saturation intensity for wider pulse duration was also observed in MoS_2 monolayer. As the pulse duration increased from 65 fs, 10 ps to 10 ns, the saturation intensity increased from 0.37 GW/cm^2, 7.65 GW/cm^2 to 18.56 GW/cm^2, respectively.(Zhang *et al.*, 2018)

The dependence of SA on the pulse duration can be explained using excitation carrier dynamics. For instance, MoS_2 monolayer is a direct bandgap semiconductor and the excited carrier relaxation is mainly via carrier-carrier scattering, carrier-phonon scattering and direct recombination, with characteristic times of 2.6 ps, 74 ps and 850 ps, respectively.(Shi *et al.*, 2013b) [67]

This recovery time (τ_r 940 ps) of monolayer MoS_2 is far shorter than the nanosecond excited pulse duration (τ_E =10 ns), i.e., $\tau_r < \tau_E$, while much longer in comparison to the femtosecond pulse duration (τ_E =65 fs), i.e., $\tau_r > \tau_E$. For cases where $\tau_r < \tau_E$, the conduction band of MoS_2 can be fully filled by the accumulation of excited carriers in the time τ_r and therefore the saturated density of the excited carrier (Ns) can be approximately calculated by:

$$N_s = \alpha \frac{I_s \tau_r}{hv} \tag{2.15}$$

Here h represents the photon energy. In contrast, in another case where $\tau_r > \tau_E$, the time that photons contribute to the extinction of carriers is τ_E and can be

expressed:

$$N_s = \alpha \frac{I_s \tau_E}{hv} \tag{2.16}$$

These two equations indicate that the saturation intensity is larger for longer laser pulse duration, which explains the dependence of SA on the pulse duration observed in both graphene/PVA thin films and MoS_2 monolayer, and other 2D nanomaterials.

2.2.3 Summary

In this section, the saturable absorption, the methods to study saturable absorption and broadband NLO response of 2D nanomaterials including graphene, layered TMDs and 2D Ground-V elements are introduced. The NLO properties of the 2D nanomaterials as slow- or fast- saturable absorbers were compared based on the modified Frantz-Nodvik model or the steady-state solution of Hercher's rate equations. The dependence of SA in 2D nanomaterials on excited wavelength, linear absorption coefficients and pulse duration are summarised with qualitative and quantitative analysis.

2.3 Photonic devices based on SA

After exploiting the above SA properties of 2D nanomaterials, some SA based photonics devices have been reported. In this section, the NLO properties of saturable absorption mirrors (SAMs) and composite thin films based on 2D nanomaterial devices designed for mode-locking are reviewed and analysed.

2.3.1 2D nanomaterials-SAMs

Benefiting from the wide-spectral NLO response, novel excited carrier dynamics and low-cost of fabrication, 2D nanomaterials show both commercial and scientific potential to develop SAMs for generating laser pulses with high repetition rate, higher power, short duration in a wide wavelength range. Particularly, layered black phosphorus SAMs (BP-SAMs) have been experimentally demonstrated to produce ultrafast pulses in a wide wavelength range from 1.0 μm to 3.5 μm.(Kong *et al.*, 2016; Ma *et al.*, 2015; Qin *et al.*, 2015, 2016, 2018; Sun *et al.*, 2017; Wang *et al.*, 2016c)

Wide-spectral laser pulses have been reported for Graphene and TMD SAMs, such as WS_2 TiSe2 and MoS_2.(Chen *et al.*, 2016; Cunning *et al.*, 2011; Hou *et al.*,

2014; Kong *et al.*, 2015; Liu *et al.*, 2018; Xie *et al.*, 2012; Xu *et al.*, 2011d,e) Taking graphene saturable absorber mirrors (GSAM) as an example, several aspects of 2D nanomaterials-SAMs are reviewed, including their fabrication, NLO characterizations and analysis, and their mode-locking capabilities. Figure 2.9 shows a saturable absorption mirrors (GSAM) and the sample characterization.(Wang *et al.*, 2017a)

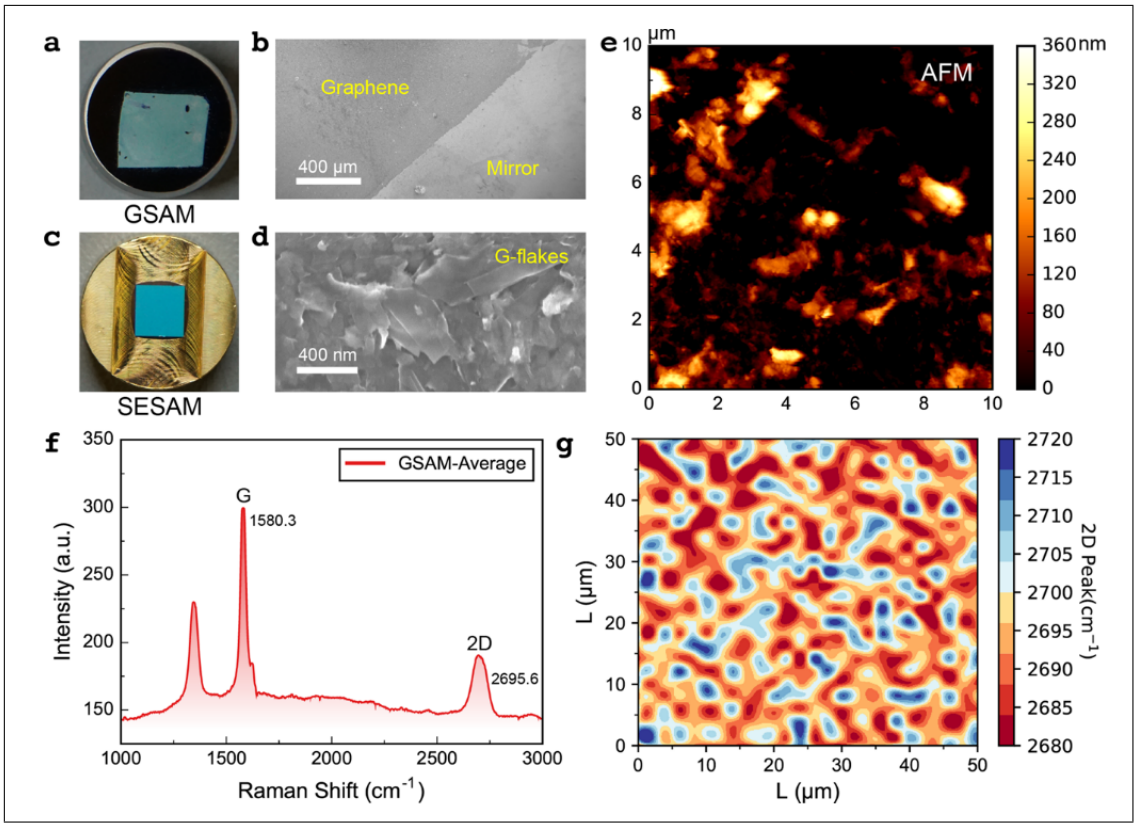

Figure 2.9: A graphene saturable absorption mirror (GSAM). (a) The photo of the GSAM. SEM images with relatively (b) low and (d) high magnification. (c) A commercial SESAM from company BATOP (SAM-2000-44-10ps) for reference at the wavelength of 2 μm. (e) An AFM image from a 10 μm 10 μm area to characterize the surface of the GSAM. (f) The mapping of the 2D Raman peak of the graphene films. (g) The average Raman spectra from a 200 μm 100 μm area of the sample. Reproduced from (Wang *et al.*, 2017a).

Liquid-phase-exfoliated graphene flakes were employed to prepare graphene films via vacuum filtration by a nitrocellulose porous membrane. Subsequently, the graphene film was transferred and tightly attached to a silver coated mirror with proactive SiO_2. Similar methods were utilized to produce high quality BP- and TMD- SAMs.(Chen *et al.*, 2016; Kong *et al.*, 2016, 2015; Wang *et al.*, 2016c),

Scanning electron microscopy (SEM), atomic force microscopy (AFM) and Raman techniques were employed to confirm the quality of the GSAM. A clear boundary of graphene on the mirror surface can be seen via low-magnification SEM, as shown in Figure 2.9 (b), indicating a homogeneous deposition of the graphene film on the mirror. As shown in Figure 2.9 (d), high magnification SEM clearly shows the graphene flakes, implying that the graphite was effectively exfoliated into graphene and majority of the graphene flakes are in the size range of 500 nm. The AFM image in Figure 2.9 (e) shows that most of the graphene film has a 100 nm height variation and a calculated surface roughness of 57.42 nm.

The 2D Raman peak shifts for monolayer graphene, bilayer graphene and graphite bulk have been reported to increase from 2680, 2700 to 2720 cm^{-1} respectively.(Zhang *et al.*, 2016d) The average 2D peak located at 2695.6 cm^{-1} in Figure 2.9 (f) and the red area (< 2700 cm^{-1}) in the 2D peak mapping in Figure 2.9 (g) indicate that the graphene flakes of the GSAM were mainly composed of mono- and bi-layers graphene.

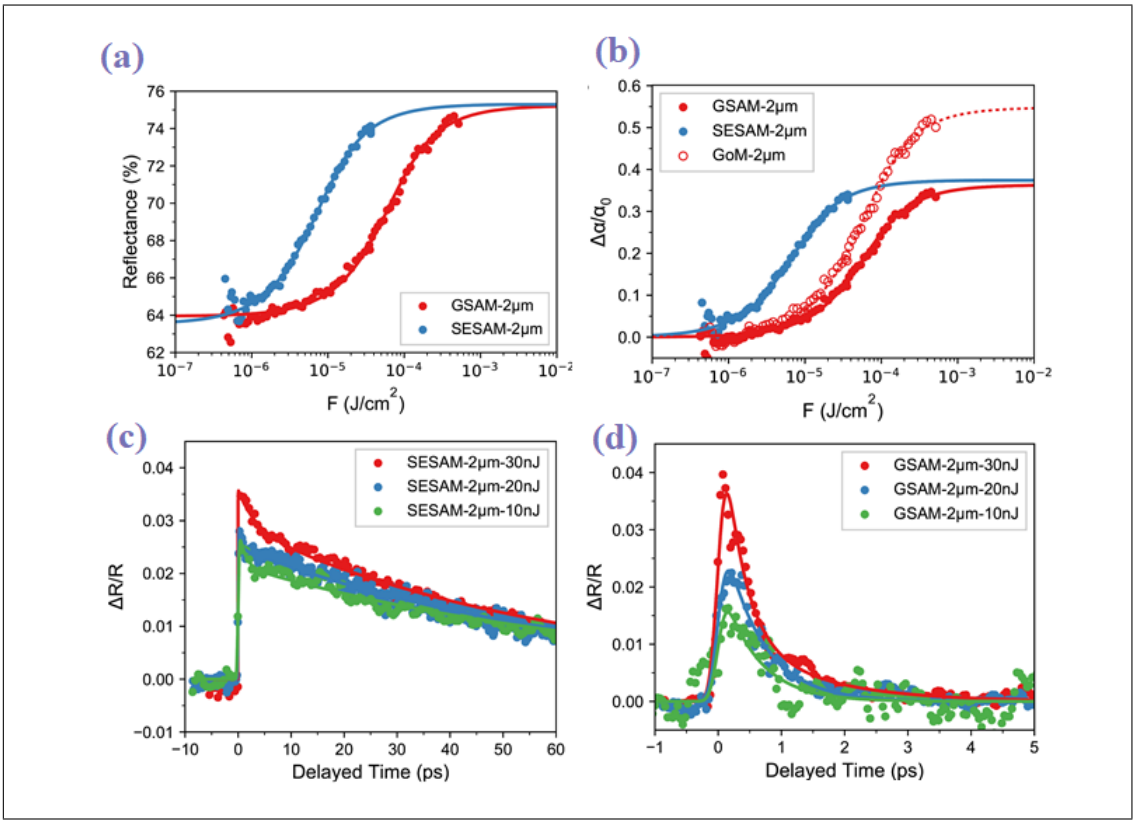

Figure 2.10: (a) The NLO reflectance of the GSAM and SESAM as a function of pulses fluence. (b) The differential absorption of the GSAM and commercial SESAM at 2 μm. By subtracting the surface scattering from the GSAM, graphene on mirror (GoM) shows much better NLO performance, see hollow circles. The excited carrier dynamics of (c) the GSAM and (d) commercial SESAM. Scatters stand for the experimental data and the solid lines for fitting results. Reproduced from (Wang *et al.*, 2017a).

After fabrication and characterization, the SA properties of the GSAM were studied and compared to a commercial SESAM via I-scan and wavelength-degenerate pump-probe techniques. The I-scan results in Figure 2.10 (a) indicate that both the GSAM and SESAM possess SA properties, i.e. the reflectance increases as the laser fluence increases. The relaxation of excited carriers in both the GSAM and SESAM showed bi-exponential decay, see Figure 2.10 (c) and (d), respectively. Hence the bi-exponential model, i.e., Equation 2.6 was employed to fit the carrier dynamics data with the fitting short (τ_1) and long (τ_2) excited carrier relaxation times of 0.168 ps and 1.190 ps for the GSAM, and 1.109 ps and 63.0 ps for the SESAM, respectively.(Wang *et al.*, 2017a) τ_1 was taken as the recovery time (τ_p) and both SAMs can be utilized as slow-absorber for 150 fs exited laser pulses. Used as a slow-absorber for mode-locking, the minimum duration of generated pulses

could be 37 fs for graphene and 2 ps for the SESAM because the still limited to $\tau_p/30$.(Dong *et al.*, 2016a)

To analyse the slow-SA properties of the SAMs, a reflective slow-SA model is needed. On the first pass of the light through the graphene film, the transmission, T(F), can be expressed by Equation 2.12. The transmitted light would be reflected by the silver mirror in a very short time and the excited saturable absorber has not yet recovered. The second transmission is expressed as $T(F + F \cdot T(F))$. Hence the reflective slow-SA model for SAMs can be expressed as:

$$R = T(F)\cdot T(F+F\cdot T(F)), \Delta R = R_{max} - R_0 = T_{max}^2 - T_0^2, A_{ns} = 1 - R_{max} = 1 - T_{max}^2 \tag{2.17}$$

Here δR is the NLO modulation depth and A_{ns} represents the non-saturable loss. This reflective slow-SA model was employed to fit the I-scan data of the GSAM and SESAM, which fit well with the experimental results, see Figure 2.10 (a). The saturation intensity, NLO modulation depth, non-saturable loss and the absorptive cross-section ratio of the excited state over ground state were modelled to be 542 MW/cm^2, 12.6%, 9.9% and 0.442 for the GSAM, and 69.2 MW/cm2, 13.2% 23.2% and 0.615 for the SESAM, respectively.(Wang *et al.*, 2017a) The mode-locked lasers based on GSAMs have successfully produced ultrafast pulses with durations in the femtosecond region.(Cunning *et al.*, 2011; Hou *et al.*, 2014; Xie *et al.*, 2012; Xu *et al.*, 2011d,e) Laser pulses were also obtained in a wide wavelength range from 1 μm to 3.5 μm based on BP-SAMs.(Kong *et al.*, 2016; Ma *et al.*, 2015; Qin *et al.*, 2015, 2016, 2018; Sun *et al.*, 2017; Wang *et al.*, 2016c) More details on the pulsed lasers based on SAMs will be introduced in the last section.

2.3.2 2D nanomaterials/polymer composites

Another important photonic device based on 2D nanomaterials is their polymer composite thin films, which help utilise liquid-phase-exfoliated 2D materials for practical applications. Liquid-phase-exfoliation (LPE) is a low-cost, effective and high yield method of producing 2D nanomaterials.(Coleman *et al.*, 2011b; Dong *et al.*, 2016b; Huang *et al.*, 2017; Sun *et al.*, 2010f; Zhang *et al.*, 2016c) A solid matrix is needed to host the 2D nanomaterials to employ LPE 2D nanomaterials for practical photonic devices.

Polyvinyl alcohol (PVA) is a popular choice due to its low-cost, non-toxic, easy-fabrication processes and high transparency. The photographs in Figure 2.11 (a) show a solution-cast method to prepare graphene/PVA composite thin films at different stages. PVA powder was dissolved in water in a water bath at 90 C to prepare PVA solution, which, after cooling down, was employed to mix liquid-

phase-exfoliated graphene dispersion by agitation for 24 hours and sonication for 4 hours. The obtained homogeneous mixture was subsequently casted into a petri dish and a graphene/PVA composite thin film with high quality can be obtained after desiccation in an oven.

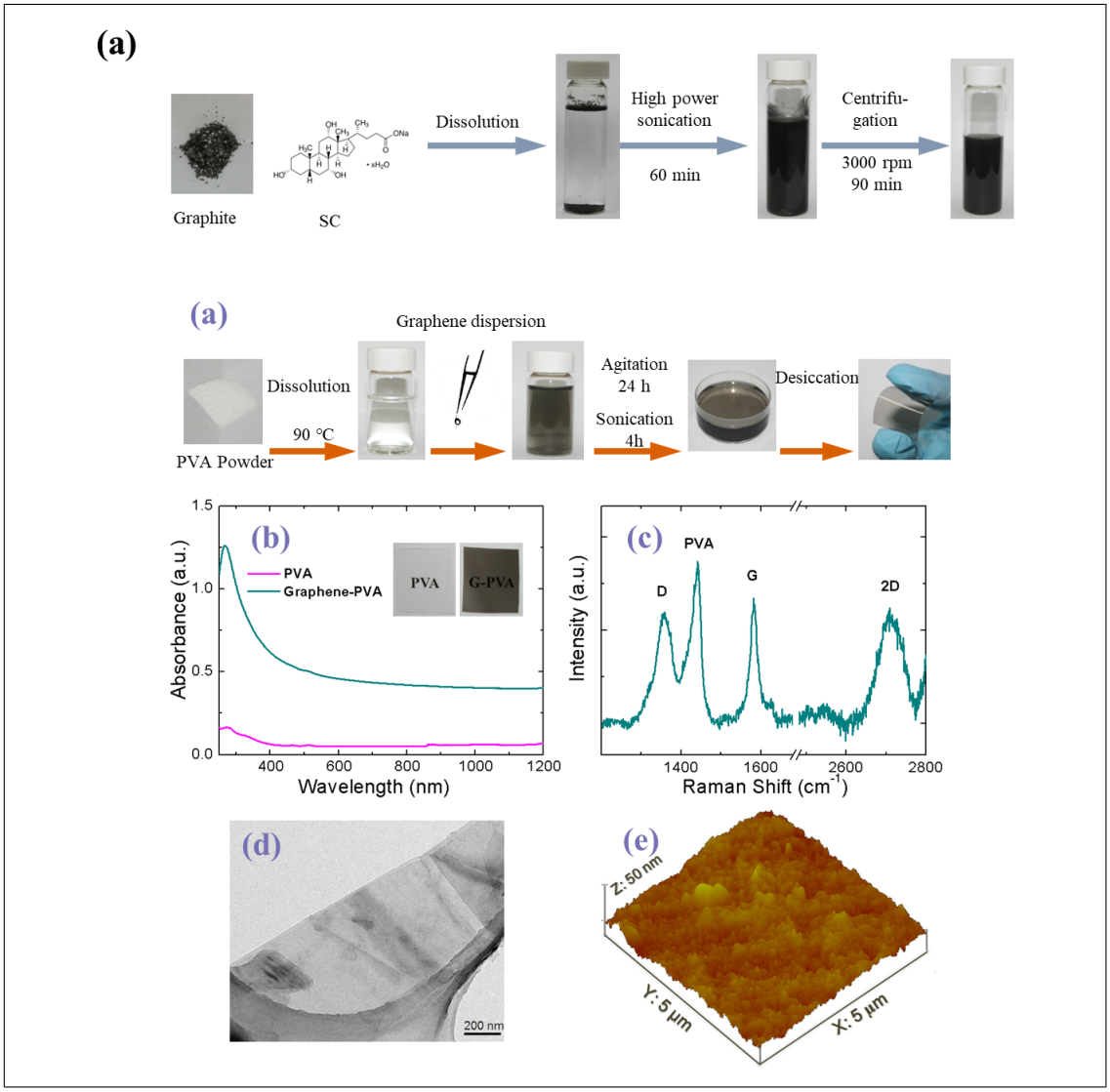

Figure 2.11: The fabrication and characterizations of graphene/PVA composite thin films. (a) A solution-cast method to prepare graphene/PVA composite thin films. (b) The absorbance of a pure PVA and graphene/PVA composite films and their photographs in the inset. (c) Raman spectrum of a graphene/PVA composite film. (d) A TEM image of a graphene. (e) An AFM image of a graphene/PVA composite film. Adapted from Feng *et al.* (2015a), OSA.

Absorption, Raman spectrum, TEM and AFM measurements were utilized to examine the quality of the Graphene/PVA composite thin films. The absorbance of graphene/PVA thin film shown in Figure 2.11 (b) is analogical to that of graphene while the absorbance of a pure PVA film is closed to zero. This indicates that the linear and nonlinear absorption of the composite thin films would originate from graphene alone with no contribution from the PVA. A Raman shift at 1440 cm^{-1} was observed for PVA and the 2D Raman peak was captured at 2700 cm^{-1}, implying a high quality of the graphene inside the polymer film, see in Figure 2.11 (c).

The edge of a bright-field TEM image in Figure 2.11 (d) shows that the graphene flake is bilayer. In Figure 2.11 (e), an AFM image of the graphene/PVA film shows that its surface roughness is 4 nm, which translates to low scattering in photonic devices.(Feng *et al.*, 2015a) By incorporating graphene/PVA films into the laser cavity as a saturable absorbers, ps to fs laser pulses at the wavelength from 1525 to 1559 nm were obtained.(Sun *et al.*, 2010a,d) PVA was also employed to host other 2D nanomaterials such as MoS_2, $MoSe_2$, WS_2, WSe_2 and BP, which were subsequently used to obtain laser pulses.(Ahmad *et al.*, 2016; Chen *et al.*, 2015; Huang *et al.*, 2014; Kärtner & Keller, 1995b; Koo *et al.*, 2016b; Luo *et al.*, 2015; Woodward *et al.*, 2015d) This will be introduced in the last section.

2.3.3 Summary

In this section, the fabrication and characterization of 2D nanomaterials based photonic devices is reviewed, including SAMs and polymer composites. A reflective slow-SA model modified from the Frantz-Nodvik equation was introduced to analyze the NLO response of the GSAM, which showed competitive SA behavior in comparison to a commercial SESAM. Taking graphene/PVA as an example, the preparation and characterization of 2D nanomaterials/polymer film for modelocked laser pulses is reviewed.

2.4 Ultrafast laser pulses based on 2D saturable absorbers

The end goal of exploiting the above SA properties is to employ these 2D nanomaterials and their photonic devices to produce short-pulsed lasers, which are becoming more and more commonplace as tools with a wide variety of applications, including biomedical research, industrial materials processing and fundamental research.(Fork *et al.*, 1981; Kärtner & Keller, 1995a) Ultrafast fiber lasers utilize the saturable absorption effect to generate pulsed operation.

Shorter pulses are usually obtained via passive mode-locking utilizing a saturable absorber, due to the fast loss modulation resulting from the fast recovery time of saturable absorbers. Another method commonly used in fiber lasers is Q-switching.(Kajava & Gaeta, 1996) In this section, a brief introduction about passive mode-locking based on saturable absorbers was initially given. Then the performance of ultrafast mode-locked lasers based on various 2D saturable absorbers is summarised: graphene, TMDs, BP and other 2D nanomaterials.

2.4.1 Passive mode-locking

Mode-locking can be further broken down into two mode-locking types, which are passive and active. A small fraction of the laser pulse partially transmitted through an output coupler out of the laser resonator. These transmissions are therefore spaced equally by the resonator round-trip time. Generally an intracavity loss modulator is employed to collect the laser light in short pulses around the minimum of the loss modulation with a period given by the cavity round-trip time, $T_R = 2L/v_g$, where L is the laser cavity length and vg is the group velocity.(Ippen *et al.*, 1980a) To actively mode-lock, an external signal must be applied to the optical loss modulator. This is generally achieved ustlising the acousto-optic or the electro-optic effect.

Whereas to passively mode-locking, a saturable absorber is needed to obtain self-amplitude modulation of the light inside of the laser cavity. Haus (1975b) The saturable absorber introduces a certain amount of loss into the intracavity laser radiation. This loss is relatively large at lower intensities, but the loss is significantly smaller at higher intensities, especially for short pulses. Therefore, such a short pulse will create a loss modulation due to the higher intensity at the peak causing greater saturation than the low intensity wings. As the high intensity pulse circulates, the laser gain medium is saturated sufficiently to compensate for the losses, whereas other low-intensity light which is circulating will have more loss than gain and will therefore die out after several cavity round-trips.

Generally, normal noise fluctuation is harnessed to begin passive mode-locking when a sufficiently strong noise spike reaches the saturable absorber and the loss is significantly reduced.(Ippen *et al.*, 1980b) The noise spike is then more strongly amplified during the subsequent cavity round trips, which therefore will continue to reduce the loss experienced and continue the growth until reaching a steady state. When this has occurred, a train of stable pulses have been formed.

Shorter pulses are usually obtained via passive mode-locking ustilising a saturable absorber, due to the fast loss modulation resulting from the fast recovery time of saturable absorbers.(Haus, 1975a) The mode-locked pulses can produce ideal fast loss modulation as the pulses are significantly shorter than the cavity round trip time. These are inversely proportional to the pulse envelope. Whereas,

electronically driven loss modulation is significantly slower due to the sinusoidal loss modulation.

2.4.2 Graphene

Due to the strong and wide-spectral SA response, graphene was widely utilized by the laser community to achieve mode-locked operation in fiber (Cui & Liu, 2013; Fu *et al.*, 2013a,b; Luo *et al.*, 2012a; Wang *et al.*, 2012a) and bulk (Liu *et al.*, 2012; Wang *et al.*, 2012c; Zhang *et al.*, 2011b) lasers. The first sub-100 fs bulk solid-state laser using graphene as a saturable absorber was fabricated by the Petrov group in the 2 μm spectral range utilizing a monoclinic Tm3+-doped MgWO4 crystal as the active medium.(Wang *et al.*, 2017b)

Stable, self-starting mode-locked operation was achieved at mid-infrared with nearly Fourier-limited pulses as short as 86 fs.(Wang *et al.*, 2017b) The first all-fiber stretched-pulse laser operating beyond 2 μm with nanomaterial-based SA was reported by Pawliszewska et al.(Pawliszewska *et al.*, 2018) Their all-fiber holmium-doped laser generated 190 fs pulses with a bandwidth of 53.6 nm, centred at 2060 nm and reaching 2.55 nJ of energy. It can be seen from Table 2.2 that a larger output power can be achieved in a longer duration pulses. A graphene mode-locked laser can obtain an output power as large as 3 W.

As 1.55 μm is a popular telecom optical wavelength, graphene was widely utilized for mode-locking Erbium doped fiber lasers at this wavelength, whose parameters and performance are summarized in Table 2.3. A very short pulse with the duration less than 200 fs was obtained at this wavelength with repetition rate of 27.4 MHz and output power of 1.2 mW.(Cunning *et al.*, 2011; Popa *et al.*, 2010) Most of the pulse duration of Erbium doped fiber lasers using graphene as saturable absorbers are several hundred fs and the long duration can go to 200 ns, see Table 2.3.

Table 2.2: Graphene Mode-Locking on Fiber Lasers

Coupling Method	SA Prep Method	λ (nm)	Laser τ	Repetition Rate (MHz)	P (mW)	Ref.
		Ytterbium	Doped			
Sandwiching	GO	1029	191 ps, 1.68 ns	-	539	(Dal Conte *et al.*, 2015b)
		Thulium	Doped			
Sandwiching	LPE	1940	3.6 ns	6.46	2	(Ge *et al.*, 2015)
Evanescent	GO	1910	1.3 ps	15.9	0.5	(Li *et al.*, 2013)
Wave	GO	1950	0.59 ps	33.25	142	(Zhang *et al.*, 2012c)
		Raman	Laser			
Sandwiching	LPE	1180	200 ns	0.4	60	(Jung *et al.*, 2012)
		Nd:YAG	Laser			
Transmittive	RGO	1064	4 ps	88	100	(Jung *et al.*, 2013)
		Nd:YVO_4	Laser			
Transmittive	GO	1064	11.3 ns	88	1200	(Wang *et al.*, 2012c)
Transmittive	GO	1064	8.8 ps	84	3060	(Zhang *et al.*, 2012b)
		Nd:$GdVO_4$	Laser			
Transmittive	GO	1063	12 ps	130	680	(Tan *et al.*, 2010)
Reflective	GO	1064	4.5 ps	70	1100	(Fu *et al.*, 2013b)
Reflective	CVD	1065	16 ps	43	360	(Hou *et al.*, 2014)
Reflective	LPE	1341	11 ps	100	1290	(Feng *et al.*, 2013b)
		Yb:KGW	Laser			
Reflective	LPE	1031	428 fs	86	504	(Xu *et al.*, 2011a)
		Yb:LSO	Laser			
Reflective	GO	1058	9.8 ps	87	950	(Xu *et al.*, 2012d)
		Tm:YAP	Laser			
Transmittive	GO	2023	<10 ps	71.8	268	(Luo *et al.*, 2012a)
		Yb	Laser			
Butt-Coupled	LPE	1039	1.06 ps	1.5 GHz	202	(Xu *et al.*, 2011b)
		Ho	Laser			
Fiber Facet	-	2060	190 fs	21	2.55 nJ	(Zhang *et al.*, 2011b)

Table 2.3: Erbium doped fiber lasers mode-locked by graphene at the wavelength of 1.55 μ m

Coupling Method	SA Prep Method	λ (nm)	Laser τ	Repetition Rate (MHz)	P (mW)	Ref.
Evanescent	LPE	1567	650 fs	25	-	(Feng *et al.*, 2013a; Mary *et al.*, 2013)
Wave	RGO	1555	510 fs	506.9	80	(Lin *et al.*, 2013a; Sun *et al.*, 2010e)
		1557	15.7 ps	3.33	4.2	(Cui & Liu, 2013; Dong *et al.*, 2016b)
		1561	1.3 ps	6.99	15.5	(Song *et al.*, 2010b; Wang *et al.*, 2017b)
	GO	1560	780 fs	14.64	0.36	(Choi *et al.*, 2012; Song *et al.*, 2010a)
		1561	4.85 ns	7.68	4.3	(Lee *et al.*, 2013a; Martinez *et al.*, 2010a)
Sandwiching	LPE	1530	8.8 ps	8.03	3.56	(Liu *et al.*, 2011b; Wang *et al.*, 2012a)
		1530	900 fs	8.4	-	(Martinez *et al.*, 2010b)
		1532	850 fs	5.27	-	(Martinez *et al.*, 2010a; Wang *et al.*, 2012a)
		1525-1559	1 ps	8	1	(Dong *et al.*, 2016b; Martinez *et al.*, 2011)
		1550	0.6-1.17 ps	60.6	3	(Lau *et al.*, 2018)
		1557	800 fs	-	-	(Mary *et al.*, 2013; Qin *et al.*, 2016)
		1559	464 fs	19.9	1	(Haus, 1975a; Sun *et al.*, 2010e)
		1560	630 fs	19.9	-	(Luo *et al.*, 2012b; Song *et al.*, 2010a)
		1560	174 fs	27.4	1.2	(Rosa *et al.*, 2017; Wang *et al.*, 2017b)
		1560	1 ps	13.6	3.7	(Martinez *et al.*, 2011; Zhao *et al.*, 2013)
		1562	865 fs	9.67GHz	316	(Liu *et al.*, 2011b; Zhang *et al.*, 2009b)
		1565	190 fs	42.8	0.4	(Fu *et al.*, 2013a; Qin *et al.*, 2016)
	FG	1570	1.08 ps	6.95	-	(Haus, 1975c; Ippen *et al.*, 1980b)
	GO	1596	770 fs	21.79	0.85	(Ippen *et al.*, 1980b; Luo *et al.*, 2012b)
	RGO	1560	1.64 ps	2.57	-	(He *et al.*, 2012; Ippen *et al.*, 1980b)
		1560	9.15 ps	7.05	-	(Ippen *et al.*, 1980b; Song *et al.*, 2010b)
		1560	18 ps	7.47	1.2	(Cui & Liu, 2013; Zhao *et al.*, 2013)
		1562	950 fs	502.8	2.3	(Fu *et al.*, 2013a; Lin *et al.*, 2013a)
		1562	938 fs	15.2	4.1	(Lee *et al.*, 2013a; Zhang *et al.*, 2009b)
		1572	-	91.5	-	(Choi *et al.*, 2012; He *et al.*, 2012)
		1576	415 fs	6.84	-	(Feng *et al.*, 2013a; Rosa *et al.*, 2017)
Free-Space	LPE	1558	3-20 ns	0.2-1.5	553	(Gui *et al.*, 2011; Kim *et al.*, 2011)
		1564	2.47 ps	1.21	-	(Xu *et al.*, 2012c; Zheng *et al.*, 2012a)
	RGO	1560	395 fs	58	1.96	(Kim *et al.*, 2011; Sobon *et al.*, 2012)
	GO	1531	0.5-20 ns	0.5	19.5	(Paul *et al.*, 2013)
		1560	0.2-3 ps	0.93-23	5.8	(Gui *et al.*, 2011; Sobon *et al.*, 2012)
		1561	400 fs	49.45	1	(Kim *et al.*, 2011; Zheng *et al.*, 2012a)

Benefitting from the fast excitation carrier lifetime, the repetition rate of graphene mode-lock laser can go up to 9.67 GHz. The power obtained from graphene saturable absorber at 1550 nm is generally several mW. Bulk lasers based on GSAMs can generate higher output power with hundreds of fs pulse durations, which are highlighted in Table 2.4. For instance, a Nd:GdVO4 laser with an output power up to 360 mW with a pulse duration of 16 fs is the shortest pulse duration reported thus far.(Xu *et al.*, 2011e) Based on GSAMs, Tm:YAP lasers can operate at 2 μm and obtain output powers of 362 mW. As the recovery time of excited carriers in GSAMs is 2 ps,(Wang *et al.*, 2017a) the repetition rate can easily reach 99.9 MHz.

2.4.3 Transition Metal Dichalcogenides (TMDs)

Some 2D TMDs have been found to possess stronger SA response than graphene, and they have been utilized as saturable absorbers in a wide range of pulsed lasers.(Wang *et al.*, 2013a) Like MoS_2, few-layered WS_2 has remarkable physical properties that have been exploited as a saturable absorber to generate ultrashort laser pulses. Mao et al. reported soliton mode-locking operations generated by an erbium-doped fiber laser using two types of WS_2-based saturable absorbers, the first fabrication method consisted of WS_2 nanosheets deposited on a D-shaped fiber, whereas the second method involved mixing WS_2 solution with polyvinyl alcohol which was then evaporated on a substrate.

At a maximum pump power of 600 mW, each type of saturable absorber stably mode-locked without damage, which indicated that few-layer WS_2 devices are promising as high-power flexible saturable-absorber for ultrafast optics.(Wang *et al.*, 2014b) In the mode-locking operation, the laser obtained femtosecond output pulse width of 595 fs and high spectral purity of 75 dB extinction ratio in the radio frequency spectrum. In the Q-switching operation, the laser had tunable repetition rates from 90 kHz to 125 kHz and output pulse energy of a few tens of nanojoule. Recently, layered platinum diselenide ($PtSe_2$) with relatively wider response range was utilized as a saturable absorber in a Nd:LuVO4 passively mode-locked solid-state laser to obtain 15.8 ps pulses with power of 180 mW and repetition rate of 61.3 MHz at 1066.6 nm.(Tao *et al.*, 2018)

Among layered TMDs, 2D MoS_2 was the most popular SA used to generate laser pulses. Wang et al. reported the first short-pulsed laser that utilised a few-layer MoS_2 SA, which was a Q-switched bulk laser.(Xu *et al.*, 2014a) The first Q-switch fiber laser based on few-layer MoS_2 obtained stable operation with 2.7 μs pulses at a repetition rate of 67 kHz and a maximum power of 0.5 mW at 1569 nm.(Zhang *et al.*, 2014a) The first mode locked fiber laser to use a few-layer MoS_2 saturable absorber was successfully operating at 1054 nm.(Zhang *et al.*, 2014c)

Since then, other papers have been published which display successful pulse

Table 2.4: GSAMs mode-locking on bulk lasers

Laser Type	SA	λ (nm)	Laser τ	Repetition Rate	P (mW)	Ref.
Tm:YAP	GSAM	2000	735 ns	42.4 kHz	362	(Sun *et al.*, 2017)
Yb:YCOB	GSAM	1037	152 fs	99.9 MHz	53	(Cunning *et al.*, 2011)
Tm:CLNGG	GSAM	2010	354 fs	99.9 MHz	97	(Cunning *et al.*, 2011)
Cr:ZnSe	GSAM	2310-2426	116 fs	-	66	(Cunning *et al.*, 2011)
Tm:CLNGG	GSAM	2015	882 fs	95 MHz	60	(Hou *et al.*, 2014)
Nd:GdVO4	GSAM	1065	16 fs	43 MHz	360	(Xu *et al.*, 2011d)

generation using MoS_2 SAs at 1060 nm (Du *et al.*, 2014; Xu *et al.*, 2014b; Zhan *et al.*, 2015; Zhang *et al.*, 2014a,c), 1420 nm (Xu *et al.*, 2014a), 1550 nm (Huang *et al.*, 2014; Khazaeinezhad *et al.*, 2015; Khazaeizhad *et al.*, 2014; Li *et al.*, 2015; Liu *et al.*, 2014a; Xia *et al.*, 2014b), 2032 nm (Luo *et al.*, 2014), 2100 nm (Luo *et al.*, 2014) and other wavelengths, as shown in Table 2.5. Ref.(Woodward *et al.*, 2015b) presents a detailed review on the ultrafast lasers mode-locked by few-layer MoS_2 and, as such, there is no need to repeat the discussion in this paper.

Table 2.5: Laser pulses generation utilising MoS_2 SA

Laser Type	Integration Platform	SA Prep Method	λ (nm)	Laser τ	Repetition Rate	P (mW)	Ref.
			Q-Switched				
Er:Fiber	Fiber Facet	CVD	1550	1.6 μs	173 kHz	4.7	(Xia *et al.*, 2014b)
	Fiber Facet	ME	1563	3.9 μs	41 kHz	3.5	(Khazaeizhad *et al.*, 2014)
Nd:GdYVO4	Quartz	PLD	1060	970 ns	732 kHz	227	(Wang *et al.*, 2014b)
Tm:Ho:YGG	Quartz	PLD	2100	410 ns	149 kHz	206	(Wang *et al.*, 2014b)
Nd:YGG	Quartz	PLD	1420	729 ns	77 kHz	52	(Wang *et al.*, 2014b)
Nd:YAlO3	BK7 Glass	LPE	1080	227 ns	233 kHz	260	(Xu *et al.*, 2014a)
Tm:CLNGG	Q-switched	–	1979	400 μs	187 MHz	62	(Kong *et al.*, 2015)
			Mode-Lock				
Er:Fiber	Fiber Facet	CVD	1569	1.28 ps	8.3 MHz	5.1	(Zhang *et al.*, 2014c)
	Side-polished fiber	CVD	1568	4.98 ps	26 MHz	2	(Zhan *et al.*, 2015)
	Side-polished fiber	CVD	1568	637 fs	33.5 MHz	-	(Zhan *et al.*, 2015)
	Microfiber	SP-I	1558	3 ps	2.5 GHz	5.4	(Liu *et al.*, 2014b)
Yb:Fiber	Microfiber	SP-I	1043	656 ps	6.7 MHz	2.4	(Du *et al.*, 2014)
	Fiber Facet	SP-I	1054	800 ps	6.6 MHz	9.3	(Zhang *et al.*, 2014b)

Table 2.6: Pulsed Lasers with BP and other 2D saturable absorbers

SA	Laser Type	Coupling Method	λ (nm)	Laser τ	Repetition Rate	P (mW)	Ref.
BP	Tm:Fiber	Fiber Connector Tip	1910	739 fs	36.8 MHz	400	(Luo *et al.*, 2014)
BP	Er:ZBLAN	Q-Switched	2800	1.18 μs	63 kHz	485	(Qin *et al.*, 2015)
BP	Er:Fiber	Q-Switched	3462	2.05 μs	66.33 kHz	120	(Kong *et al.*, 2016)
BP	Er:Fiber	Mode-lock	3489	p̃s	28.91 MHz	40	(Kong *et al.*, 2016)
BP	Er:Fiber	Mode-lock	1555	102 fs	23.9 MHz	1.7	(Jin *et al.*, 2018b)
Bi	Er:Fiber	Mode-lock	1559	652 fs	8.83 MHz	153	(Woodward *et al.*, 2015c)
Bi	Er:Fiber	Mode-lock	1561	192 fs	8.85 MHz	5.6	(Xu *et al.*, 2012b)
Bi	Er:Fiber	Q-Switched	1558	1.3-2.2 μs	39.4- 51.1 kHz	62-212	(Song *et al.*, 2017a)
TiO2	Tm-Ho:Fiber	Mode-lock	1979	10.29 ps	9 MHz	15	(Sotor *et al.*, 2015a)
Bi_2Se_3	Yb:Fiber	Q-Switched	1060	1.95 μs	8.3-29 kHz	–	(Rusdi *et al.*, 2017)
Sb_2Te_3	Er:Fiber	Mode-lock	1558.6	1.8 ps	4.75 MHz	0.5	(Sotor *et al.*, 2014a)
MXene	–	Q-Switched	1060	359 ns	186 kHz	2.04 W	(Liu *et al.*, 2014c)

2.4.4 Black Phosphorus (BP) and other layered nanomaterials

In comparison to 2D TMDs, layered black phosphorus (BP) can be utilized as a saturable absorber for short pulsed laser with a wider wavelength range, see Table 2.6. The Sotor group referred to earlier in this section also reported the first usage of BP as a saturable absorber for mode-locking a thulium-doped fiber laser.(Sotor *et al.*, 2015a) Their SA was based on mechanically exfoliated BP deposited on a fiber connector tip. The laser generated 739 fs pulses centered at 1910 nm and reached a power of 400 mW. Whereas Qin et al. employed liquid phase exfoliated BP as a saturable absorber in a passively Q-switched Er-doped ZBLAN fiber laser at 2.8 μm.(Qin *et al.*, 2015) The modulation depth and saturation fluence of the black phosphorus SA was measured to be 15% and 9 μJ/cm2, respectively. Under Q-switched operation their fiber laser delivered a maximum average power of 485 mW and a corresponding pulse width of 1.18 μs and pulse energy of 7.7 μJ at a repetition rate of 63 kHz.

The same group later reported both Q-switching and mode-locking at 3.5 μm in the same paper by transferring BP flakes onto an Au-coated mirror to fabricate a BP SAM, which was utilized in a dual-wavelength pumping (DWP) scheme Er:ZBLAN fiber laser.(Qin *et al.*, 2018) The Q-switched operation reached an average power of 120 mW with a pulse energy of 1.83 μJ, pulse width of 2.05 μs, and a repetition rate of 66.33 kHz at a wavelength of 3462 nm. Whereas under mode-locking operation, the group obtained picosecond pulses with an average power of 40 mW and a repetition rate of 28.91 MHz at 3489 nm.(Qin *et al.*, 2018)

Recently, Jin et al. utilized ink-jet printing of BP to fabricate their saturable absorber in an Er-doped fiber laser. The laser generated 102 fs pulses at 1,555 nm with 40 nm spectral bandwidth.(Jin *et al.*, 2018a) These are summarized in Table 2.6, along with Group-V and other 2D saturable absorbers.

Bismuthene saturable absorbers were reported for the first time to display an optical modulation depth of 2.03% and a saturable intensity of 30 MW/cm2, due to the direct energy bandgap at 1550 nm.(Zhang *et al.*, 2009a) Applying this bismuthene SA device to an Er-doped fiber laser resulted in 652 fs pulse generation centered at 1559.18 nm.(Zhang *et al.*, 2009a) The Sulaiman Wadi Harun group reported the first demonstration of mode-locking using layered Titanium Dioxide (TiO_2) film as a saturable absorber in a thulium-holmium doped fiber laser (THDFL) at 1979 nm. Stable generation of 10.29 ps pulses occurred with a repetition rate of 9 MHz and a maximum output power of 15 mW and pulse energy of 1.66 nJ.(Rusdi *et al.*, 2017)

A newer class of the Dirac-materials referred to as three dimensional topological insulators (TI) have been investigated. It has been discovered that Bi_2Se_3, Bi_2Te_3 and Sb_2Te_3 display graphene-like electronic-band structure.(Sotor *et al.*, 2014a) As

shown in Table 2.6, Bi_2Se_3 was used as a saturable absorber to passively Q-switch an ytterbium-doped fiber (YDF) laser, which is the first reported use of a few-layer topological insultator (TI) in such a scenario.(Luo *et al.*, 2013) The laser generated Q-switched pulses at 1.06 μm with a pulse duration of 1.95 μs, maximum pulse energy of 17.9 nJ and a tunable repetition-rate from 8.3 to 29.1 kHz.

The Sotor group demonstrated an erbium-doped fiber mode-locked laser based on a antimony telluride saturable absorber first.(Sotor *et al.*, 2014b) The group mechanically exfoliated their 40-100 nm Sb_2Te_3 which was then deposited onto the fiber core. The laser generated an optical soliton centered at 1558.6 nm with 1.8 ps duration and 105 pJ pulse energy at 4.75 MHz repetition rate.

Several of the mentioned 2D nanomaterials have been employed to fabricate PVA composites, which were utilized in fiber lasers to achieve pulsed operation, as highlighted in Table 2.7. The Ferrari group was the first to demonstrate a graphene/PVA mode-locked ultrafast laser, which achieved ultrashort pulses with durations up to 464 fs at a central wavelength of 1559 nm.(Sun *et al.*, 2010a)

Table 2.7: Pulsed Lasers with 2D materials/PVA composite saturable absorber

Laser Type		SA in PVA	Laser λ (nm)	Parameters τ	f	P (mW)	Reference
Er:fiber	Mode-lock	Graphene	1525-1559	1 ps	8 MHz	1	Sun *et al.* (2010d)
Er:fiber	Mode-lock	Graphene	1559	464 fs	19.9 MHZ	5.35	Sun *et al.* (2010a)
Er:fiber	Q-switched	MoS_2	1520-1568	5 μs	35 kHz	1.5	Huang *et al.* (2014)
Er:fiber	Q-switched	MoS_2	1565	7.5 μs	11.9 kHz	1.7	Luo *et al.* (2014)
Er:fiber	Q-switched	MoS_2	1550	9-13.5 μs	7.41 kHz	50-170	Chen *et al.* (2015)
Tm:fiber	Q-switched	MoS_2	2032	2.06 μs	38.4 kHz	47.3	Luo *et al.* (2014)
Yb:YAG	Q-switched	MoS_2	1030	12 μs	17 kHz	250	Zhan *et al.* (2015)
Yb:fiber	Q-switched	MoS_2	1068	2.7 μs	67 kHz	0.5	Woodward *et al.* (2014)
Er:fiber	Mode-lock	MoS_2	1535-1565	1 ps	13 MHz	-	Zhang *et al.* (2015a)
Er:fiber	Mode-lock	MoS_2	1570	710 fs	12.1 MHz	1.8	Liu *et al.* (2014a)
Er:Fiber	Q-Switched	WS_2	1550	3.9-6.7 μs	47-77.9 kHz	400-720	Sun *et al.* (2010d)
Er:Fiber	Q-Switched	WSe_2	1550	4-9 μs	46-85 kHz	280-720	Sun *et al.* (2010d)
EDFL	Mode-lock	$MoSe_2$	1558	1.45 ps	600 MHz	33.4	Huang *et al.* (2014)
Er:Fiber	Q-Switched	$MoSe_2$	1565	59.1-30.4 μs	16.9-32.8 kHz	22.4-102	Sun *et al.* (2010a)
Er:Fiber	Q-Switched	$MoSe_2$	1550	4-6.5 μs	60-66.8 kHz	570-720	Sun *et al.* (2010d)
Er:Fiber	Mode-lock	$MoSe_2$	1555.6	737-798 fs	3.27 GHz	-	Chen *et al.* (2015)
Er:Fiber	Q-Switched	$MoSe_2$	1566	7.9-4.8 μs	26.5-35 kHz	18.9-29	Koo *et al.* (2016b)
Tm:Fiber	Q-Switched	$MoSe_2$	1924	16-5.5 μs	14-21.8 kHz	0.13	Koo *et al.* (2016b)
Yb:Fiber	Q-Switched	$MoSe_2$	1060	4.6-2.8 μs	60-74.9 kHz	6.26-8.7	Koo *et al.* (2016b)
Er:Fiber	Q-Switched	$TiSe_2$	1530	1.126 μs	70-154 kHz	11.54	Xie *et al.* (2012)
Er:Fiber	Q-Switched	BP	1563	2.96 μs	7.8-34.3 kHz	6.67	Luo *et al.* (2015)

In contrast, lasers pulses obtained from Q-Switching operation based on 2D TMDs/PVA thin films have relatively long pulse duration, which are mainly in the order of magnitude of microsecond (μs).

Interestingly, PVA was employed to host layered BP, which produced 2.96 μs Q-Switching pulses at the central wavelength of 1563 nm with a repetition rate of 7.8-34.3 kHz and output power of 6.67 mW. Except for fiber and bulk lasers, 2D saturable absorbers have also employed waveguide resonators to generate laser pulses. Graphene was utilized for a Q-switched laser operation in Yb: YAG channel waveguides to obtain 1.33 MHz, 79 ns and 64 nJ pulses.(Kim *et al.*, 2016) In a Tm: ZBLAN waveguide chip laser, bismuth telluride was used as a saturable absorber to achieve laser irradiation with a maximum output of 16.3 mW.(Koo *et al.*, 2016a)

Based on Tables 2.1, 2.2, 2.3, 2.4, 2.5, 2.6, 2.7, it can seen that the relaxation time of excited carriers plays an important role in both the pulse duration and repetition rate of lasers. Since the recovery time of graphene and BP is fast, lasers mode-locked by the two saturable absorbers achieve pulses with durations mainly in the femtosecond (fs) regime. In contrast, 2D TMDs saturable absorbers mode-locked lasers operate with relatively longer pulse durations due to the longer excited carrier relaxation time. In addition, a laser using a saturable absorber with low saturation intensity requires relatively low pump power. If the ratio of NLO modulation depth over non-saturated loss of the saturable absorber is smaller, the mode-locked laser can operate while producing less absorptive heat.

Another interesting phenomenon regarding the ultrafast photonics in layered materials is that bulk-like 2D materials can be also utilized as saturable absorbers to generate ultrafast lasers.(Chang *et al.*, 2010a,b; Chi *et al.*, 2014; Lee *et al.*, 2014). The biggest difference between the bulk and monolayer limits is the energy band structure. A transition from indirect bandgap in bulk to direct bandgap in monolayer forms have been observed in many layered materials. This results in a different spectral response range, which has been discussed in Section 2.2.2

Other differences could be the absorption cross-sections and relaxation time of excited carriers, which will affect the modulation depth and the pulse repletion rate, respectively.

2.4.5 Summary

After the gold rush of research into graphene as a mode-locker for ultra-fast pulsed lasers (Cui & Liu, 2013; Fu *et al.*, 2013a,b; Luo *et al.*, 2012a; Wang *et al.*, 2012a), the field has since moved on to newer 2D nanomaterials, such as TMDs, topological insulators and black phosphorus. These other materials have their own strengths and weaknesses, and help to round out the parameters of different fibers and bulk lasers.

2.5 Conclusion and outlook

In conclusion, most 2D nanomaterials possess wide-spectral SA properties with large nonlinear absorption coefficient, absorptive cross-sections, low saturated intensities and fast relaxation time of excited carrier. These SA properties display a certain dependence on excited wavelength, linear absorption and pulse duration. By incorporating 2D nanomaterial as SAMs or polymer composite thin film in laser cavities, mode-locked ultrafast pulses with an extremely wide-spectral range and high repetition rate can be produced.

Graphene exhibits a strong SA response from the visible to the radio-wave region, whereas BP displays a wide-spectral SA behavior from the visible to the mid-infrared region, with a saturation intensity of 58 to 600 GW/cm^2. Due to the fast relaxation time of excited carriers, lasers mode-locked by both graphene and BP generally achieve pulse durations in the order of fs. In contrast, 2D TMDs saturable absorbers mode-locked lasers usually operate at the visible wavelength range with pulse durations of microseconds (μs) to nanoseconds (ns). Ultrafast lasers using other 2D saturable absorbers like topological insulators can also achieve pulses with sub-200 fs duration. In terms of the output power, the majority of fiber lasers generally obtain a couple of milliwatts (mW) for femtosecond (fs) pulses, compared to hundreds of milliwatts (mW) for microseconds (μs) and nanosecond (ns) pulses.

The novel SA properties of 2D nanomaterials provide a new avenue for generating ultrafast laser pulses. One method to further nanomaterials optical research is to test each new 2D material at each wavelength, and subsequently publish one paper with little new physics. This approach is not ideal for the NLO research community. However, a systematic NLO study on a 2D material would provide a better guideline for photonic researchers.

The NLO performance of some 2D nanomaterials as fast- or slow-absorbers is still unknown and therefore further analysis is required to clarify these aspects. There is also potential to improve the NLO research methods in order to obtain more accurate values for saturation intensity and nonlinear absorption of 2D nanomaterials. Overall, the output power of pulsed lasers mode-locked by 2D nanomaterials has not met the requirement in some intense photonic applications. One method is to enhance the damage threshold of the 2D devices and this issue could be solved by doping the 2D nanomaterials into glass or quartz.

Another potential aspect that can be improved for future SA studies in 2D materials is to enhance the accuracy of the NLO parameters. In some cases, published NLO parameters for the same material can vary greatly. One possible explanation for the large error in NLO results is due to issues in experimental measurements. Firstly, the response of many detectors is not linear when the light

intensity is relatively high. This can be avoided by making sure that the intensity of light is under the linear threshold value of detectors. Secondly, laser fluctuations could be another source of error, particularly in a manual NLO measurement using power meters. It requires significant time to manually collect data by recording numbers from the power meters, resulting in a possibility of measurements during the fluctuation of the laser.

Meanwhile, the accuracy of a power meter is generally not high enough for the NLO measurements. To eliminate this error, it is recommended that a computer program is employed to shorten the measurement time, coupled with a photodiode or balance detector. Another potential error could be introduced during the data fitting. In some papers, the fits were judged by eye to determine if the fit was in the best agreement with the experimental data. This can result in a relatively large error for published NLO absorption coefficient and the third-order optical susceptibility. In the future work, a nonlinear least-squares algorithm is suggested to fit the data. Finally, some researches show that ultrafast laser pulses can be obtained from bulk-like 2D materials. It would be interesting to know the differences of mode-locking between bulk and 2D saturable absorbers. A systematical study is required to give a detailed comparison.

Finally, a large number of ultrafast lasers utilising 2D materials as saturable absorbers has been reported in the last decade. This implies that it is a hot topic with interesting photonics applications. However, there also exist great hype in this research area. Once a new 2D material is experimentally obtained, many papers rush to report the applications in many ultrafast lasers to demonstrate the outstanding performance, such as wide spectral response, ultrashort laser pulses up to the order of femtosecond, high repetition rate, etc. However, very little research has studied the stability and the generated heating of the ultrafast lasers based on 2D saturable absorbers, which is very important for practical applications. From commercial and industrial points of view, a follow-up study on these ultrafast lasers is needed after the demonstration of the excellent performances. For the future work in this area, one would recommend more of a focus on the possibility of practical and industrial applications of ultrafast lasers using 2D materials. Another related suggestion is to carry out a systematic study for publication instead of a simple demonstration of good performance.

3

Instrumentation and Experimental Methods

In this chapter, the instrumentation and experimental methods used are discussed in more detail. The nonlinear optical properties of graphene is explored with the Z-scan and I-scan methods.

3.1 Instruments

To develop a mode-locker, the potential materials must exhibit fast and strong nonlinearity. In particular, it is necessary for a successful mode-locker to be a saturable absorber (SA). To explore potential media for such SA traits, it is necessary to have reliable methods of measuring the nonlinear optical properties (i.e. Nonlinear Absorption Cofficient (β), and Nonlinear Refractive Index (n_2)). To achieve this, the Z-scan method was used, which is widely recognised as one of the most reliable techniques for obtaining β and n_2 of condensed media. Throughout this section, it is demonstrated that both of these parameters can be obtained utilising the Z-scan technique.

This section also discusses I-scan, an alternative technique. While the Z-scan technique examines the transmission spectra through media and determines the nonlinear optical properties, the I-scan technique is used to examine the nonlinear optical properties using the reflectance of a material.

3.1.1 Z-Scan

The so-called Z-scan technique has become the standard method for measuring the nonlinear optical properties of materials due to the both the simplicity of use and the low cost to set up. The Z-scan technique allows the user to determine both the nonlinear absorption coefficient, β, and the nonlinear refractive index (or Kerr nonlinearity), n_2. Often, it is possible to calculate β and n_2 directly from the Z-scan data.

It should be noted that one, single Z-scan experiment does not allow separation of the contributions of different mechanisms of the optical nonlinearity to β and n_2. This can be achieved by performing a number of measurements with several different laser sources and applying different detection techniques.

One of the greatest advantages of the Z-scan technique is the ability to obtain the nonlinear optical properties of the material by measuring just the optical power in the far field. Also, the β and n_2 can be separated in a single measurement cycle by using the so called Open-Aperture (OA) and Closed-Aperture (CA) Z-scan configurations respectively.

The generic open-aperture Z-scan set-up is shown in figure 3.1:

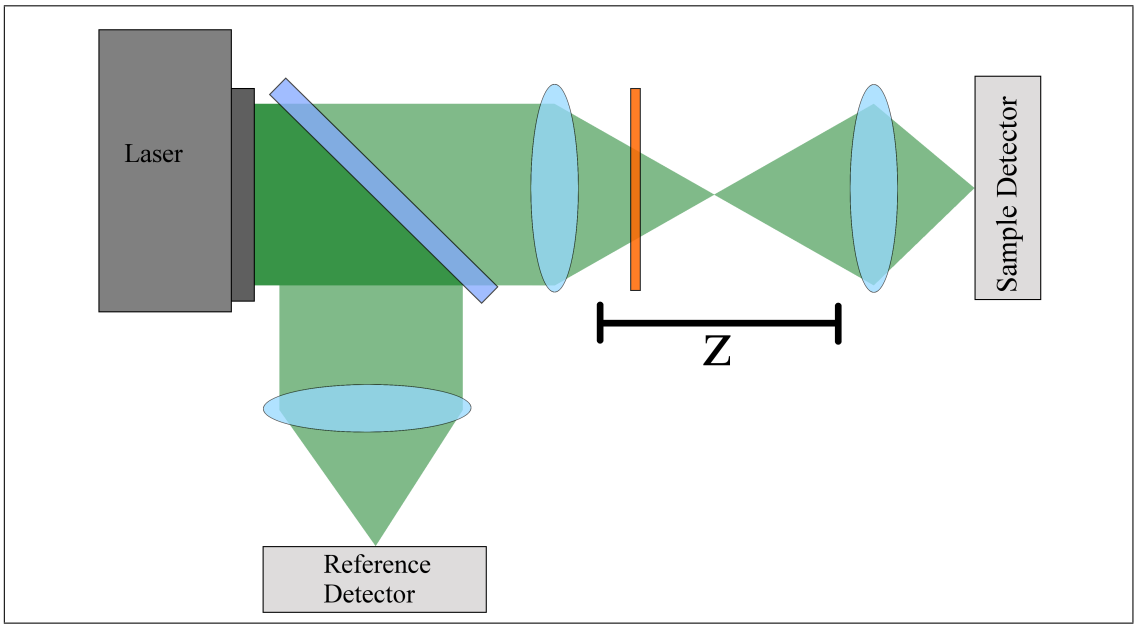

Figure 3.1: Basic Z-scan set-up

In such a set-up, a lens focuses the laser to a point. The sample travels in the so-called "Z direction", and is brought through the focal point of the laser, which is $z = 0$. This achieves a distance-dependence intensity gradient. The scanning distance depends on the pulse parameters and the sample thickness, L. In theory,

the scanning range can be thought to equal the Rayleigh Length (Z_0), $\pm Z_0$.

$$Z_0 = \pi w_0^2/\lambda \tag{3.1}$$

For sufficiently thick samples ($L \leq Z_0$), a range of $\geq \pm 5Z_0$ is preferred. This simplification significantly eases the interpretation of the results obtained for the samples with a rough surface or when optical beam imperfections adds noise into the measurement system.

Generally, in practical cases, due to significant fluctuations of the laser power during the scan, it is necessary to add a reference detector to the set-up.

The position of the aperture in the closed-aperture scans can vary, but the aperture should be placed between the lens and the detector at a distance from the lens which is far longer than Z_0. Often the distance varies between 20 Z_0 and 100 Z_0.

In regard to the closed-aperture set-up, the aperture diameter provides the transmittance, S, of the optical system in the linear regime in the preferred range of $0.1 < S < 0.5$. S is the ratio of the closed aperture far-field (linear) transmission to the open aperture far-field transmission. In this case, the linear regime is when the sample is placed far from the focal point.

In the open-aperture set-up (at $S = 1$), all the incident light passes through the aperture. Therefore the method is insensitive to any nonlinear optical distortions of the beam caused by nonlinear refraction effects. For such reasons, Z-scan methods with $S = 1$ are mostly intended for nonlinear absorption measurements.

3.1.1.1 Nonlinear absorption coefficient in transparent media

β, the nonlinear absorption coefficient, can be calculated from the open-aperture Z-scan measurements. A schematic of the open aperture graphs obtained from the Z-scan technique are shown in Figure 3.2 For small third-order nonlinear losses, which is when $\Delta\alpha L = \beta I L_{eff} \ll 1$ (where $\Delta\alpha$ is the change of the absorption coefficient), and when the response time is much less than the pulse duration, the transmittance for a Gaussian pulse as a function of the sample position z is given by:

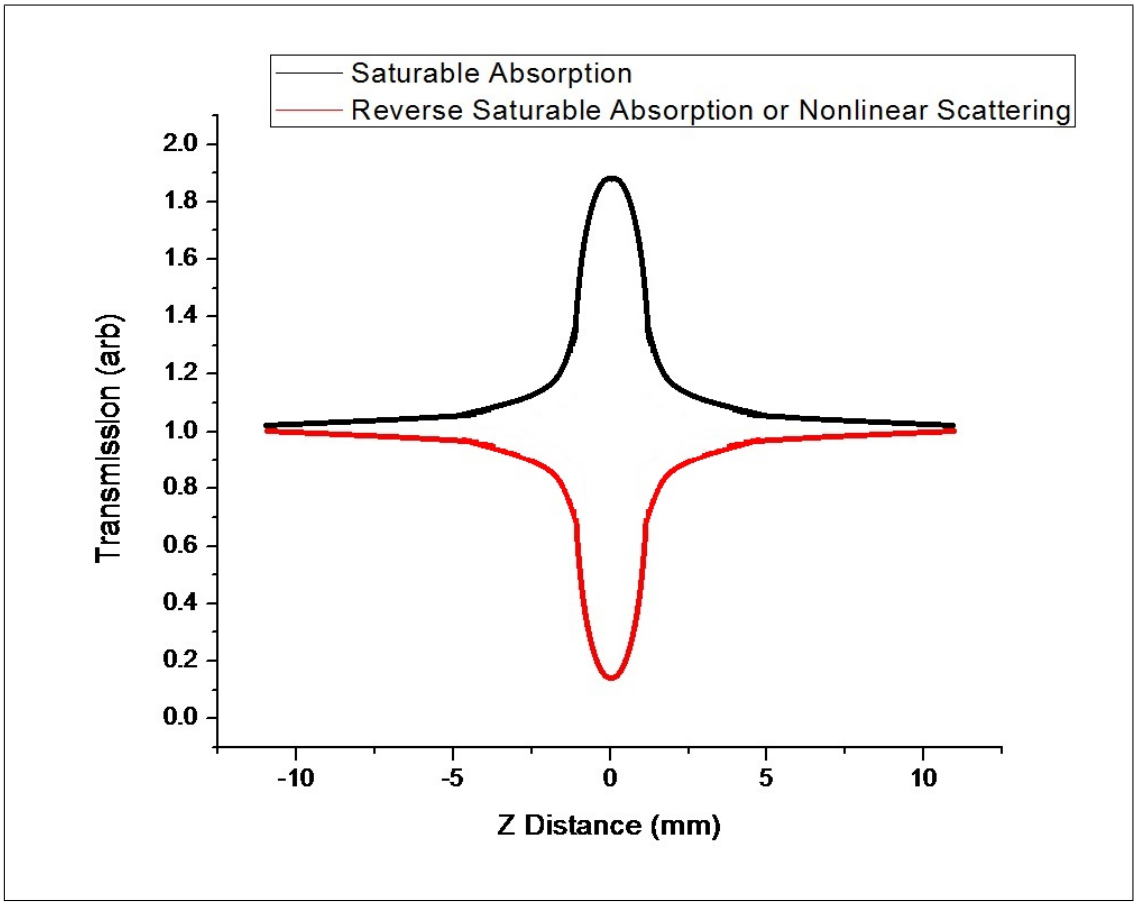

Figure 3.2: Schematic of Open Aperture Z-scan Graphs

$$T(z) = 1 - \frac{q_0}{2\sqrt{2}} \frac{1}{\left[1 + \frac{z^2}{Z_0^2}\right]} \tag{3.2}$$

In which $q_0 = \beta I_0 L_{eff}$ and $|q_0| \ll 1$. It should be noted that if the response time is much higher than the pulse duration, the $2\sqrt{2}$ factor in 3.2 can be simplified by replacing it with 2. Therefore the open-aperture Z-scan data returns to the nonlinear absorption coefficient β.

3.1.1.2 Nonlinear refractive index in transparent media

Shown below, in Figure 3.3, is a typical graph from a closed-aperture Z-scan measurement with a thin sample exhibiting the nonlinear refraction. The valley, followed by a peak, in the normalised transmittance when the sample is scanning from the negative to the positive z, is the signature of self-focusing. This is essentially a change in the refractive index which is self-induced.

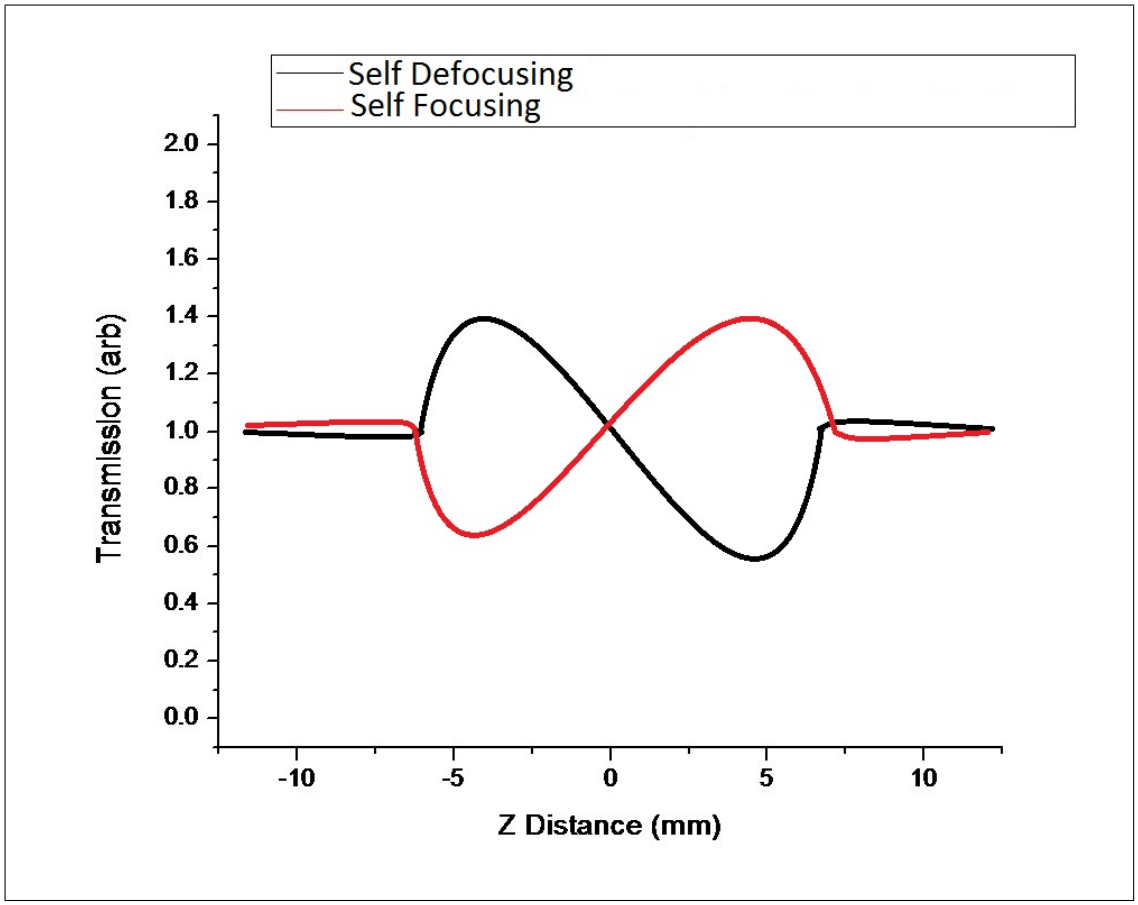

Figure 3.3: Schematic of Closed Aperture Z-scan Graphs

When an optical pulse propagates in the nonlinear media in question due to Kerr lensing, self-focusing occurs. Therefore, the beam diameter is decreased compared with that of a weak pulse. This mechanism is based on Kerr nonlinearity with a positive $\chi^{(3)}$ due to higher optical intensities on the beam axis, when compared with the wings of the spatial intensity distribution, which causes an effectively increased refractive index for the inner portion of the beam. Therefore, this modification of the refractive index distribution acts akin to a focusing lens.

This also works in the reverse. A negative $\chi(3)$ leads to a self-defocusing.

From a closed-aperture Z-scan experiment, one can obtain the nonlinear refractive index of a medium via the difference between the maximum T_p and the minimum T_v of the normalised transmittance, $\Delta T_{pv} = T_p - T_v$. For the third-order nonlinear refraction in the absence of the nonlinear absorption, the ΔT_{pv} can be presented in the following way:

$$\Delta T_{pv} = 0.406(1 - S)^{0.27}\Delta\Phi_0 \tag{3.3}$$

In which

$$\Delta\Phi_0 = \frac{2\pi}{\lambda} n_2 I_0 L_{eff} \tag{3.4}$$

where $\Delta\Phi_0$ is the on-axis peak nonlinear phase shift with the sample at focus ($z = 0$), n_2 is the third-order nonlinear refractive index, I_0 is the light intensity in the focus, $L_{eff} = \frac{[1-exp(-\alpha_0 L)]}{\alpha_0}$ is the effective length of the sample, and α is the absorption coefficient. The sign of $\Delta\Phi_0$, and subsequently, n_2 are determined by the relative position of the maximum and the minimum.

It is generally a challenging task during an experiment to obtain a precise definition of the laser intensity in the focal plane. There is an intriguing trait of $T(z)$ dependence obtained from the closed-aperture Z-scan experiments, which should be acknowledged. Specifically, when the nonlinear refraction is due to the third-order nonlinearity and the sample thickness L is much less than Z_0. the distance between the maximum and the minimum of $T(z)$ dependence is summarised by the following:

$$\Delta z \cong 1.7 Z_0 \tag{3.5}$$

Therefore, when the normalised transmittance curve is analysed, one can determine the spatial parameters of the focused beam.

3.1.1.3 Simultaneous measurements of the nonlinear absorption coefficient and nonlinear refractive index

The nonlinear absorption coefficient in the presence of the nonlinear refraction can be determined from the closed-aperture measurements. This can be achieved by utilising the sample transmittance equation:

$$T(x) = 1 - \frac{4x}{(x^2+9)(x^2+1)}\Delta\Phi_0 - \frac{2(x^2+3)}{(x^2+9)(x^2+1)}\Delta\Psi_0 \tag{3.6}$$

Note that $x = z/Z_0$, and $\Delta\Psi_0$ and $\Delta\Phi_0$ in equation 3.6 stand for the nonlinear phase shift near the focus due to the nonlinear absorption and refraction, respectively.

$$\Delta\Psi_0 = \frac{1}{2}\beta I_0 L_{eff} \tag{3.7}$$

$$\Delta\Phi_0 = k n_2 I_0 L_{eff} \tag{3.8}$$

The previous formulae (3.6) can be simplified if we introduce $\varrho = \frac{\beta}{2kn_2}$. Then:

$$T = 1 - \frac{2(\varrho x^2 + 2x + 3\varrho}{(x^2+9)(x^2+1)}\Delta\Phi_0 \tag{3.9}$$

Using the above formula, the best fit of the closed-aperture Z-scan data gives ϱ and $\Delta\Phi_0$, which allows one to calculate both the nonlinear absorption coefficient, β, and the Kerr nonlinearity, n_2.

This equation can also be used to obtain β and n_2 from the separate measurements. β can be extracted from the open-aperture Z-scan experimental data. This then allows $\Delta\Psi_0$ to be calculated. Finally, the measured transmittance during closed-aperture configuration and the previous formula can be used to obtain n_2.

A different method to obtain β and n_2 using the Z-scan technique requires experimental measurements with both open- and closed-aperture modes in operation; this is without and with an aperture respectively. When the normalised transmittance data from the open-aperture is divided by the normalised transmittance from the closed-aperture, the Kerr nonlinearity, n_2, can be determined.

It should be noted that this method assumes the nonlinear refraction is a larger factor than the nonlinear absorption as a mechanism for nonlinearity, while non-zero $\Delta\alpha$ gives a minor additive correction to the transmittance in the closed-aperture configuration.

3.1.1.4 Specific Z-scan set-up evolution

The Z-scan set-up used went through several iterations and improvements. The original set-up consisted of two detectors, one sample and one reference detector.

This was improved upon with the introduction of a third detector, and the overhaul of the detection software to enable the three signals to be measured at the same time. This then allowed for both open- and closed-aperture to be measured at the same time, a photo of which can be seen in Figure 3.4.

When the switch was made to the other laser system, the system was significantly changed. Instead, only one detector was used, in unison with an optical chopper. The optical chopper gave the reference signal and sample signal different frequencies. Through careful alignment, these two signals could be picked up by the same detector. Finally, utilising a lock-in amplifier, the two signals could be separated due to the different frequencies from the optical chopper.

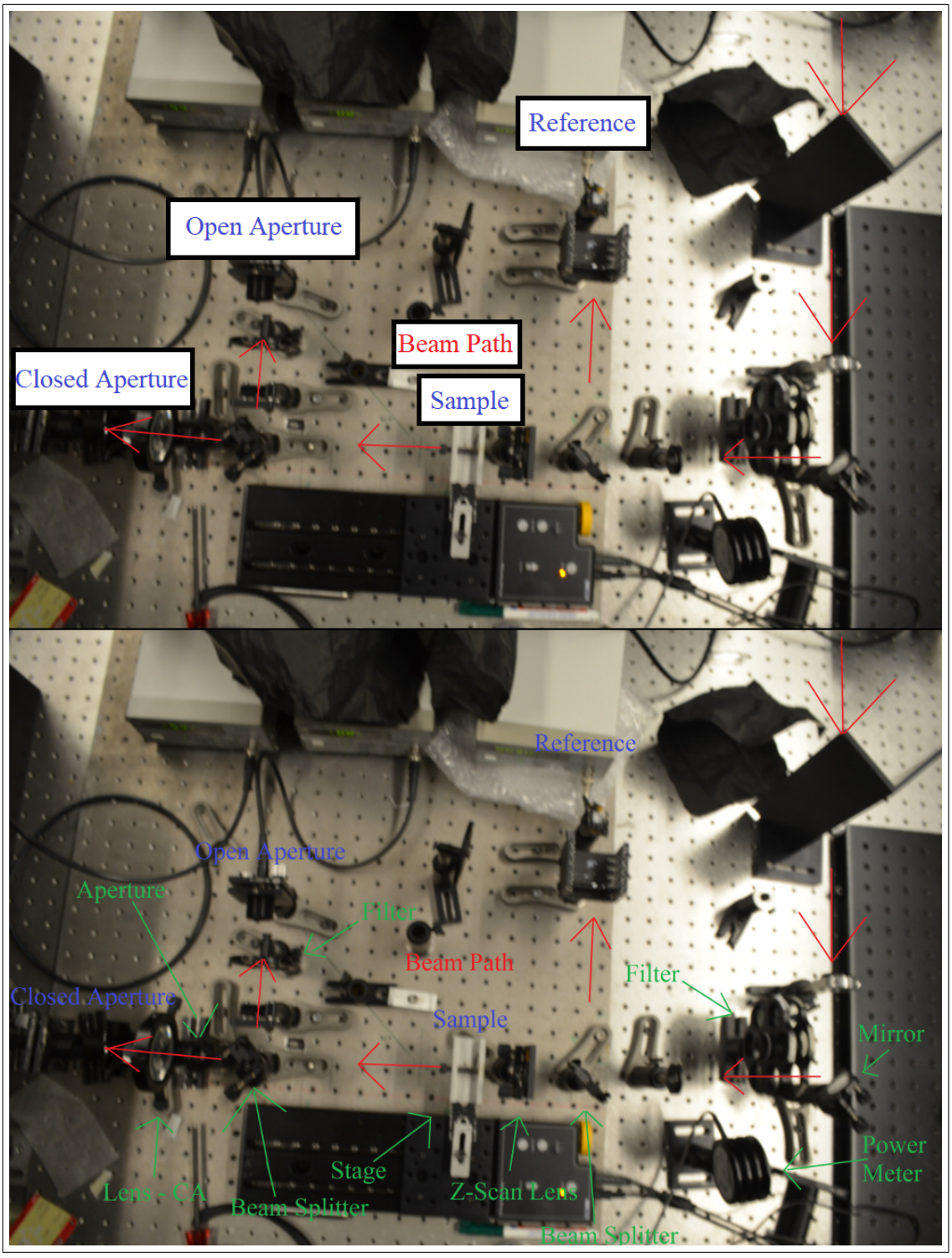

Figure 3.4: Original Z-scan set-up. The red arrows indicate the path of the laser beam.

3.1.2 I-Scan

While Z-scan is well suited to determine the nonlinear optical properties of transparent materials, via examination of the transmittance through such a media, the so-called I-scan technique is more geared towards determining the same nonlinear optical properties, β and n_2, when examining a reflective sample. As such, the I-scan was the ideal method to utilise to test the potential mode-locking capabilites of the custom-made graphene saturable absorber mirrors (graphene Saturable Absorber Mirror (SAM)s).

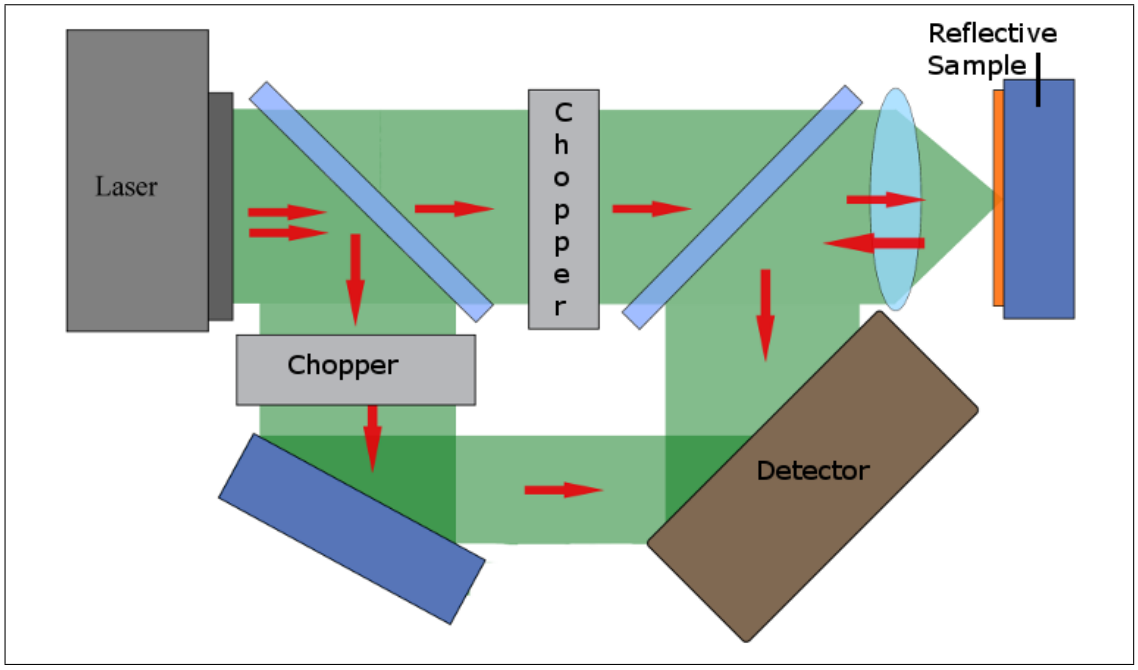

Figure 3.5: Basic I-scan Set-up

The I-scan technique has the same aim as the Z-scan technique, though the method through which it achieves this aim is slightly different. In the Z-scan technique, the laser beam goes through a lens to create an intensity gradient and the sample is brought through the focus of the laser in the "z" direction. While in the I-scan method, the sample is left stationary in the focus of the beam, and a varying filter is moved through the laser beam, as can be seen in Figure 3.5. This therefore achieves a similar varying intensity to the Z-scan method.

3.1.3 Pump-Probe Measurements

Pump-probe measurements can be utilised to extract ultrafast phenomena of materials, and the setup is summarised in Figure 3.6. A pump pulse generates an

excitation by hitting a sample. Controlled by an optical delay line, after some variable time delay, a probe pulse subsequently hits the same sample and the transmission (or reflection) is measured.

Information on the decay of the generated excitation can be extracted through monitoring of the probe signal as a function of the time delay.

These pump-probe measurements are an excellent method of monitoring the recovery of a saturable absorber after the excitation.

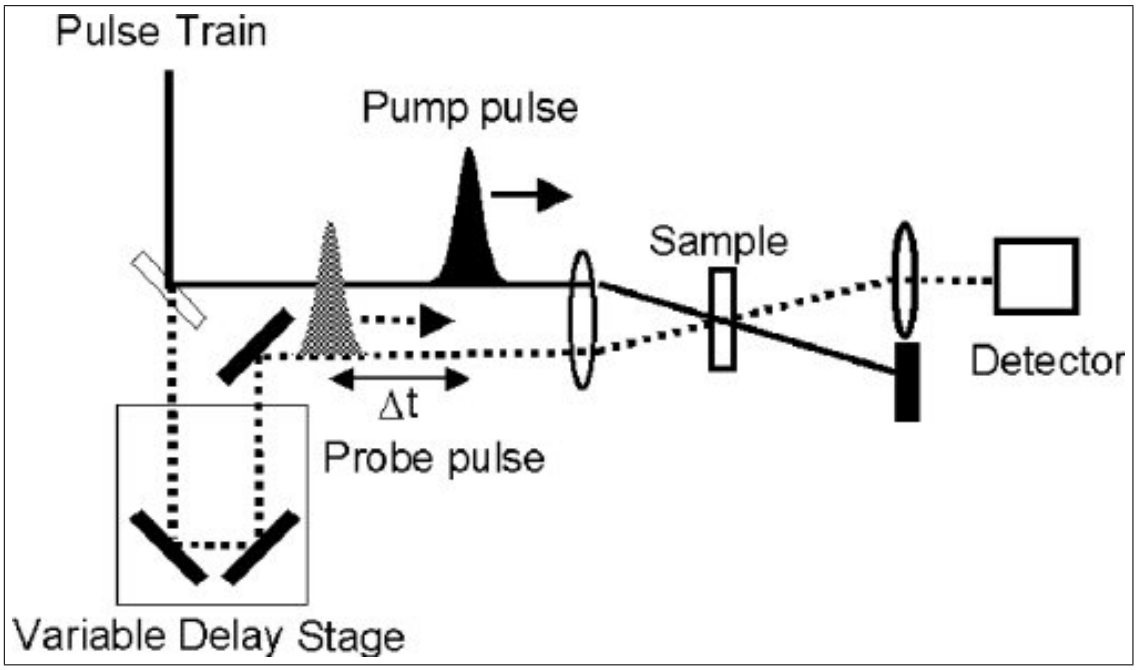

Figure 3.6: Basic pump-probe Set-up, as appears in (Lin *et al.*, 2005)

3.1.4 Laser

Both laser systems used at Trinity College Dublin during the experiments were from Coherent Inc., one of the world leading providers of lasers and laser-based technology for scientific, commercial and industrial customers. A Pharos ultrafast laser was used at the University of Ottawa.

3.1.4.1 Pharos Z-scan laser

The laser used during the collaboration with Prof. Mnard at the University of Ottawa was a Pharos fs laser. The PHAROS from Light Conversion is a compact single-unit, Yb:KGW femtosecond laser system designed to be turn-key out of the box. Delivering sub 190 fs pulses with average powers of up to 20 W and 2 mJ per pulse from single show 1 MHz repetition rate at 1028 nm.

The laser was tunable in both pulse duration (190 fs to 15 ps) and repetition rate (1 kHz to 1 MHz), and was primarily used at 200 fs and 25 kHz, respectively.

3.1.4.2 Micra Z-scan laser

The main laser used in the original Z-scan set-up was a Coherent Mira 900 oscillator, which was a mode-locked Ti:Sapphire laser system operating at 100 fs and 80 MHz. The native available wavelength range for the Mira 900 is 700nm to 1,000 nm, but for $2\mu m$, we required the use of a synchronously-pumped optical parametric oscillator (OPO) to extend the wavelength range into the IR.

The Mira-900 was pumped by a Coherent Verdi V10, a 10W laser operating at 532nm (green light). The Verdi series used a $Nd:YVO_4$ crystal gain medium, pumped by diode lasers.

3.1.4.3 RegA Z-scan and I-scan laser

The main laser operating in the final Z-scan and I-scan set-up was a Coherent RegA 9000, also a Ti:Sapphire laser system operating at 100 fs and 100 kHz. Similarly, to reach the wavelengths required, an optical parametric amplifier was necessary to extend the viable range of the system to 2 μm.

Similarly to the system in Section 3.1.4.2, the RegA was pumped by a Coherent Verdi V10.

4 Graphene Production

In this chapter, the methods with which the graphene used during our experiments were made. While there are many methods for producing graphene, LPE was the preferred method for most of the experiments, with some CVD graphene used also.

4.1 Materials

4.1.1 Pseudo-2D Material Preparation

Much of our 2D materials (graphene, Molybdenum Disulphide (MoS_2), Boron Nitride (BN), WS_2), were prepared via liquid-phase exfoliation (LPE). The first essential step in producing a high-quality colloidal dispersion of any 2D material, is to pick a suitable solvent.

The next portion will outline the production of graphene via liquid phase exfoliation, but the principles can be extended to any 2D material of the same ilk.

The LPE technique depends on the utilisation of a special solvent, in which the interaction between the graphene and the solvent is comparable to the interaction already present between the graphene flakes when stacked as graphite. The acoustic waves from the sonic bath then give the graphene the necessary energy to separate, and due to the now similar interaction with the solvent, these graphene flakes remain separated. Therefore, this method requires matching the surface energies of the solvent to those of the graphene as closely as possible.

As the overall goal of the Integrated disruptive componentS for 2μm LAsers

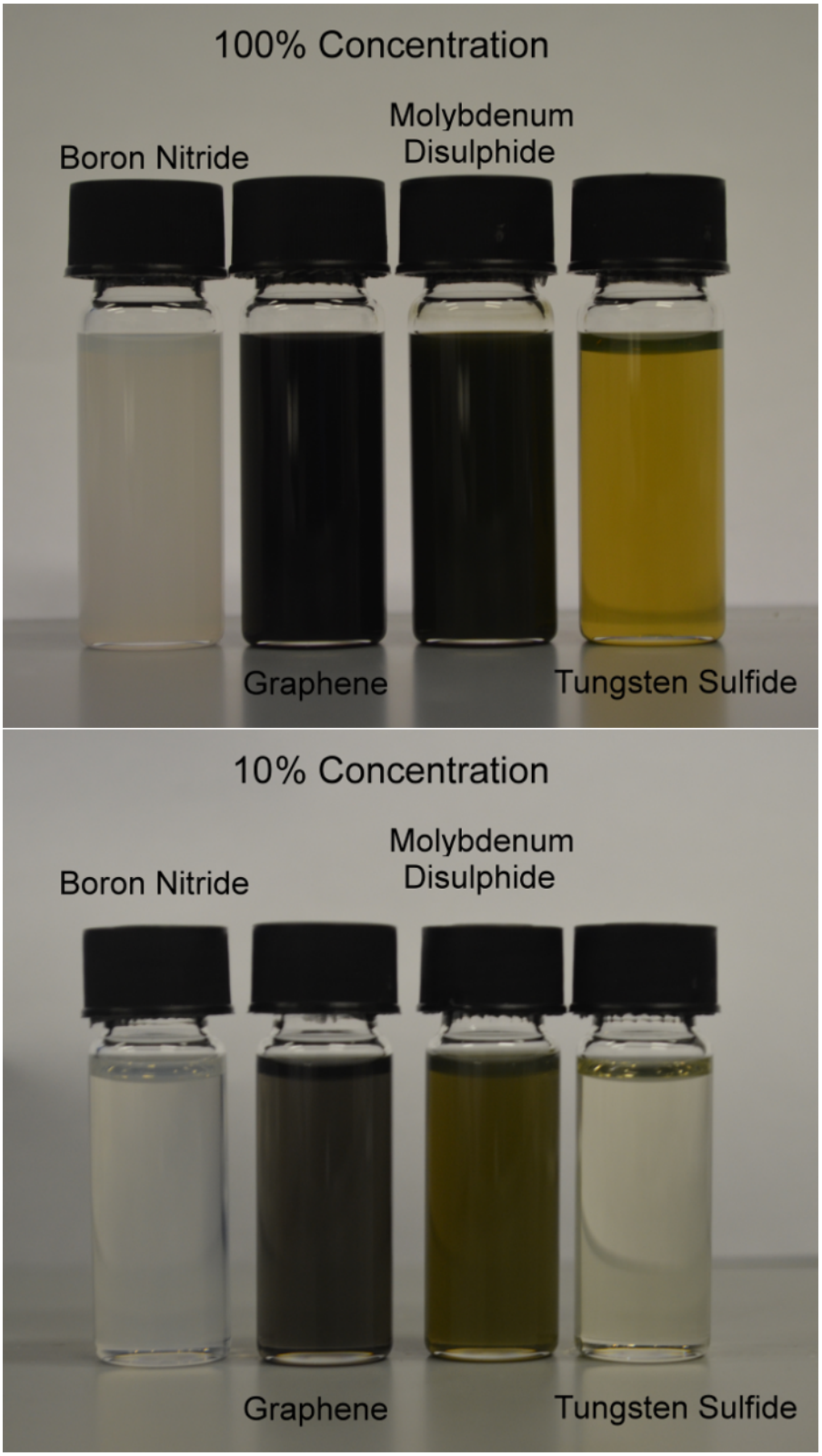

Figure 4.1: Vials of 2D Material Dispersions in NMP. The top image is the stock dispersion, with a concentration around 1 mg/ml, whereas the lower image is diluted to 10% of the original concentration, around 0.1 mg/ml

(ISLA) project was to develop components designed for $2\mu m$ operation, and ultimately the construction of functional $2\mu m$ fibre lasers, it was thought best to employ a solvent that not only successfully disperses graphene, but that is also transparent (or close to transparent) at $2\mu m$.

With this in mind, several solvents were determined to be potentially viable for dispersing the graphene flakes, and so the linear optical absorption of each was measured using a Ultra Violet-Visible (UV-VIS) spectrometer. These solvents were:

- γ-Butyolactone (GBL)
- Dimethylformamide (DMF)
- N-Methyl-2-pyrrolidone (NMP)
- Tetrahydrofuran (THF)
- Tolune
- Water (H_2O)

Each solvent was placed in a 1 cm cuvette, and measured in the UV-VIS. The resulting graph of linear absorption is shown in figure 4.2

As seen in Figure 4.2, the plots are saturated due to too much solvent being present. This was a deliberate choice, as this highlights whether or not the solvent will absorb at all at 2 μm. This also helps check to see if there is any water present, due to the characteristic absorption around this optical region.

Due to complete transparency at 2 μm, THF appeared to be an excellent choice as the dispersant. A batch of graphene in THF was attempted, but the resulting dispersion aggregated extremely quickly - in a matter of an hour or so - and therefore was of little use.

While NMP has a very slight absorption around the 2 μm region (as seen in Figure 4.2), it was already proven to be an effective solvent for graphene dispersion and so was chosen as the main dispersant during the project.

Test dispersions were prepared with the other potential solvents, such as DMF, which has no absorption in the two micron range. However, the quality was not as good as the NMP dispersions.

4.1.1.1 Liquid-Phase Exfoliation - Sonic Bath

For all of the 2D materials, batches were made in NMP, with roughly 10 mg/ml of the initial substance. This solution was then placed in a round bottom flask, and

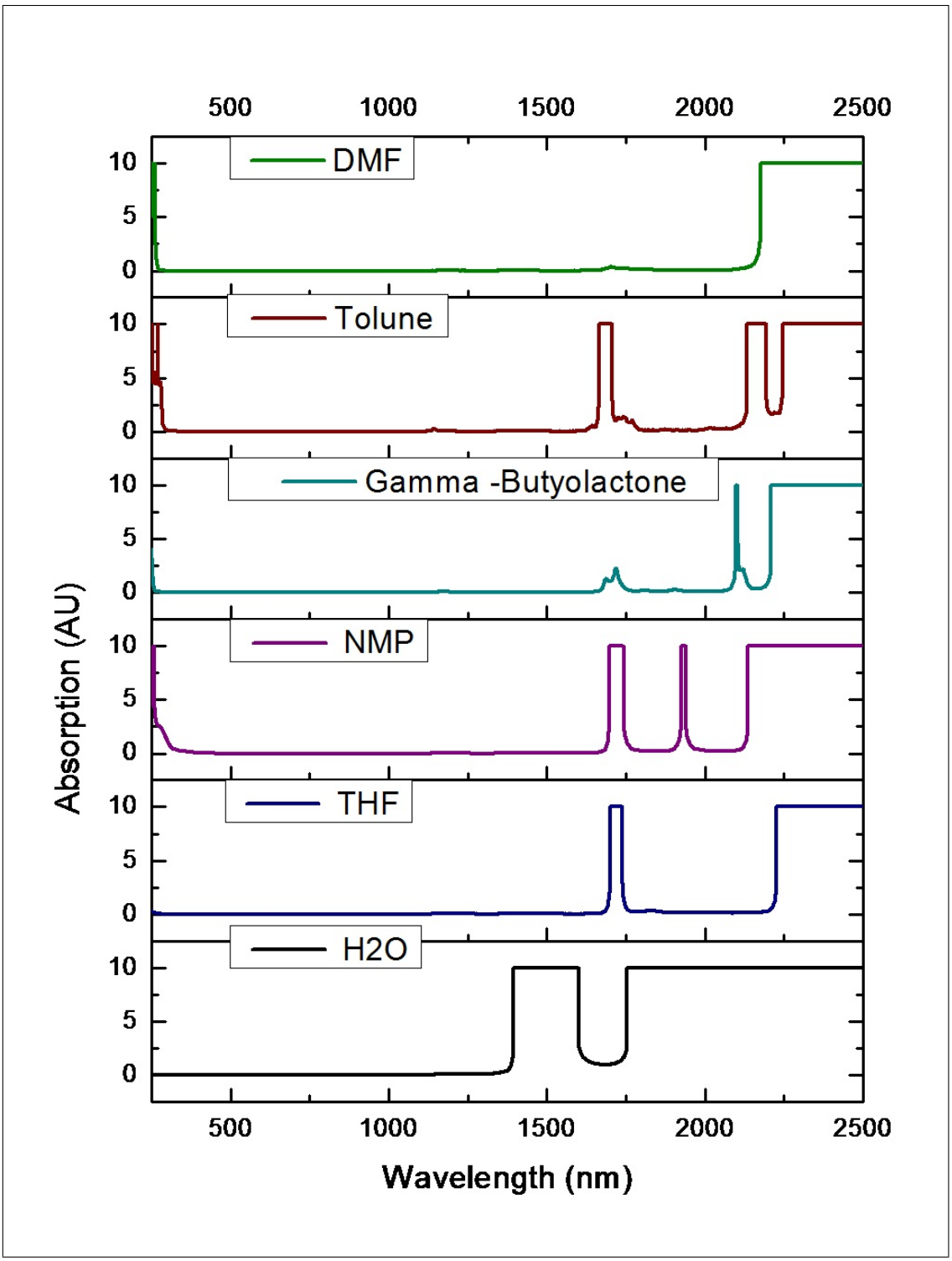

Figure 4.2: Optical Absorption of Potential Dispersion Solvents.

this mixture was then left in a sonic bath (1510 Branson) for around 170 hours, with the water level kept as constant as possible.

The resulting solution was then left overnight and centrifuged the following day (in a Mikro 220R from Hettich Zentrifuge) to remove any aggregates. For the first batch, several rotation speeds were tested (500 rpm, 750 rpm, 1,000 rpm, 1,500 rpm and 2,000 rpm) for 45 minutes each. A sample from each rotation of this initial dispersion was examined using a transmission electron microscope (TEM), and the 2000 rpm stock was determined to be the best.

Many batches were prepared under these conditions, but the rotations were increased to 3,000 per minute in later batches, and the centrifugation time was increased to an hour.

As the dispersions were all made using the same techniques, a concentration of 1 mg/ml was consistent across dispersions.

The graphene obtained via this method consisted of a lot of single layer flakes, similar to the example shown in Figure 4.3. The graphene-NMP solution was dropped onto holey carbon grids, and examined on a Joel 2100 TEM at the Centre for Microscopy and Analysis (CMA).

The fact that these 2D material dispersions are solutions allows for easy fabrication of thin films and composites via wet chemistry techniques, which is advantageous over other preparation methods.

Utilising the wet chemistry methods, graphene-polymer composites were prepared with accurate weight percentages (wt%) of graphene. Another advantage of dispersing the graphene (and other 2D materials) in NMP is that it is also adept at dissolving many common polymers.

Graphene-Poly(Methly Methacrylate) (PMMA) composites were prepared for testing at 1.2 μm, while graphene-polystyrene composites were prepared for examining at 2 μm. This is because while PMMA is viable at 1.2 μm, it is much more absorbent at 2 μm. The absorption of several different polymers was examined by final-year undergraduates, and polystyrene was determined to be the optimal choice for operating at 2 μm.

The thin films of graphene and the graphene-polymer nanocomposites were fabricated through either drop casting or spin coating. Spin coating entails placing the substrate (in this case glass cover slips), onto the chuck of the spin coater, with the substrate held in place via the suction of a vacuum pump in most models. A predetermined volume of the solution in question was dropped onto the substrate, which was then rotated at high speed. This causes the viscous liquid to spread and form a relatively uniform film on the substrate.

The samples prepared in this way were then left in a vacuum oven at 200 °Celsius overnight, to ensure that the solvent had entirely evaporated. Several speeds and durations were tested, and through trial and error, 1000 rpm for 60 s

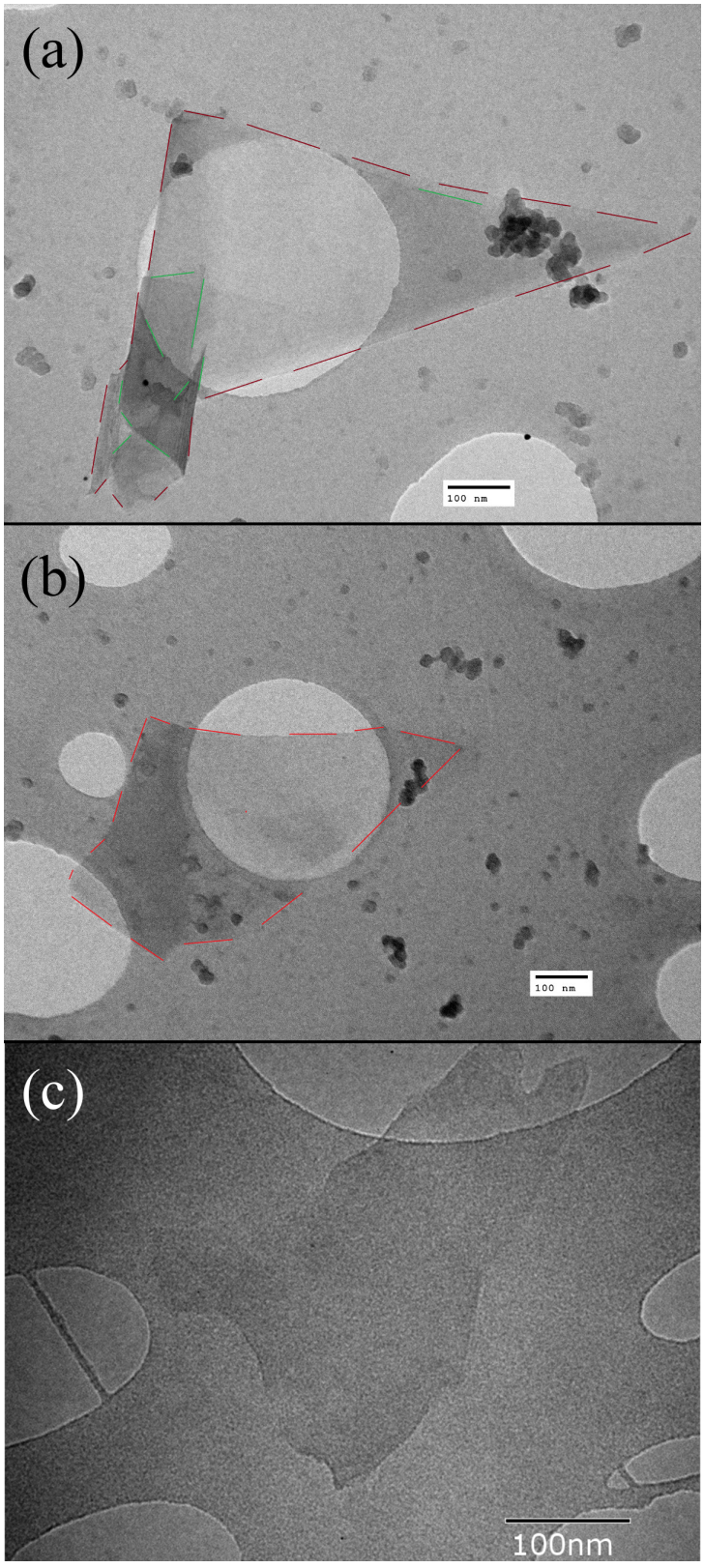

Figure 4.3: TEM images of various graphene flakes. (b) TEM showing twisted graphene flakes.

(after a gradual ramp up over 90 s) was discovered to work best for the samples used.

Due to the requirement that the solution being spin coated be quite viscous, only some of the low graphene wt% composites were viable, due the viscosity gained from the high polymer content. Spin coating was less suitable for the solutions with low polymer levels (including the pure graphene-NMP) due to their increased fluidity, and for this reason drop casting was employed for such samples.

Drop casting is achieved by simply placing a small, predetermined volume of the solution (20 μL) on the substrate, and drying it out either by placing in the oven at 200°Celsius, or in vacuum desiccator (low pressure environment) at room temperature. Samples prepared via this method had somewhat inhomogeneous film thicknesses, with an increased thickness toward the edge of the samples.

4.1.1.2 Liquid-Phase Exfoliation - Sonic Tip

The procedure for preparing graphene and other 2D materials is very similar to the process described in section 4.1.1.1, except the obvious difference is the use of a sonic tip, in place of the sonic bath.

Unlike the bath, the sonic tip is actually inserted in the solvent/material solution, and the sonication times are much shorter. While this may vary, four hours of sonication is a typical time.

4.1.1.3 Blends

As shown in Figure 4.5, mixtures were made from the dispersions of Boron Nitride, Molybdenum Disulphide and Tungsten Disulphide in NMP, and combined with graphene/NMP, with specific weight percentages of graphene.

Interestingly, the blends with the transition metal dichalcogenides (MoS_2 and WS_2) and graphene were extremely unstable, and the dispersions aggregated within 24 hours.

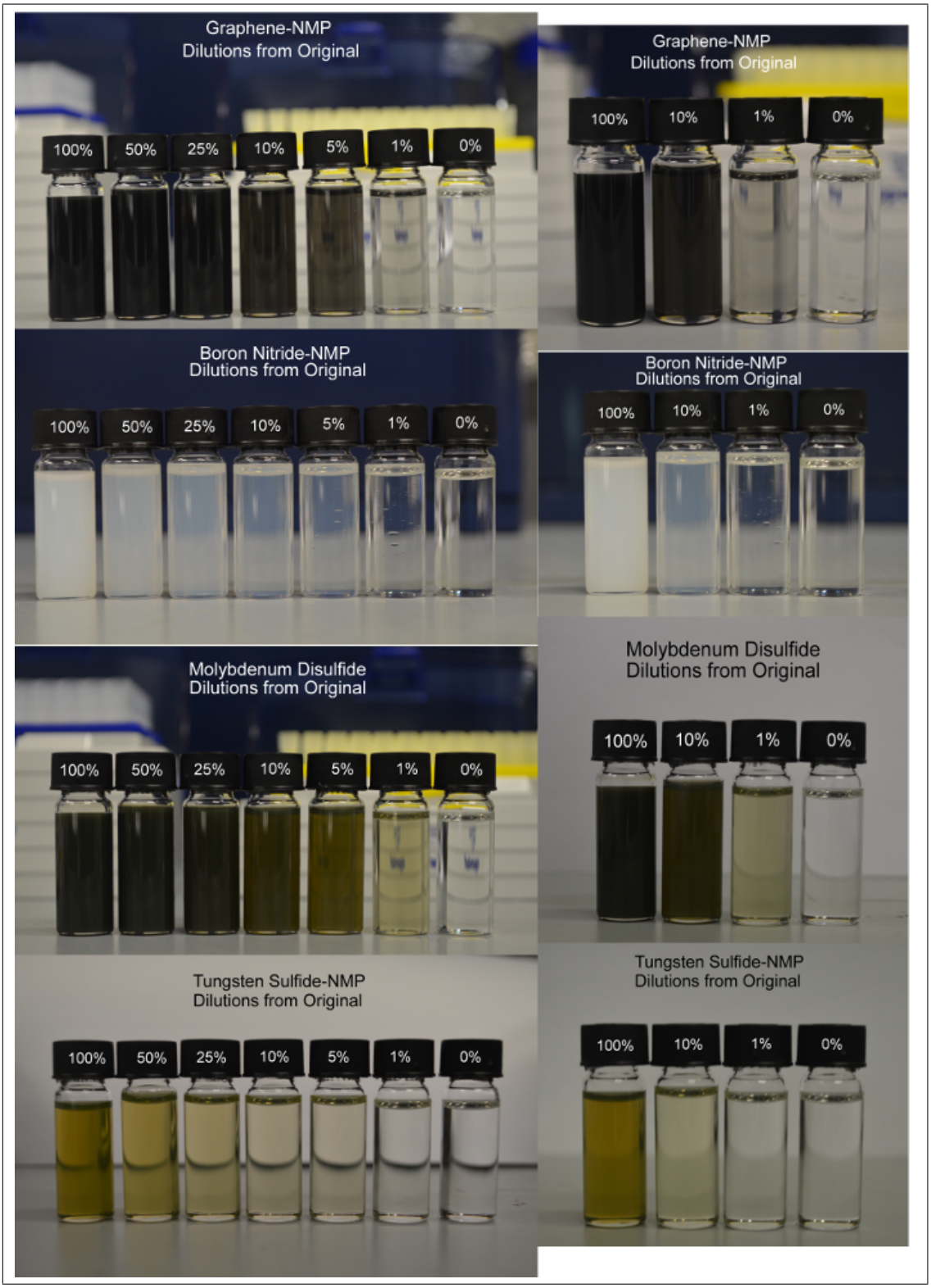

Figure 4.4: Varying Concentrations of 2D Dispersions in NMP

Figure 4.5: Blends of Graphene and Other 2D Materials in NMP

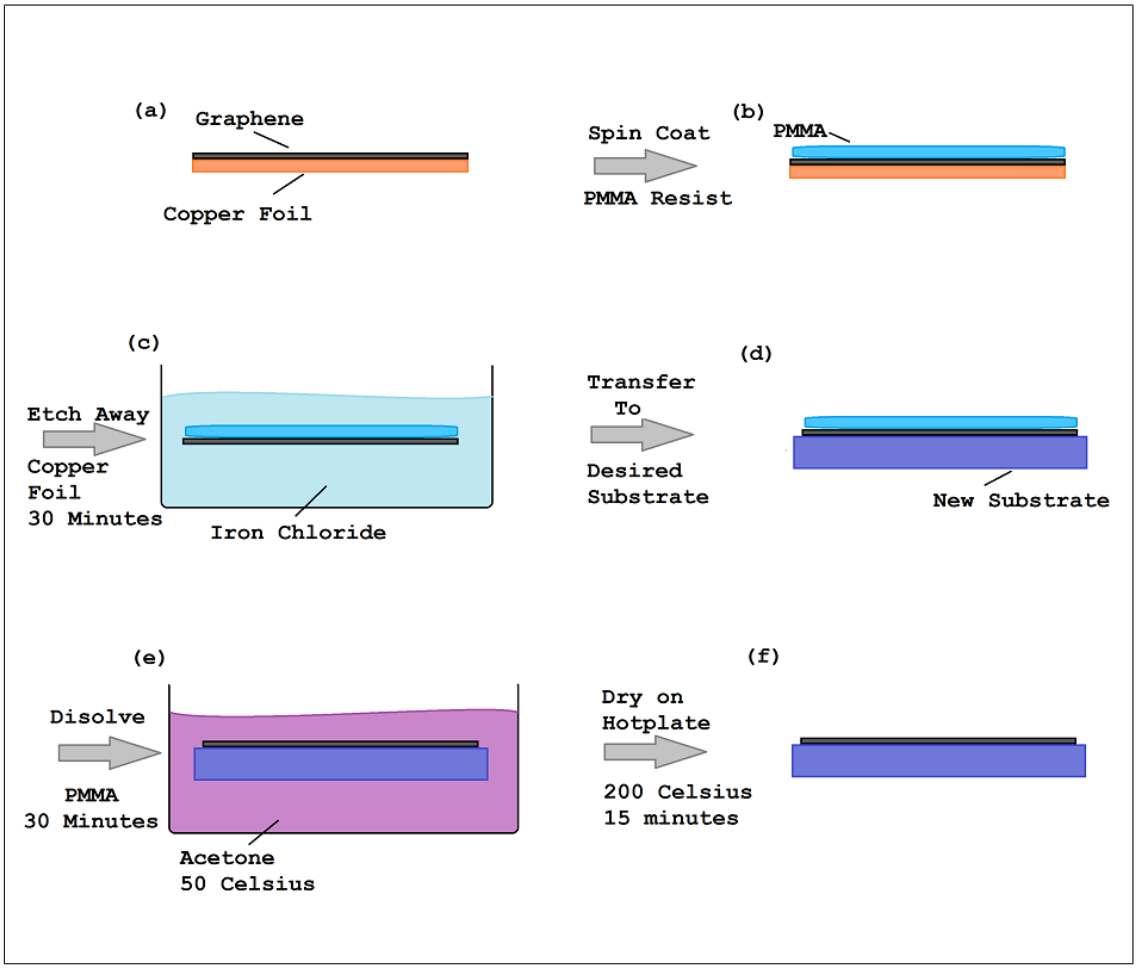

Figure 4.6: Workflow for transferring as grown CVD graphene from a copper foil to an arbitrary substrate

4.1.1.4 Chemical Vapour Deposition

CVD prepared graphene on copper foil and nickel (on silicon substrate) was purchased from Graphene Supermarket. The graphene prepared via CVD on copper is generally single layer, whereas the samples grown on nickel is generally at least bilayer graphene.

Transferring the CVD graphene from the metallic substrates to silver mirrors from Thor Labs to create Graphene Saturable Absorber Mirror (G-SAM) was a several step process, as shown in 4.6. To summarise:

1. Coat with PMMA Resist
2. Etch away metal substrate

3. Transfer to chosen substrate

4. Dissolve away PMMA

To achieve the first goal, the CVD graphene on copper, for example, was placed on a spin coater, and a solution of 3% PMMA dissolved in anisole (referred to as A3) was placed on the sample. The spin coater was then run at 2,000 rpm for a minute before the sample was placed on a hotplate at 200 Celsius to anneal for 10 minutes.

There are actually several methods that can be used to separate the graphene from the metal, such as exposing the CVD sample to an oxygen plasma for 1 minute, or a simpler scotch tape peeling method. Chemical etching was chosen instead.

Iron chloride ($FeCl_3$ in HCL/H_2O (1M-5M)) was chosen as the solution capable of etching away the copper. Other candidates included iron (III) nitrate solution, ammonium persulfate (0.1M) and toxic copper (II) chloride.

The iron (III) chloride solution was prepared by adding 63 g of $FeCl_3$ to 92.9 g of deionised water (100 ml) followed by 1.6 g of HCL was added.

The Cu/graphene sample and PMMA resist were left in the solution was for a little over 30 minutes. The bulk Cu foil was etched after 25 minutes, and then the sample was left for 5+ minutes to etch away any residue.

The final substrate, silver mirrors in this case, was then used to scoop up the remaining graphene + PMMA resist, and was cleaned off with DI water.

The device (mirror, graphene and resist) were left to dry on a hotplate at 150 Celsius for 15 minutes. This also allows the graphene to adhere to the substrate.

To then remove the PMMA resist, the device were submerged in acetone at 50 Celsius for 30 minutes.

Finally, the graphene/substrate are left on the hotplate at 200 Celsius for 15 minutes. An example of a graphene SAM prepared in such a manner is shown in Figure 4.15.

4.1.2 Sample Preparation

4.1.2.1 Thin Film Preparation - Drop Casting

Drop casting is a very simple process, involving pipetting a known volume of the dispersion onto the chosen substrate. In this case, 10-20 μl of the 2D material-NMP dispersions was placed on borosilicate glass coverslips to make optical thin film samples to examine via Z-scan, as shown in Figures 4.7 and 4.8.

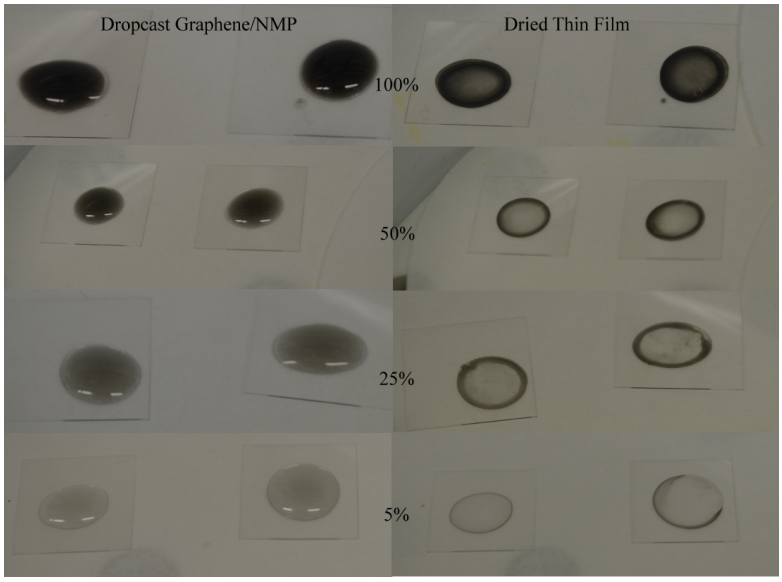

Figure 4.7: Graphene Thin Films Prepared via Drop-Casting, on Borosilicate Coverslips

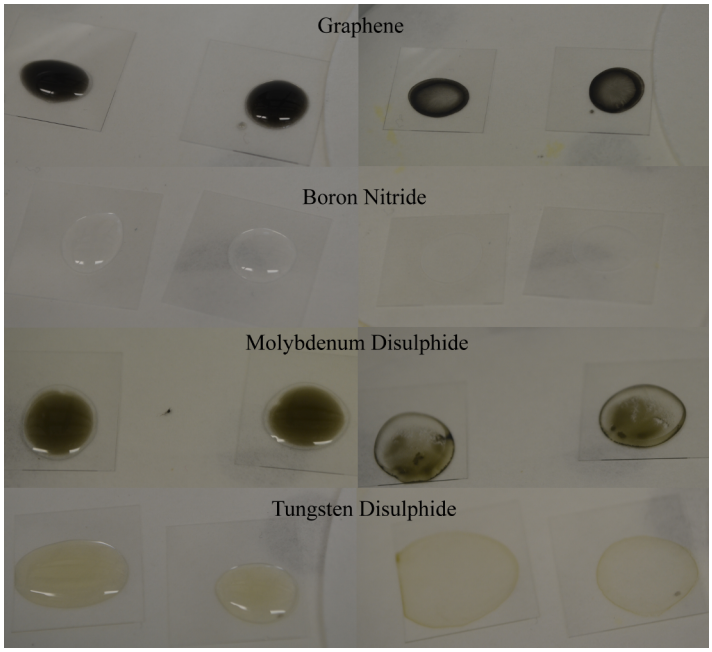

Figure 4.8: Thin Films of Graphene, Boron Nitride, Molybdenum Disulphide, and Tungsten Disulphide Prepared via Drop-Casting, on Borosilicate Coverslips. The dropcast sample is shown on the left, with the dried sample on the right

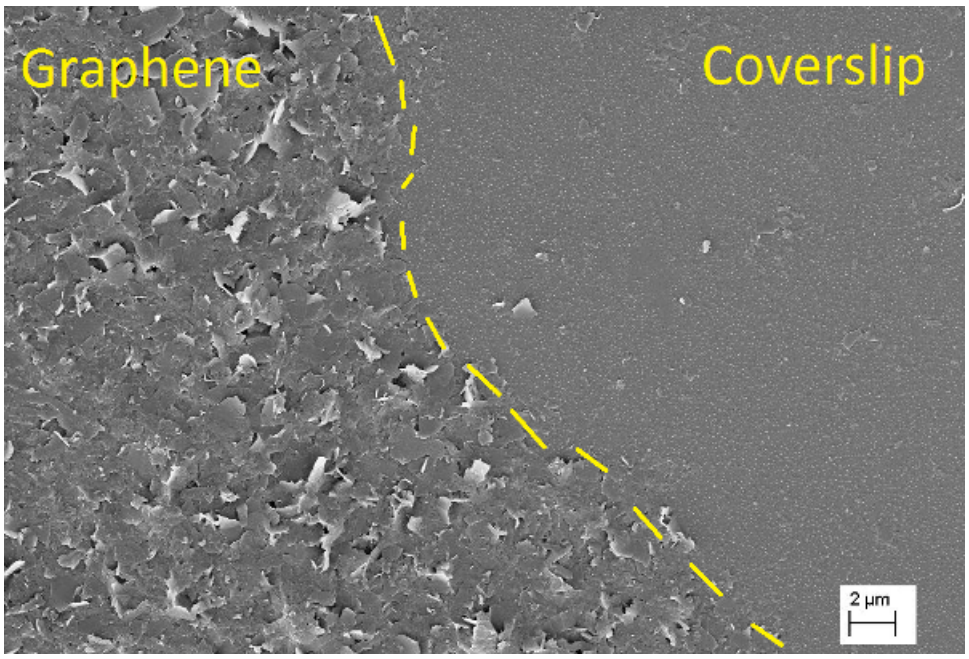

Figure 4.9: SEM image of the drop-cast graphene on a coverslip, showing the graphene boundary.

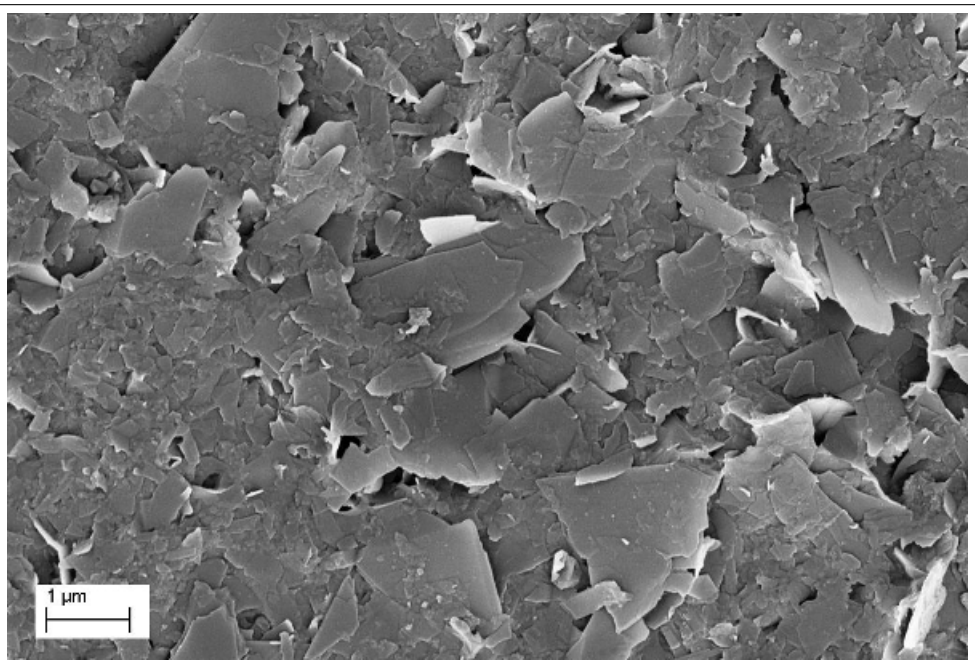

Figure 4.10: Closer SEM image of the drop-cast graphene on a coverslip than Figure 4.9

These samples were then dried. To achieve this, two methods were utilised. Samples were **either** placed in an oven at 200 Celsius overnight, or were placed in a vacuum desiccator for a comparable amount of time. A Scanning Electron Microscopy (SEM) image of the drop-cast graphene thin films on borosilicate glass is displayed in Figures 4.9 and 4.10, with the boundary of the graphene film visible in 4.9.

The main issue with this method is that the resulting films were fairly inhomogeneous, particularly around the edges. This problem was exacerbated when using a higher concentration dispersion, whereas for lower concentration samples suffered somewhat less, as can be seen in Figure 4.14. This was simply due to how the droplet dries.

4.1.2.2 Silver Mirrors

Silver coated mirrors are known to boast the highest reflectance in the visible-NIR spectrum of any metallic mirror (450nm-2μm, R_{avg} >97.5%). On top of this, they also exhibit high reflectance in the IR regime (2-20μm, R_{avg} >96%), as can be seen in Figure 4.11.

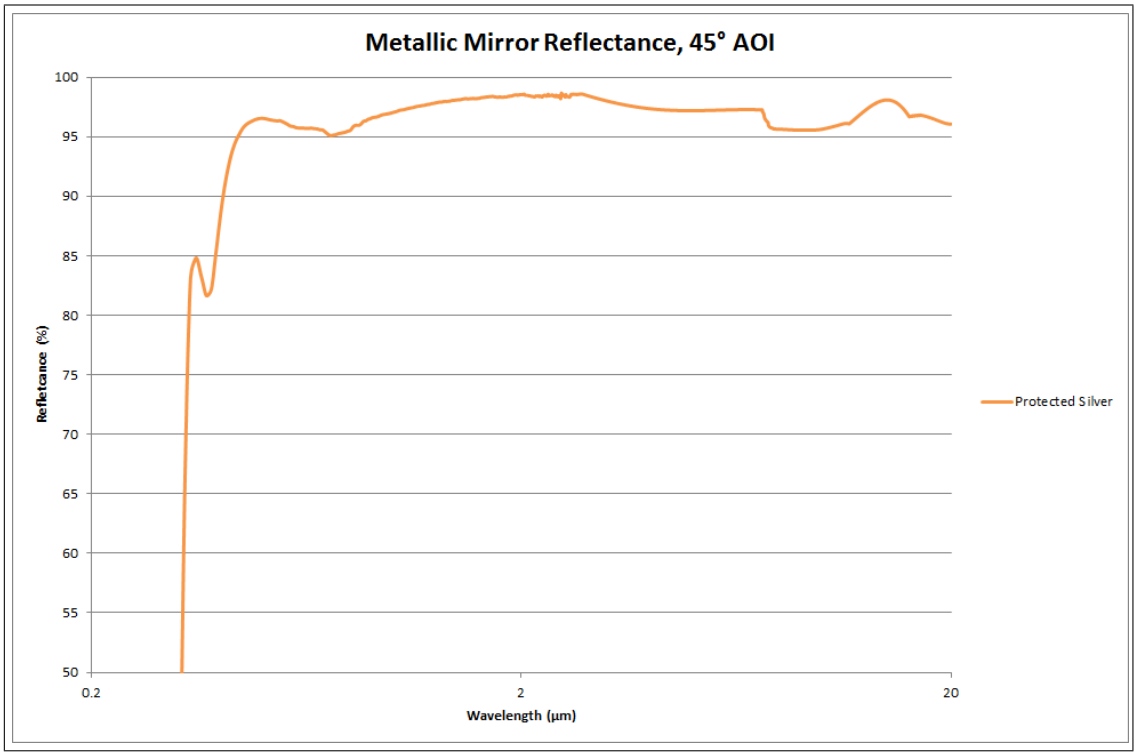

Figure 4.11: The reflectance of the Thorlabs silver mirrors between 0.2 to 20μm

To ensure protection from oxidation, the silver on these mirrors has an 100nm

thick SiO_2 layer. When using these mirrors as the base for our graphene SAMs, this protection layer did not lead to any unwanted effects. Testing the blank mirrors with the I-scan method, no nonlinear optical effects were observed from the SiO_2 layer, as shown in Figure 4.12.

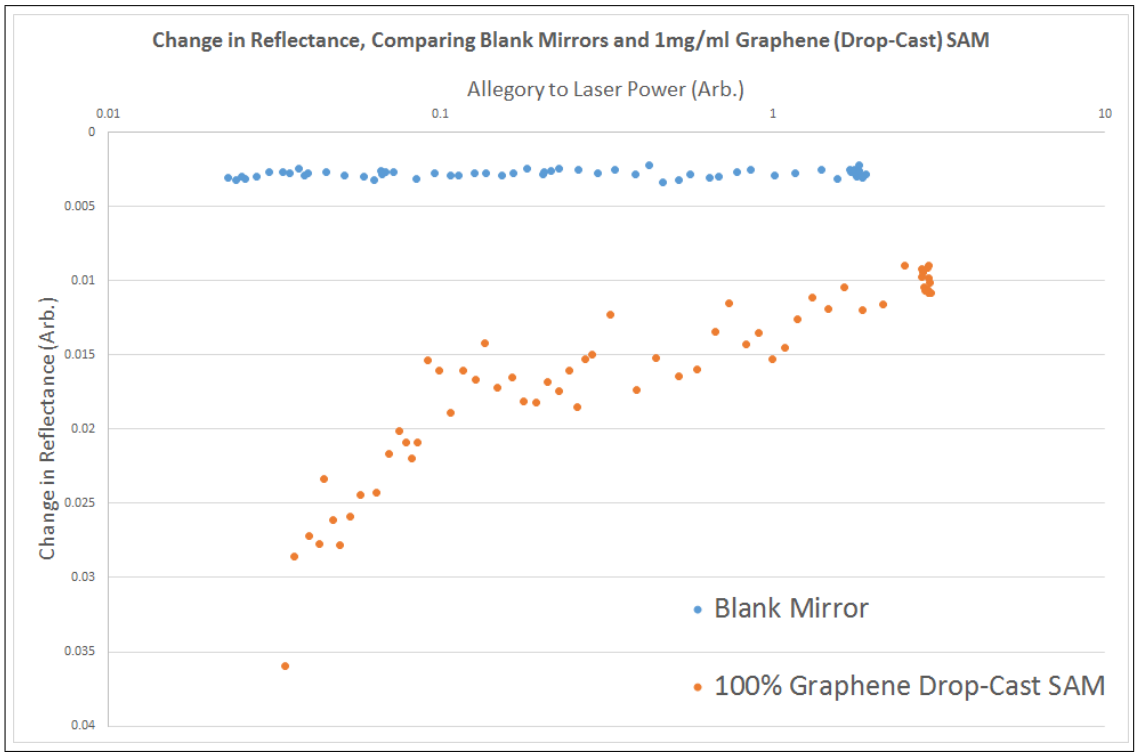

Figure 4.12: Change in reflectance in respect to increasing laser power. The blank ThorLab silver shows no change in reflectance, whereas the graphene SAM exhibits increasing reflectance, due to saturable absorption.

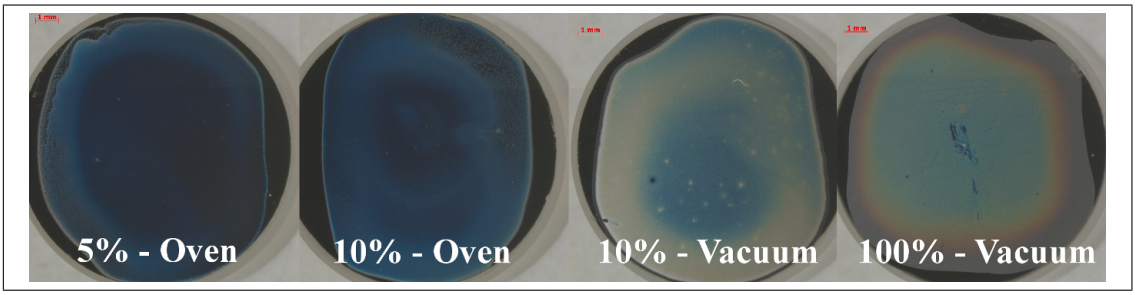

Figure 4.14: Graphene SAMs Prepared via Drop-Casting

4.1.2.3 Graphene SAM Preparation

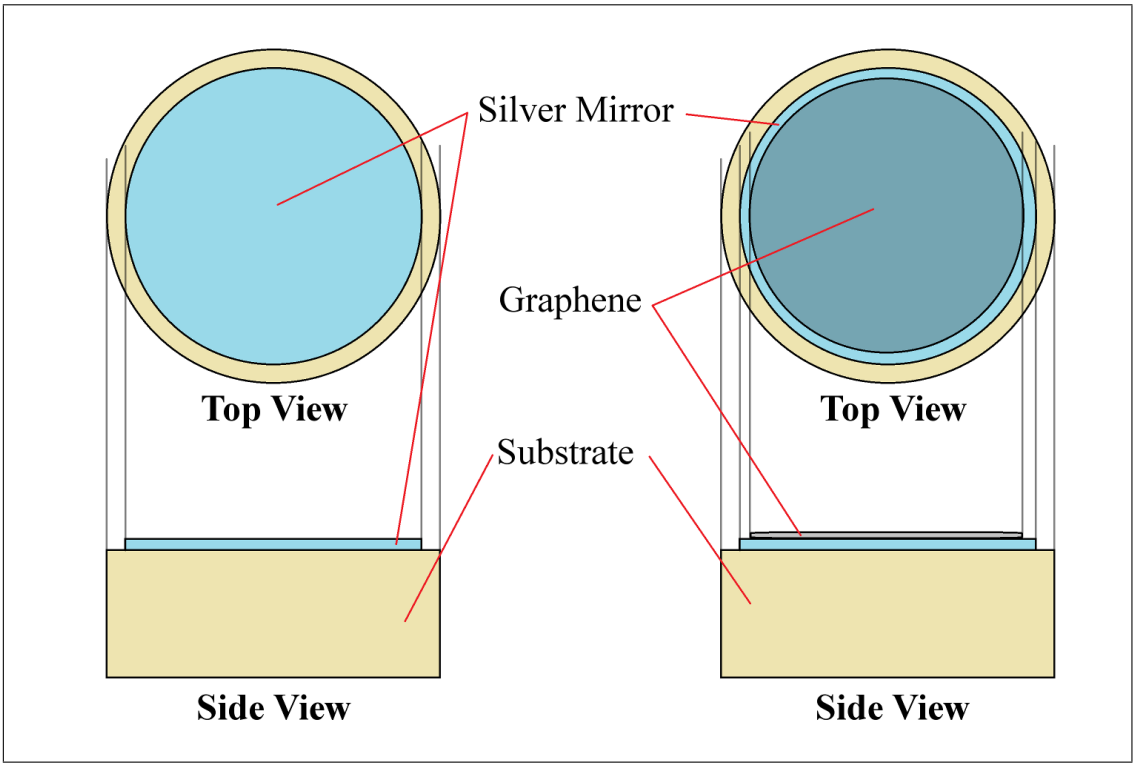

Figure 4.13: Basic graphene SAM schematic

Graphene SAM samples can be prepared using the same method describe in Section 4.1.2.1, by replacing the coverslip substrate with the required mirror, in this case Silver Mirrors from Thor Labs, and is shown in Figure 4.13. Samples prepared as such can be seen in Figure 4.14.

Whereas the method to produce CVD prepared graphene SAMs was described in detail in Section 4.1.1.4, and an example can be seen in Figure 4.15.

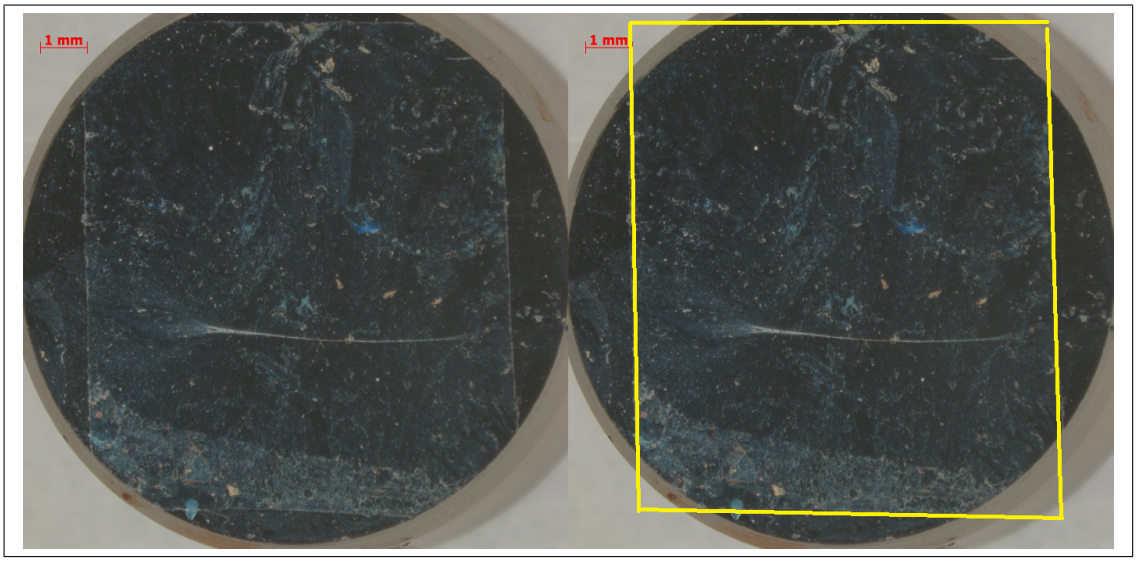

Figure 4.15: Graphene SAMs Prepared via CVD Transfer Methods. The image on the right outlines the CVD graphene on the silver mirror

4.1.2.4 Graphene SAM Preparation - Vacuum Filtration

Other prototype graphene SAMs were manufactured by transferring a vacuum filtrated graphene film onto a silver coated mirror. The procedure is similar to previous work undertaken by the group on MoS_2 (Feng *et al.*, 2015a), and is described visually in Figure 4.16.

Graphite and sodium cholate (99%) were purchased from Sigma-Aldrich. The porous nitrocellulose membranes for filtration were products of Millipore with 100 nm pore size. The protected silver coated mirrors were from Thorlabs.

First, the graphite was exfoliated by liquid phase exfoliation (LPE) method in distilled water using sodium cholate as surfactant (Hernandez *et al.*, 2008a). The concentrations of graphite and sodium cholate were 5 mg/mL and 0.1 mg/mL respectively. After 6 hours sonication by high power sonic tip, the primary dispersions were centrifuged with 3000 rpm speed by 3 hours. The top 2/3 dispersions were collected for vacuum filtration. Then the graphene nanoflakes were deposited onto porous membranes during vacuum filtration. The wet membrane was attached onto the reflective surface of silver mirrors with 1 kg weight and dried in air for 12 hours. Finally, the nitrocellulose membrane was dissolved by acetone and the silver mirrors coated with graphene film were obtained.

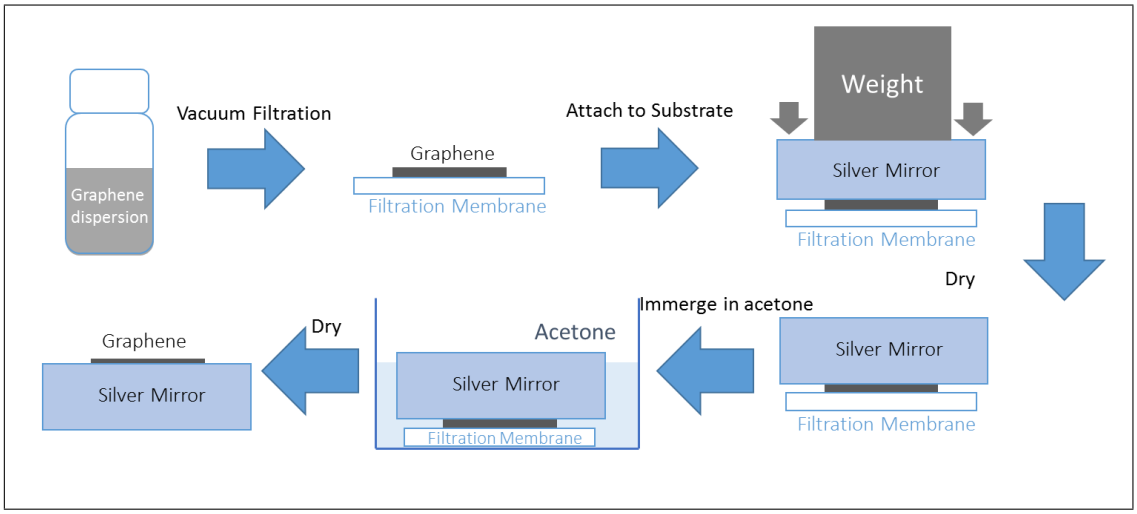

Figure 4.16: Procedure for preparing graphene SAM using vacuum-filtration film transferring techniques

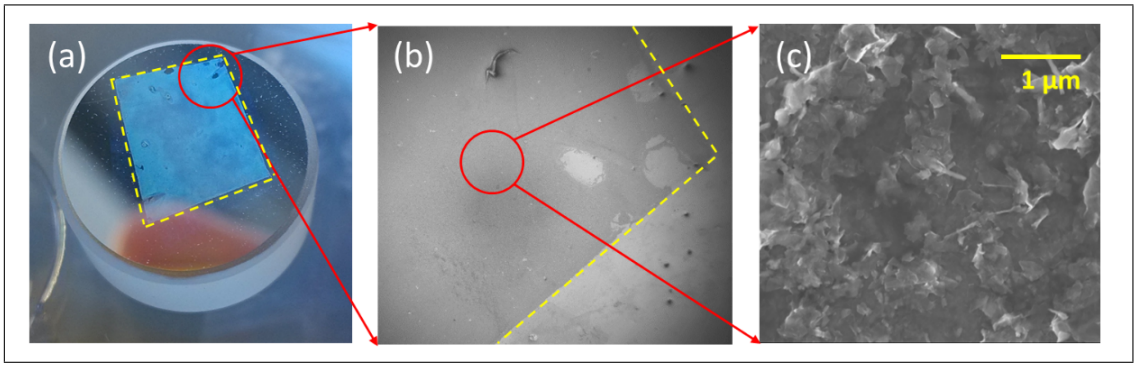

Figure 4.17: (a) The photo of graphene coated silver mirror prepared by vacuum filtration; (b) and (c) SEM image of graphene film in (a). Yellow dash lines indicate the boundary of graphene

The image of graphene SAM prepared by vacuum filtration is presented in Figure 4.17 (a). The dashed yellow lines indicates the boundary of the transferred graphene film. The geometry of the as-coated graphene film is observed by scanning electron microscope (SEM), as shown in Figure 4.17 (b) and (c).

Although a few holes exist near the boundary, the SEM image in Figure 4.17 (b) shows quite a neat and homogeneous graphene film, implying that vacuum filtration is quite a good deposition method of LPE graphene into a functional film. The higher magnification image of graphene film is presented in Figure 4.17 (c), and shows the film was formed by the segregation of several micrometre graphene nanoflakes.

4.1.2.5 Raman Spectrometry of Graphene

When developing technologies and devices based upon graphene, methods to accurately determine the layer thickness for materials under investigation is required. Raman spectroscopy can be utilised to provide a quick, non-destructive means of determining layer thickness for graphene thin films.

Raman spectroscopy is a vibrational technique that is extremely sensitive to geometric structure and bonding within molecules. Even tiny differences in the geometric structure leads to significant differences in the observed Raman spectrum of a molecule.

This sensitivity to geometric structure is extremely useful for the study of the different allotropes of carbon (i.e. diamond, carbon nanotubes, buckminster fullerenes, carbon nanoribbons, etc.) where the forms are only different in the relative position of their carbon atoms, as well as the nature of their bonding to one another. Raman spectroscopy has evolved to become a fantastic tool in laboratories pursuing research into the fledgling field of carbon nanomaterials.

There are three peaks in the Raman spectra that are characteristic of graphene. These are the so-called G, D and 2D bands.

The G Band is sharp around 1,587 cm^{-1}, and is representative of the in-plane vibrational mode involving the sp^2 hybridised carbon atoms that make the graphene sheet. This band is highly sensitive to the number of layers that are present in the sample. Therefore, the position of this band is one method for determining layer thickness.

The D Band is referred to as the "disorder band" or the "defect band". It represents a ring breathing mode of the sp^2 carbon rings, but to be active the ring must be adjacent to a graphene edge or defect. It is therefore very weak in graphite, as well as high quality, pristine, large, single-layer graphene flakes.

The 2D Band is the second order of the D Band. It results due to a two phonon lattice vibrational process, and does not need a defect/edge to activate. Because of this, it is always strong in graphene.

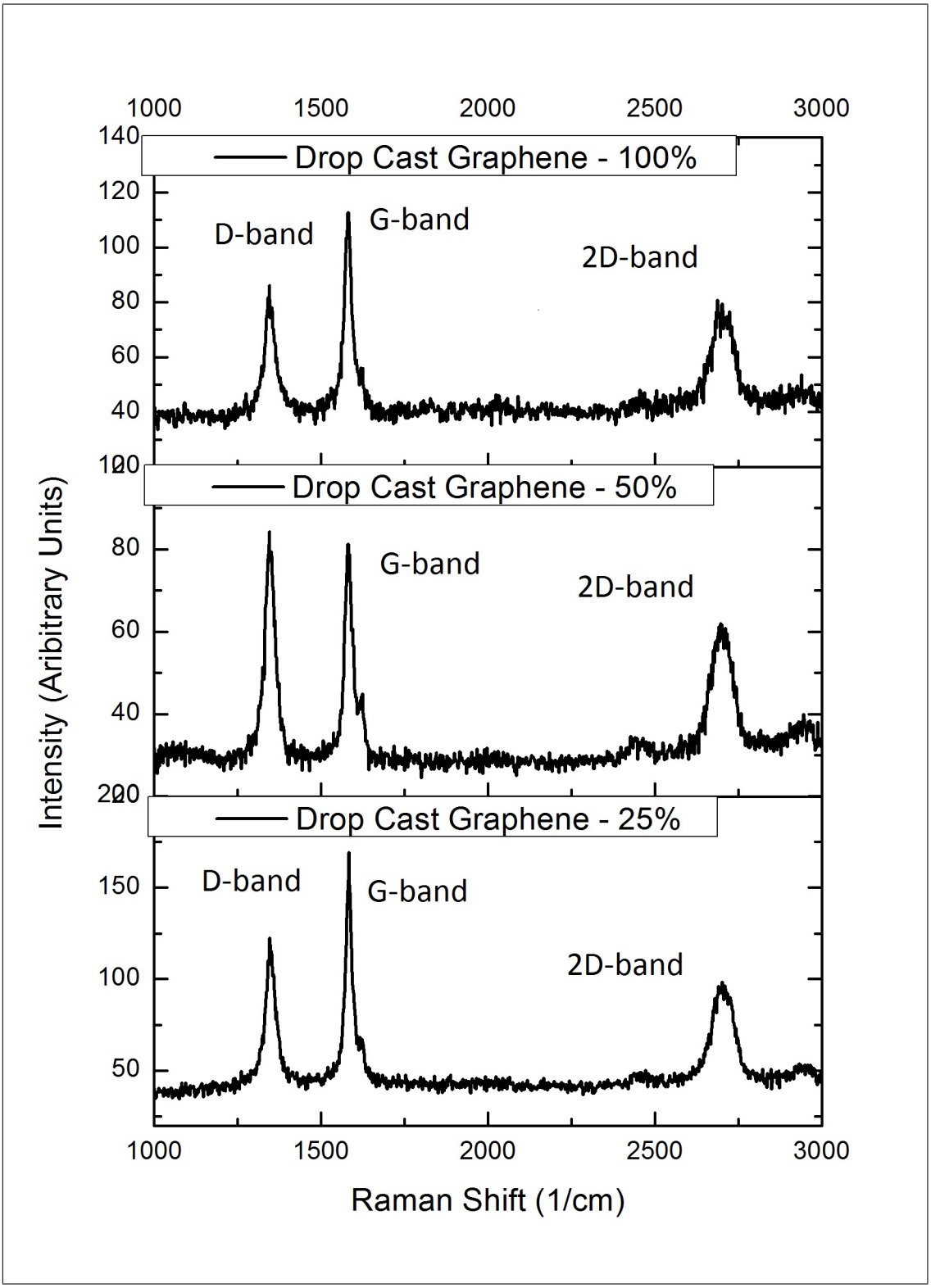

Figure 4.18: Raman Spectra for the drop-cast graphene films. The large D-band is present due to the edges of the graphene flakes

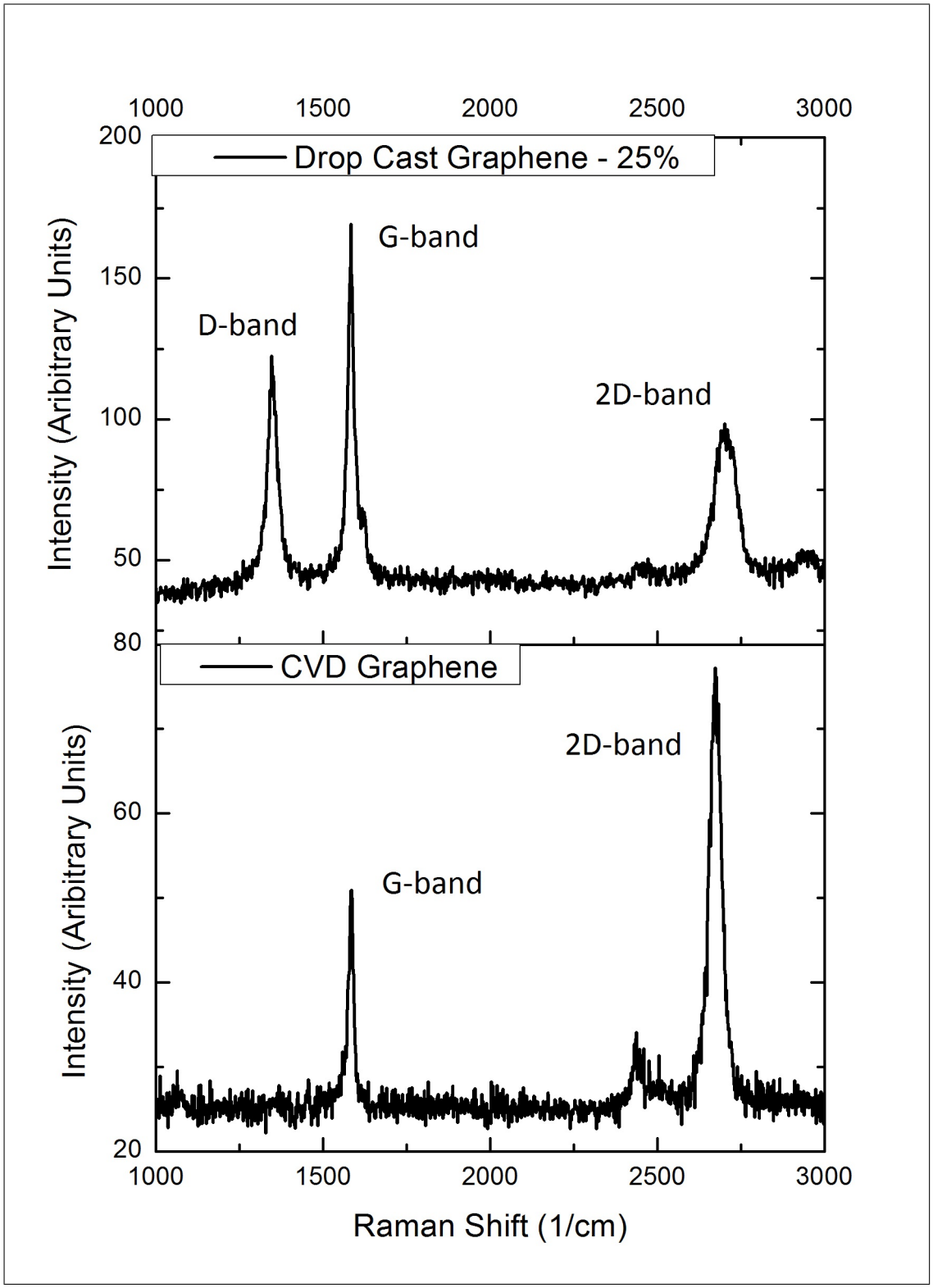

Figure 4.19: Raman Spectra comparing the CVD graphene to the drop-cast graphene films.

The Raman spectra for the drop-cast graphene films can be seen in Figure 4.18. The large D band is present due to the edges of the graphene flakes. The Raman spectra of CVD graphene grown on copper and then transferred to a quartz substrate is displayed in Figure 4.19. The absence of D band in the CVD graphene is due to the lack of edges, unlike the dropcast graphene. The smaller 2D band in the drop-cast spectra is due to the presence of multilayer graphene.

As mentioned, the drop-cast graphene films exhibited a large D band, which is only active when next to defect or an edge. While at first this may just appear to be due to being poor quality graphene, this is not the case. Due to the relatively small individual flake size, and the presence of many flakes per sample, it is the presence of edges that is being represented by the notable D band. Also of note, the D band is very weak in actual graphite samples, so the presence of a D band at all is generally indicative of graphene.

The D band is conspicuous by its absence in the CVD graphene Raman spectra, which is because it is a large area, single sheet of graphene, with little to no defects and no edges at the section examined.

The 2D to G band ratio for the CVD graphene is 2:1, which is characteristic of single layer graphene. Whereas the drop cast graphene sample ratio is closer to 1:2, and with a less sharp 2D peak, both of which imply the presence of thicker graphene stacks, as well as the single layer flakes. Which is to be expected with the liquid phase exfoliation methods for graphene synthesis.

Overall, the Raman spectra of the drop-cast thin-film samples shows the graphene to be of high quality.

5

Nonlinear Optical Properties of Thin Films of 2D Materials

In this chapter, the performance of pure graphene films is investigated by employing Z-scan techniques. The saturable absorption SA of graphene films is thus directly confirmed.

Liquid phase exfoliation LPE is a scalable and easy preparation technique which boasts low cost, and is especially suited for industrial fabrication (Coleman *et al.*, 2011b; Hernandez *et al.*, 2008a). The effective exfoliation of graphite to graphene nanosheets and successfully preparation of several graphene films using different techniques was demonstrated in Chapter 4.

Coating glass or quartz substrates with a graphene film and characterising graphene on such substrates is a prerequisite for both the planned mode-locked 2 micron laser (discussed in 6.6) which uses a SAM structure and fibre integrated lasers such as described in literature where a glass fibre can be coated in the same way as described in Chapter 4 (Bonaccorso *et al.*, 2010; Martinez & Sun, 2013). With the successful demonstration of saturable absorption in graphene at 2 μm, it was possible to advance to performance investigations of graphene film on mirrors, which is the topic of Chapter 6.

5.1 Z-scan

The theory behind the Z-scan technique was explored in more detail in Section 3.1.1.

As an easy and fast method to determine the nature of the nonlinearity of materials (Chapple *et al.*, 1997; Said *et al.*, 1992), the Z-scan technique was employed in this thesis to study the saturable absorption of graphene.

As described in Section 3.1.1, the idea behind the Z-scan technique is to move the sample through a tightly focused laser beam along the propagation direction, which generally can be described by a Gaussian function. At different parts of the Gaussian beam, the sample is subjected to different intensities as it moves through the focus. This gives the relationship between sample position and laser intensity. With this relationship, the nonlinear absorptivity and non-saturable loss can be obtained.

According to Non-Linear Optical (NLO) theory, the equations for the intensity decay when laser propagates in a saturable medium can be expressed as follows in equation 5.1:

$$\frac{\partial I}{\partial z} = -\frac{\alpha_0 I}{1 + I/I_S} \tag{5.1}$$

where I is laser intensity, α_0 is the linear absorptivity that can obtained by linear optical transmission, and I_S is saturated intensity. With Gaussian equation that describing laser beam, one can obtain the I_S from Z-scan curve fitting.

The open aperture Z-Scan data can be fit according to the thin film version of the equations as described in the original z-scan paper by Sheik-Bahae et al., as shown in Equation 5.2.

$$T_{open} = 1 + \frac{\beta I_0 L_{eff}}{2\sqrt{2}\left[1 + (\frac{z}{z_0})^2\right]} \tag{5.2}$$

$$L_{eff} = \frac{(1 - e^{-\alpha L})}{\alpha} \tag{5.3}$$

where L is the film thickness, L_{eff} is the effective thickness, α is the linear absorption coefficient, z_0 is the Rayleigh Length, and β is the nonlinear absorption coefficient.

$$I_0 = \frac{P_{peak}}{\pi\omega_0^2} = \frac{E_{pulse}}{D_{pulse}\pi\omega_0^2} \tag{5.4}$$

$$z_0 = \frac{\pi\omega_0^2}{\lambda} \tag{5.5}$$

Pearson's chi-squared goodness of fit test can be utilised to find the best fit for the open aperture data. As a matter of note, this chi-squared, χ^2, test should not be confused with the third order nonlinearity, $\chi^{(3)}$. This test allows us to examine how close observed values are to expected values. In is expressed in the following form, in Equation 5.6:

$$\chi^2 = \sum \frac{(observed - expected)^2}{expected} \tag{5.6}$$

Each data point is compared to the expected value in the fit given in Equation 5.2, and the best fit possible can be obtained by varying applicable variable as such to minimise the sum of chi-squared. This assumes the data to be fit adheres to the nonlinearity set out by Equation 5.2.

In a simplified sense, for a gaussian fit the Rayleigh Length can be viewed to set the FWHM value of the curve and the β controls the height of the curve. As such, software can be used to alter both β and the beam waist, ω_0, such as to minimise the sum of chi-squared. As shown in Equations 5.5 and 5.4, ω_0 is proportional to square-root of z_0 and inversely proportional to the square-root of I_0, respectively. Using this method, a very good fitting of the open aperture data can be obtained, and an accurate value for β can be extracted.

β can be utilised to calculate the imaginary part of the third order nonlinearity, $\chi^{(3)}$:

$$Im(\chi^{(3)})(esu) = (\frac{10^{-2}\epsilon_0 c^2 n_0^2 \lambda}{4\pi^2})\beta(cm/GW) \tag{5.7}$$

The closed aperture scan can be fit with Equation 5.8, which can be utilised to obtain the nonlinear refractive index, n_2, of a material. To fit the closed aperture data, the closed aperture normalised transmission must first be divided by the open aperture normalised transmission.

$$T_{closed} = 1 - \frac{4(\frac{z}{z_0})\Delta\phi_0}{((\frac{z}{z_0})^2 + 9)((\frac{z}{z_0})^2 + 1)} \tag{5.8}$$

$$\Delta\phi_0 = \frac{\Delta T_{pv}}{0.406(1-S)^{0.27}} = \frac{2\pi n_2 I L_{eff}}{\lambda} \tag{5.9}$$

where S is the fraction of the closed aperture baseline to the open aperture baseline. ΔT_{pv} is the difference between the peak and the valley in the normalised transmission of the closed aperture data.

n_2 can be utilised to calculate the real part of the third order nonlinearity, $\chi^{(3)}$:

$$Re(\chi^{(3)})(esu) = (\frac{10^{-4}\epsilon_0 c^2 n_0^2}{\pi})n_2(cm^2/GW) \tag{5.10}$$

With both the real and imaginary parts of $\chi^{(3)}$ calculated, it becomes easy to calculate $\chi^{(3)}$ itself with Equation 5.11

$$\left|\chi^{(3)}\right| = \sqrt{(Re(\chi^{(3)}))^2 + (Im(\chi^{(3)}))^2} \tag{5.11}$$

5.2 Graphene

5.2.1 Z-Scan - Pharos Laser - 1 μm

The measurements featured in this section (Section 5.2.1) were part of a collaboration with Prof. Mnard at the University of Ottawa. For this work, I brought graphene dispersions that I prepared at Trinity College Dublin to the Advanced Research Centre (ARC) at the University of Ottawa. I used these dispersions to create thin films, which were then measured with a z-scan system I set up in the photonics laboratory.

The results discussed in this subsection are a selection of the larger dataset of measurements taken. The scans shown are the average of atleast three scans per pulse energy, to help ensure accuracy of the measurement.

5.2.1.1 Laser

The schematic for the z-scan set-up utilised in this section is shown in Figure 5.1, and a photograph in Figure 5.2.

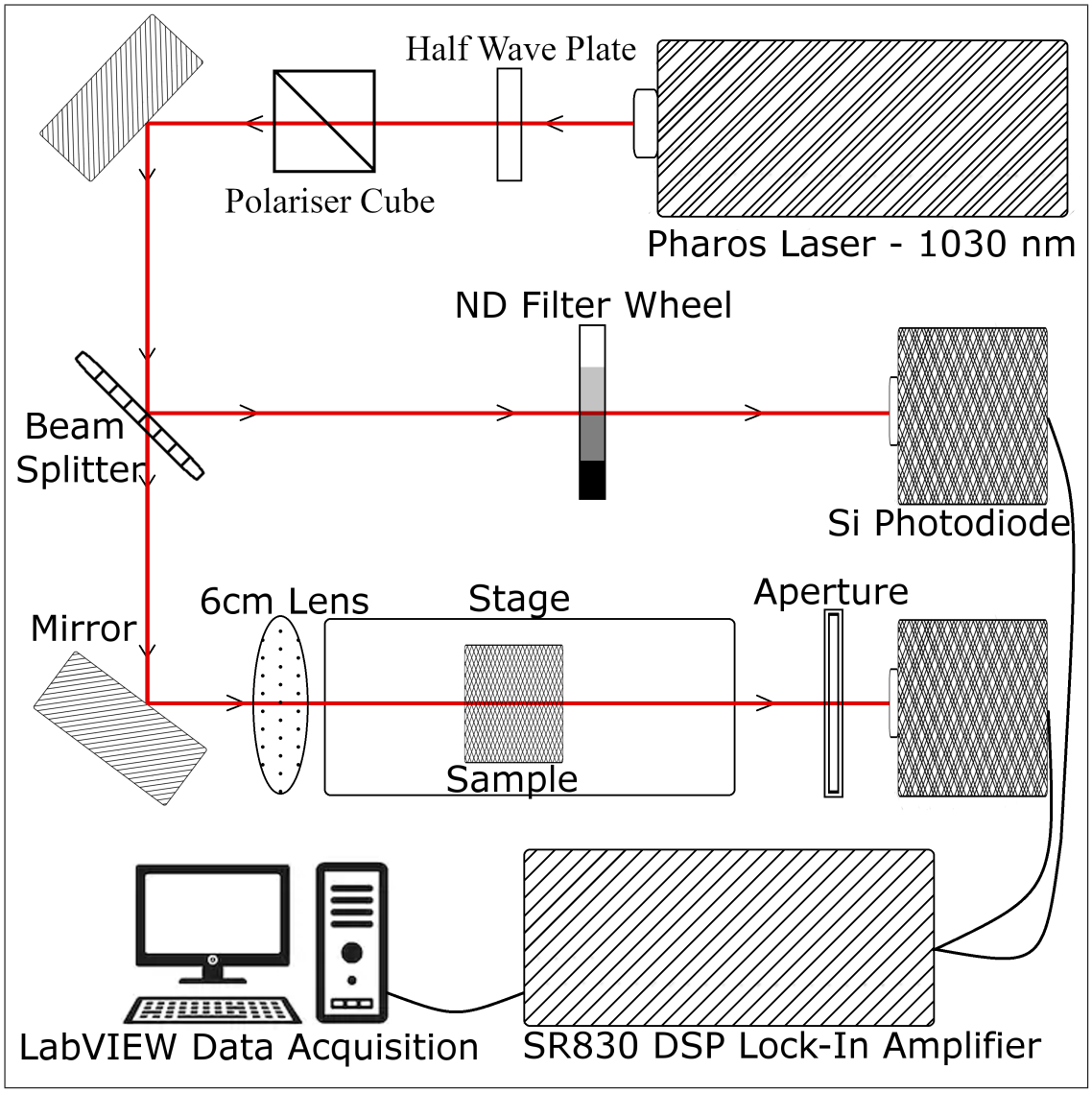

Figure 5.1: Schematic of the Z-scan setup utilising the 1030 nm, 200 fs Pharos laser

This set-up utilised a Pharos laser, a laser diode-pumped Yb medium operating at 1030 nm, 25 kHz with a 200 fs to 15 ps tunable pulse duration, with a maximum average power output of 6 W. With a 6 cm focal length Z-Scan lens and 1 mm beam diameter, we expect a beam waist of 79 μm and a Rayleigh length of 18 mm. However, through the fitting of the open aperture data, a beam waist of 8 μm and a Rayleigh length of 0.2 mm is actually obtained.

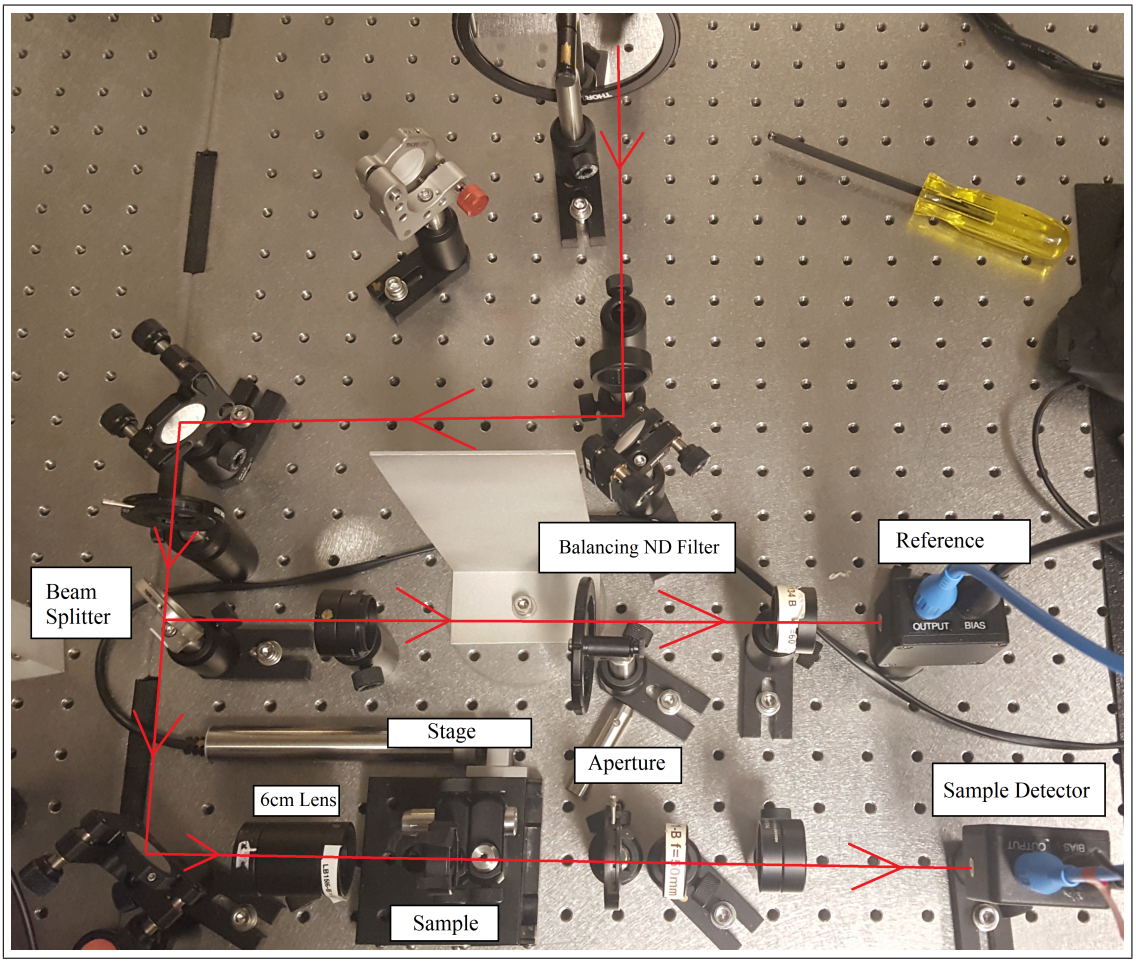

Figure 5.2: Photograph of the Z-scan setup utilising the 1030 nm, 200 fs Pharos laser

An automated half-wave plate, combined with a polarisation cube, is utilised to accurately control the average power at the Z-scan apparatus with high repeatability.

5.2.1.2 Materials

The batch of graphene/NMP dispersion utilised in this section was sonicated in a sonic bath for a week, and then followed by size-selection via iterative centrifugation. These dispersions are shown in Figure 5.3.

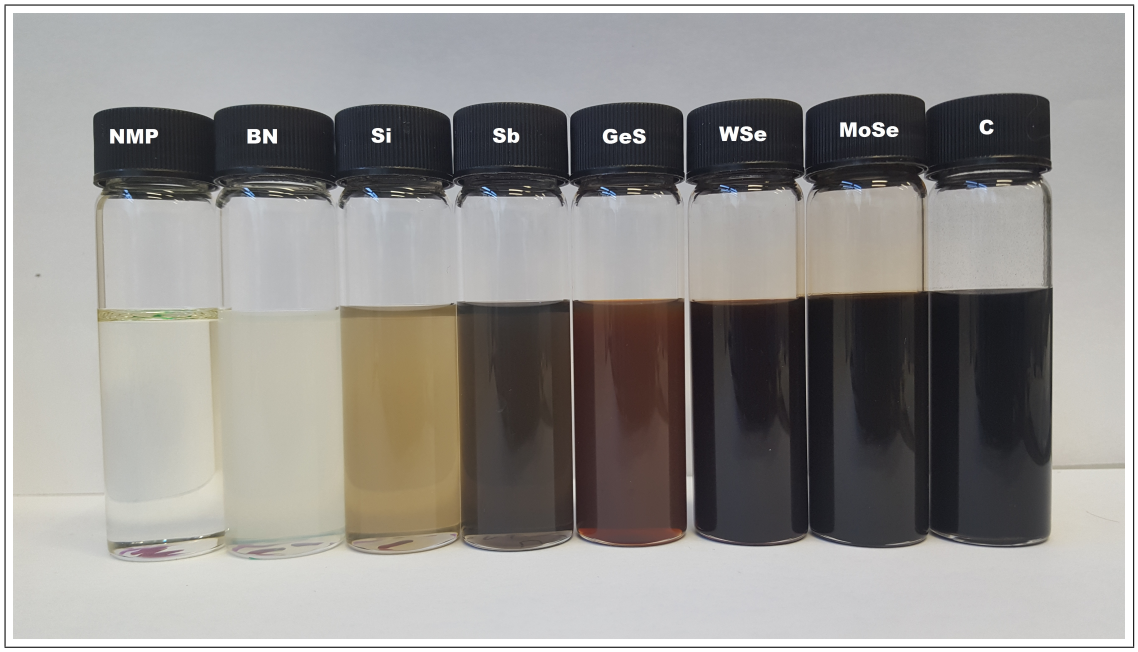

Figure 5.3: Photograph of various 2D material/NMP dispersion produced around the same time as the graphene/NMP dispersion utilised in this section.

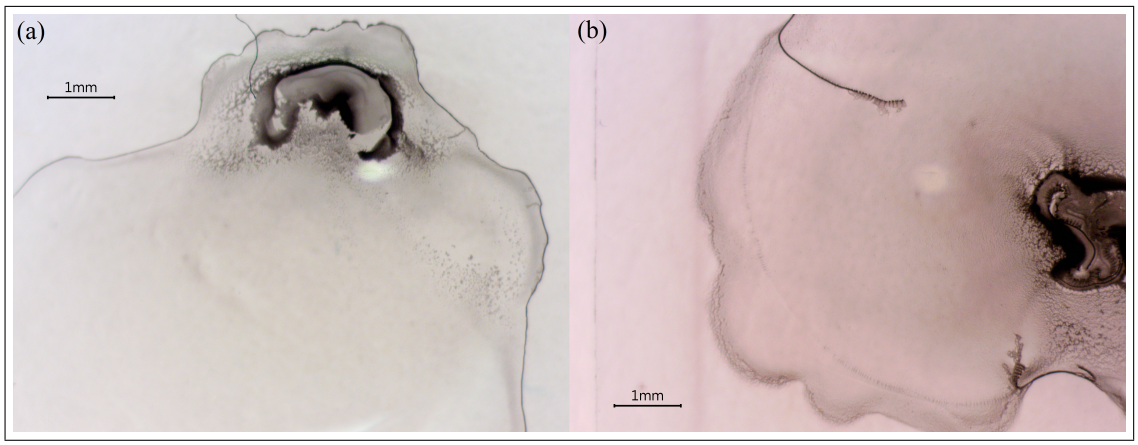

Figure 5.4: Micrograph of (a) C_{5K} and (b)C_{3K}.

As explored by the Coleman group, the graphene concentration of the dispersion can be extracted utilising the Lambert-Beer law:(Hernandez *et al.*, 2008b)

$$A = \alpha C_G l \tag{5.12}$$

Where A is the absorbance, l is the cuvette cell length, C_G is the graphene concentration and α_{660nm} is the absorption coefficient at 660 nm, which is known

to be 3,620 $mLmg^{-1}m^{-1}$.(Khan *et al.*, 2010) This yields a calculated concentration of 0.15 mg/ml and 0.05 mg/ml for $C_{3{,}000RPM}$ and $C_{5{,}000RPM}$ respectively.

Graphene thin films were prepared from these graphene/NMP dispersion via drop-casting the colloidal dispersion onto cleaned BK7 glass coverslips. These were placed in a vacuum-oven and annealed at 200 C, as shown in Figure 5.4.

To obtain accurate film thickness, the thin films were scratched with the side of a razor blade to expose a section of the BK7 substrate. These scratches through the graphene worked well, leaving clean sections of the bare substrate adjacent to the thin films. Atomic Force Microscopy (AFM) was performed to measure the thickness and roughness of the films. A sample of the CVD graphene (C_{CVD}), 3,000 RPM (C_{3K}) and 5,000 RPM graphene (C_{5K}) AFM scans are shown in Figures 5.5 and 5.6.

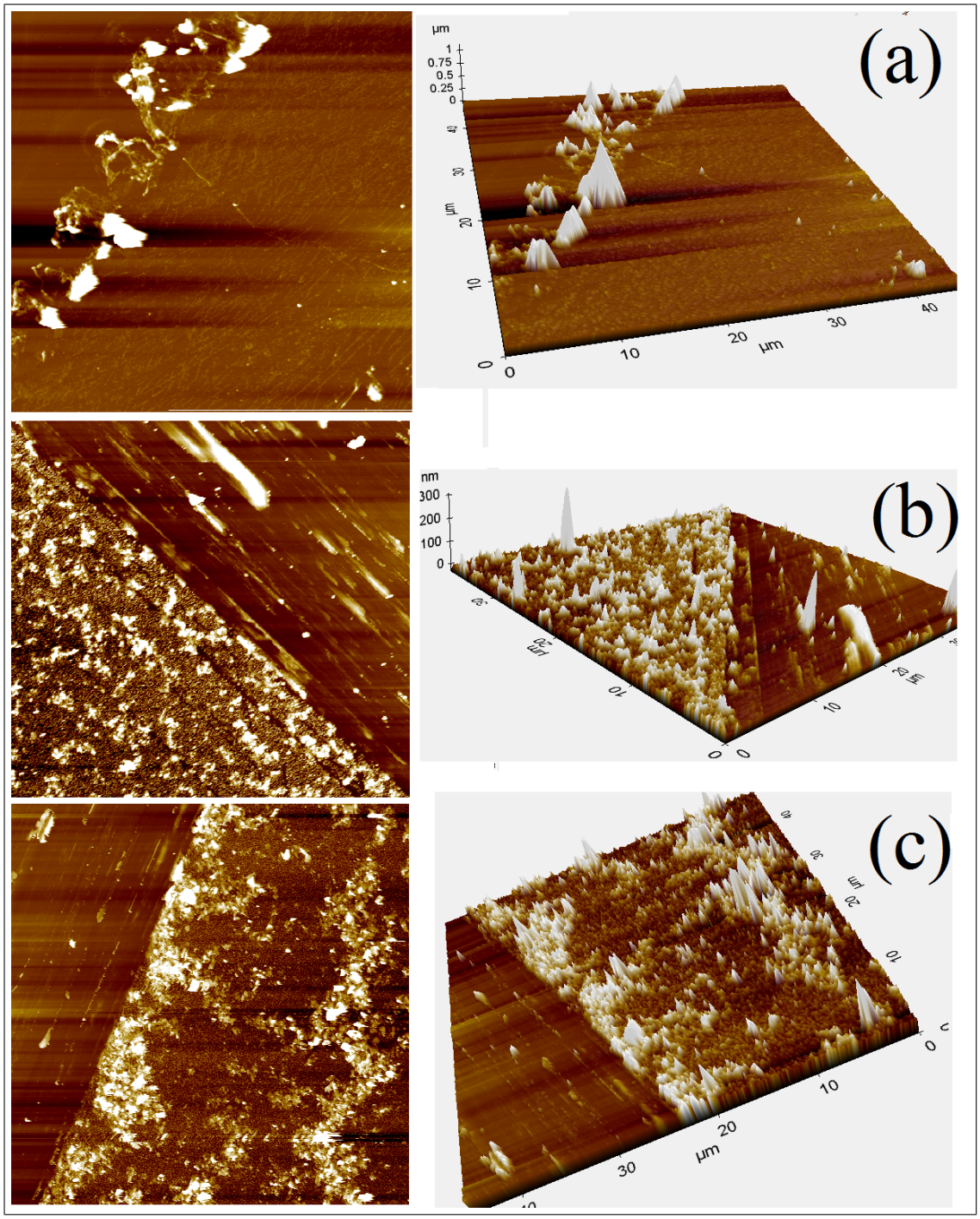

Figure 5.5: Atomic Force Microscopy scans of (a) CVD Graphene, (b) 5,000 RPM graphene and (c) 3,000 RPM graphene drop-cast thin films, showing both the thin film and the BK7 glass substrate below

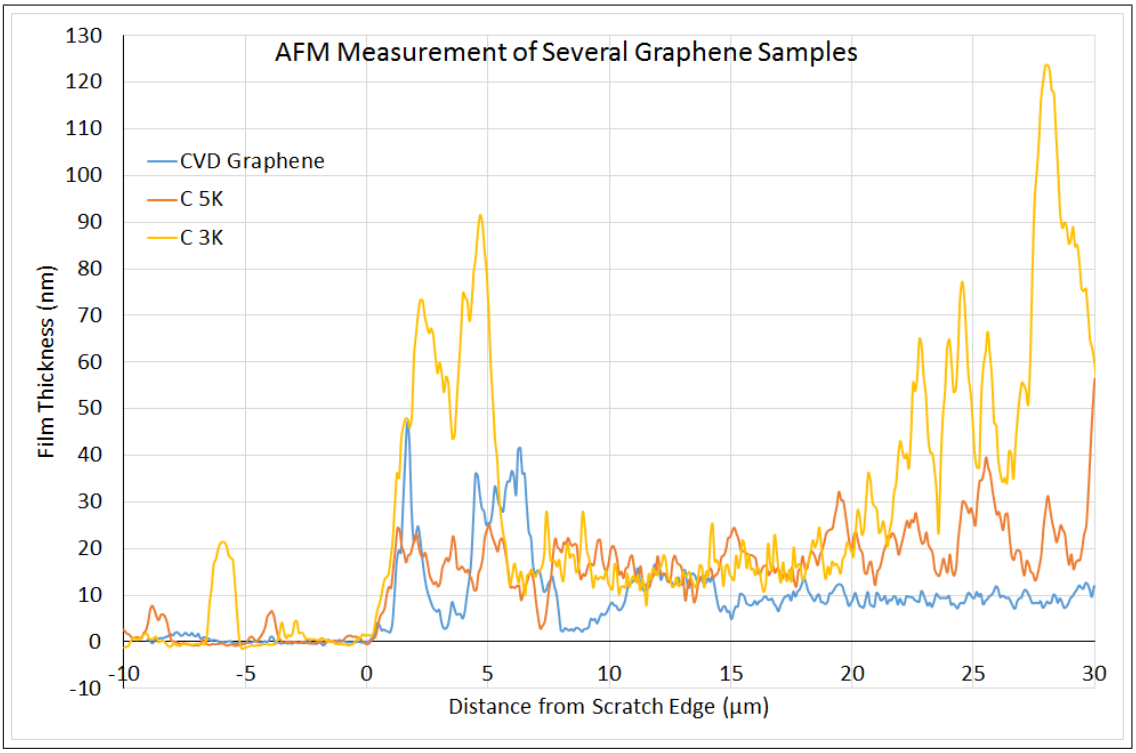

Figure 5.6: Atomic Force Microscopy line scans of CVD Graphene, 5,000 RPM graphene and 3,000 RPM graphene drop-cast thin films, showing both the thin film and the BK7 glass substrate below. The substrate was exposed via a scratch.

The graphene dispersion size-selected at 5,000 RPM produced films with a general thickness of 19 nm and a roughness (R_a and R_q) of 5 nm and 7 nm respectively, with the 3,000 RPM film with thicker sections of around 48 nm with R_a of 18.5 nm and R_q of 23 nm. Considering the difference in the dispersion concentrations, the film thicknesses are reasonable.

CVD graphene on the same substrate was produced to make a direct comparison to the drop-cast samples and a thickness of around 9.7 nm was observed. While ideally single layer graphene has a thickness of 0.335 nm, this is generally not observed in AFM scan of this size due to wrinkles in the graphene and accuracy of the measurements. Along with the nonsaturable losses and modulation depths, this implies the drop-cast thin films are likely only a few layers thick on top of each other.

5.2.1.3 Open Aperture Z-Scan

The nonlinear optical parameters (β, n_2 and $\chi^{(3)}$) of C_{CVD}, C_{5K} and C_{3K} obtained via open and closed aperture z-scan measurements for various pulse energies (and

subsequently different intensities) are summarised in Tables 5.1, 5.3/5.4 and 5.5, respectively.

The open aperture z-scan measurements of all the graphene samples exhibit clear and strong saturable absorption. The CVD graphene exhibited excellent saturable absorption tendencies, which is shown for two positions in Figures 5.8 and 5.9.

The open aperture signal for the C_{5K} varied based on the film thickness, with a max modulation depth varying from around 0.8% (as shown in Figure 5.10), 1.5% (as shown in Figure 5.11) and to 2.5% (as shown in Figure 5.12), corresponding to positions E, A and B in Figure 5.7 (b), respectively.

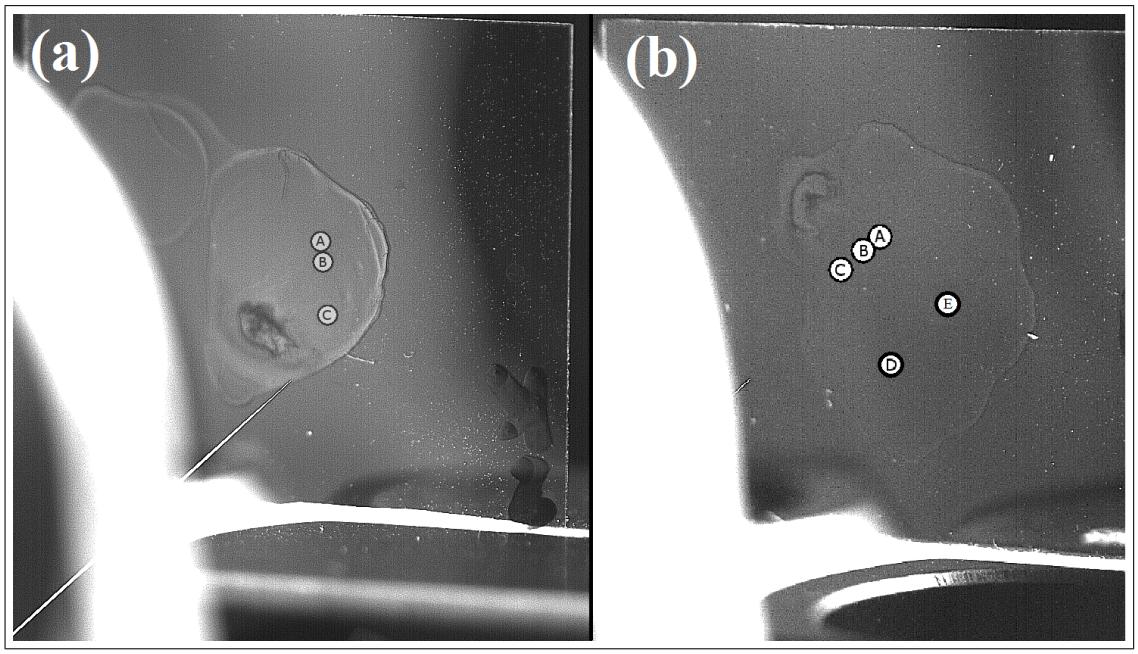

Figure 5.7: Photograph of a (a) 3,000 RPM and (b) 5,000 RPM graphene film with the examined positions overlaid.

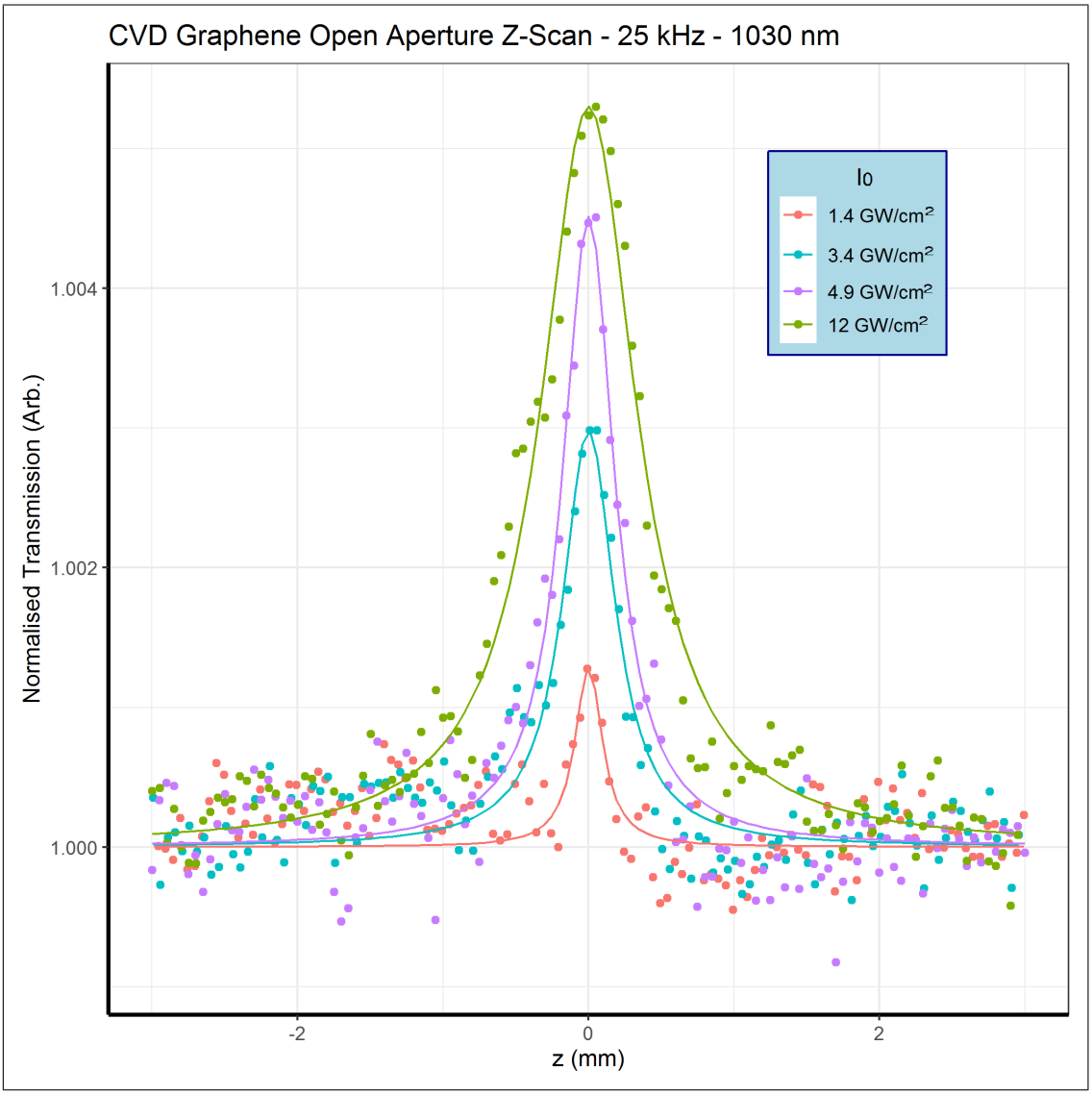

Figure 5.8: Open Aperture Z-Scan measurements of C_{CVD} various intensities at 25 kHz, 1030 nm. First position.

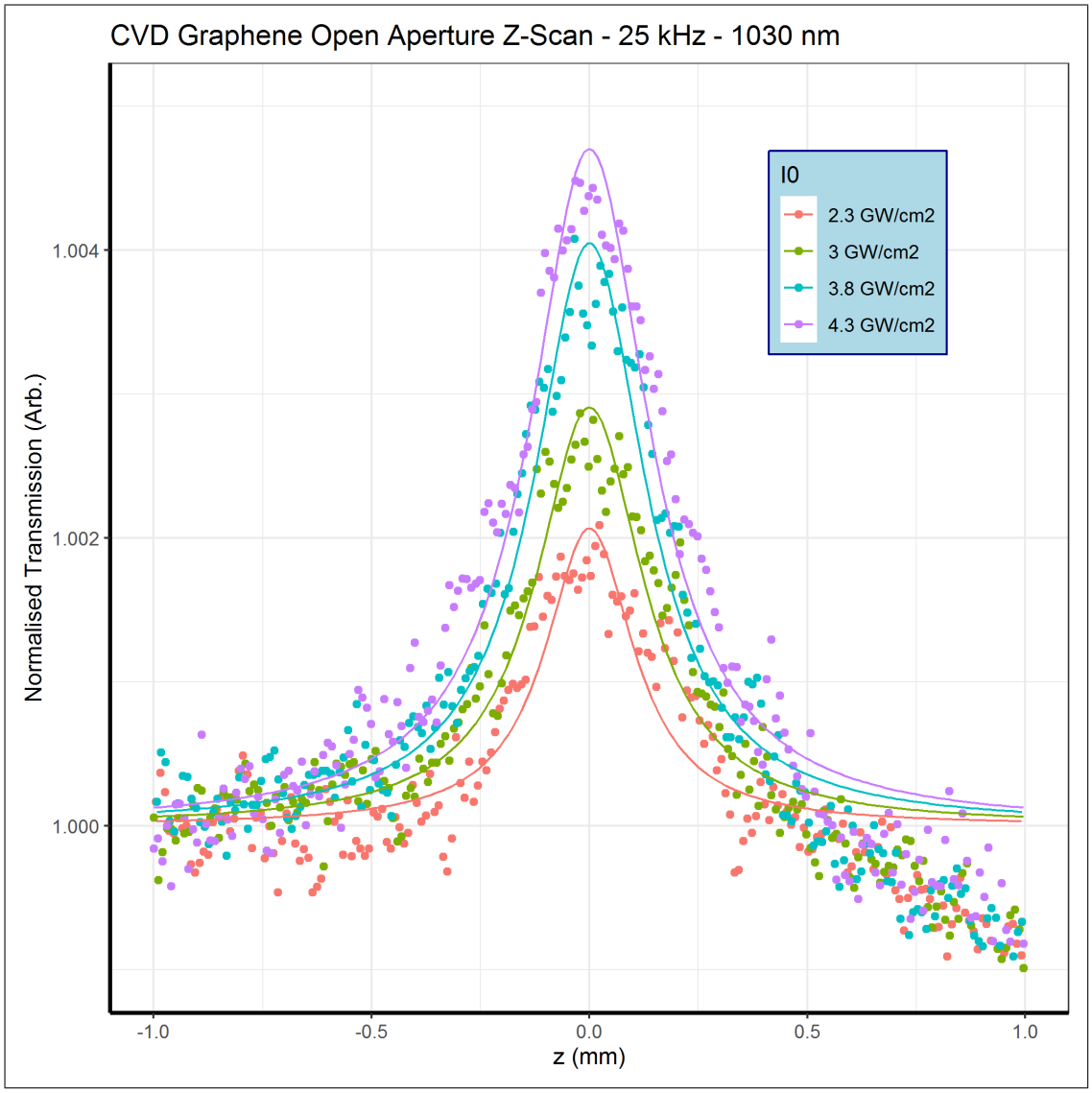

Figure 5.9: Open Aperture Z-Scan measurements of C_{CVD} various intensities at 25 kHz, 1030 nm. Second Position.

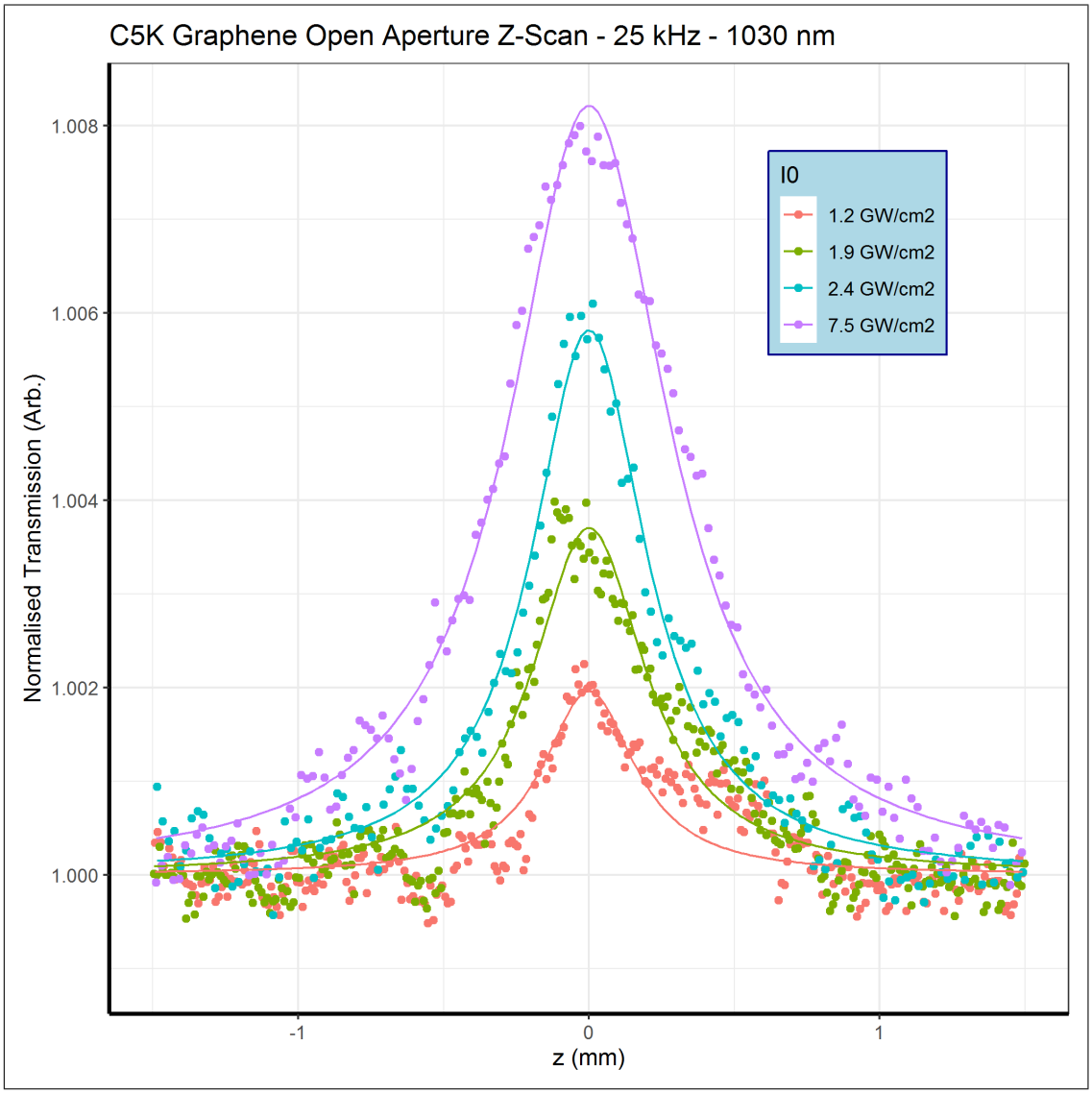

Figure 5.10: Open Aperture Z-Scan measurements of C_{5K} for a various intensities at 25 kHz, 1030 nm, reaching a max modulation depth of around 0.8%. This corresponding to position E in Figure 5.7 (b)

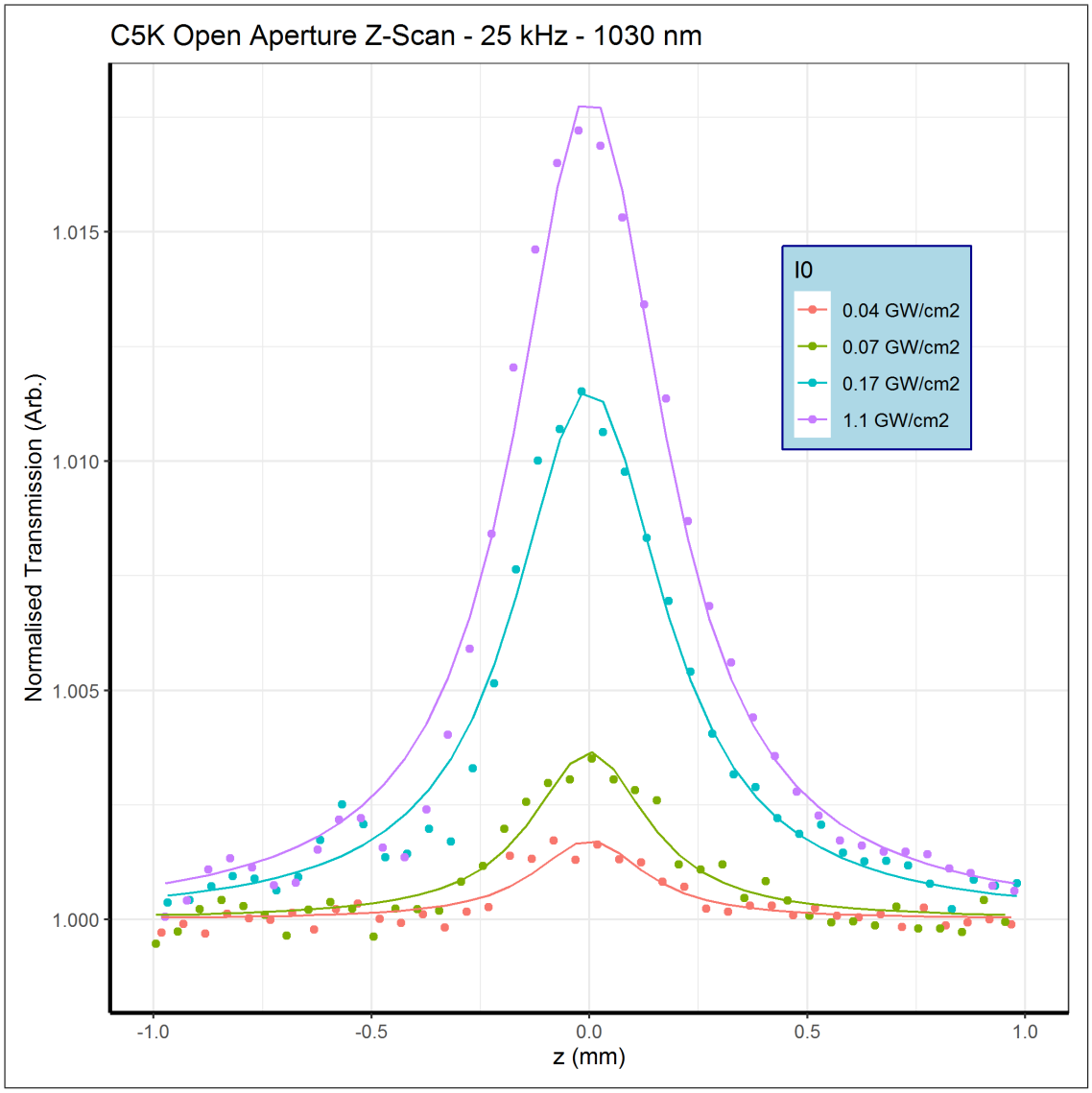

Figure 5.11: Open Aperture Z-Scan measurements of C_{5K} for a various intensities at 25 kHz, 1030 nm, reaching a max modulation depth of around 1.5%. This corresponding to position A in Figure 5.7 (b)

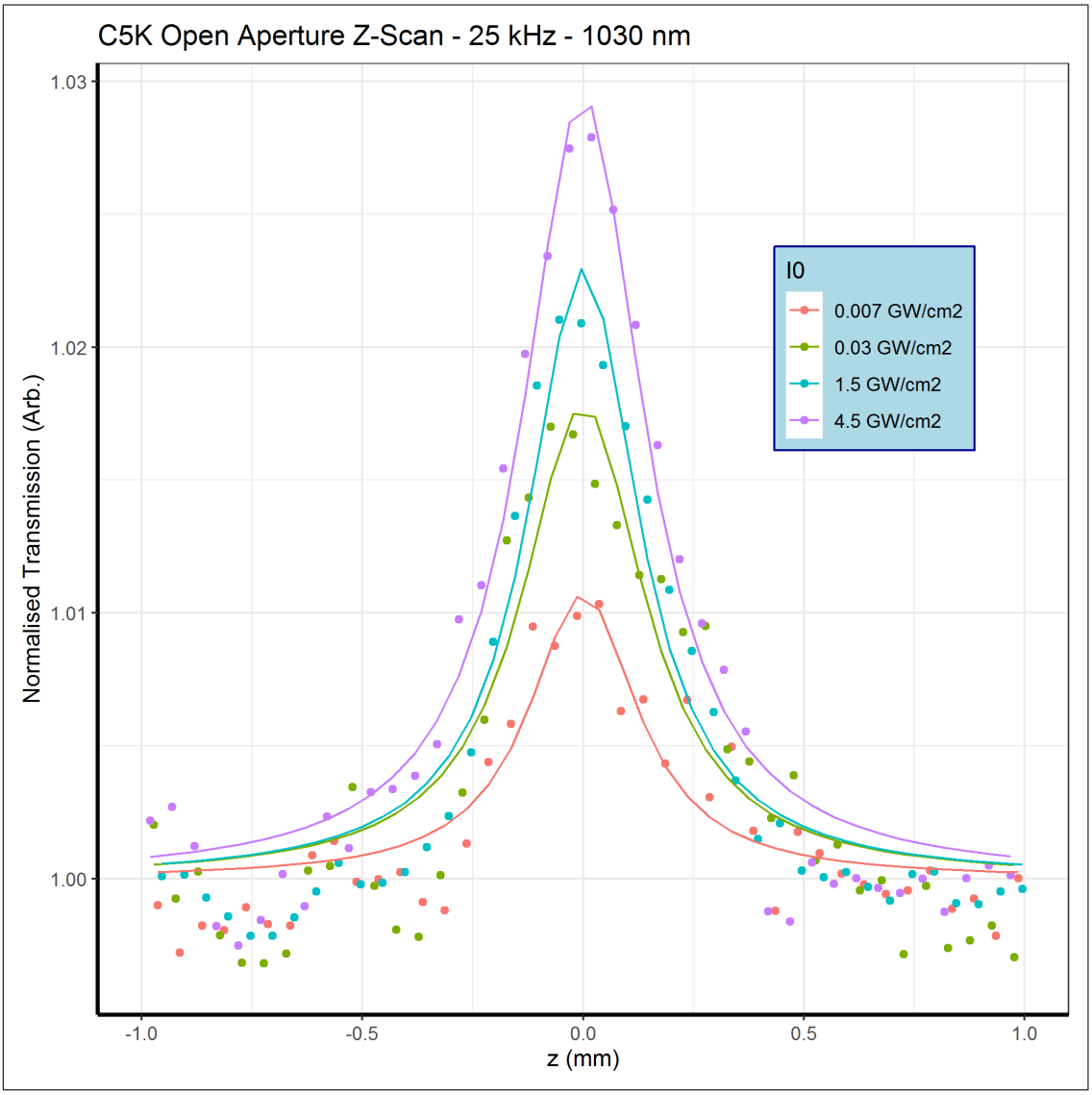

Figure 5.12: Open Aperture Z-Scan measurements of C_{5K} for a various intensities at 25 kHz, 1030 nm, reaching a max modulation depth of around 2.5%. This corresponding to position B in Figure 5.7 (b)

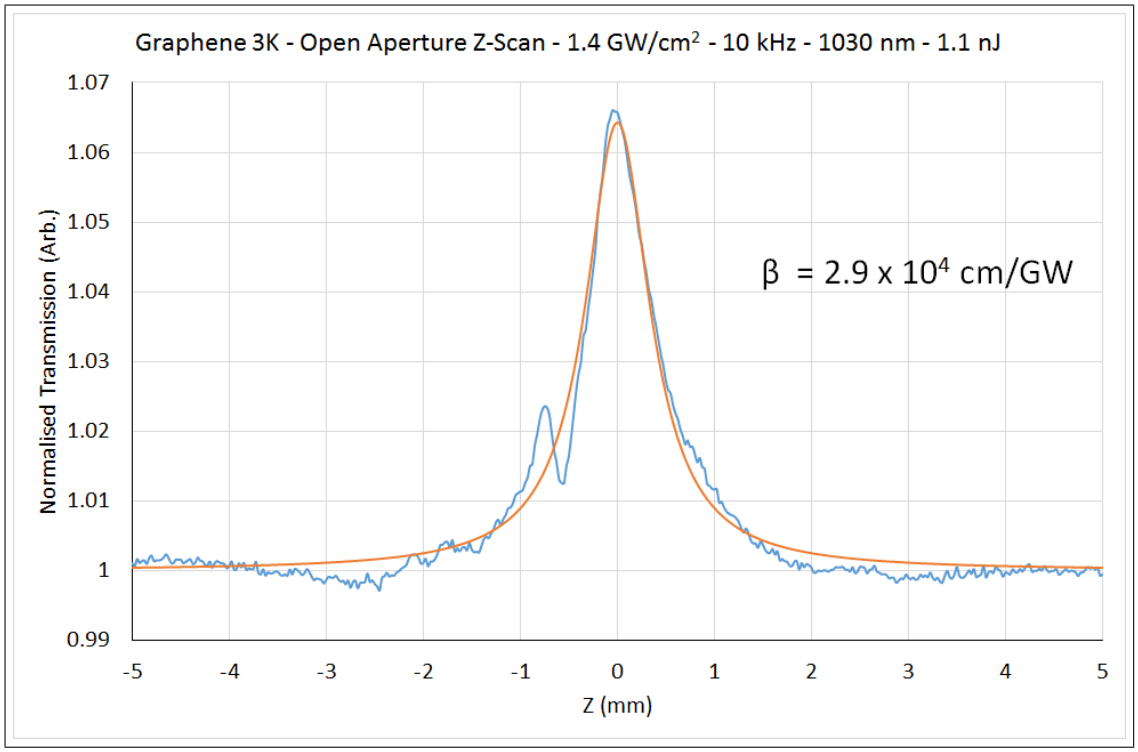

Figure 5.13: Open Aperture Z-Scan measurements of the C_{3K} thin-film for 1.4 GW/cm^2 (1 nJ) at 10 kHz, 1030 nm, displaying a β of 2.9 $\times$ 10^4 cm/GW, which agrees well with literature values. This is position A on (a) in Figure 5.7.

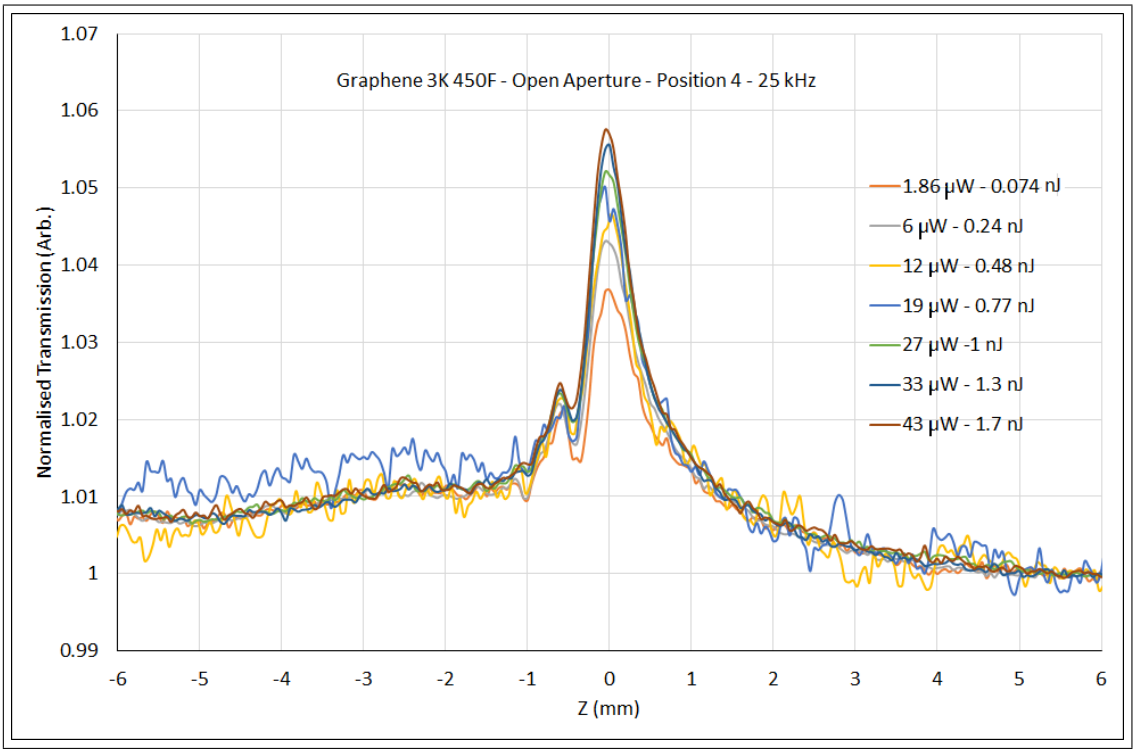

Figure 5.14: Open Aperture Z-Scan measurements of the C_{3K} thin-film for a various intensities at 25 kHz, 1030 nm. This is position C on (a) in Figure 5.7.

The C_{3K} thin film was thicker than the C_{5K} samples, with a thickness of around 48.7 nm, and an R_a roughness of 18 nm. As shown with both the C_{CVD}, C_{5K} and C_{3K} samples, there is a trend to larger max modulation depth with increasing film thickness. The modulation depth reaches around 5% for the C_{3K} thin film before the material saturates, as shown in Figures 5.13 and 5.14. As shown in Figure 5.14, the β of 2.9 $x10^4 cm/GW$ agrees well with literature values (Demetriou *et al.*, 2016).

The max modulation depth against peak pulse power for a selection of positions on C_{CVD}, C_{3K} and C_{5K} are presented in Figure 5.15. As discussed previously, each graphene sample exhibited a strong saturable absorption effect. The max modulation depth begins as a linear relationship with peak pulse energy (which is proportional to intensity) at lower energies. The slope of which increases with the number of graphene layers (or film thickness).

The max modulation depth saturates for each sample, and the modulation depth plateaus. For single-layer, CVD graphene, the max modulation depth plateaus around 0.5%, and increases with film thickness, up to a maximum of around 5% in the measurements for C_{3K} at a thickness of around 50 nm. As shown for C_{CVD} and C_{5K}, there is a linear portion at lower pulse energies (which corresponds

to lower peak intensities) and the slope of which increases with film thickness. This increased slope also causes the saturation to begin at lower pulse energies as the thickness increases. Finally, the max modulation depth achievable scales with film thickness.

The open aperture scan of C_{CVD} at 1.3 nJ ($I_0 = 3.8GW/cm^2$) revealed a nonlinear refractive index,β, of $-3900cm/GW$, as shown in Figure 5.8. This agrees relatively well with published results of around $-10^4cm/GW$. The nonlinear optical properties of CVD graphene for various intensities is summarised in Table 5.1. There is a consistency in these measurements, which remain around $-3000cm/GW$ for β with a $Re(\chi^{(3)})$ of $2.8x10^{-8}esu$ and a $\chi^{(3)}$ of $2.9x10^{-8}esu$.

The open aperture scan of C_{5K} at 1.5 nJ ($I_0 = 4.5GW/cm^2$) revealed a nonlinear absorption coefficient,β, of $-9,800cm/GW$, as shown in Figure 5.12. Similarly to the CVD Graphene, this agrees well with published results of around $-10,000cm/GW$. The nonlinear optical properties of C_{5K} for various intensities is summarised in Tables 5.4, 5.3 and 5.2.

The open aperture scans of C_{5K} at Position E for a range of intensities exhibited a nonlinear absorption coefficient,β, around $-3,000cm/GW$, as shown in Figure 5.10 and summarised in Table 5.2. This consistent value for β agrees well with the values extracted from the C_{CVD} sample, summarised in Table 5.1. The modulation depth of this sample matches double that of the C_{CVD}, as shown in Figure 5.15. Along with the AFM thickness of the C_{5K} being close to twice that of the C_{CVD} (Figure 5.6), Position E appears to be effectively bi-layer graphene. The other positions for C_{5K} may have had aggregates within the measured area, effectively increasing the thickness of the material. As such, as the other positions also use 19.3 nm as the film thickness, the reported β values may be higher than expected. If the aggregate thickness could be incorporated, those β values would likely agree more closely with the C_{CVD} sample.

The open aperture scan of C_{3K} at 1.1 nJ ($I_0 = 1.4GW/cm^2$) revealed a nonlinear refractive index,β, of $-2,900cm/GW$, as shown in Figure 5.14. This agrees well with the previous C_{5K} and C_{CVD} measurements. The nonlinear optical properties of C_{3K} for various intensities is summarised in Table 5.5.

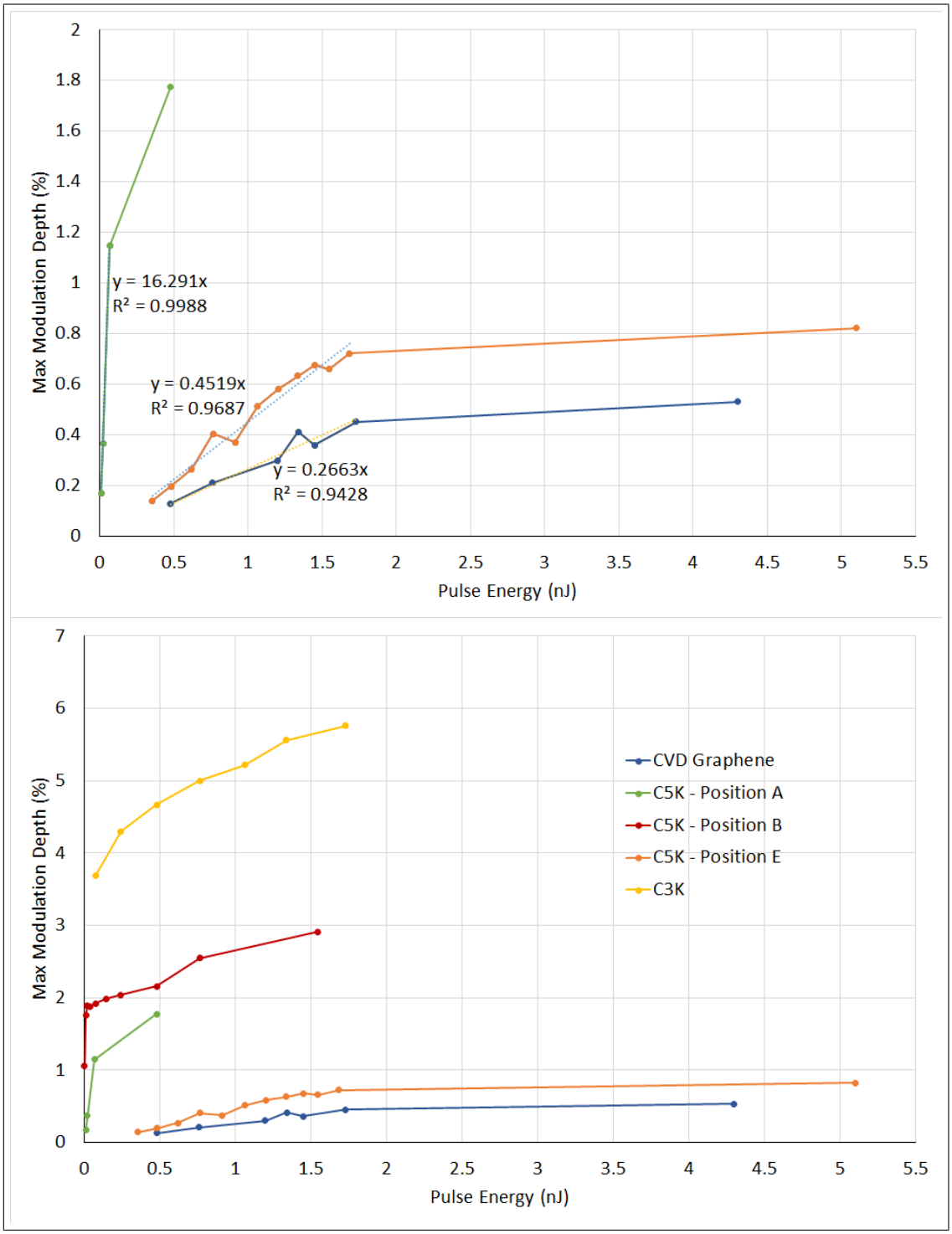

Figure 5.15: Max modulation vs Pulse Energy of C_{CVD}, C_{3K} and C_{5K} for a various intensities at 25 kHz, 1030 nm

Table 5.1: Nonlinear optical properties of CVD Graphene of 9.7 nm thickness from various z-scan experiments at different pulse energies at 200fs, 25 kHz, 1030 nm.

Pulse Energy (nJ)	I_0 (GW/cm^2)	Modulation Depth (%)	β ($X10^3$ cm/GW)	$Im(\chi^{(3)})$ ($-X10^{-8}$ esu)	n_2 ($-cm^2/GW$)	$Re(\chi^{(3)})$ ($X10^{-8}$ esu)	$\chi^{(3)}$ ($X10^{-8}$ esu)	ΔT_{pv} (%)
0.48	1.2	0.13	1.9	0.28	-	-	-	-
0.61	1.6	0.27	4.9	0.7	-	-	-	-
0.76	1.7	0.21	3	0.46	-	-	-	-
1.2	2.7	0.3	3.3	0.5	0.13	2.5	2.5	0.27
1.34	3.1	0.41	3.9	0.59	0.15	2.8	2.9	0.32
1.45	3.7	0.36	2.9	0.43	0.15	2.8	2.8	0.36
1.7	3.9	0.45	3.4	0.52	0.11	2.1	2.1	0.5
4.3	5.2	0.53	3	0.46	0.031	0.57	0.73	0.5

Table 5.2: Nonlinear optical properties of C_{5K} Graphene of 19.3 nm thickness from various z-scan experiments at different pulse energies at 200fs, 25 kHz, 1030 nm. Measured at Position E in Figure 5.7 (b).

Pulse Energy (nJ)	I_0 (GW/cm^2)	Modulation Depth (%)	β ($X10^3$ cm/GW)	$Im(\chi^{(3)})$ ($-X10^{-8}$ esu)	n_2 ($-cm^2/GW$)	$Re(\chi^{(3)})$ ($X10^{-8}$ esu)	$\chi^{(3)}$ ($X10^{-8}$ esu)	ΔT_{pv} (%)
0.36	1.1	0.14	1.9	0.29	-	-	-	-
0.48	1.2	0.2	2.4	0.37	-	-	-	-
0.62	1.5	0.27	2.7	0.41	-	-	-	-
0.77	1.8	0.4	3.2	0.48	-	-	-	-
0.9	1.93	0.37	2.9	0.45	-	-	-	-
1.1	2.6	0.51	3	0.455	-	-	-	-
1.2	2.4	0.58	3.6	0.54	-	-	-	-
1.3	3.2	0.63	3	0.455	-	-	-	-
1.45	3.2	0.68	3.1	0.46	-	-	-	-
1.5	3.3	0.66	3.1	0.46	-	-	-	-
1.7	4	0.72	2.7	0.4	-	-	-	-
5.1	7.5	0.82	1.7	0.25	0.02	0.4	0.48	0.78

Table 5.3: Nonlinear optical properties of C_{5K} Graphene of 19.3 nm thickness from various z-scan experiments at different pulse energies at 200fs, 25 kHz, 1030 nm. Measured at Position A in Figure 5.7 (b).

Pulse Energy (nJ)	I_0 (GW/cm^2)	Modulation Depth (%)	β ($X10^3$ cm/GW)	$Im(\chi^{(3)})$ ($-X10^{-8}$ esu)	n_2 ($-cm^2/GW$)	$Re(\chi^{(3)})$ ($X10^{-8}$ esu)	$\chi^{(3)}$ ($X10^{-8}$ esu)	ΔT_{pv} (%)
0.012	0.04	0.17	68	10	-	-	-	-
0.023	0.07	0.36	80	12	4.9	91	92	3.9
0.07	0.17	1.15	100	15	4.1	77	78	3.3
0.48	1.12	1.78	24	360	0.77	14	15	4

Table 5.4: Nonlinear optical properties of C_{5K} Graphene of 19.3 nm thickness from various z-scan experiments at different pulse energies at 200fs, 25 kHz, 1030 nm. Measured at Position B in Figure 5.7 (b).

Pulse Energy (nJ)	I_0 (GW/cm^2)	Modulation Depth (%)	β ($X10^3$ cm/GW)	$Im(\chi^{(3)})$ ($-X10^{-8}$ esu)	n_2 ($-cm^2/GW$)	$Re(\chi^{(3)})$ ($X10^{-8}$ esu)	$\chi^{(3)}$ ($X10^{-8}$ esu)	ΔT_{pv} (%)
0.002	0.007	1.06	2200	340	-	-	-	-
0.01	0.03	1.75	790	120	54	990	1000	5.5
0.02	0.07	1.89	420	60	-	-	-	-
0.037	0.086	1.87	365	55	-	-	-	-
0.07	0.17	1.92	185	28	-	-	-	-
0.15	0.35	1.98	93	14	-	-	-	-
0.24	0.57	2.03	59	8.8	1.75	32	34	3.16
0.48	1.2	2.16	30	4.6	0.46	8.6	9.7	2.5
0.77	2.1	2.5	18	2.7	0.49	9	9.48	2.8
1.5	4.5	2.9	9.8	1.5	0.28	5	5	3.2

Table 5.5: Nonlinear optical properties of C_{3K} Graphene of 48.7 nm thickness from various z-scan experiments at different pulse energies at 200fs, 1030 nm.

Pulse Energy (nJ)	Rep Rate (kHz)	I_0 (GW/cm^2)	Modulation Depth (%)	β ($X10^3$ cm/GW)	$Im(\chi^{(3)})$ ($-X10^{-8}$ esu)	n_2 ($-cm^2/GW$)	$Re(\chi^{(3)})$ ($X10^{-8}$ esu)	$\chi^{(3)}$ ($X10^{-8}$ esu)
1.1	10	1.4	6.4	29	4.4	-	-	-
1.7	25	2	6	17.9	2.7	0.28	5.2	5.9

Table 5.6: Nonlinear optical properties of C_{CVD}, C_{5K} and C_{3K} from various z-scan experiments at different pulse energies at 200fs, 1030 nm.

Sample	Pulse Energy (nJ)	I_0 (GW/cm^2)	Modulation Depth (%)	β ($X10^3$ cm/GW)	$Im(\chi^{(3)})$ ($-X10^{-8}$ esu)	n_2 ($-cm^2/GW$)	$Re(\chi^{(3)})$ ($X10^{-8}$ esu)	$\chi^{(3)}$ ($X10^{-8}$ esu)
C_{CVD}	1.7	3.9	0.45	3.4	0.52	0.11	2.1	2.1
$C_{5K(A)}$	0.48	1.12	1.78	24	360	0.77	14	15
$C_{5K(B)}$	1.5	4.5	2.9	9.8	1.5	0.28	5	5
$C_{5K(E)}$	1.45	3.2	0.68	3.1	0.46	-	-	-
C_{3K}	1.7	2	6	17.9	2.7	0.28	5.2	5.9

5.2.1.4 Closed Aperture Z-Scan

The closed aperture scans can be divided by the open aperture scans at the same power to reveal the kerr nonlinearity of a material, also known as the nonlinear refractive index, n_2. For these closed aperture scans, the aperture was closed until the baseline signal was set to be 20% (S = 0.2) of the open aperture baseline signal.

The closed aperture scan of C_{CVD} at 1.3 nJ ($I_0 = 3.8GW/cm^2$) revealed a nonlinear refractive index, n_2, of -0.15 cm^2/GW, as shown in Figure 5.16. This agrees well with published results of around $-1.1cm^2/GW$ (Dremetsika *et al.*, 2016). Graphene exhibits an enormous n_2, compared to around $10^{-5}GW/cm^2$ for glass.

The closed aperture scan of C_{5K} at 1.5 nJ ($I_0 = 4.5$ GW/cm^2) revealed a nonlinear refractive index, n_2, of -0.28 cm^2/GW, as shown in Figure 5.17. Similarly to the CVD Graphene, this agrees well with published results of around -1.1 GW/cm^2.

The closed aperture scan of C_{3K} at 1.1 nJ ($I_0 = 1.4GW/cm^2$) revealed a nonlinear refractive index, n_2, of -0.28 cm^2/GW, as shown in Figure 5.18. This agrees well with the previous C_{5K} and C_{CVD} measurements.

The signal for closed aperture scans is somewhat noisy, which is expected for closed aperture scans at such relatively low pulse energies. The signal is fairly small, which is already hidden within an output containing the open aperture signal, and so can be difficult to extract from the noise. There may also be other sources of noise introduced, such as film inhomogeneity or unevenness in the stage.

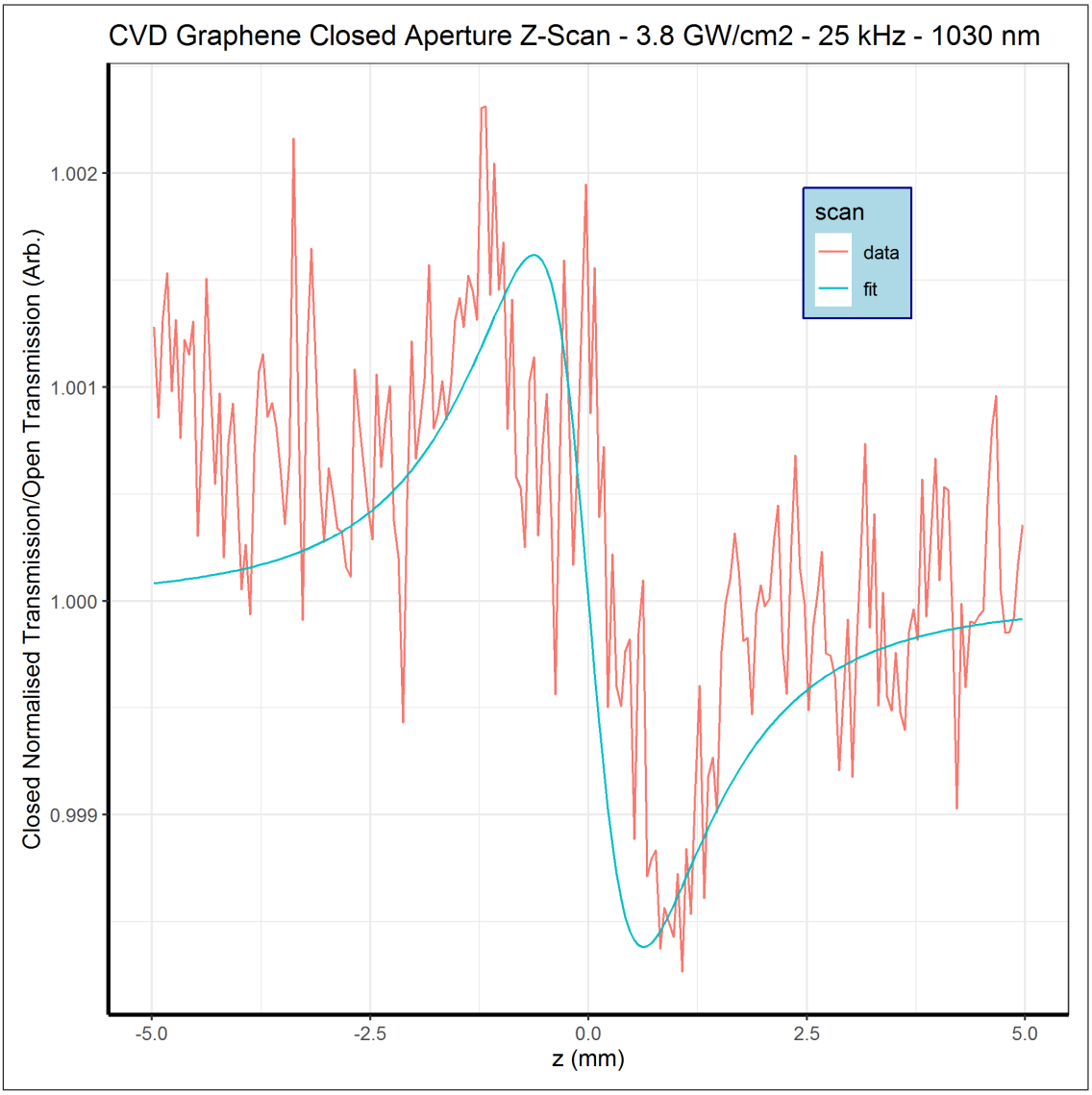

Figure 5.16: Closed Aperture scan for C_{CVD} at 1.3 nJ ($I_0 = 3.8\ GW/cm^2$) at 1030 nm and 25 kHz. A large n_2 value of $-0.15\ cm^2/GW$ is exhibited.

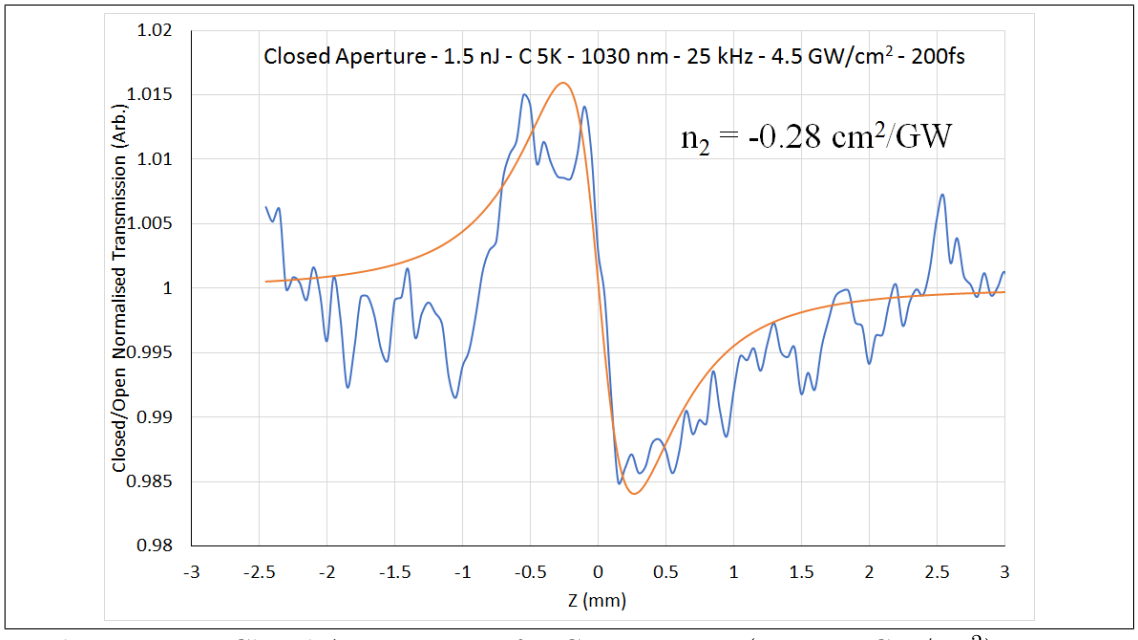

Figure 5.17: Closed Aperture scan for C_{5K} at 1.5 nJ ($I_0 = 4.5\ GW/cm^2$) at 1030 nm and 25 kHz. A large n_2 value of $-0.28\ cm^2/GW$ is exhibited.

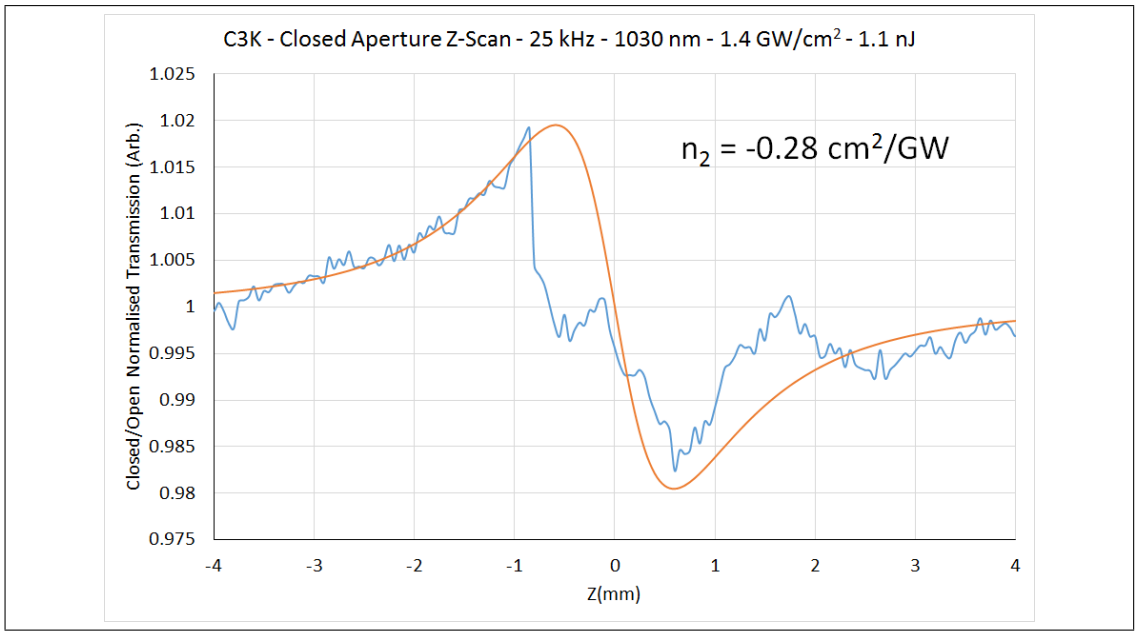

Figure 5.18: Closed Aperture scan for C_{3K} at 1.1 nJ ($I_0 = 1.4\ GW/cm^2$) at 1030 nm and 25 kHz. A large n_2 value of $-0.28\ cm^2/GW$ is exhibited.

5.2.1.5 Pulse Duration Comparison

Open and closed aperture Z-Scan measurements of $C_{5{,}000RPM}$ were taken for several pulse durations, ranging from 200 fs to 15 ps, at 25 kHz, 1030 nm and 1.5 nJ peak pulse energy, as shown in Figure 5.19.

The max modulation depth of the sample varied with pulse duration, as shown in Figure 5.21. The modulation depth increases with decreasing pulse duration, with a sharp increase below 1 ps. This may be due to the pulse duration decreasing below the short (τ_1) excited carrier relaxation times at 1.190 ps (Dong *et al.*, 2016a) for graphene thin-films prepared via LPE.

Similar to 200 fs, the 300fs closed aperture scans showed strong kerr nonlinearity, with an n_2 of 0.15 cm^2/GW, as show in Figure 5.20.

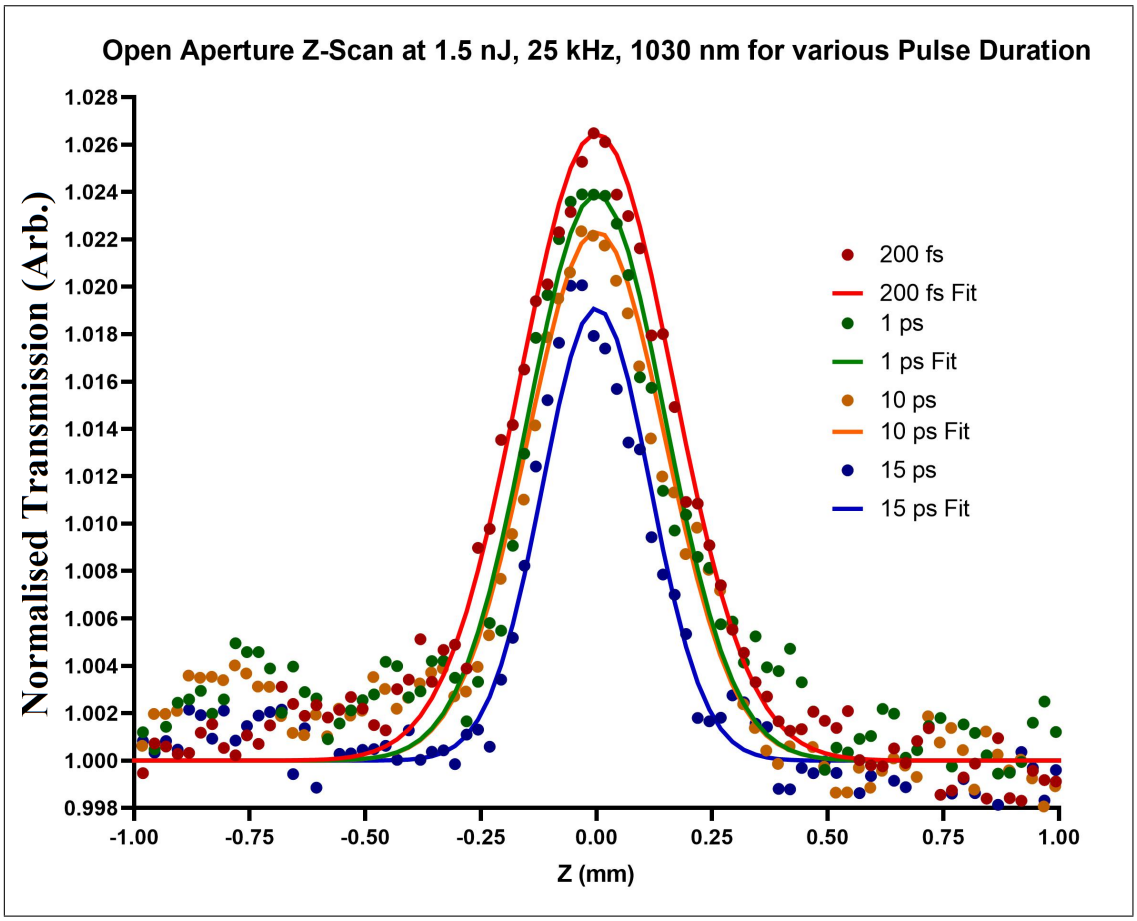

Figure 5.19: Open Aperture Z-Scan measurements of C_{5K} for a various pulse durations at 25 kHz, 1030 nm and 1.5 nJ peak pulse energy

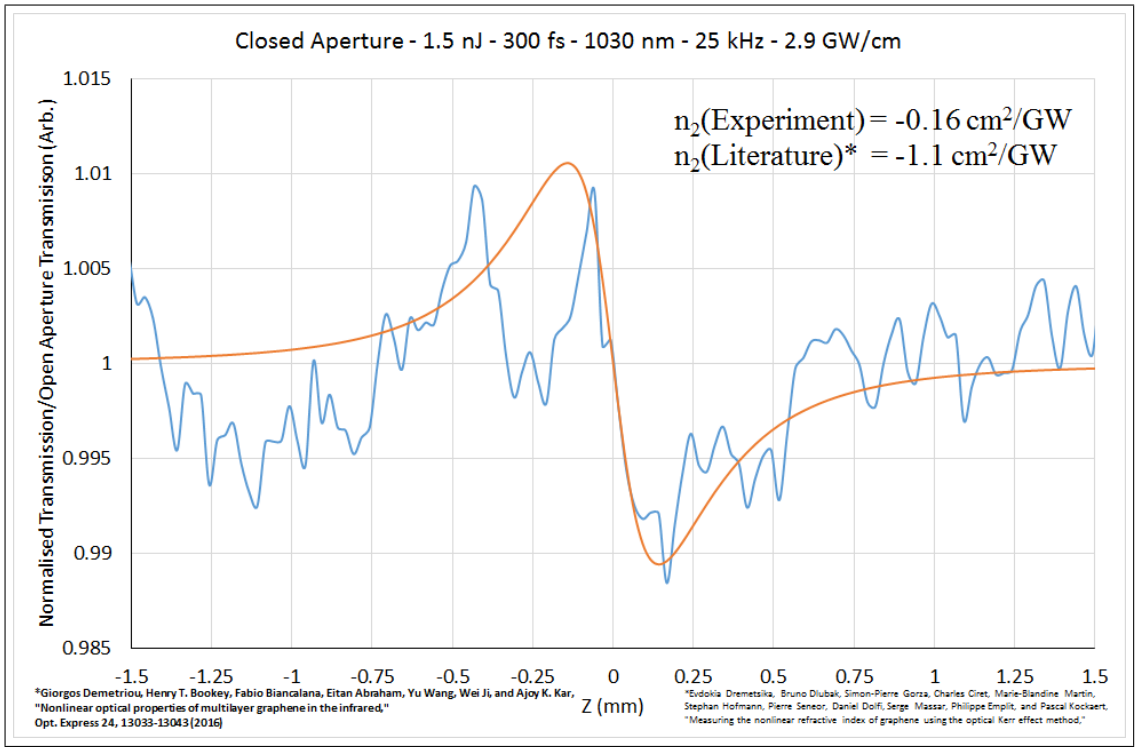

Figure 5.20: Closed Aperture Z-Scan measurements of C_{5K} for at 300 fs at 25 kHz, 1030 nm and 1.5 nJ peak pulse energy (3 GW/cm^2) with an n_2 of -0.15 cm^2/GW

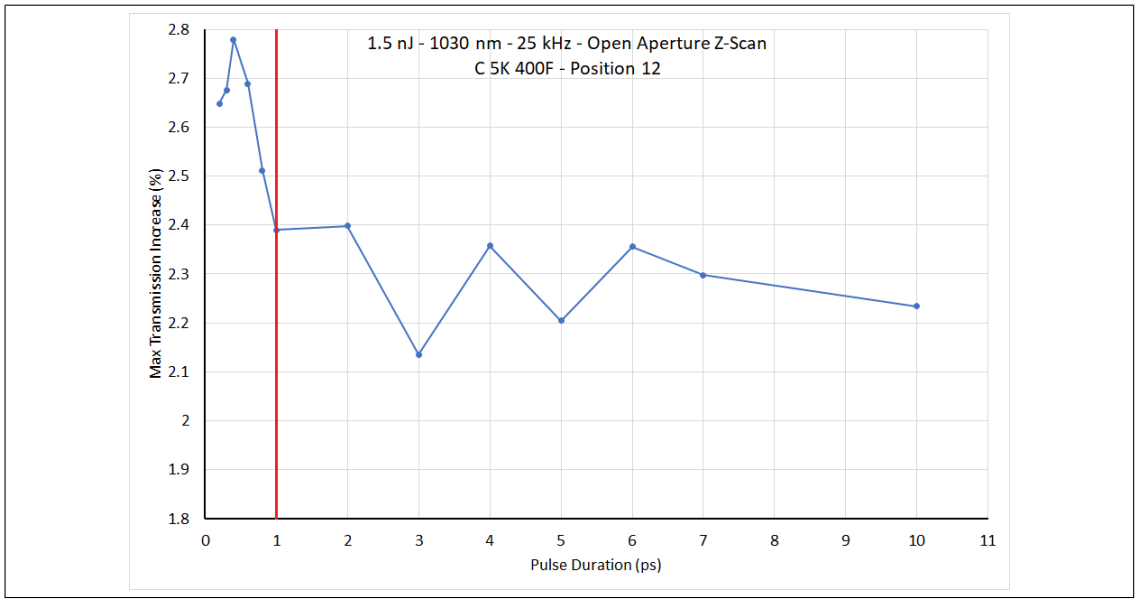

Figure 5.21: Max modulation of C_{5K} for a various pulse durations at 25 kHz, 1030 nm and 1.5 nJ peak pulse energy

Table 5.7: Nonlinear optical properties of CVD Graphene of 9.7 nm thickness from various z-scan experiments at different pulse durations at 1.5 nJ, 25 kHz, 1030 nm.

Pulse Duration (fs)	I_0 (GW/cm^2)	Modulation Depth (%)	β ($X10^3$ cm/GW)	$Im(\chi^{(3)})$ ($-X10^{-8}$ esu)	n_2 ($-cm^2/GW$)	$Re(\chi^{(3)})$ ($X10^{-8}$ esu)	$\chi^{(3)}$ ($X10^{-8}$ esu)	ΔT_{pv} (%)
200	4.5	2.73	9.2	1.39	0.072	1.3	1.9	1.27
300	2.9	2.7	14	2.13	0.15	2.8	3.5	0.32
400	2.2	2.79	19	2.87	-	-	-	-
600	1.5	2.64	26.9	4.07	-	-	-	-
800	1.15	2.58	34.2	5.16	-	-	-	-
1000	0.98	2.53	39.20	5.93	-	-	-	-
2000	0.5	2.44	73.1	11	-	-	-	-
3000	0.3	2.18	110	16	-	-	-	-
4000	0.26	2.45	141	21.3	-	-	-	-
5000	0.21	2.26	164	25	-	-	-	-
6000	0.15	2.32	242	36	-	-	-	-
7000	0.13	2.2	266	40	3.5	65	77	1.73
10000	0.099	2.32	356	54	-	-	-	-
15000	0.095	2.11	342	52	0.74	14	54	2.06

5.2.1.6 Damage Threshold Measurements

Z-scan measurements were taken at higher peak pulse powers to test the damage threshold of the graphene films, as shown in Figure 5.22. These measurements were taken at 30 kHz, 1030 nm.

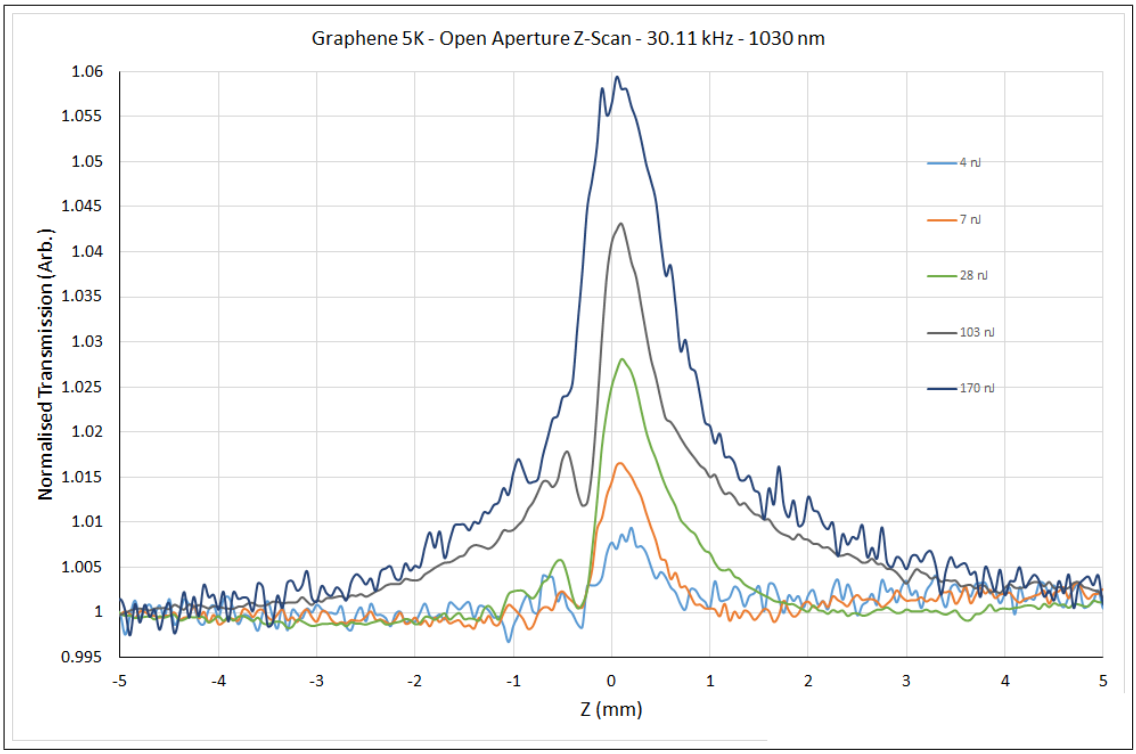

Figure 5.22: High peak pulse power (or high intensity) open aperture z-scan measurements of $C_{5{,}000RPM}$ at 30 kHz, 1030 nm

To test if the graphene film would damage easily, these were measured at a significant intensity/peak pulse power. From the continued symmetry of the open aperture signals, it is clear that the graphene remained undamaged, even after such high intensities. The asymmetric dips around -0.25 mm on the Z-axis present in the 28 nJ and 103 nJ signals are due to the kerr nonlinearity (n_2) of the BK7 substrate, which further shows the high intensities used.

5.2.1.7 Antimonene

Antimonene thin-films were prepared via LPE, identically to the graphene described previously, as shown in Figure 5.3. AFM measurements of the Sb thin-films give a thickness of 17 nm and a roughness of 2 nm and 3 nm for R_a and R_q respectively, as shown in Figure 5.23. The thickness of the film compares favourably with

the graphene samples shown in the previous section, with slightly lower roughness.

The Sb film (shown in Figure 5.25 also exhibited strong saturable absorption, similar to the graphene samples.

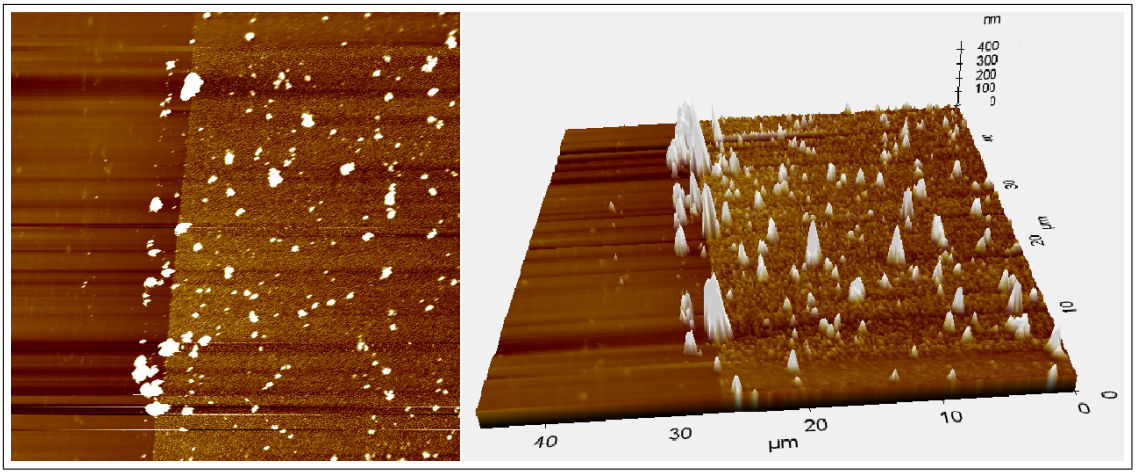

Figure 5.23: Atomic Force Microscopy (AFM) measurement of the Sb thin film, showing both the thin film and the BK7 glass substrate below

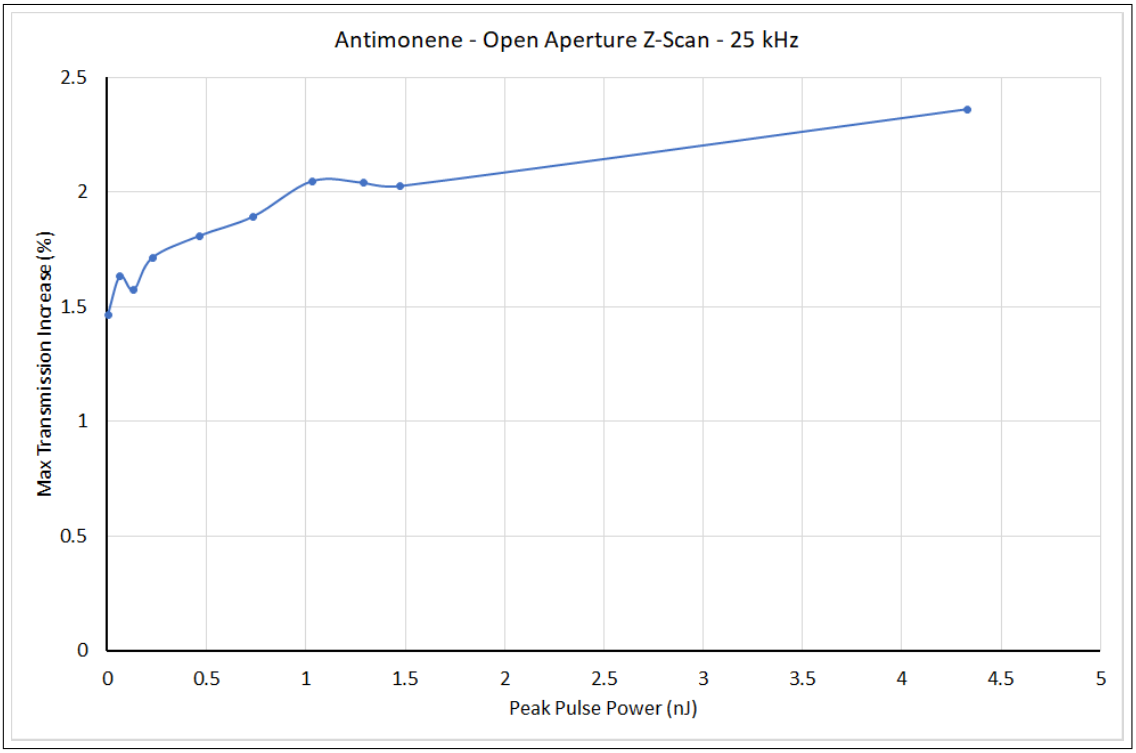

Figure 5.24: Max modulation of the Sb thin film for a various peak pulse energies at 25 kHz, 1030 nm and 200 fs

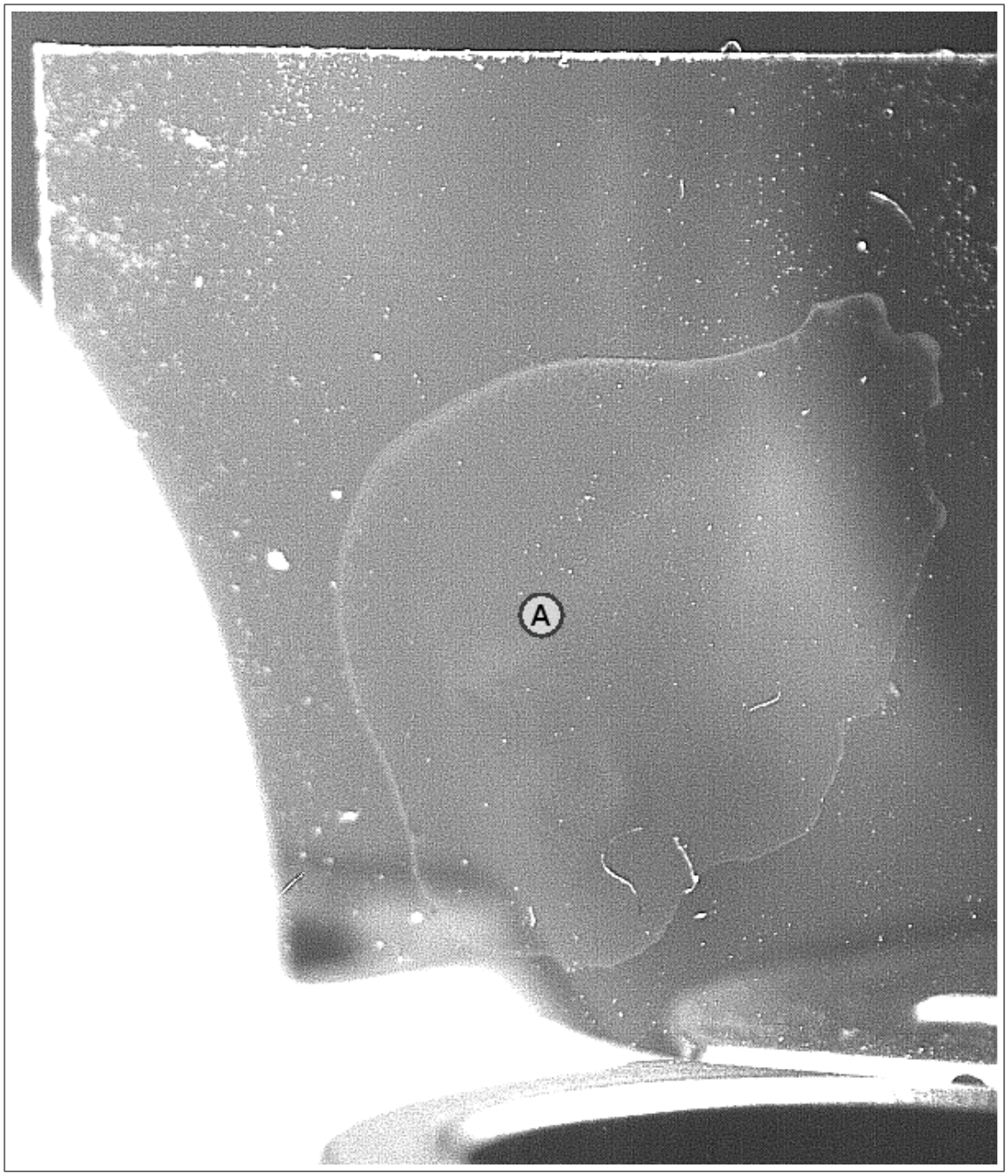

Figure 5.25: Photograph of a Sb film with the examined position overlaid.

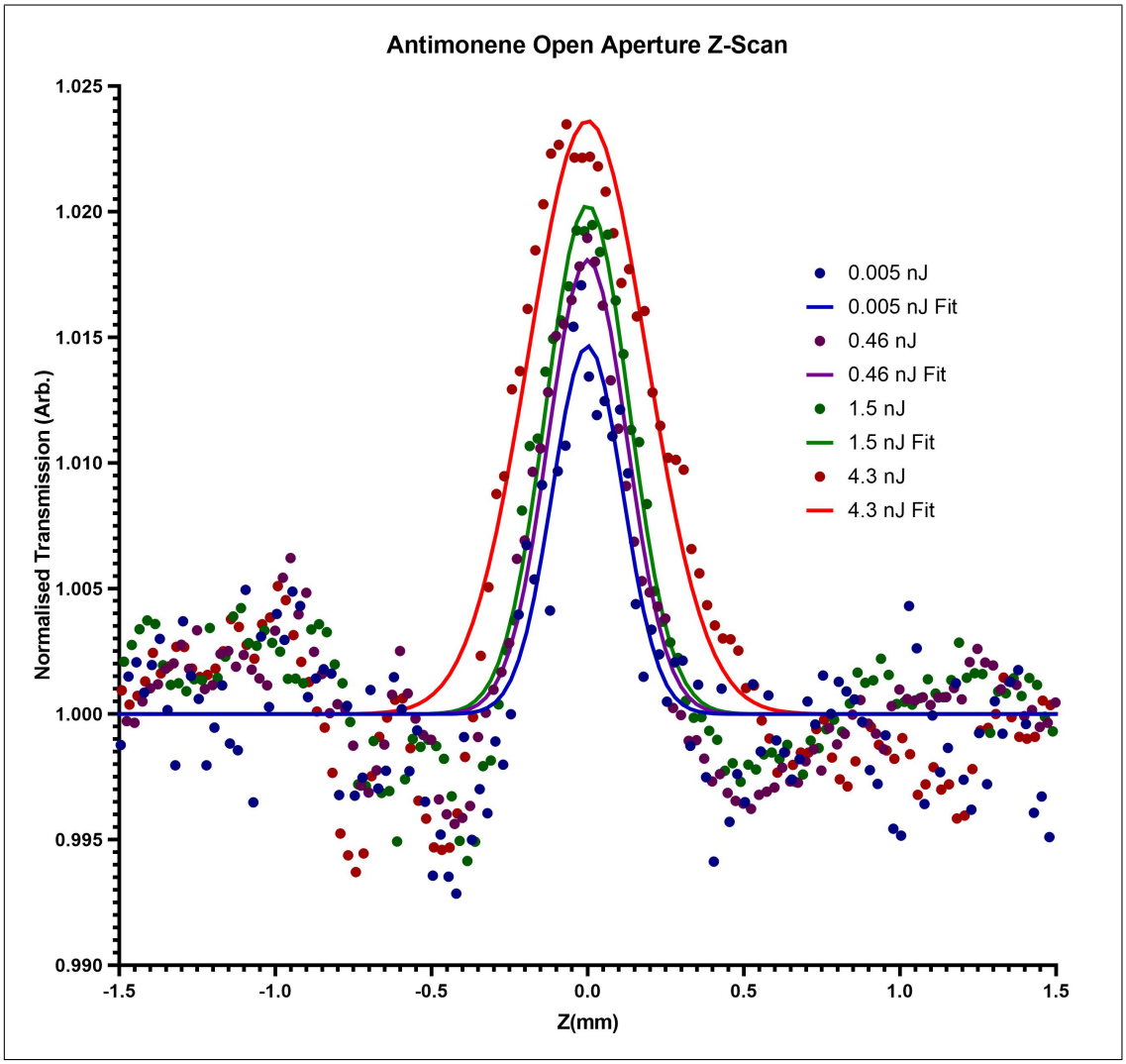

Figure 5.26: Open Aperture Z-Scan measurements of the Sb thin-film for various peak pulse energies at 25 kHz, 1030 nm

The antimonene has a similar evolution of the modulation depth (as shown in Figure 5.24) as the 5,000 RPM graphene shown in Figure 5.15. The modulation depth increases with peak pulse power (or intensity) up to around 2% before it begins to plateau.

These results show that, for particular wavelengths, Sb can be used as a saturable absorber, comparable to graphene. This goes to show the wide range of 2D materials available and their potential uses.

Table 5.8: Nonlinear optical properties of Sb thin film of 17 nm thickness from various z-scan experiments, at 200fs, 25 kHz, 1030 nm.

Pulse Energy (nJ)	I_0 (GW/cm^2)	Modulation Depth (%)	β ($X10^3$ cm/GW)	$Im(\chi^{(3)})$ ($X10^{-8}$ esu)	n_2 (cm^2/GW)	$Re(\chi^{(3)})$ ($X10^{-8}$ esu)	$\chi^{(3)}$ ($X10^{-8}$ esu)	ΔT_{pv} (%)
0.005	0.011	1.67	8420	1270	-	-	-	-
0.011	0.037	1.91	2960	450	-	-	-	-
0.022	0.081	2.82	1980	300	-	-	-	-
0.066	0.22	1.81	480	72	-	-	-	-
0.134	0.35	1.82	300	45	-	-	-	-
0.23	0.75	1.89	140	22	-	-	-	-
0.66	1.89	2.12	64	9.7	-	-	-	-
1.5	4.5	2.28	29	4.4	1.28	23.6	24	36
4.3	8.6	2.67	18	2.7	-	-	-	-

5.2.1.8 Z-Scan Conclusions

Both the CVD graphene and the LPE graphene thin films exhibit enormous saturable absorption. This corresponds to a β value around -3,000 cm/GW. Similarly, the samples exhibit enormous Kerr nonlinearity, with n_2 of -0.15 cm^2/GW.

As exemplified in Figure 5.15, the modulation depth of the graphene samples increase with respect to film thickness. Figure 5.27 displays measurements taken at the same I_0, namely around 1 GW/cm^2.

The max modulation depth achievable scales with film thickness. This shows that the relevant nonlinear parameters for optical devices can be tailored through control of the film thickness. The strong saturable absorption displayed by all graphene samples indicate that such a material has potential as a mode-locker for ultra-fast pulsed lasers.

The variance between C_{3K} and C_{5K} appears be due to the differences in film thickness, which resulted from the higher dispersion concentration of the C_{3K}/NMP. There may be a contribution from the flake size difference, though more data would be required to confirm.

The nonlinear optical parameter calculations are based on the film thicknesses observed during the AFM measurements. The CVD graphene measured close to 10 nm, which is higher than expected. Ideally, monolayer graphene is 0.33 nm thick, though due to the wrinkles such a thickness is rarely observed in CVD graphene. The C_{CVD} displayed a β of $0.3x10^4 cm/GW$, though with an actual thickness closer to 1 nm, the calculated value may be closer to the $10^4 cm/GW$ range.

Similarly, the β value reached up to a $10^6 cm/GW$ range for the C_{5K} samples,

which is based on the measured thickness via AFM.

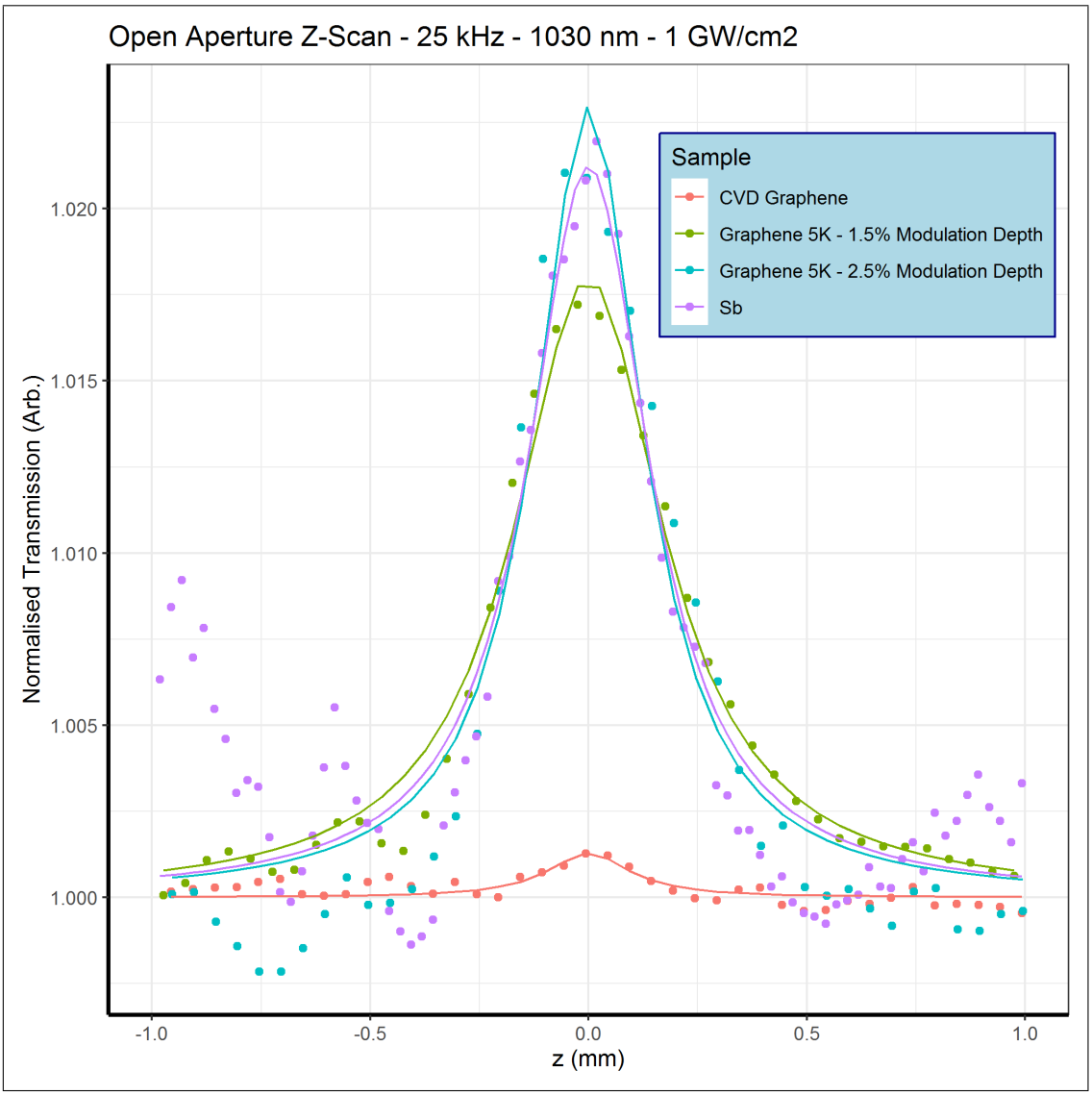

Figure 5.27: Open Aperture Z-Scan measurements of C_{CVD}, C_{5K}, C_{3K} and Sb for around 1 GW/cm^2 intensities at 25 kHz, 1030 nm

5.2.2 Graphene - Micra 900-F - 1.2 μm 2 μm

As the goal of the ISLA project was to develop a 2μm laser, z-scan measurements were also taken at 2μm utilising a Ti:sapphire laser. The graphene dispersion, pure graphene films and graphene-polymer films were all tested using the Z-scan technique. Two wavelengths were tested, 1.2 μm (as a comparison for current

technology) and 2 μm. During this subsection, the laser used was a Micra 900-F (utilising a Mira OPO to extend the wavelength range) from COHERENT with a pulse duration of 130 fs and a repetition rate of 80 MHz. This was done to compare it to higher repetition rates than the previous section.

During the 1.2 μm runs, only two detectors were used at a time, a sample and a reference detector. As such, only either an open or closed scan could be performed per run. However, for the 2 μm measurements, the system was upgraded to accommodate 3 detectors. So during these measurements, both open and closed scans could be performed at the same time. This helps ensure the accuracy of the closed aperture runs, as they are dependent on the open data. It also allowed twice as many scans to be run in a given time frame.

For these tests, samples of graphene-NMP dispersions, pure graphene thin films and graphene-PMMA composite films (1.2 μm) and graphene-polystyrene composite films (2 μm) were prepared.

5.2.2.1 Graphene/NMP Dispersions

The graphene dispersions, with a concentration of roughly 1 mg/ml, were examined in the z-scan system in 1 mm cuvettes, at several different laser intensities. The dispersions experience clear nonlinear scattering shown by the valley in the OA z-scan measurements at 1.2 μm and 2 μm, as seen in Figure 5.32 and 5.37, respectively. As expected, this effect increases with increasing laser intensity. Also as assumed, the valley widens with higher intensity at the focus, as the previous focus intensity is achieved earlier in the run.

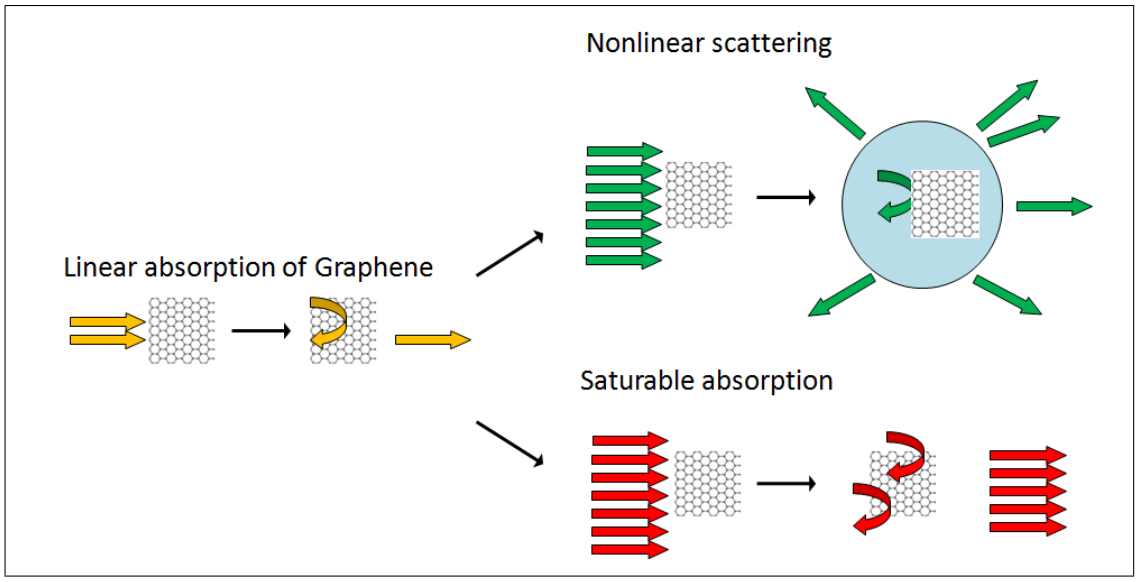

Figure 5.28: Overview of the nonlinear optical response of graphene

It is clear from the poor fit of the z-scan fitting in the graphene/NMP dispersions at 1.2 μm that the optical limiting is not due to two-photon absorption, and is instead due to scattering.

This scattering is due to nonlinear scattering, caused when graphene absorbs light and releases thermal energy to the surrounding solvent, as summarised in Figure 5.28. Microbubbles are thought to form in the solvent, which act as scattering centres. While this theory would explain the observed signals, the microbubbles themselves are unobservable without more specialised equipment. With an alternate Z-scan set up, which has a detector at a constant fixed angle to the moving detector, it is possible to also measure this scattered signal. This was not the set-up available, partially because the main interest was in saturable absorption.

Due to the nature of the particular solvent used, NMP, it is unlikely to be able to harness this particular dispersion as a viable optical limiter device. This is due to the general health risks of NMP including skin irritation and possible reproductive damage. As well as the general problems faced when trying to use a liquid as an optical limiter. The origin of the small peaks within the valley at higher intensities is believed to be due to the saturable absorptive nature of graphene.

5.2.2.2 1.2 μm Graphene/NMP Dispersions

The 1.2 μm open aperture z-scan scans from the graphene/NMP are summarised in Figure 5.32. Individual scans at $3.2\times10^{-3}GW/cm^2$ (Figure 5.29), $8\times10^{-3}GW/cm^2$ (Figure 5.29) and $1.8 \times 10^{-2}GW/cm^2$ (Figure 5.29) are shown, with the fittings showing a nonlinear absorption coefficient of 0.85 cm/GW, 1.8 cm/GW and 1,700 cm/GW respectively. These results are summarised in a table later in the chapter.

Perhaps to the longer path length of cuvettes (1cm thickness), the fitting used does not seem to work as well for the dispersions as it does for the thin film samples, which are shown later in this chapter. Though the fitting at 2 μm seems to be much closer to the experimental data. This may indicate that two-photon absorption is occuring for 2 μm.

Another factor that may contribute to the bad wings of the fittings in Figures 5.29 to 5.32 is the combination of unconsidered effects. It may also be the interaction between the saturable absorption of the graphene flakes, and the nonlinear scattering of the dispersion, and the formulae used does not take the conflicting phenomena into account.

The unusual peaks on either size of the focal point within the main valley (shown in Figures 5.30 and 5.31) are characteristic of higher-order effects (such as $\chi^{(5)}$) interacting with the $\chi^{(3)}$ NLO effect.

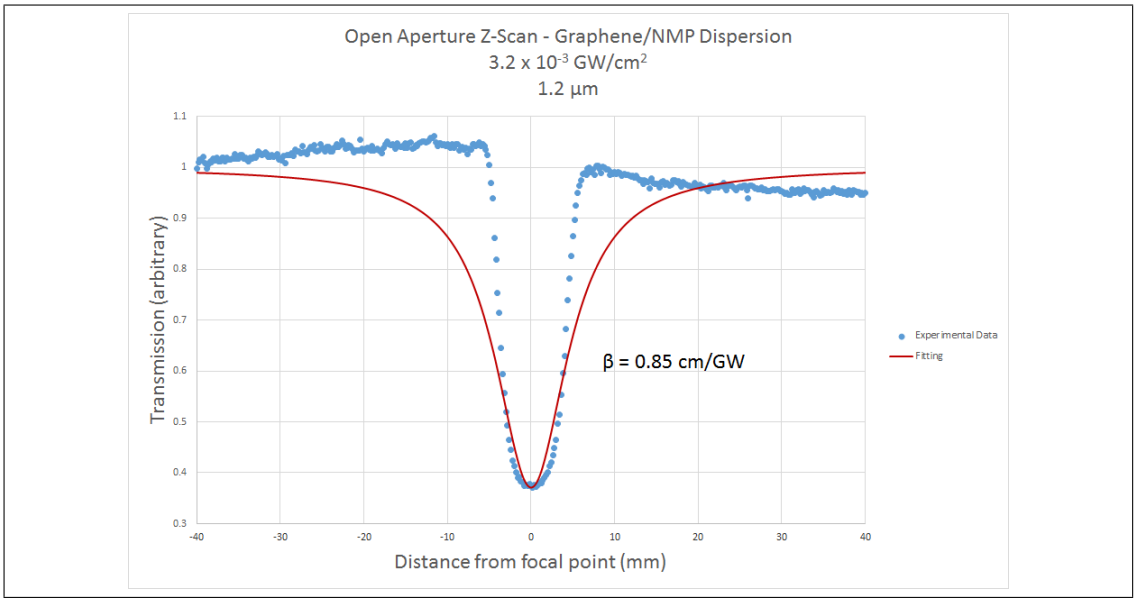

Figure 5.29: Open Aperture Z-Scan of graphene/NMP dispersions (∼1 mg/ml) at 1.2 μm, at an intensity of $3.2 \times 10^{-3} GW/cm^2$. The nonlinear absorption (β) for these parameters was 0.85 cm/GW, via fitting

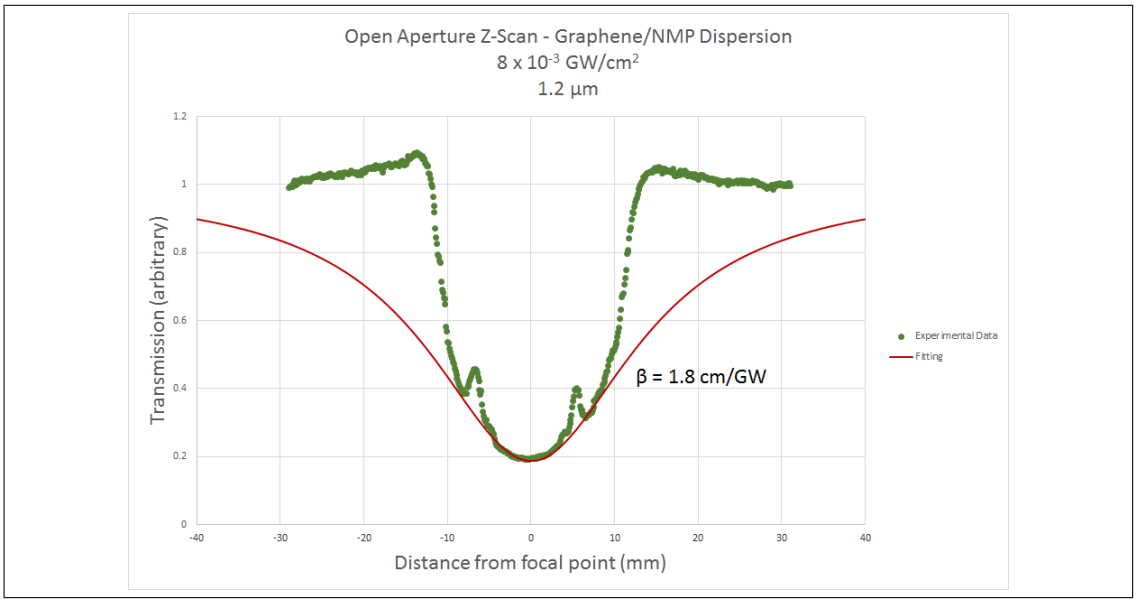

Figure 5.30: Open Aperture Z-Scan of graphene/NMP dispersions (∼1 mg/ml) at 1.2 μm, at an intensity of $8 \times 10^{-3} GW/cm^2$. The nonlinear absorption (β) for these parameters was 1.8 cm/GW, via fitting

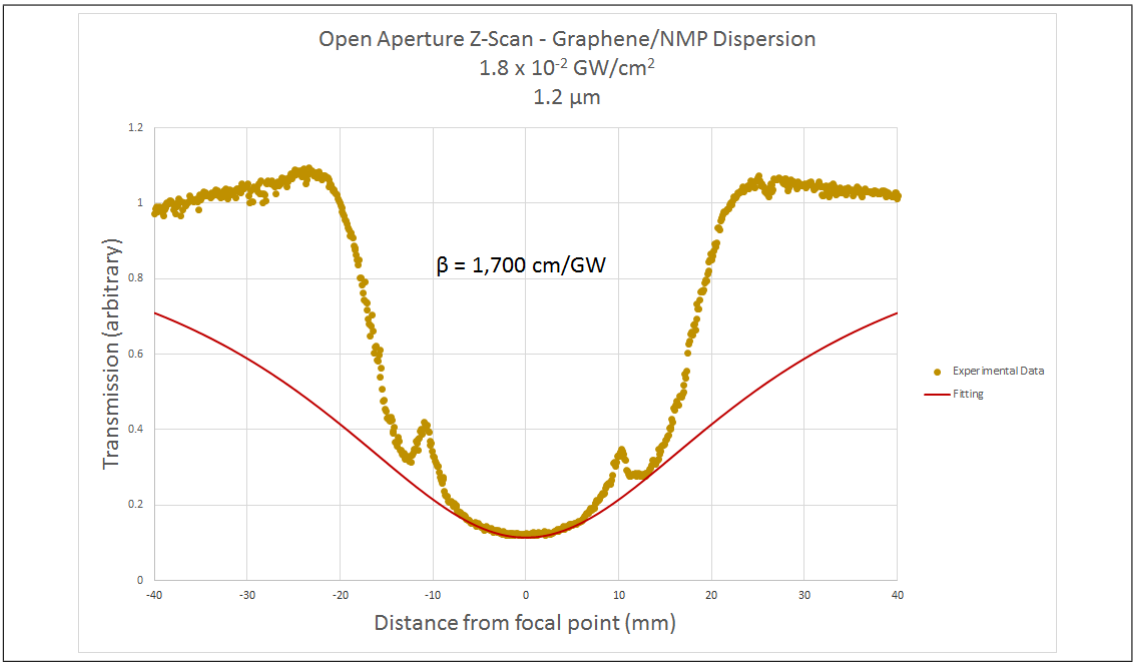

Figure 5.31: Open Aperture Z-Scan of graphene/NMP dispersions (∼1 mg/ml) at 1.2 μm, at an intensity of $1.8 \times 10^{-2} GW/cm^2$. The nonlinear absorption (β) for these parameters was 1,700 cm/GW, via fitting

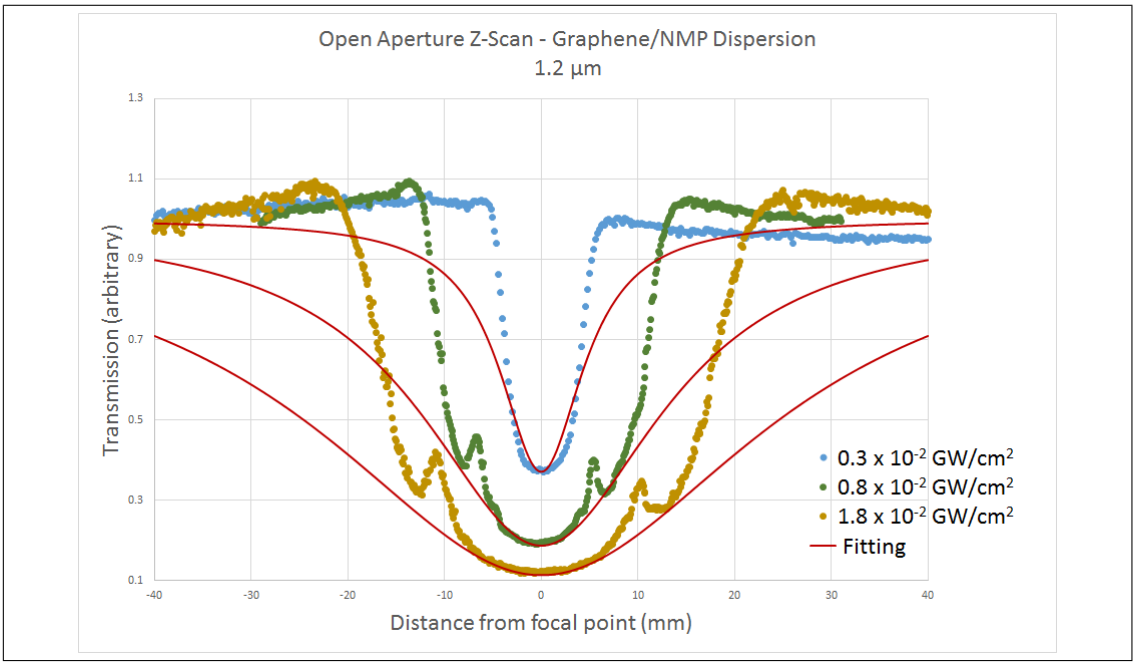

Figure 5.32: Open Aperture Z-Scan of graphene/NMP dispersions (∼1 mg/ml) at 1.2 μm, at several intensities

The Kerr nonlinearity was explored via the closed aperture mode of the graphene-NMP dispersions. As shown in Figure 5.33, for an intensity of $2.7 * 10^{-2} GW/cm^2$ an $n_2 = 1.16 * 10^{-6} cm^2 W^{-1}$. This agrees fairly well with the literature value of $-10^{-7} cm^2 W^{-1}$ (Zhang *et al.*, 2012a). The difference between the two values may be due to the imperfect fit shown in said figure.

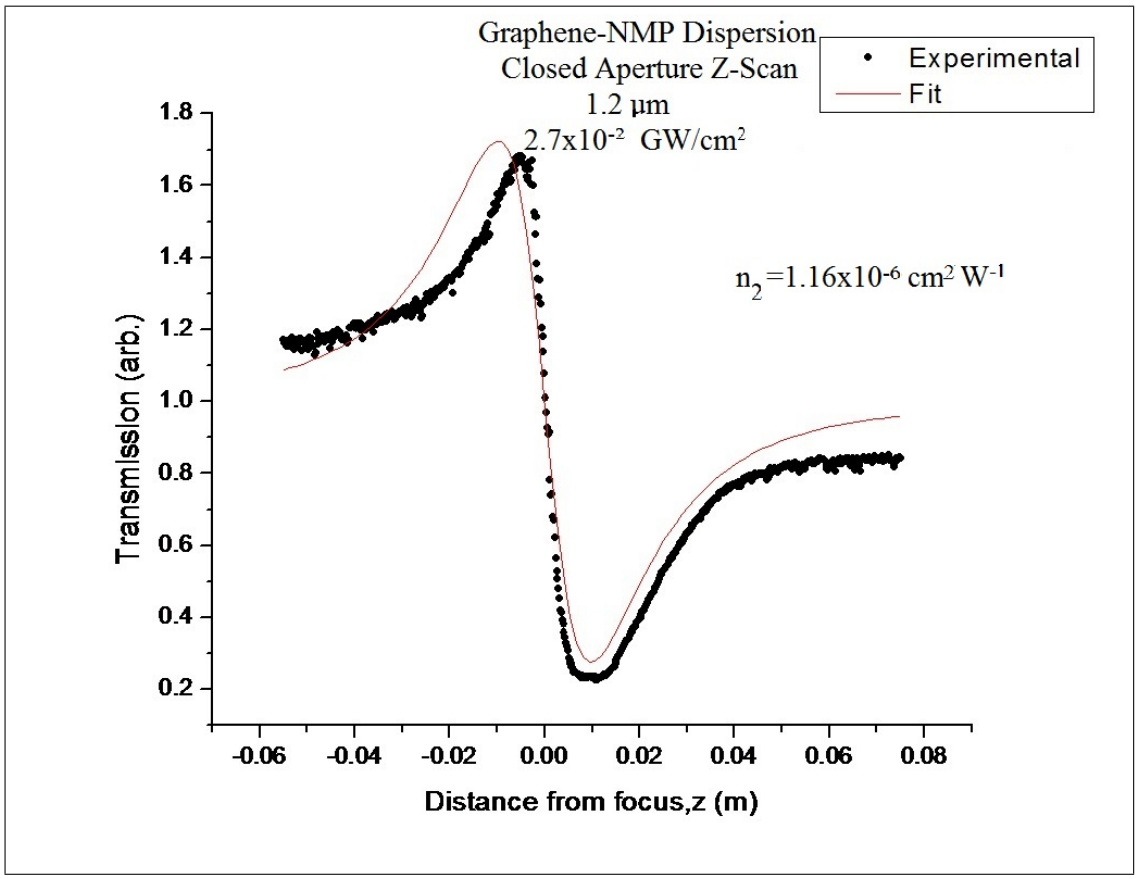

Figure 5.33: Closed Aperture Z-Scan of graphene/NMP dispersions (∼1 mg/ml) at 1.2 μm, at $2.7 * 10^{-2}$ GW/cm^2. The Kerr Nonlinearity (n_2) is shown in the fitting to be 1.16x10^{-6} $cm^2 W^{-1}$

5.2.2.3 2 μm Graphene/NMP Dispersions

The 2 μm open aperture z-scan scans from the graphene/NMP are summarised in Figure 5.37. Individual scans at $9.5 \times 10^{-3} GW/cm^2$ (Figure 5.34), $3.2 \times 10^{-2} GW/cm^2$ (Figure 5.35) and $4.3 \times 10^{-2} GW/cm^2$ (Figure 5.36) are shown, with the fittings showing a nonlinear absorption coefficient of 12.8 cm/GW, 3.7 cm/GW and 4.8 cm/GW respectively.

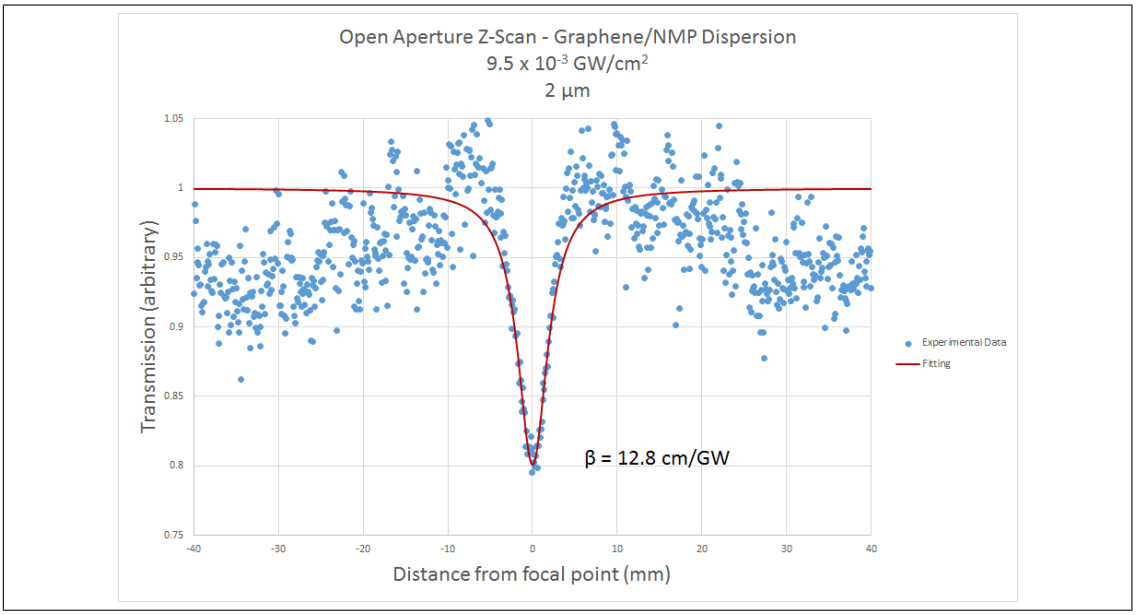

Figure 5.34: Open Aperture Z-Scan of graphene/NMP dispersions (∼1 mg/ml) at 2 μm, at an intensity of $9.5 \times 10^{-3} GW/cm^2$. The nonlinear absorption (β) for these parameters was 12.8 cm/GW, via fitting

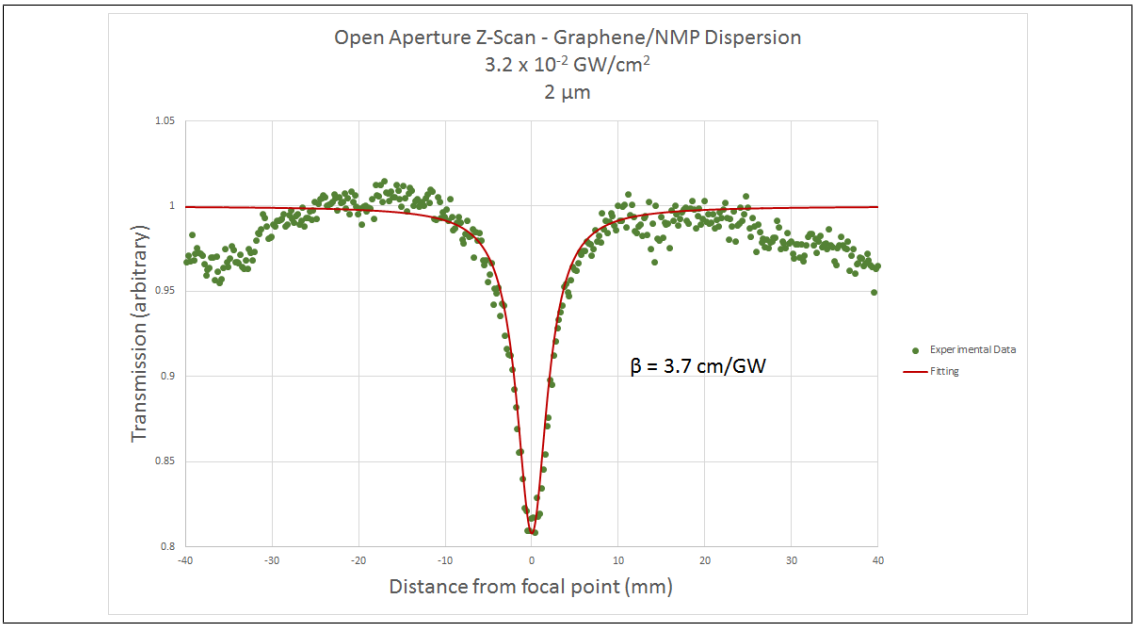

Figure 5.35: Open Aperture Z-Scan of graphene/NMP dispersions (∼1 mg/ml) at 2 μm, at an intensity of $3.2 \times 10^{-2} GW/cm^2$. The nonlinear absorption (β) for these parameters was 3.7 cm/GW, via fitting

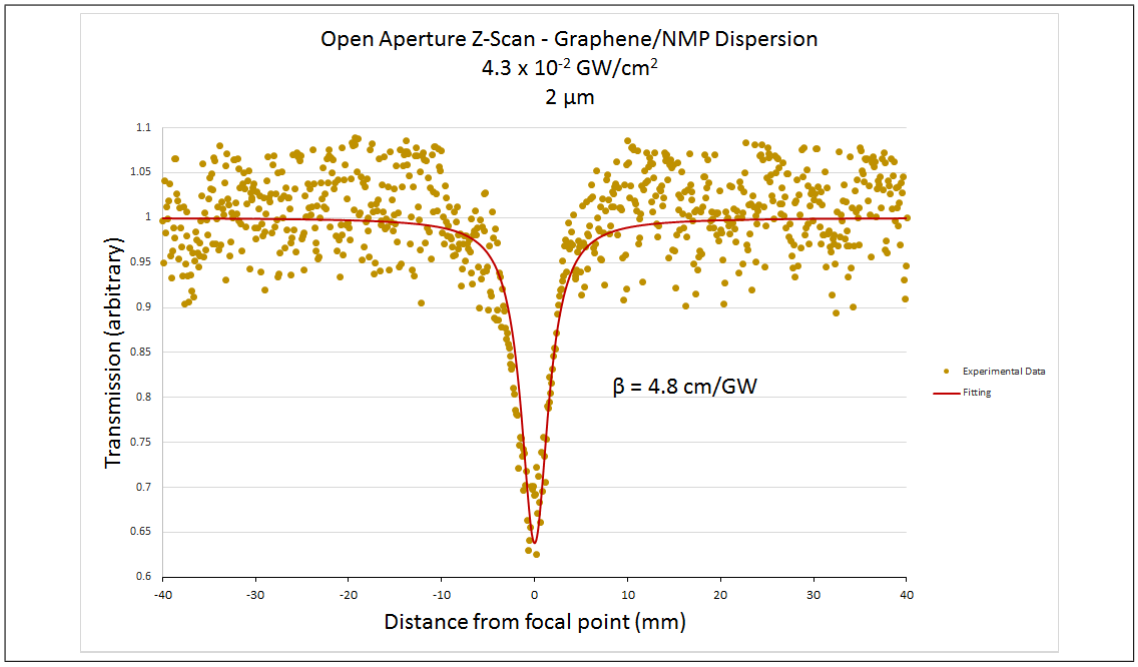

Figure 5.36: Open Aperture Z-Scan of graphene/NMP dispersions (∼1 mg/ml) at 2 μm, at an intensity of $4.3 \times 10^{-2} GW/cm^2$. The nonlinear absorption (β) for these parameters was 4.8 cm/GW, via fitting

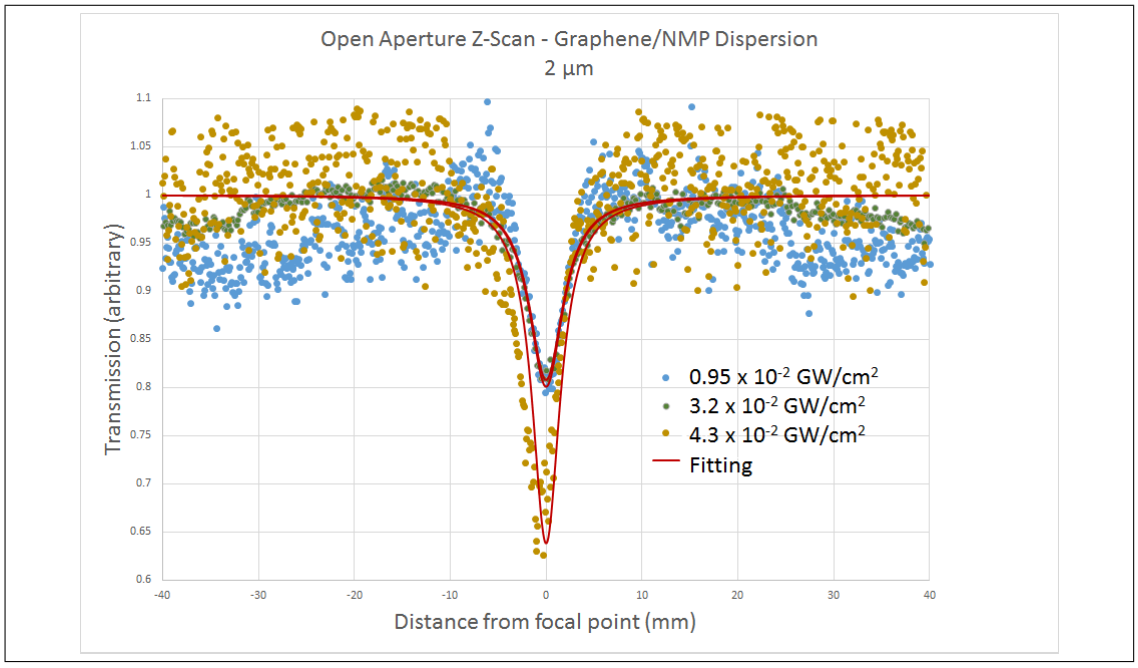

Figure 5.37: Open Aperture Z-Scan of graphene/NMP dispersions (∼1 mg/ml) at 2 μm, at several intensities

5.2.2.4 Graphene Thin Films

The thin films of pure graphene were prepared via drop casting, with thicknesses determined to be <100nm for films made using the highest concentration dispersion ($\geq$1 mg/ml) by white light interferometry (Omniscan MicroXam), an example of which is shown in Figure 5.38. This was achieved by scratching the graphene thin film with a razor blade, and measuring the height difference between the surface of the coverslip and the top of the thin film. Films made with dilutions were, as expected, generally thinner.

5.2.2.5 1.2 μm Graphene Thin Films

The pure graphene thin films exhibit a very strong saturable absorption signal at 1.2 μm, the SA increasing with higher intensity, as displayed in Figure 5.44. The trailing end was blocked by the particular sample holder used at the time, and so the affected data points are omitted.

The 1.2 μm open aperture z-scan scans from the graphene thin films are summarised in Figure 5.44. Individual scans at $4.8 \times 10^{-3} GW/cm^2$ (Figure 5.39), $3.2 \times 10^{-2} GW/cm^2$ (Figure 5.40), $5.3 \times 10^{-2} GW/cm^2$ (Figure 5.41), $1.1 \times 10^{-1} GW/cm^2$ (Figure 5.42) and $2.8 \times 10^{-1} GW/cm^2$ (Figure 5.43) are shown, with the fittings showing a nonlinear absorption coefficient of -22.2×10^6 cm/GW, -7.3×10^6 cm/GW, -4.2×10^6 cm/GW, -2.3×10^6 cm/GW and 0.95×10^6 cm/GW respectively.

Examples of the open aperture response of graphene thin films at 2 μm are shown in Figures 5.45 and 5.46. Both show clear saturable absorption, though the signal is less strong than the 1.2 μm results shown previously. This may be due to the limitations of the laser systems used, and the relatively low power attainable.

As can be seen in Figure 5.46 and A.1, there appears to be slight optical limiting in these measurements, though due to the high noise to signal ratio it is difficult to say for sure.

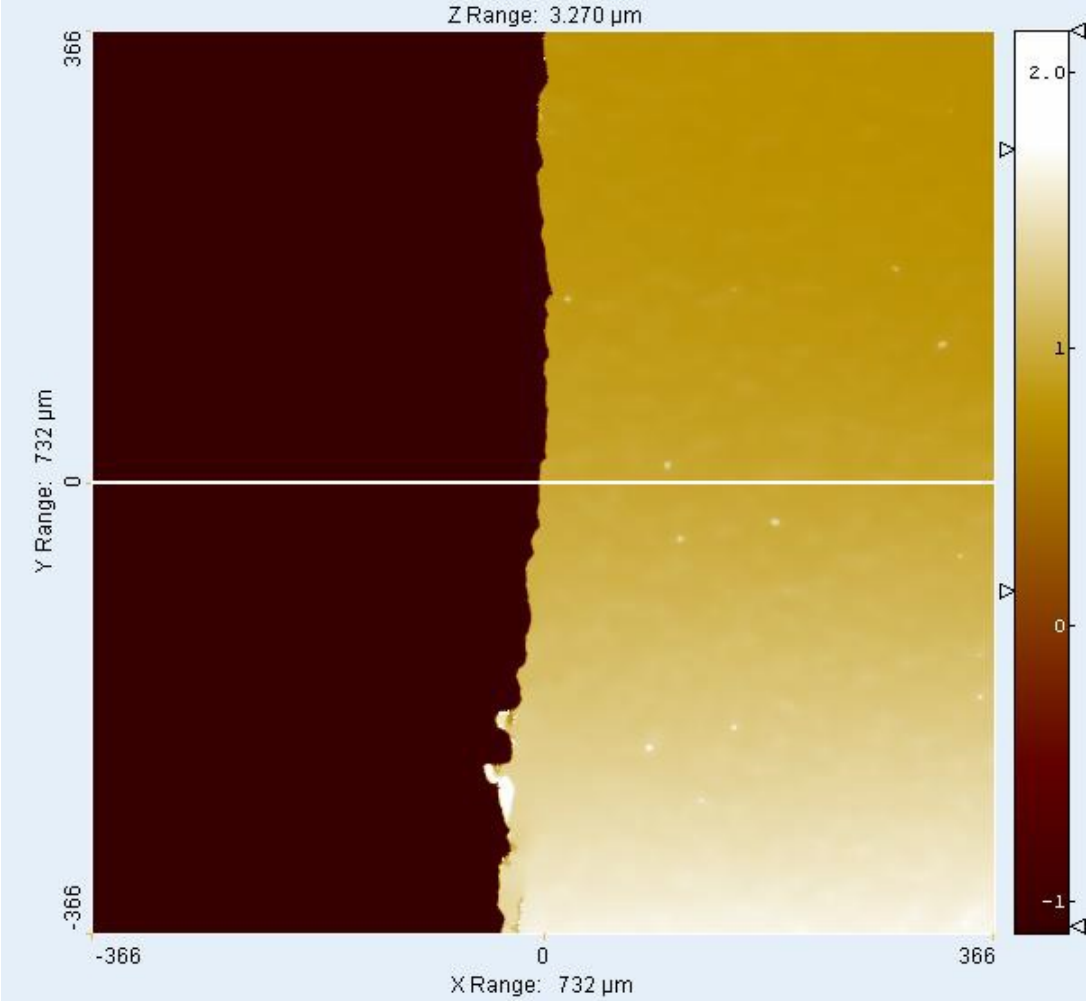

Figure 5.38: White light interferometer image utilised to determine graphene film thickness

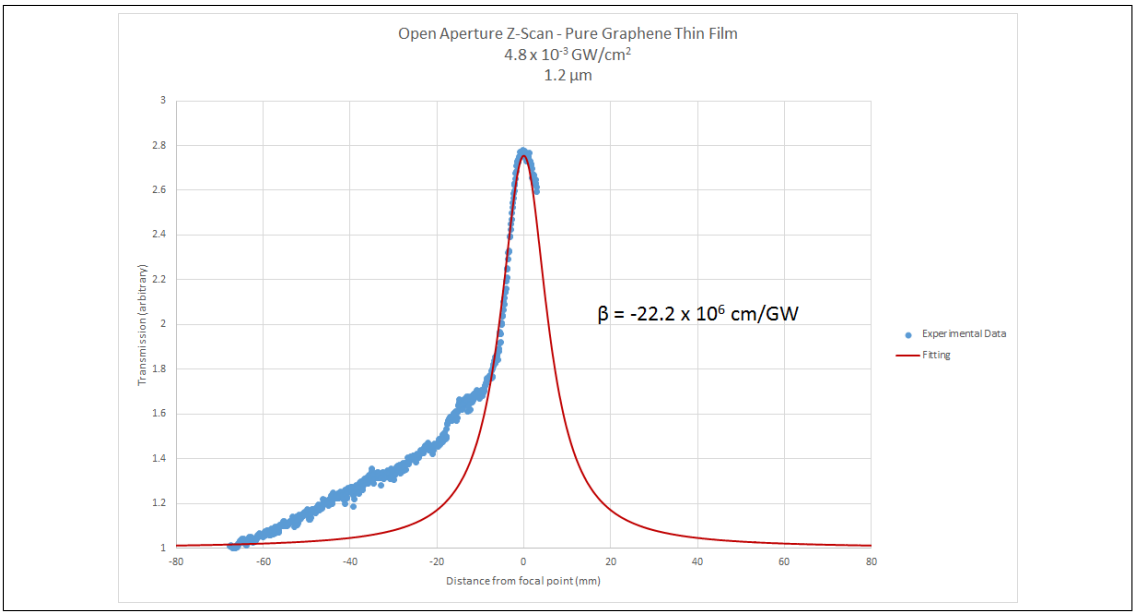

Figure 5.39: Open Aperture Z-Scan of graphene thin films (∼100 nm thickness) at 1.2 μm, at an intensity of $4.8 \times 10^{-3} GW/cm^2$. The nonlinear absorption (β) for these parameters was -22.2×10^6 cm/GW, via fitting

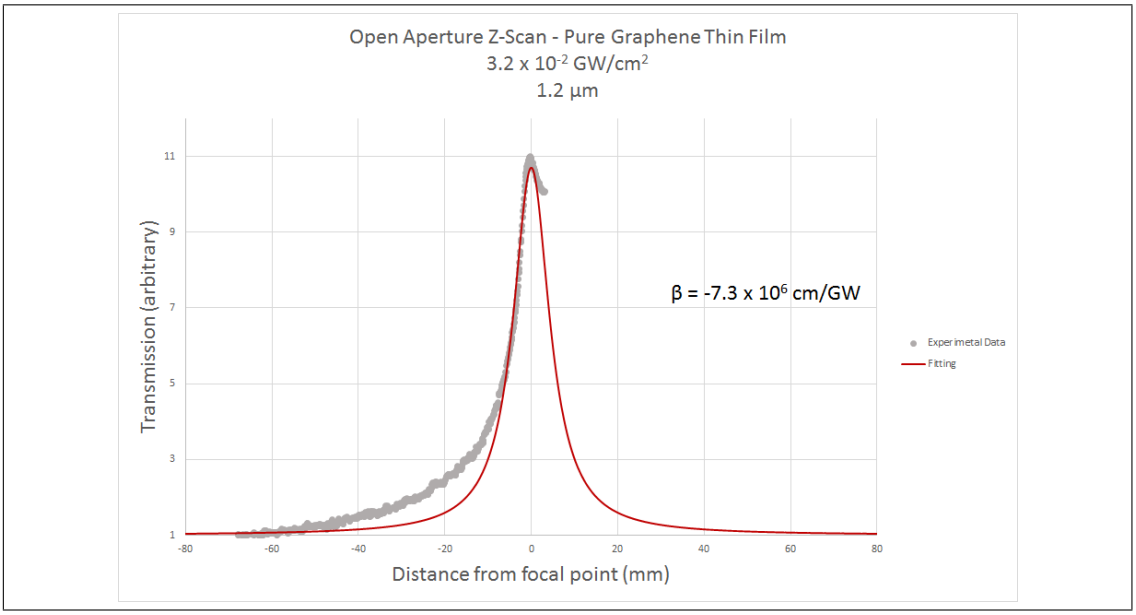

Figure 5.40: Open Aperture Z-Scan of graphene thin films (∼100 nm thickness) at 1.2 μm, at an intensity of $3.2 \times 10^{-2} GW/cm^2$. The nonlinear absorption (β) for these parameters was -7.3×10^6 cm/GW, via fitting

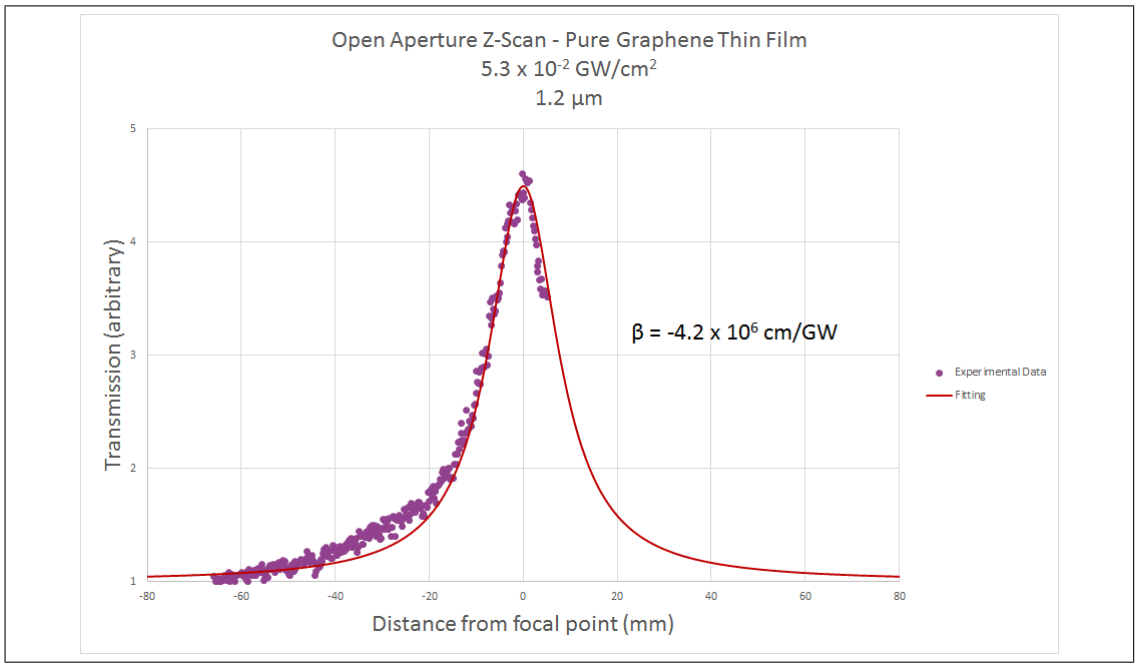

Figure 5.41: Open Aperture Z-Scan of graphene thin films (∼100 nm thickness) at 1.2 μm, at an intensity of $5.3 \times 10^{-2} GW/cm^2$. The nonlinear absorption (β) for these parameters was -4.2×10^6 cm/GW, via fitting

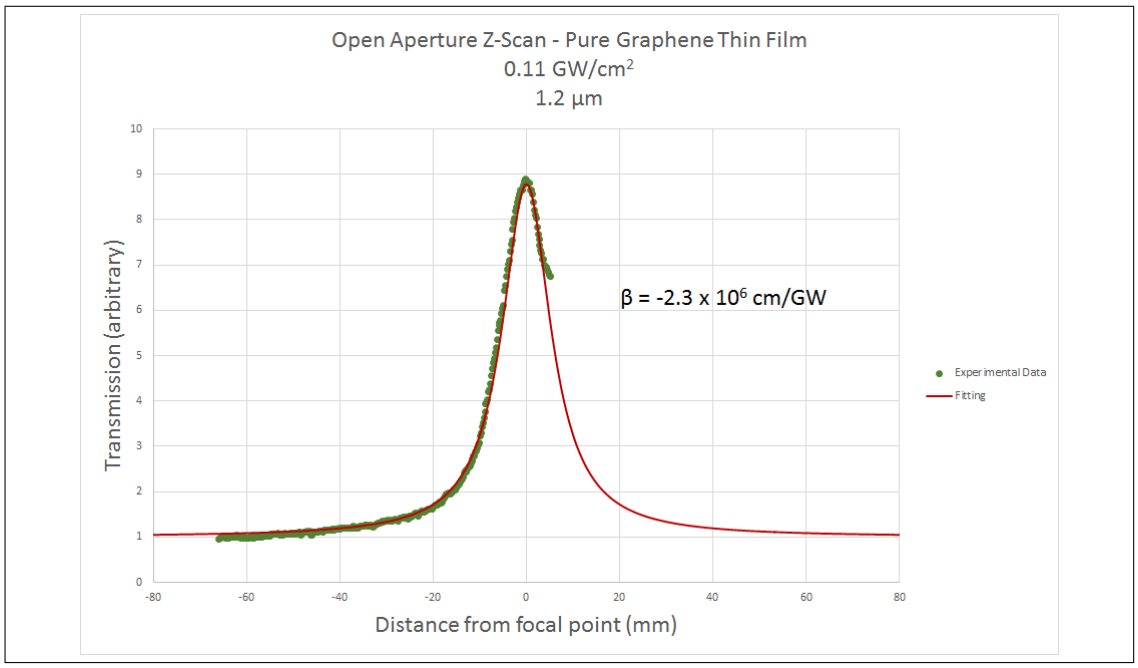

Figure 5.42: Open Aperture Z-Scan of graphene thin films (∼100 nm thickness) at 1.2 μm, at an intensity of $1.1 \times 10^{-1} GW/cm^2$. The nonlinear absorption (β) for these parameters was -2.3×10^6 cm/GW, via fitting

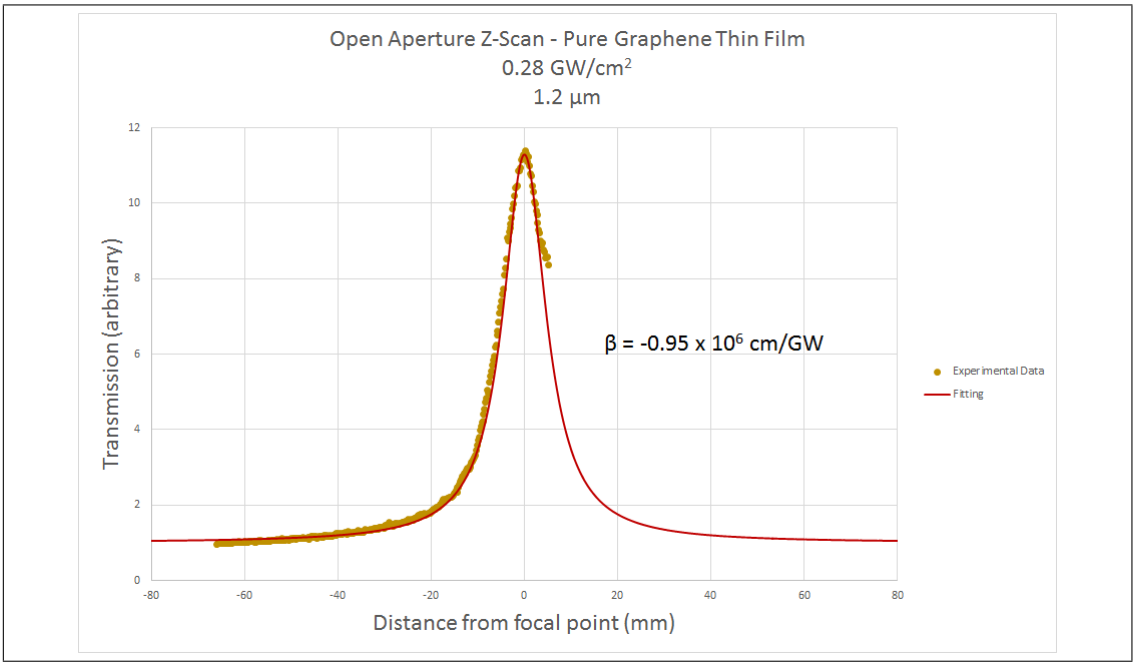

Figure 5.43: Open Aperture Z-Scan of graphene thin films (∼100 nm thickness) at 1.2 μm, at an intensity of $2.8 \times 10^{-1} GW/cm^2$. The nonlinear absorption (β) for these parameters was 0.95×10^6 cm/GW, via fitting

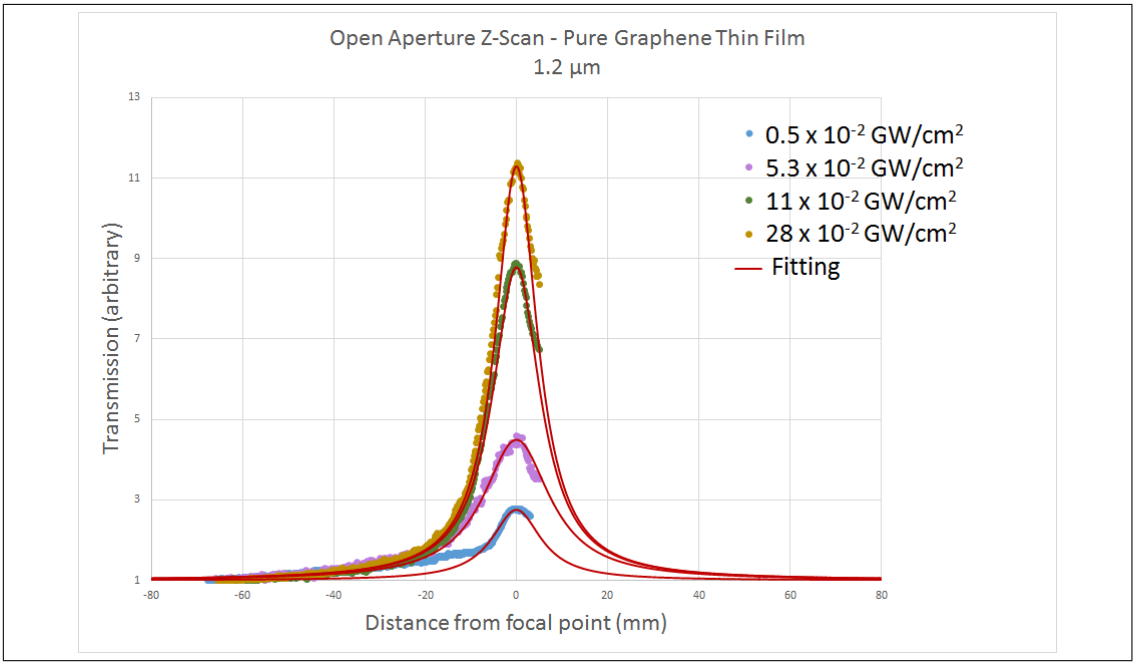

Figure 5.44: Open Aperture Z-Scan of graphene thin films (∼100 nm thickness) at 1.2 μm, at several intensities

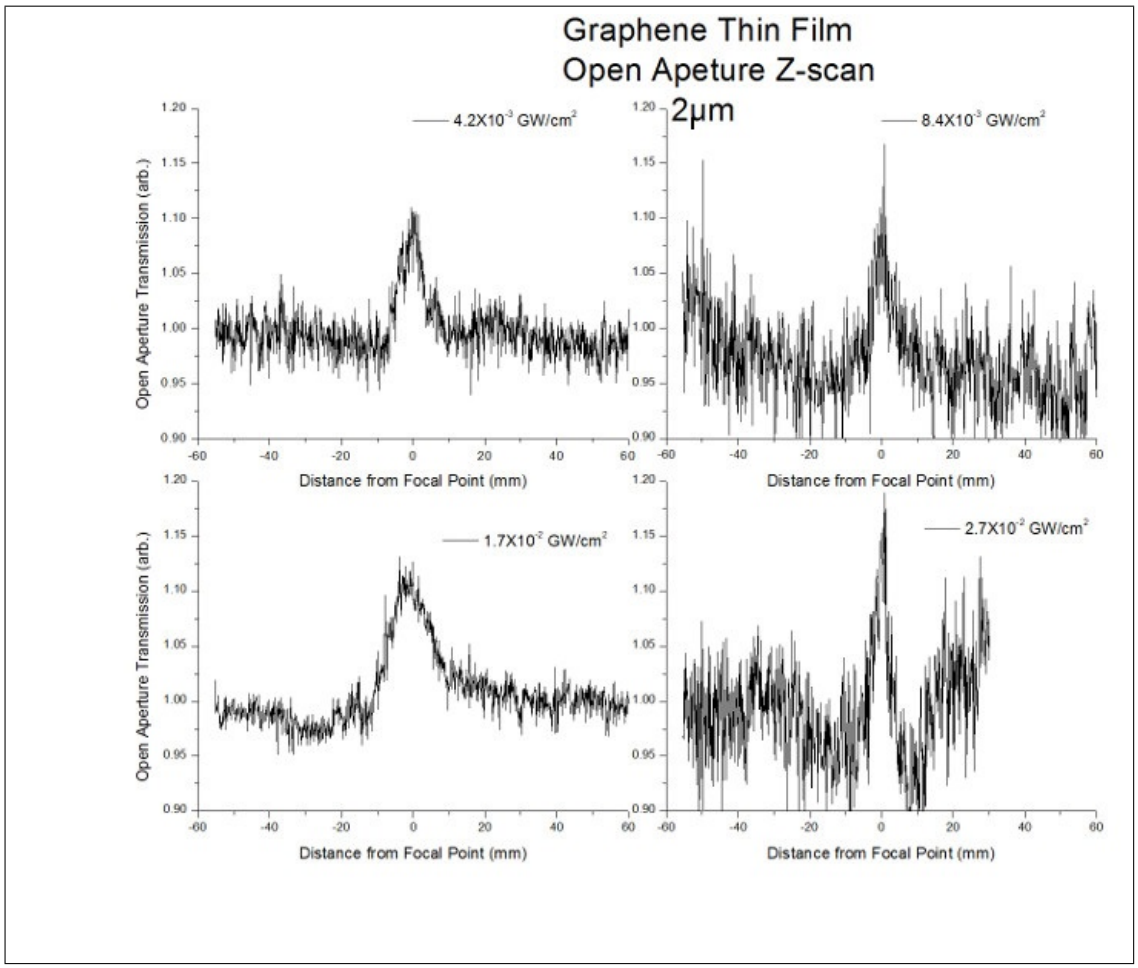

Figure 5.45: Graphene thin film open aperture Z-scan at at 2 μm.

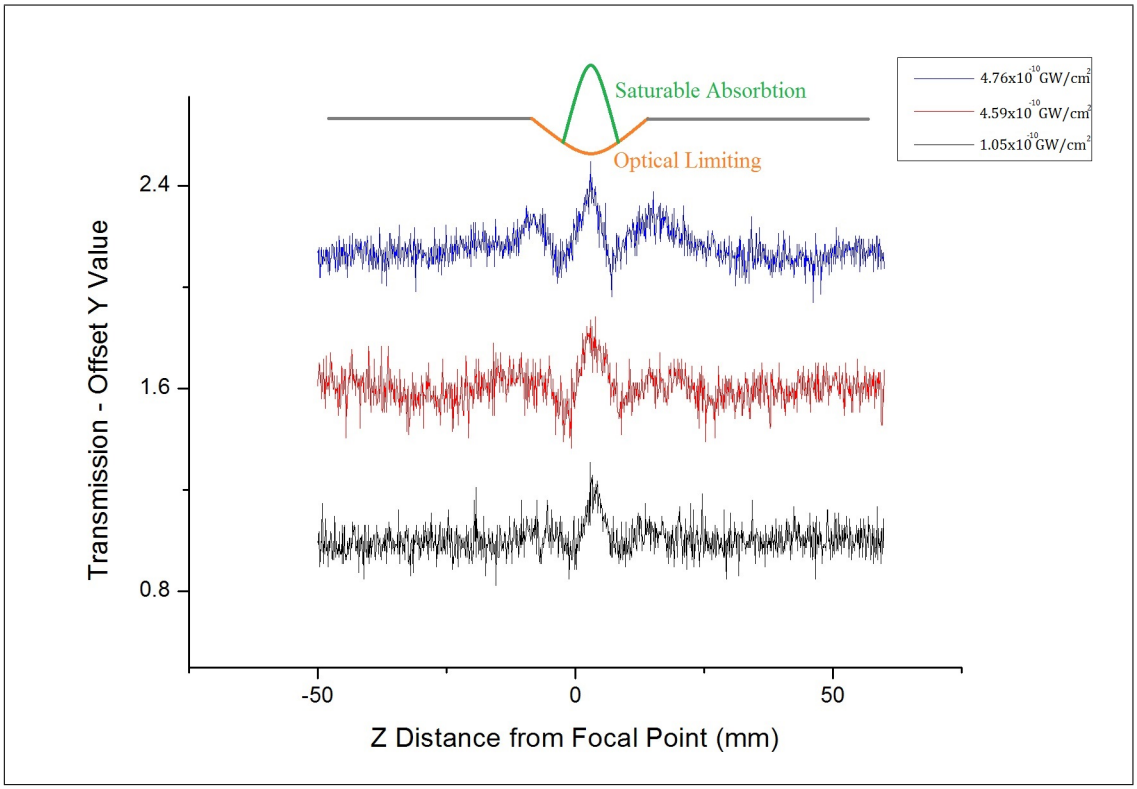

Figure 5.46: Graphene thin film open aperture Z-scan at at 2 μm. Displaying slight optical limiting.

The 2 μm open aperture z-scan scans from the graphene thin films are shown below. Individual scans at $8 \times 10^{-3} GW/cm^2$ (Figure 5.47), $1.6 \times 10^{-2} GW/cm^2$ (Figure 5.40), $2.1 \times 10^{-2} GW/cm^2$ (Figure 5.49) and $4.5 \times 10^{-2} GW/cm^2$ (Figure 5.50) are displayed, with the fittings showing a nonlinear absorption coefficient of -1.2×10^6 cm/GW, -0.86×10^6 cm/GW, -0.92×10^6 cm/GW and -0.18×10^6 cm/GW respectively.

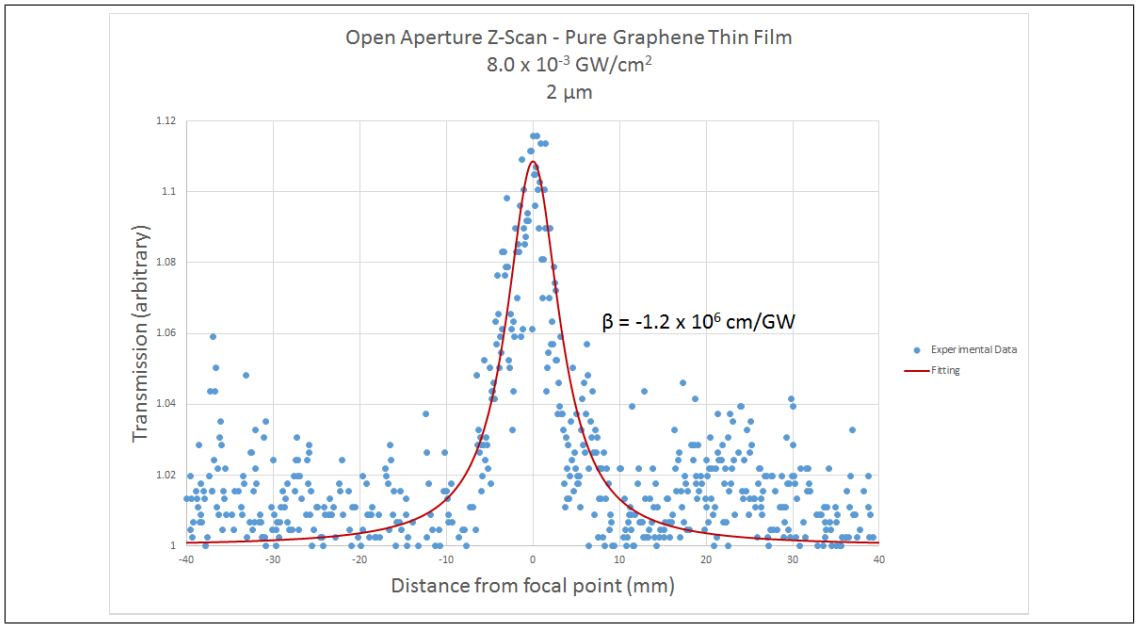

Figure 5.47: Open Aperture Z-Scan of graphene thin films (∼100 nm thickness) at 2 μm, at an intensity of $8 \times 10^{-3} GW/cm^2$. The nonlinear absorption (β) for these parameters was -1.2×10^6 cm/GW, via fitting

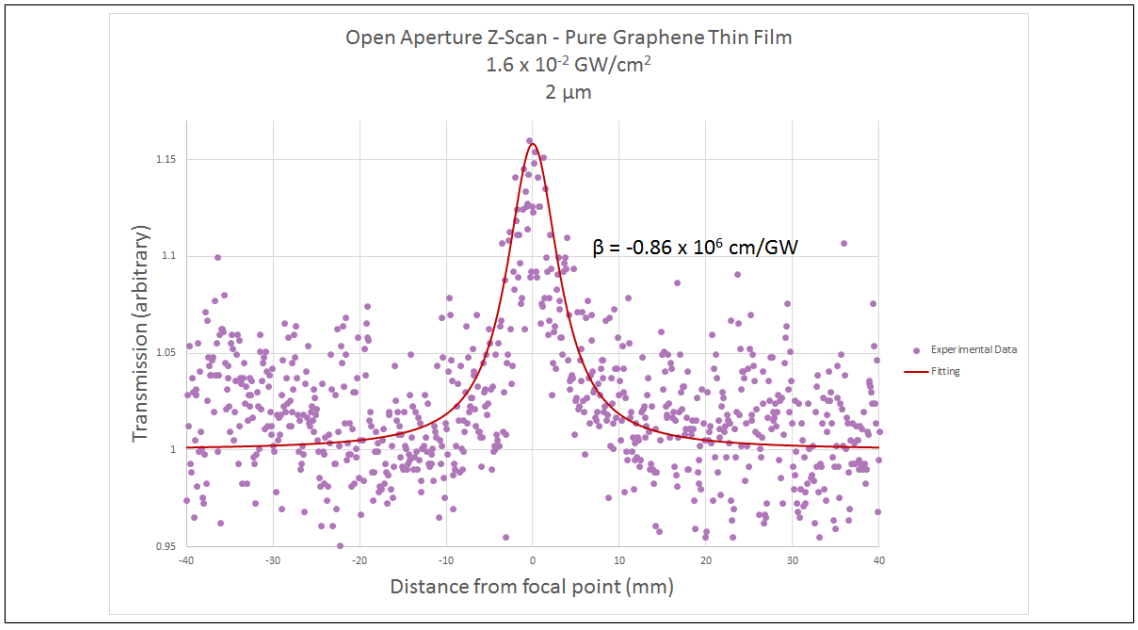

Figure 5.48: Open Aperture Z-Scan of graphene thin films (∼100 nm thickness) at 2 μm, at an intensity of $1.6 \times 10^{-2} GW/cm^2$. The nonlinear absorption (β) for these parameters was -0.86×10^6 cm/GW, via fitting

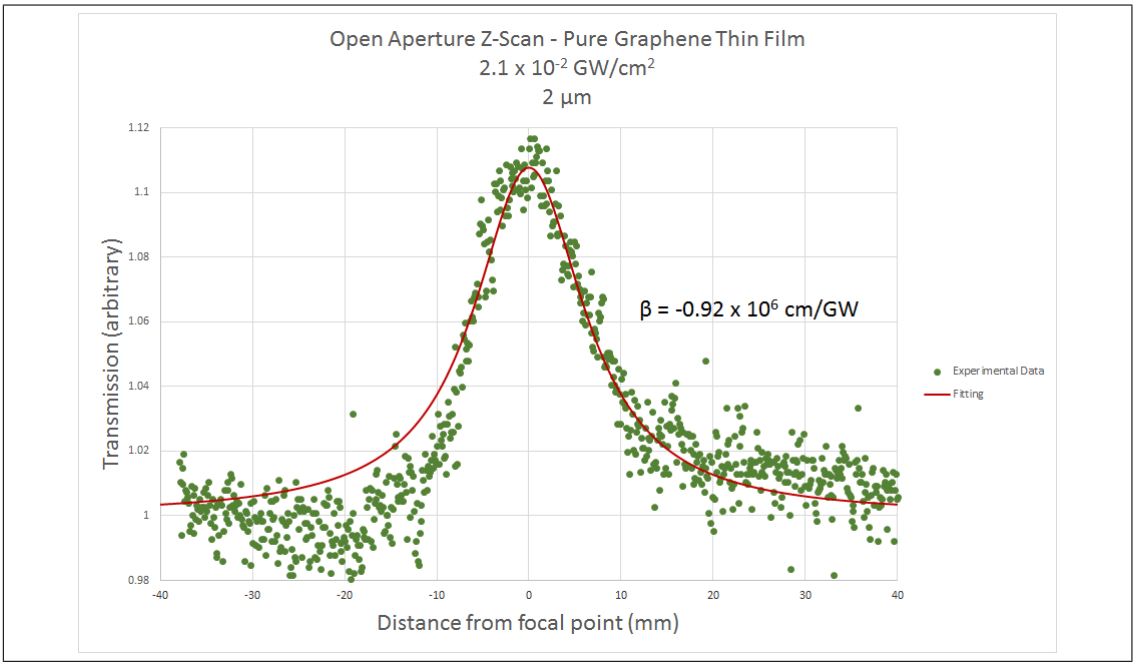

Figure 5.49: Open Aperture Z-Scan of graphene thin films (∼100 nm thickness) at 2 μm, at an intensity of $2.1 \times 10^{-2} GW/cm^2$. The nonlinear absorption (β) for these parameters was -0.92×10^6 cm/GW, via fitting

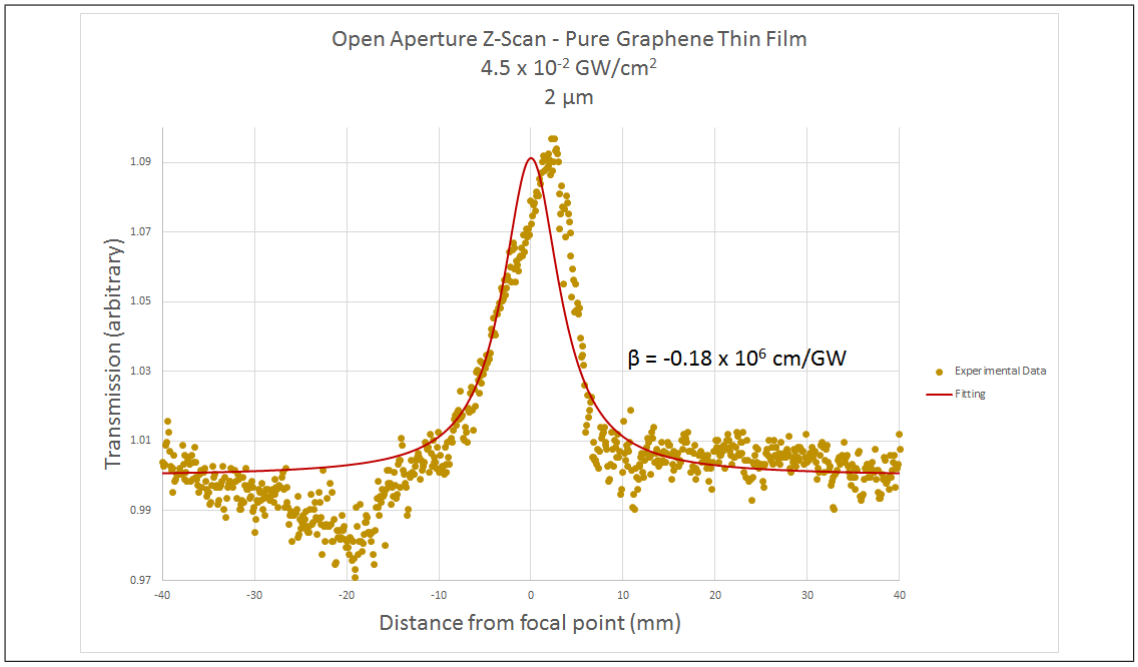

Figure 5.50: Open Aperture Z-Scan of graphene thin films (∼100 nm thickness) at 2 μm, at an intensity of $4.5 \times 10^{-2} GW/cm^2$. The nonlinear absorption (β) for these parameters was -0.18×10^6 cm/GW, via fitting

5.2.2.6 Theoretical Calculation of Nonlinear Absorption Coefficient

It is possible to theoretically calculate the nonlinear optical coefficient using quantum perturbation theory (Fan *et al.*, 2012):

$$\beta = \frac{4\pi^2}{\epsilon_\omega \omega^4 \hbar^3} \left(\frac{v_F e^2}{c} \right)^2 \tag{5.13}$$

where β is the nonlinear absorption coefficient (often associated with two-photon absorption), ϵ_ω is the dielectric constant, ω is the angular frequency of the photons, $\hbar$ is the Dirac constant (or reduced Plancks constant) $(1.054571800(13) \times 10^{-34} Js)$, v_F is the electronic group velocity ($\sim 10^6 m/s$), e is the elemental charge and c is the velocity of light.

The theoretical value of β can be calculated to be -5×10^6cm/GW at an intensity of 2.9×10^{-3} GW/cm^2, using quantum perturbation theory (Fan *et al.*, 2012) with equation 5.13.

From the fitting of the z-scan open aperture shown in Figure 5.51, an experimental β value of -4.8×10^6 cm/GW using equation 3.2 can be obtained. This agrees with the theoretical value given earlier.

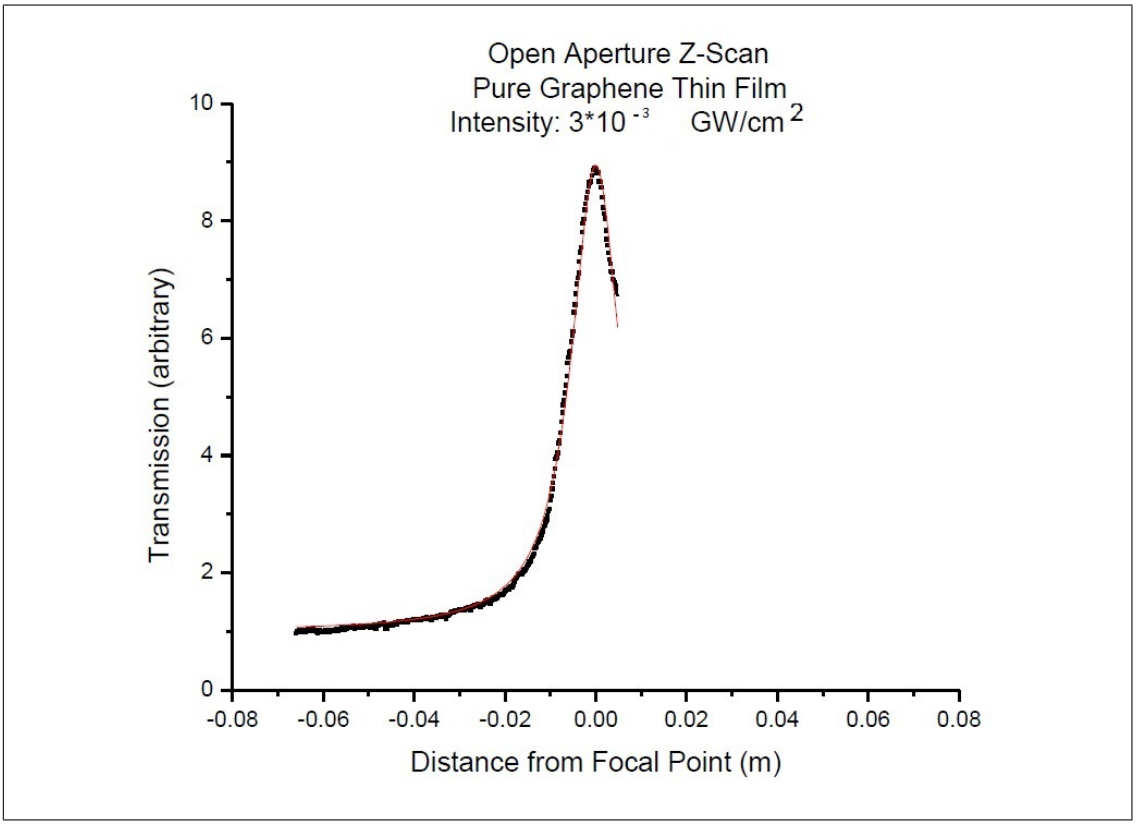

Figure 5.51: Graphene thin film open aperture Z-scan at at 1.2 μm, at an intensity of $3 \times 10^{-3} GW/cm^2$. The later half of the scan was somewhat blocked by the particular holder used during this run, and so has been removed, similar to 5.32. β can be calculated from the graph.

5.2.2.7 Graphene-Polymer Composites

The open aperture Z-scan results for graphene-PMMA (1.2 μm) and graphene-polystyrene (2 μm) are shown in Figures 5.52 and 5.53, respectively. In both cases, saturable absorption can still be clearly seen in the open aperture signal.

In Figure 5.52, the presence of the polymer in the graphene-PMMA film appears to distort the signal, perhaps due to the inhomogeneity of the graphene distribution and due to the changing spot size during a Z-scan run.

In the graphene-polystyrene samples, it should be noted that the PMMA itself appears to have a slight saturable absorption, presented in Figure 5.53.

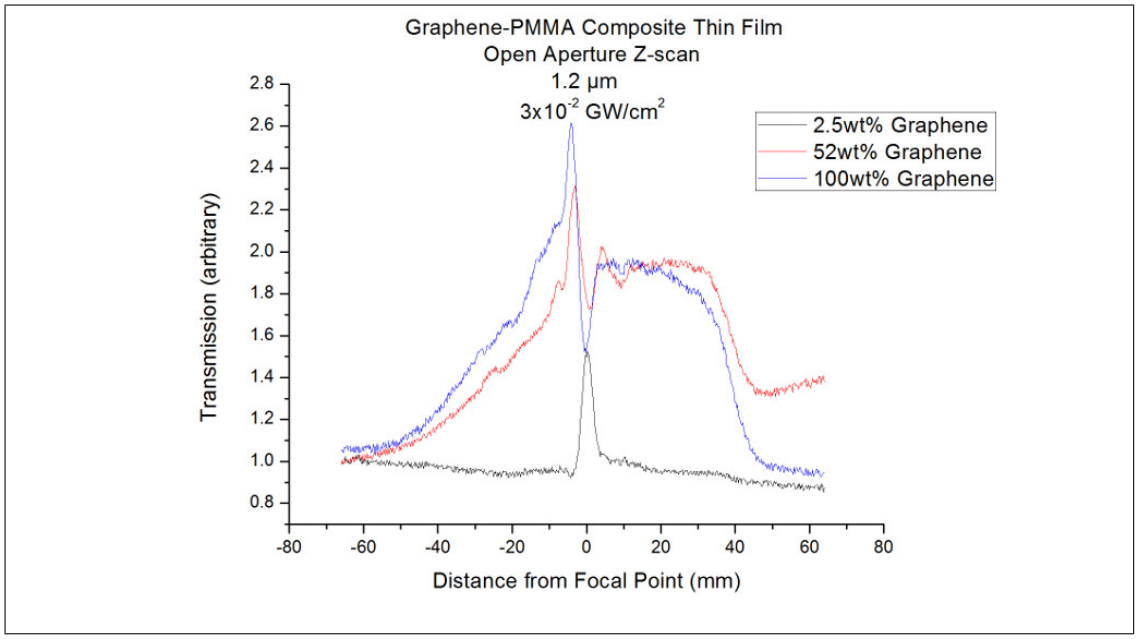

Figure 5.52: Graphene-PMMA composites open aperture Z-scan at several concentrations at 1.2 μm

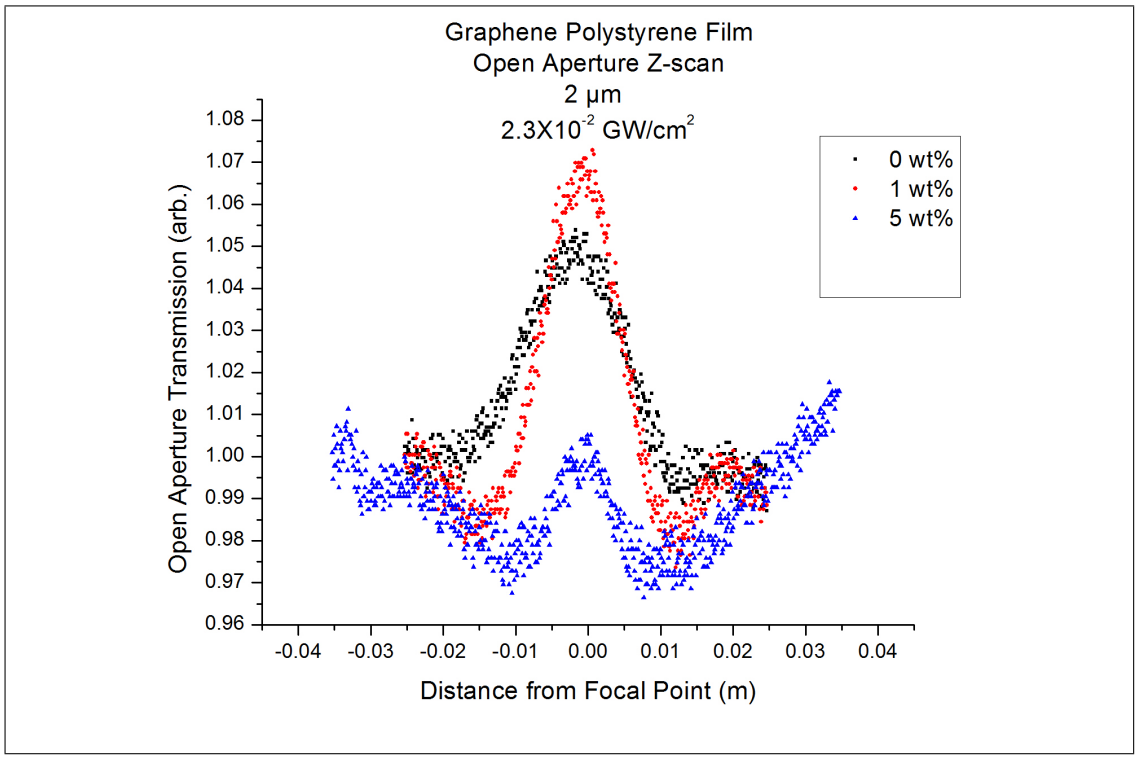

Figure 5.53: Graphene-polystyrene thin film open aperture Z-scan at 2 μm.

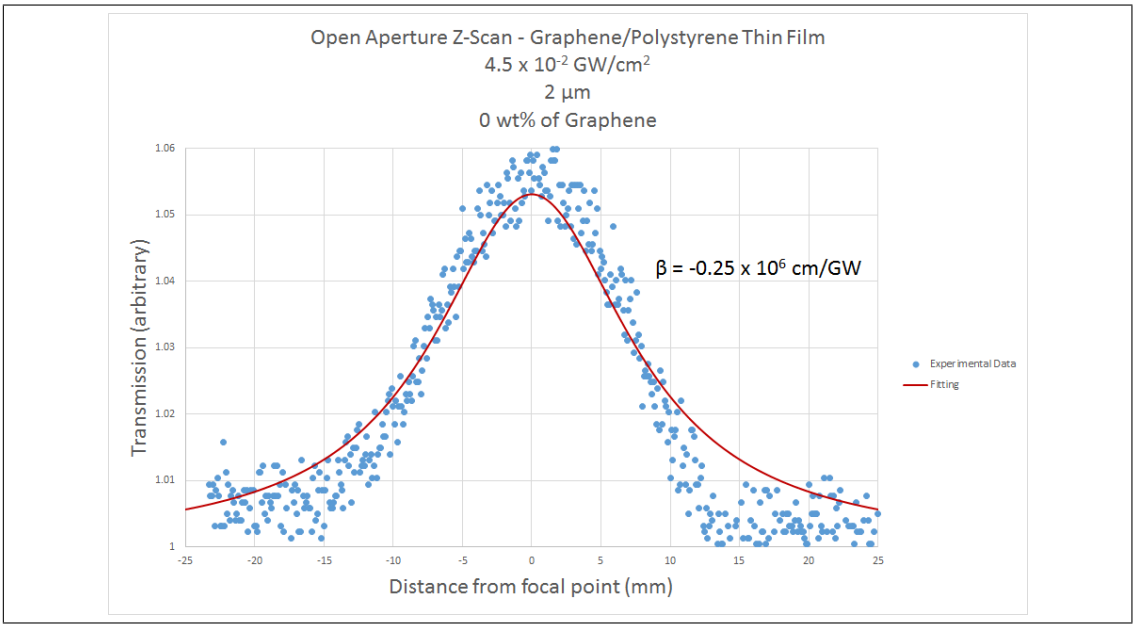

Figure 5.54: Open Aperture Z-Scan of graphene-polystyrene thin films (assuming ~100 nm thickness) at 2 μm, at an intensity of $4.5 \times 10^{-2} GW/cm^2$. The nonlinear absorption (β) for these parameters was -0.25×10^6 cm/GW, via fitting

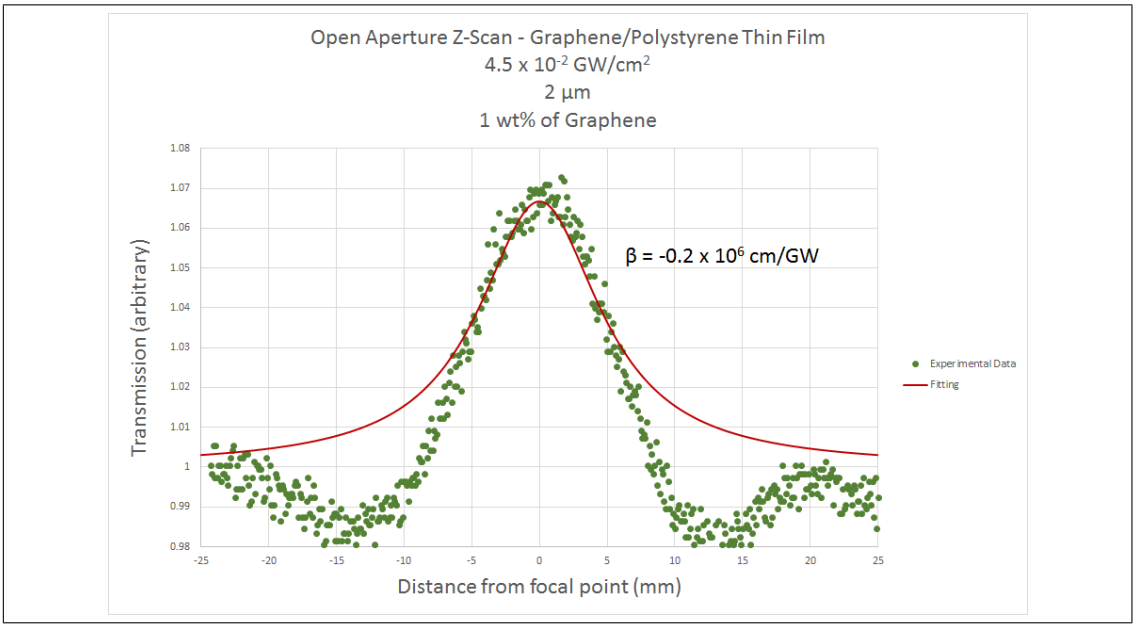

Figure 5.55: Open Aperture Z-Scan of graphene-polystyrene thin films (assuming ~100 nm thickness) at 2 μm, at an intensity of $4.5 \times 10^{-2} GW/cm^2$. The nonlinear absorption (β) for these parameters was -0.2×10^6 cm/GW, via fitting

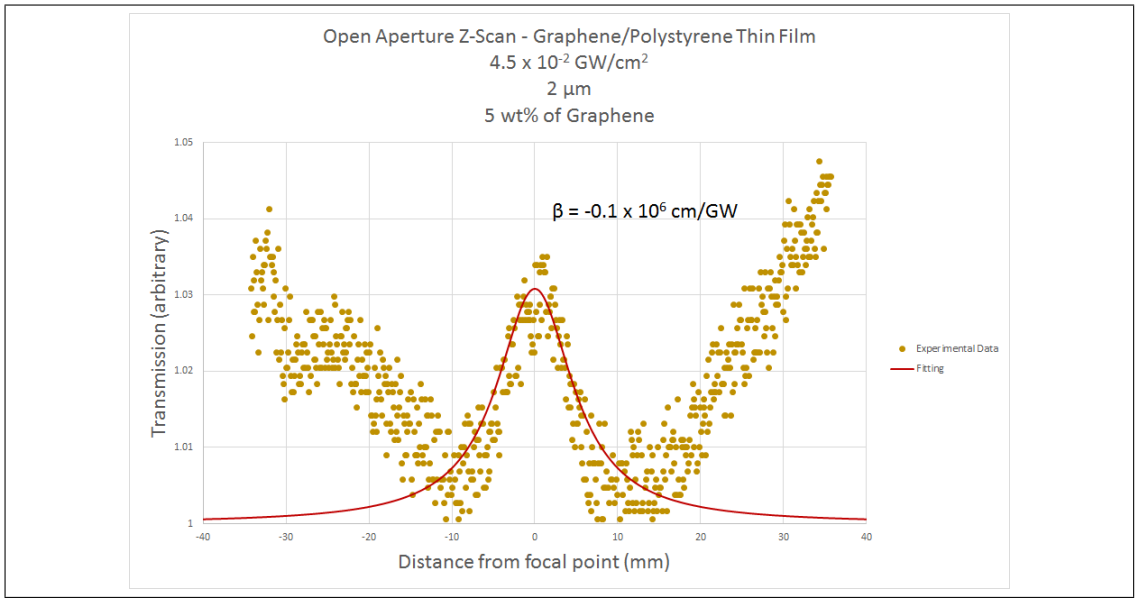

Figure 5.56: Open Aperture Z-Scan of graphene-polystyrene thin films (assuming ∼100 nm thickness) at 2 μm, at an intensity of $4.5 \times 10^{-2} GW/cm^2$. The nonlinear absorption (β) for these parameters was -0.1×10^6 cm/GW, via fitting

The 2 μm open aperture z-scan graphs from the graphene/polystrene thin films are summarised in Figure 5.53, at a consistent intensity of $4.5 \times 10^{-2} GW/cm^2$. Individual scans at 0 wt% of graphene (Figure 5.54), 1 wt% of graphene (Figure 5.55) and 5 wt% of graphene (Figure 5.56)are displayed, with the fittings showing a nonlinear absorption coefficient of -0.25×10^6 cm/GW, -0.2×10^6 cm/GW and -0.1×10^6 cm/GW respectively.

As can be seen from the graphs, the integration of the graphene filler into the polystrene matrix introduces alot of noise into the device.

Similar to Figures 5.29 to 5.32, Figures 5.55 and 5.56, exhibit "bad wings" in the fittings. This is likely due to a strange interaction between the graphene flakes and the polymer that is not understood.

5.2.3 Z-scan - OPA - 2 μm

The z-scan set-up discussed in this subsection employs an Optical Parametric Amplifier (OPA) laser system with output wavelength at 2 μm, with a repetition rate of 100 kHz and a pulse duration of ∼100 fs. The schematic of this Z-scan is shown in the Figure 5.57.

Unlike general z-scan systems, this particular z-scan set-up employs only one InGaAs photodiode (GPD Ltd., GDP3000/2.2). The beam is split then both paths are put through an optical chopper to give them different frequencies. This

photodiode collects the signal of both the reference and open-aperture z-scan of the sample simultaneously. The signals are then separated by a dual reference lock-in amplifier (Signal Recovery, Model 7270) with different frequency. Comparing to the conventional two photodiode scheme, this design can minimise the noise caused by the different response and thermal noise between the two (or more) photodiodes, such as the method employed earlier in this chapter.

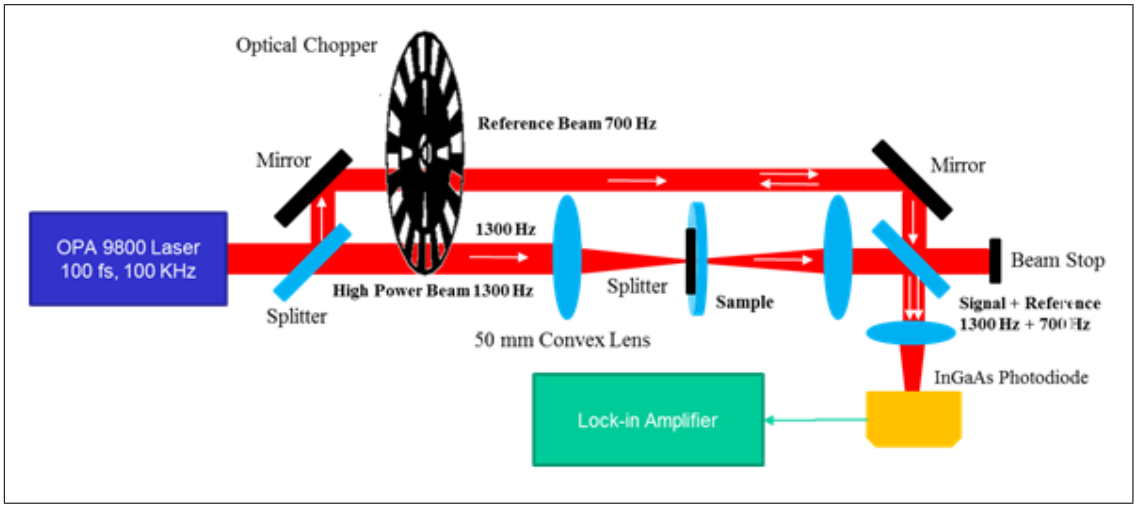

Figure 5.57: New Z-scan Schematic: Utilising a single detector

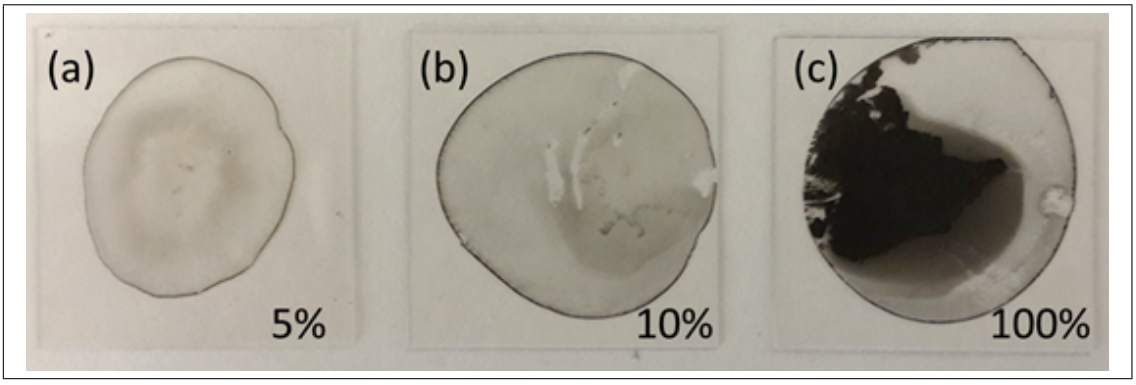

Figure 5.58: Graphene thin films on borosilicate glass prepared via drop-casting and dried in an oven at 200°C

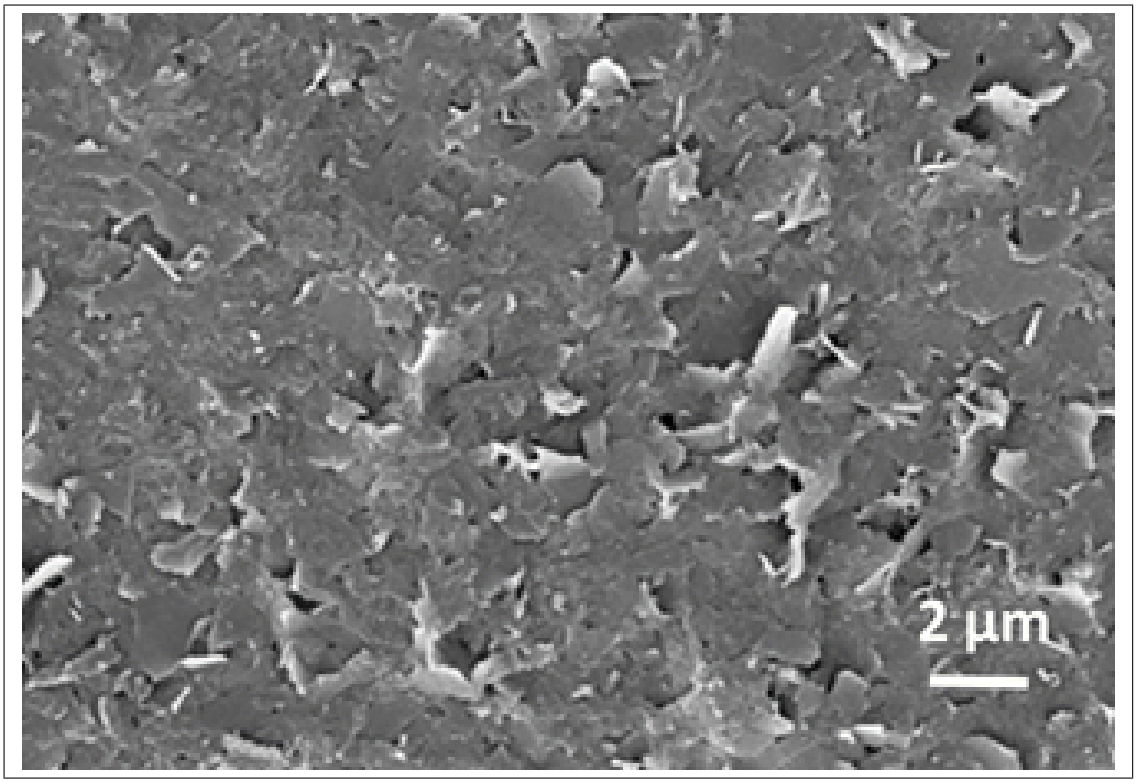

Figure 5.59: SEM image of the graphene thin film , made from the 10% concentration (0.1 mg/ml) graphene/NMP dispersion, shown in Figure 5.58

Utilising the new Z-scan at 2 μm, a typical open aperture result for the drop-cast graphene films is shown in Figure 5.60. The blank borosilicate glass substrates were also tested for comparison.

A 4% optical transmission increase was observed from the graphene film curve around the focal point of focusing lens. As shown in the figure, the blank substrate seems to have no response to the 2 μm laser irradiation.

Despite the high noises levels and the lack of perfect symmetry in the open-aperture curves, there is obvious and strong saturable absorption of the graphene film at 2 μm demonstrated in Figure 5.60.

The 2 μm open aperture z-scan graphs from the graphene thin films are summarised in Figure 5.64. Individual scans at $2.5 GW/cm^2$ (Figure 5.61), $5.1 GW/cm^2$ (Figure 5.62) and $8.9 GW/cm^2$ (Figure 5.63) are displayed, with the fittings showing a nonlinear absorption coefficient of -3.7×10^3 cm/GW, -6.4×10^3 cm/GW and -5.1×10^3 cm/GW respectively.

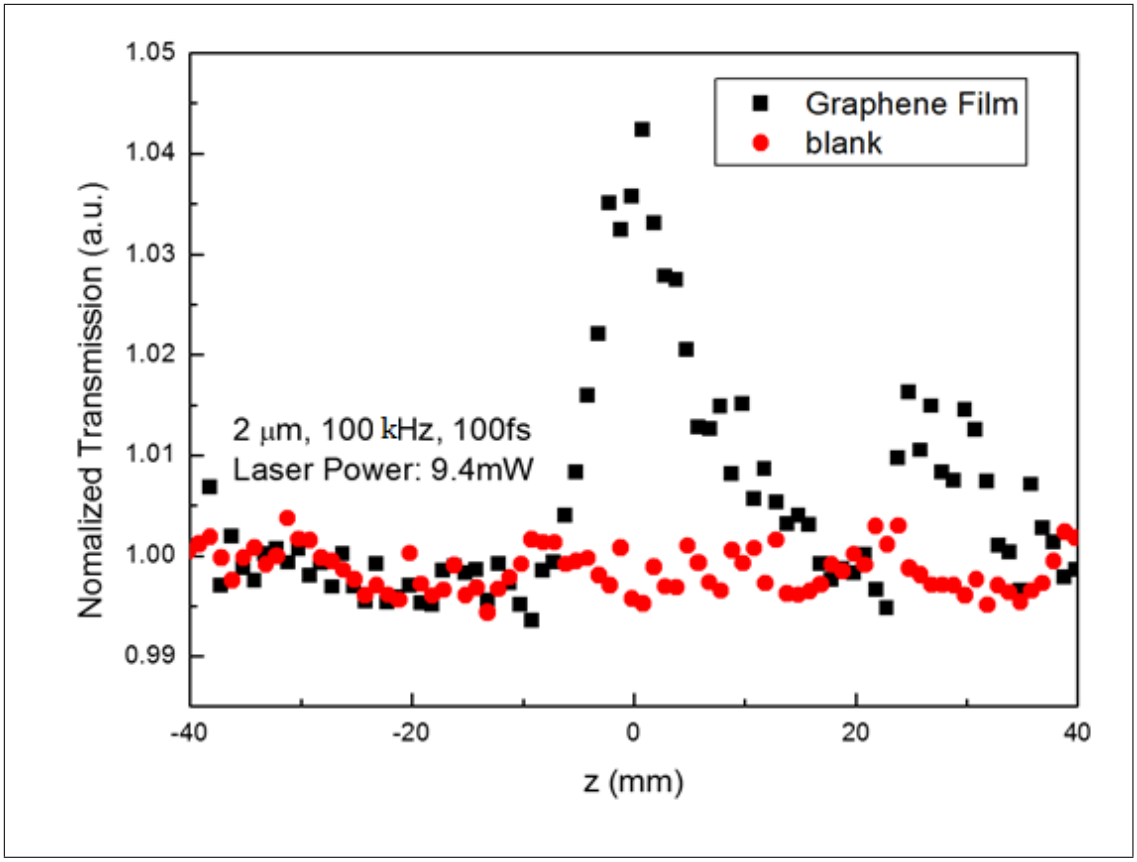

Figure 5.60: Z-scan curve from the graphene (made with a 10% conc. or 0.1 mg/ml dispersion) thin film in the new Z-scan set-up. An intensity of $12GW/cm^2$

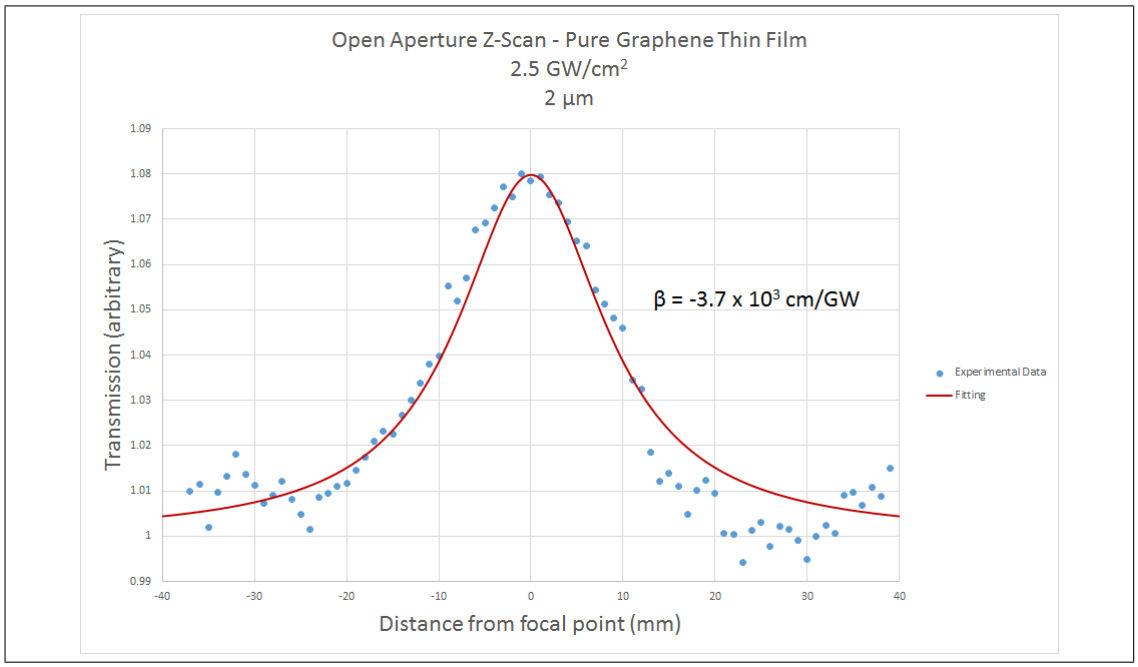

Figure 5.61: Open Aperture Z-Scan of graphene thin films (∼100 nm thickness) at 2 μm, at an intensity of $2.5 GW/cm^2$. The nonlinear absorption (β) for these parameters was -3.7×10^3 cm/GW, via fitting

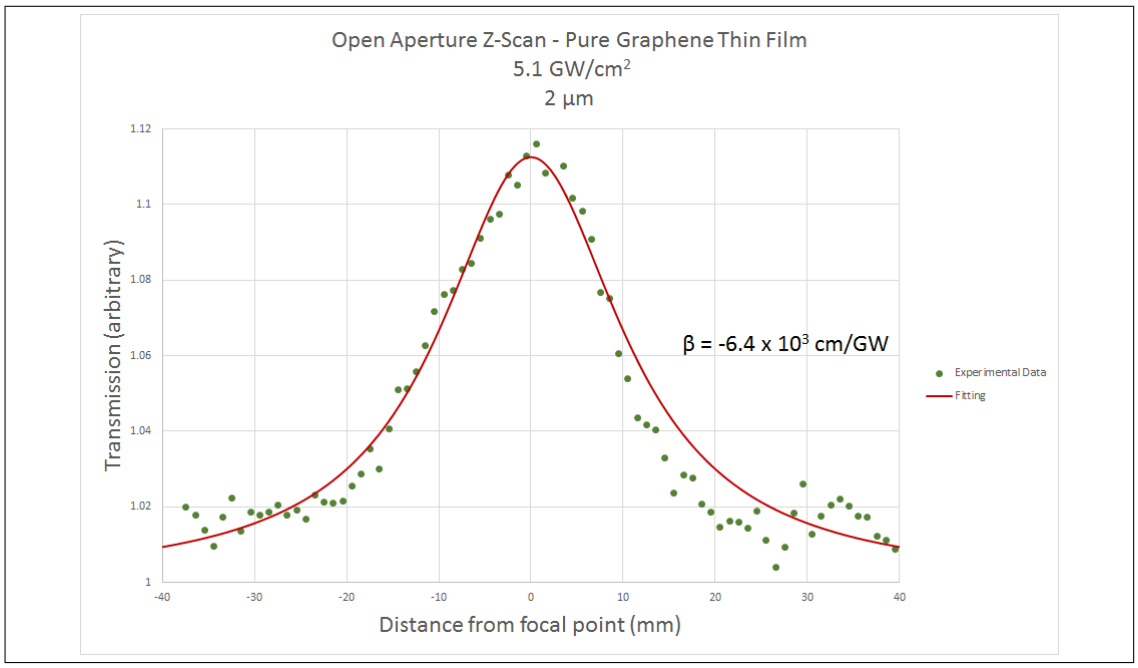

Figure 5.62: Open Aperture Z-Scan of graphene thin films (∼100 nm thickness) at 2 μm, at an intensity of $5.1 GW/cm^2$. The nonlinear absorption (β) for these parameters was -6.4×10^3 cm/GW, via fitting

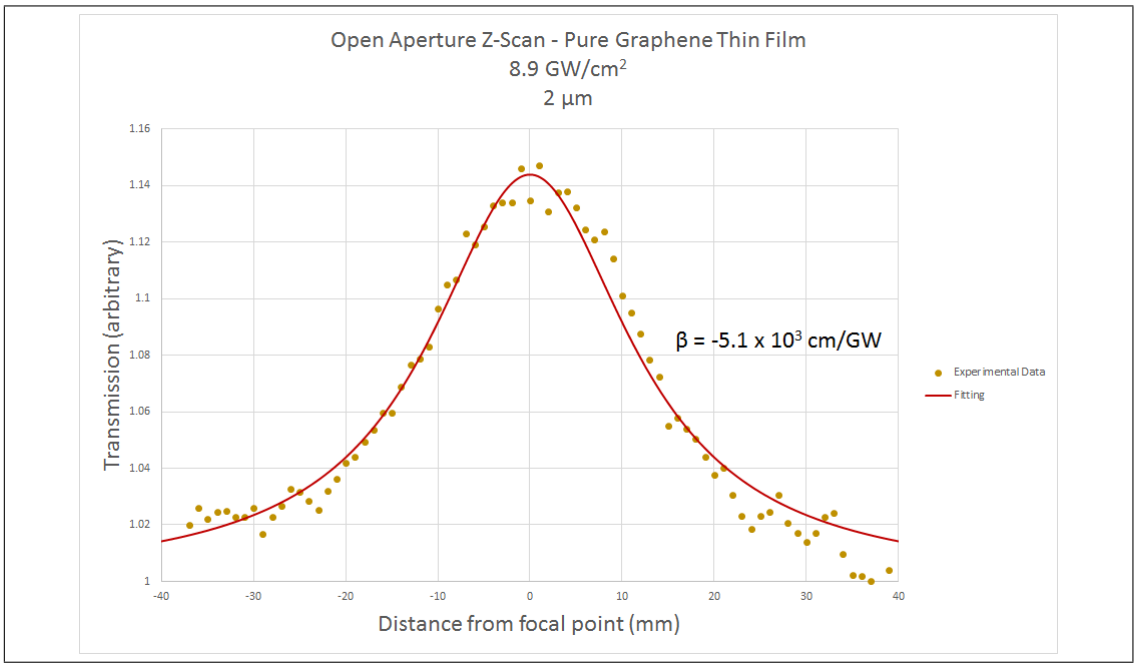

Figure 5.63: Open Aperture Z-Scan of graphene thin films (∼100 nm thickness) at 2 μm, at an intensity of $8.9 GW/cm^2$. The nonlinear absorption (β) for these parameters was -5.1×10^3 cm/GW, via fitting

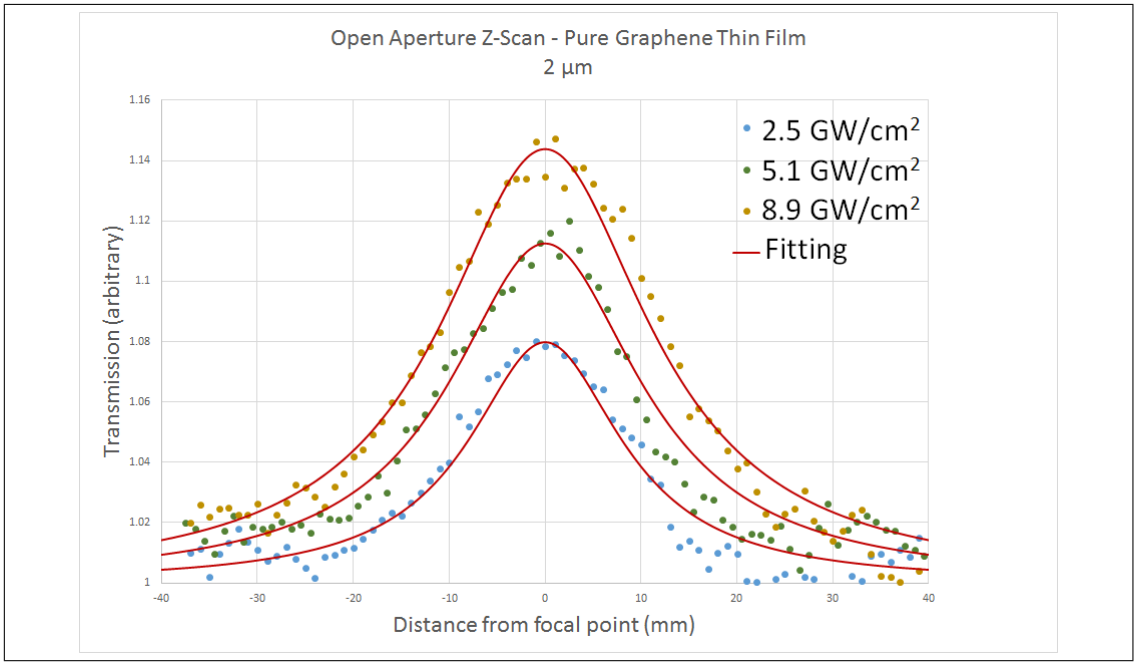

Figure 5.64: Open Aperture Z-Scan of graphene thin films (∼100 nm thickness) at 2 μm, at several intensities

5.2.4 Conclusions from the various graphene Z-scan experiments

Pure graphene films were fabricated to verify the saturable absorption response of graphene prepared by the LPE technique. The open-aperture z-scan technique was employed at 2 μm with a femtosecond laser source. The results confirmed the obvious saturable absorption of graphene, enabling the next phase of the ISLA project which involved preparing graphene SAM device fabrication utilising similar coating techniques and demonstrating the mode-locking capabilities of graphene for both Demo Laser 3 and fibre integrated lasers in general.

Overall the saturable absorption signal of graphene at 1.2 μm appears to be an order of magnitude stronger than the 2 μm, but this may be due to the higher power achievable at 1.2 μm with our system.

Generally, with the saturable absorbing scans, there is a trend for the nonlinear absorption coefficient to increase, thereby decreasing the overall absorption of the system, as expected. This increase can be seen in the graph of intensity versus β for the 1.2 μm graphene thin film samples discussed earlier, in Figure 5.65.

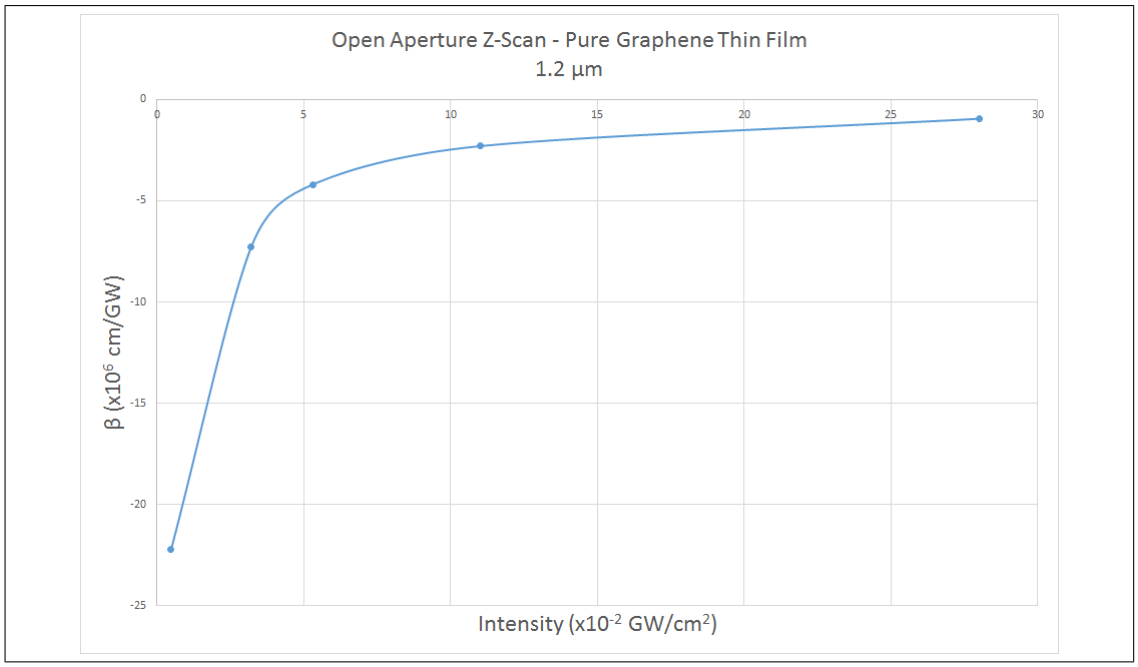

Figure 5.65: Intensity verus nonlinear optical absorption coefficient for graphene thin films at 1.2 μm

The results obtained from fitting the experimental data from this chapter are colligated in Tables 5.9 (films) and 5.10 (dispersions)

Table 5.9: Results from the various z-scan experiments, including the nonlinear optical absorption coefficient

Sample	Wavelength (μm)	Pulse Duration (fs)	Repetition Rate (MHz)	Intensity (GW/cm^2)	β ($\times 10^6 cm/GW$)
Graphene Thin Film	1.2	100	80	0.0048	-22.2
Graphene Thin Film	1.2	100	80	0.032	-7.3
Graphene Thin Film	1.2	100	80	0.053	-4.2
Graphene Thin Film	1.2	100	80	0.11	-2.3
Graphene Thin Film	1.2	100	80	0.28	-0.95
Graphene Thin Film	2	100	80	0.008	-1.2
Graphene Thin Film	2	100	80	0.016	-0.86
Graphene Thin Film	2	100	80	0.021	-0.92
Graphene Thin Film	2	100	80	0.045	-0.18
Graphene Thin Film	2	100	0.1	2.5	-0.0037
Graphene Thin Film	2	100	0.1	5.1	-0.0064
Graphene Thin Film	2	100	0.1	8.9	-0.0051
0wt% Graphene/Polystrene	2	100	80	0.045	-0.25
1wt% Graphene/Polystrene	2	100	80	0.045	-0.2
5wt% Graphene/Polystrene	2	100	80	0.045	-0.1

Table 5.11: Nonlinear optical properties of few-layer $MoSe_2$

I_0 (MW/cm^2)	Modulation Depth (%)	β (cm/GW)	$Im(\chi^{(3)})$ $(-X10^{-14}$ $esu)$
39	7.4	-0.017	-0.98
234	15.1	-0.044	-2.5

Table 5.10: Results from the various z-scan experiments, including the nonlinear optical absorption coefficient

Sample	Wavelength (μm)	Pulse Duration (fs)	Repetition Rate (MHz)	Intensity (GW/cm^2)	β (cm/GW)
Graphene/NMP	1.2	100	80	0.0032	0.85
Graphene/NMP	1.2	100	80	0.008	1.8
Graphene/NMP	1.2	100	80	0.018	1700
Graphene/NMP	2	100	80	0.0095	12.8
Graphene/NMP	2	100	80	0.032	3.7
Graphene/NMP	2	100	80	0.043	4.8

5.3 Other 2D Materials

A very brief exploration into the nonlinear optical properties of carbon nanotubes, molybdenum disulphide MoS_2 and boron nitride BN can be found in the appendix.

Our previous $MoSe_2$ measurements give a β, $Im(\chi^{(3)})$ and modulation depth of -0.017 cm/GW, -0.98x $10^{-14} esu$ and 7.4 % respectively at 39 MW/cm^2, 800

nm, 100 fs, 100 kHz, as displayed in Table 5.11 (Wang *et al.*, 2018a).

As such, the $MoSe_2$ has a β 6 orders of magnitude lower than graphene, which is reflected in the lower $Im(\chi^{(3)})$.

However, the Sb thin films examined in Section 5.2.1.7 has nonlinear optical properties closer to that of graphene, as shown in Table 5.8. For example, the Sb films exhibited β, n_2, modulation depth and $\chi^{(3)}$ 29,000 cm/GW, 1.28 cm^2/GW, 2.3 % and 24x $10^{-8} esu$ respectively at 4.5 GW/cm^2. Sb compares quite favourably with graphene.

6

Graphene Saturable Absorber Mirror (GSAM) Nonlinear Optics

In this chapter, the nonlinear optical properties of the prepared graphene saturable absorber mirrors are examined with reflected laser light via the I-scan method. Both drop-cast G-SAMs and vacuum filtrated G-SAMs performed comparably or superior to commercially available SESAMs that operate at 2 μm.

Mid-infrared ultrafast lasers have emerged as a promising platform for both science and industry because of their inherent high raw power and eye-safe spectrum. 2D nanostructures such as graphene have emerged as promising photonic materials for laser mode-locking to generate ultrashort pulses. However, there are still many unanswered questions about graphenes key advantages to be practical devices, especially over the matured semiconductor saturable absorber mirror (SESAM). In this chapter, a systematic comparisons on the nonlinear optical properties of drop-cast and vacuum filtrated graphene Saturable Absorber Mirror (SAM) and that of commercial SESAM at 2 μm wavelength was conducted. Our results showed that graphene has significant advantages over the commercial SESAM, exhibiting 28% less absorptive cross-section ratio of excited-state to ground-state and 50 times faster relaxation time. This implies that graphene can be exploited as a better mode-locker than the current commercial SESAM for high power, high repetition rate and ultrafast mid-infrared laser sources.

6.1 Saturable Absorber Devices

Two types of Graphene Satruable Absorber Mirror (GSAM) were fabricated via different methods. The primary samples were made via vacuum-filtration of our graphene dispersion onto filter paper and then transferring to silver mirrors.

A separate batch of GSAM devices were fabricate via a much simpler drop-cast method onto identical silver mirrors. These were included to show the capabilities of cheaper and simpler fabrication methods, and the ability to tailor the non-linear parameters of the device via graphene thickness which in turn is determined by the dispersion concentration.

Both sets of in-house devices were compared to a well established SESAM designed to operate at 2 μm. The comparative SESAM was purchased from BATOP (SAM-2000-44-10ps, See Figure 6.1 c). The nominal working wavelength, absorption and relaxation time are 2000 nm, 44%, and 10 ps respectively.

6.1.1 Device Fabrication

The large-area GSAM device referred to as the "vacuum-filtrated GSAM" in this work was fabricated by vacuum filtration methods using liquid-phase exfoliated graphene nanoflakes.(Coleman *et al.*, 2011a; Haus, 1975a; Hernandez *et al.*, 2008b) Briefly, graphite powder (Sigma Aldrich) was exfoliated in distilled water (5 mg/mL) by liquid-phase exfoliation with sodium cholate (0.1 mg/mL) utilised as surfactant. The dispersion was centrifuged at 3000 rpm to remove large flakes. After this, we produced graphene membrane from vacuum filtration of the graphene dispersion using a nitrocellulose porous membrane (Millipore, m = 100 nm). The wet membrane was then attached onto a silver mirror (Thorlabs, PF05-03-P01) with a 1 kg weight applied for 12 hours to ensure firm contact between the nanoflakes and the mirror. Finally, we removed the nitrocellulose membrane from the GSAM surface using acetone. After which the GSAM was ready for characterization. Figure 6.1 (a) presents the optical image of the as-fabricated GSAM, showing a large high-quality graphene film on the surface of the silver mirror.

The devices referred to as "drop-cast GSAM" were prepared via drop casting graphene/NMP dispersions and dried in the oven at 200C. The graphene/NMP dispersion fabrication was previously described in Chapter 5.

6.1.2 Device Characterisation

To investigate the geometry of the vacuum-filtrated GSAM, scanning electron microscopy (SEM) and atomic force microscopy (AFM) were employed to study the characteristics of the device. Figure 6.1 (b) shows a low magnification SEM

image on the vacuum-filtrated GSAM. The clear boundary of graphene on the mirror and flat surface implies a homogeneous deposition. As we went to higher magnification in Figure 6.1 (d), we found the graphene film was composed by many small graphene flakes around 500 nm size. Figure 6.1 (e) shows an AFM image of a 10 μm x 10 μm area. Most area has a height variation below 100 nm (dark colour), while the others with large height is presented in bright (>240 nm). From AFM measurements, the surface roughness, R_a, was measured to be 57.42 nm for the vacuum-filtrated GSAM. Raman spectroscopy is a useful way to investigate the thickness of graphene nanoflakes. With the thickness increasing from monolayer, to bilayer, to bulk, the 2D peak shifts from 2680, 2700 to 2720 cm^{-1} respectively.(Ferrari & Basko, 2013) Figure 6.1 (g) shows the mapping of 2D peak using 514 nm excitation. The blue area (>2700 cm-1) represents multi-layer flakes, whereas the red (2700 cm-1) indicates the mono- and bi-layers. It is revealed that the graphene film is composed of mixture of monolayers and few-layers. Mono- and bi-layer flakes cover the most area in the mapping. To investigate the average thickness of the graphene film, the Raman spectra was averaged for a large area 200 μm x 100 μm, which is presented in Figure 6.1 (f). The G and 2D peaks were found at 1580.3 and 2695.6 cm-1 respectively. This corresponds to an average thickness of 1.7 layers of graphene flakes composing the graphene film.

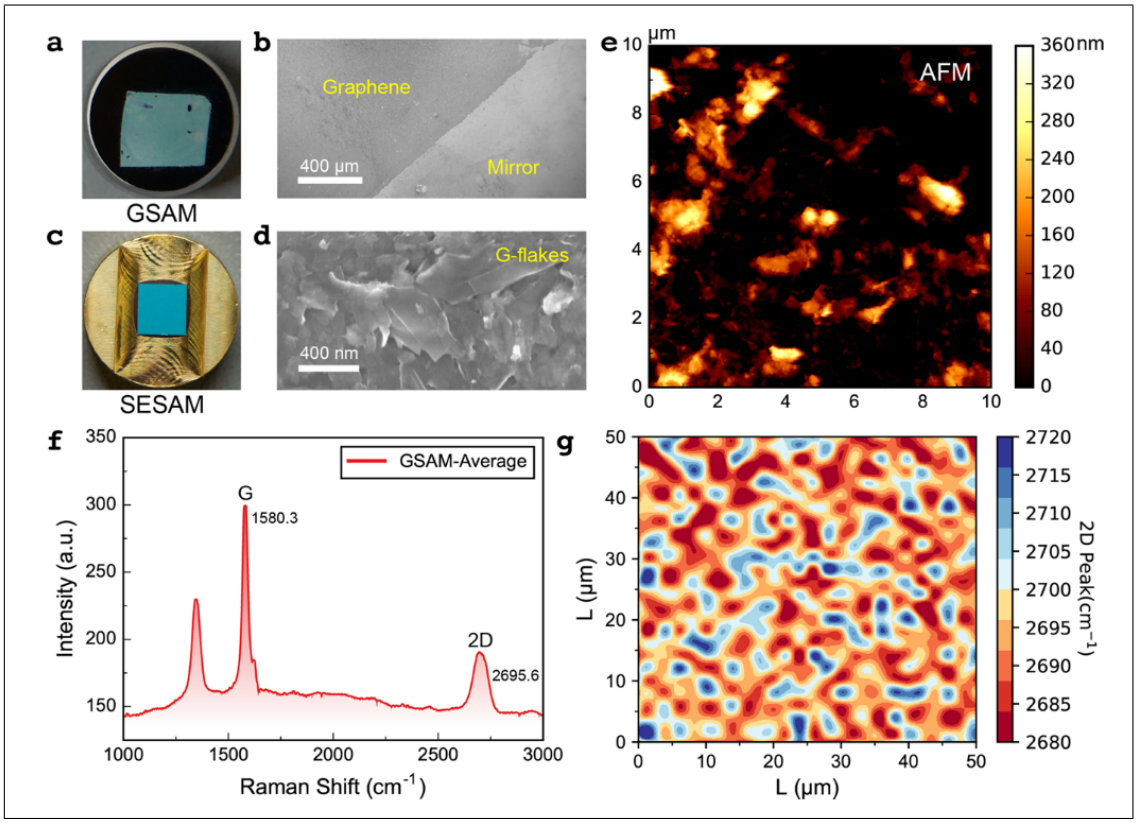

Figure 6.1: Characterizations of graphene saturable mirror (GSAM). The GSAM image taken by camera (a), low magnification SEM (b) and higher one (d). The commercial SESAM (BATOP, SAM-2000-44-10ps) for comparison is showed in (c). (e)AFM image of graphene film on GSAM. (f) is the average Raman spectra from a 200 μm x 100 μm Raman mapping of our graphene film. (g) Raman mapping representing the shift of the graphene 2D peak. The blue area (>2700 cm^{-1}) represents multi-layer flakes, whereas the red (>2700 cm^{-1}) indicates the mono- and bi-layers. (Wang *et al.*, 2017a)

As predicted by the vacuum-filtrated GSAM optical image as well as the AFM roughness in Figure 6.1(a) and (e), unneglectable surface scattering may exist on the vacuum-filtrated GSAM prototype. To subtract the effect of scattering from the NLO parameters, the surface scattering of the vacuum-filtrated GSAM was measured using a UV-Vis-NIR spectrophotometer equipped with an integrating sphere. Figure 6.10 (a) displays the reflection, scattering and the absorption of the GSAM from 1.6 μm to 2.4 μm. The solid lines are linear fittings as a visual guide. The exact values of scattering, linear reflection and absorption at 2 μm for our GSAM are determined to be 13.8%, 65.3% and 20.9% respectively. With the absorption of monolayer graphene equal to 2.3%, the average number of layers on our vacuum-filtrated GSAM sample was estimated to be 5 when considering light

passes twice through the graphene film.(Dawlaty *et al.*, 2008c)

6.2 I-Scan

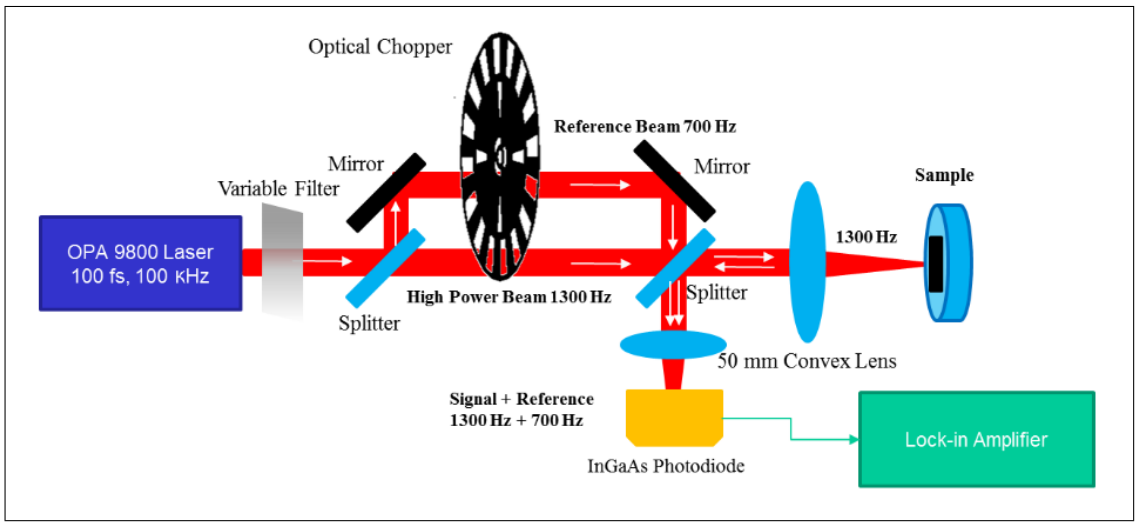

Figure 6.2: Schematic of the I-scan system used

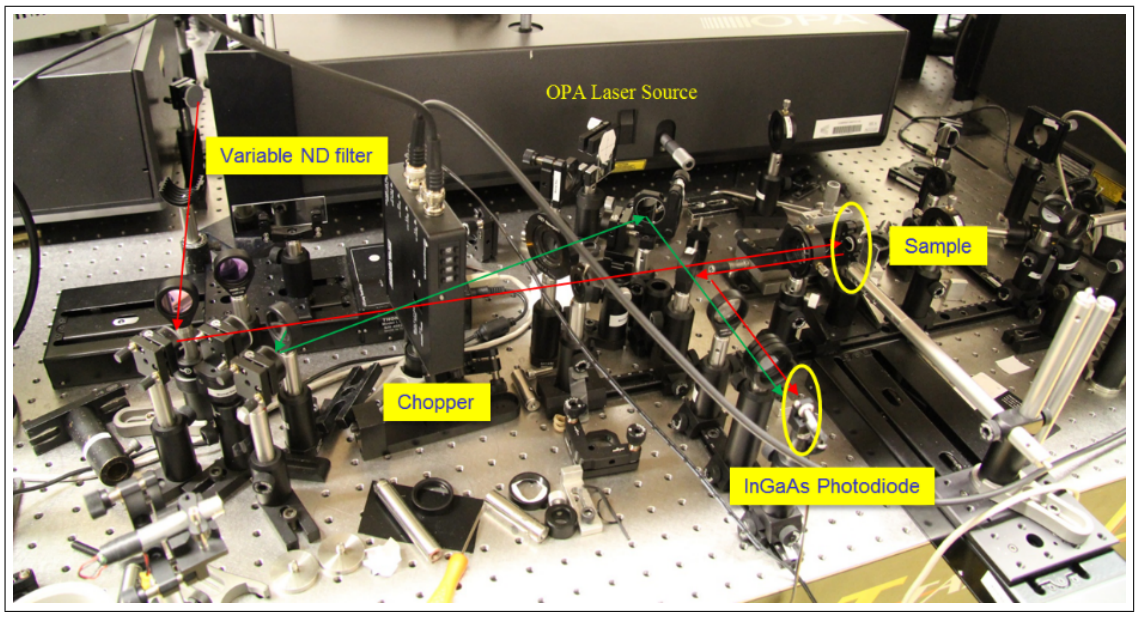

Figure 6.3: Photograph of the I-scan system used

Both I-Scan and Z-scan are widely accepted methods for measuring the optical nonlinearity of samples (Said *et al.*, 1992; Samuel *et al.*, 2013; Sheik-Bahae *et al.*, 1989b). The main idea behind I-scan is placing the sample at the focus of convex lens to obtain high laser intensity, and then change the incident laser intensity by a variable filter. The light leaving the sample, which contains the information regarding the nonlinear optical response of the sample, is collected by photodiodes. The result of the I-scan is a direct function of laser power to sample transmission or reflectance, depending on sample type.

Compared to the Z-scan technique, I-scan is more suitable for measuring samples which are less homogeneous and flat. Z-scan is actually measuring points of a line on samples because there is always an angle between the sample move trace and the laser direction. The laser spot size on sample also changes during a z-scan measurement. So the homogeneousness of the sample has a large effect on the accuracy of z-scan. However, I-scan is less sensitive to sample homogeneousness. That is because there is no movement of the sample or laser, nor any change of the laser spot size during measurements utilising the I-scan technique. I-scan can always be fixed to measure one exact point and get extremely low noise. In this report, we adopted an I-scan set-up to test our graphene SAMs.

Figure 6.2 and Figure 6.3 represent our I-scan schematic and setup respectively. The ultrafast mid-infrared laser pulses (2 μm, 100 kHz, 150 fs) for nonlinear-optical (NLO) measurements were generated by an optical parametric amplifier (Coherent OPA9800) pumped by a 800 nm Ti:Sapphire femtosecond laser. (Coherent RegA 9000). The 2 μm laser wavelength was confirmed by spectrometer (Ocean Optics, NIR Quest). Then the laser goes through a variable filter which is installed on a motorized translation stage. During an I-scan measurement, the translation stage moves and introduces a variable laser power onto the sample. After the variable filter, the laser is split into a reference beam and a high-power (sample) beam, and then said beams are modulated to 1300 and 700 Hz by an optical chopper, respectively. The high-power beam is focused on the SAM sample and reflected back to be the signal beam. Finally both signal and reference beams are combined by another beam splitter and collected by a single InGaAs photodiode. A two-channel lock-in amplifier (Signal Recovery, SR7270) was employed to collect both the reflected and reference signal. This produces curves exhibiting the nonlinear response of the sample.

In order to obtain the real effect from the graphene coating on the G-SAM, we employ comparisons between the SAM and a blank silver-coated mirror throughout all measurements. No nonlinear optical response was observed from the blank mirrors in this report.

The graph obtained from I-scan measurements from the set-up in Figure 6.2 is a reflectance function about incident laser power, but the final graph is required

to be a function of the incident laser intensity. Therefore, it is necessary to obtain the beam profile on the surface sample mirrors. To achieve this, the reflective laser power shaded by a moving blade was measured, as shown in the inset of Figure 6.5 (a). The typical result is presented in Figure 6.5 (a) and the differential curve are showed as Figure 6.5 (b). Using Gaussian fitting, the beam diameter (Full-Width at Half Max (FWHM)) can be calculated. The beam diameter was calculated to be 93.5 $\pm$ 1.7 μm and the whole setup was maintained to be exactly the same throughout the measurements in this report.

6.2.1 Performance of Graphene SAM

The ultrafast saturable absorption properties of graphene SAMs are investigated by I-scan with a 2 μm, 100 fs and 100 kHz laser from an OPA pumped by a 800 nm Ti:Sapphire femtosecond laser source, as described in Section 3.1.4.3.

There are three parameters which are important to the performance of a saturable absorber mirror for mode-locking applications

- Modulation depth
- Non-saturable loss
- Saturated intensity

Modulation depth is the reflectance range that a saturable absorber mirror can alter. It equals the Maximum Reflectance (R_{max}) subtracted by the Linear Reflectance (R_0).

Non-saturable loss is the light energy loss when the SAM is saturated and reflectance reaches its maximum R_{max}. An ideal saturable absorber will have a zero non-saturable loss.

The saturated intensity, I_S, is defined as the laser intensity when a saturable absorber reaches its half modulation depth. A good saturable absorber should have low saturable intensity and non-saturable loss while retaining a high modulation depth.

6.2.1.1 I-scan results of the vacuum-filtrated Graphene SAM

Figure 6.4 shows the results regarding the optical reflectance of vacuum-filtrated graphene SAM as a function of laser intensity. The three curves shown are from the same sample but at different test points. All tests imply obvious saturable absorption of the graphene SAM at 2 μm wavelength. When the laser intensity is

below 0.01 GW/cm^2, the graphene SAM exhibits a linear optical response with a reflectance from 63% to 67%.

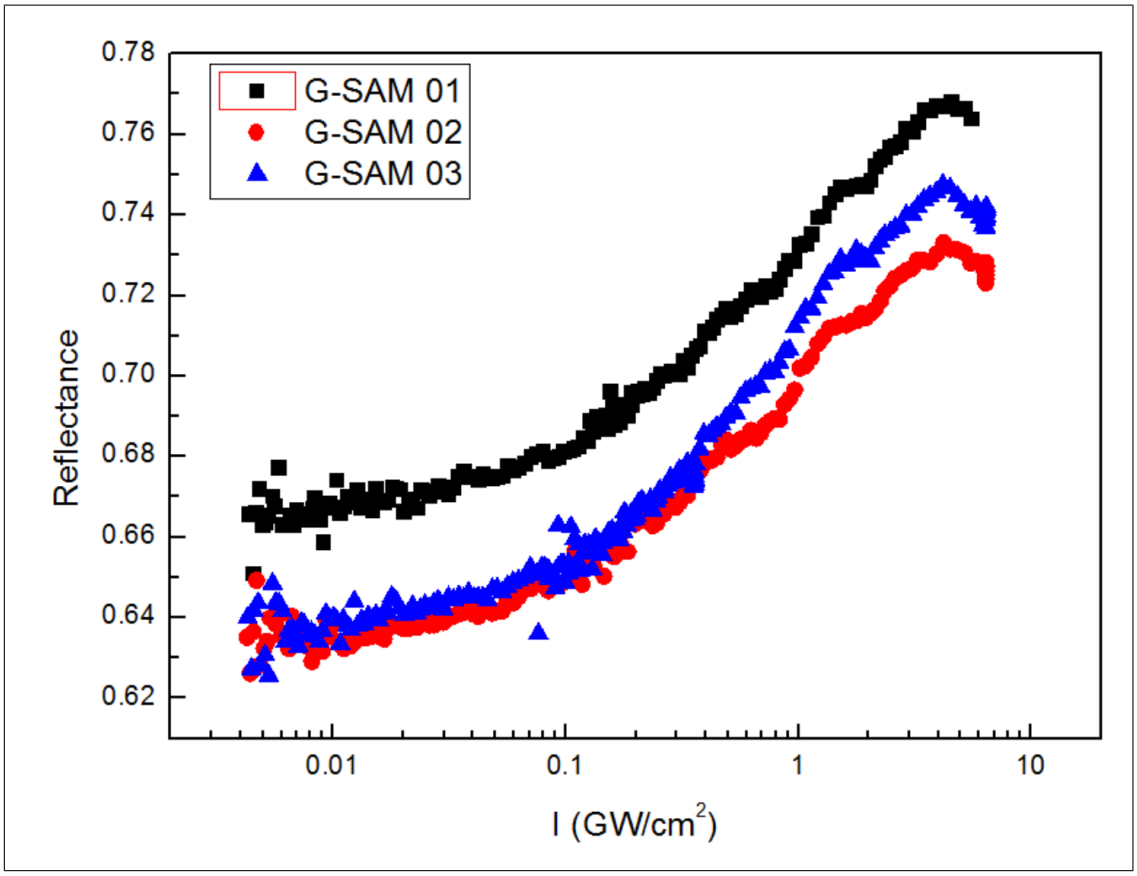

Figure 6.4: I-scan curves from the vacuum-filtration prepared Graphene SAMs at $2\mu m$, ~100 fs laser with 100 kHz repetition rate. Three curves are from the same sample but different point

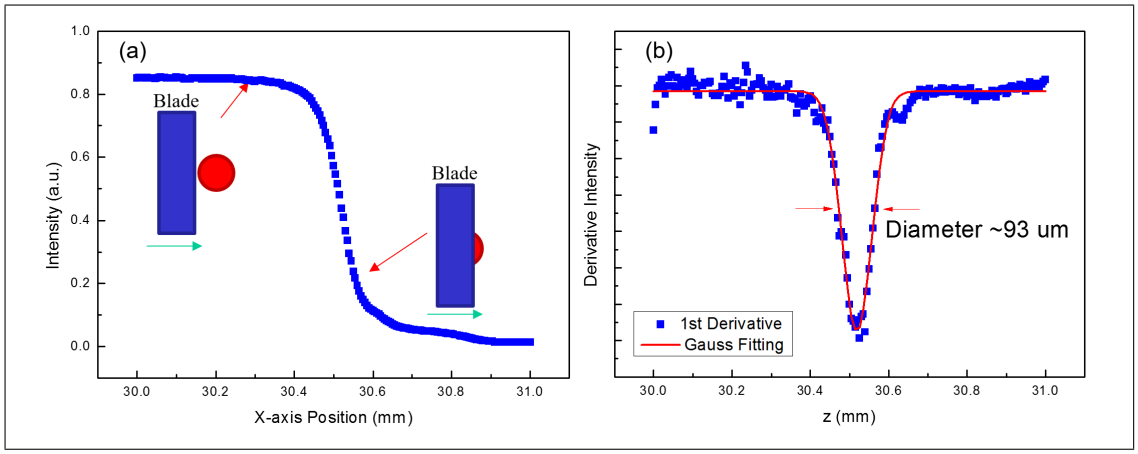

Figure 6.5: Beam Diameter Measurement

The linear reflectance deviation of the three curves suggests that there are different thicknesses of graphene film on the SAM, despite the flat appearance in Figure 4.17 (b).

Then the increasing laser power excites the graphene into the nonlinear optical region and the reflectance rises with the intensity due to the Pauli-blocking in the graphene bandgap (Bao *et al.*, 2009). After the laser intensity approaches 3 GW/cm^2, the reflectance of graphene SAM appears to reach a limit around 74%, corresponding to 36% non-saturable loss. For simplicity and clarity, all the NLO parameters obtained are summarised in Table 6.1.

6.2.1.2 I-scan results of the drop-cast Graphene SAM

The NLO response of graphene SAMs prepared via the drop-cast method was also investigated with the I-scan technique at 2μm, as shown in Figure 6.6. The results displayed were from three different graphene mirrors, prepared with 5%, 10% and 100% concentration of the graphene/NMP dispersions described in Section 3, and can be seen in Figure 6.7. The mirrors shown in said figure appear black in these images, which was set as such when viewing under the light microscope to highlight the graphene, as otherwise it would be more difficult to see.

Due to the inhomogeneousness of the drop-cast graphene films, the test points were picked randomly. As seen in Figure 6.6, all three tests exhibit saturable absorption of the graphene SAM when exposed to 2 μm ultrafast irradiation.

The 5% and 10% graphene SAMs are both saturated at high laser intensity, while the reflectance of the 100% graphene SAM seems to still be increasing at our highest intensity. The linear reflectance of 5%, 10% and 100% are 79.6%, 43.4% and 10.5% respectively, which corresponds with the graphene dispersion concentration.

However, the modulation depth and saturated intensity does not seem to have the similar trends with dispersion concentration. This may be attributed to the scatter of graphene nanosheet segregations on the mirror surface.

Again, all the NLO parameters obtained from Figure 6.6 are also summarised in Table 6.1.

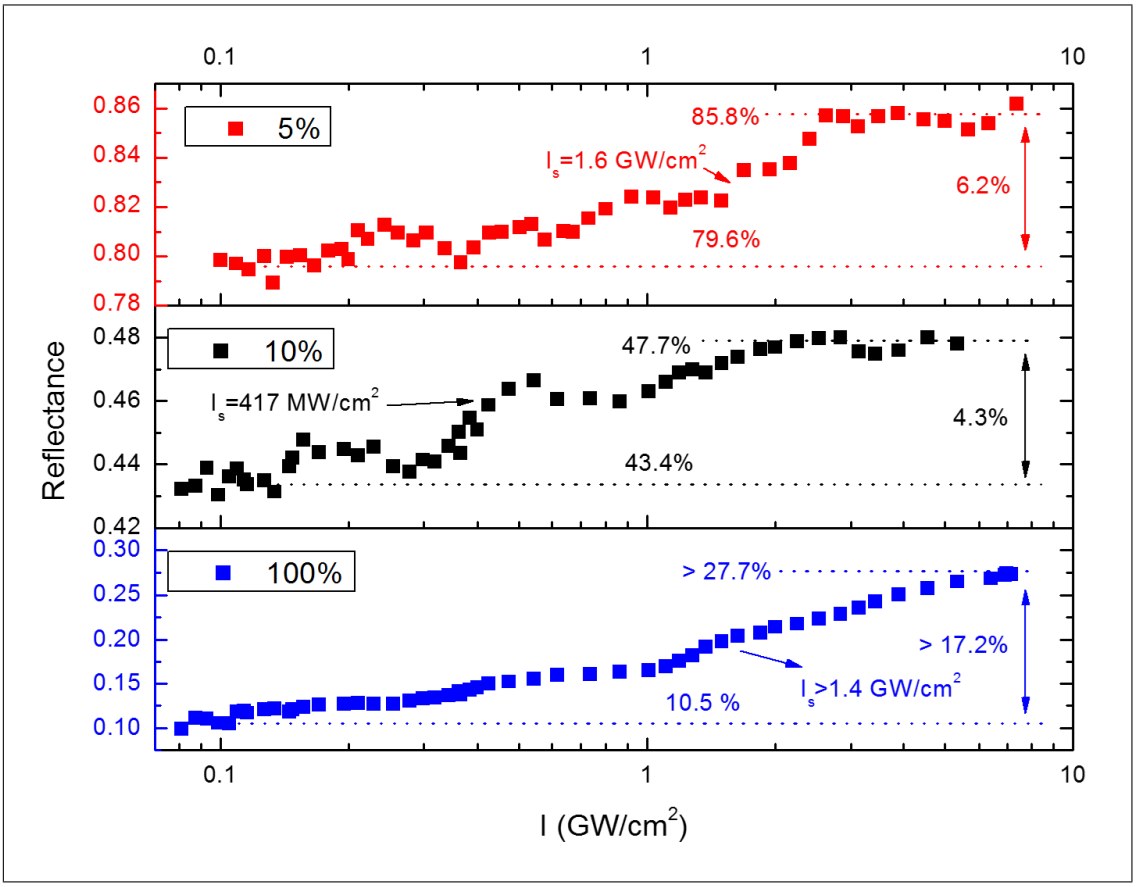

Figure 6.6: I-scan curves from the drop-cast Graphene SAMs at $2\mu m$. 5%, 10% and 100% indicate the concentration of graphene dispersions used for graphene SAM preparations. All the test points are randomly picked

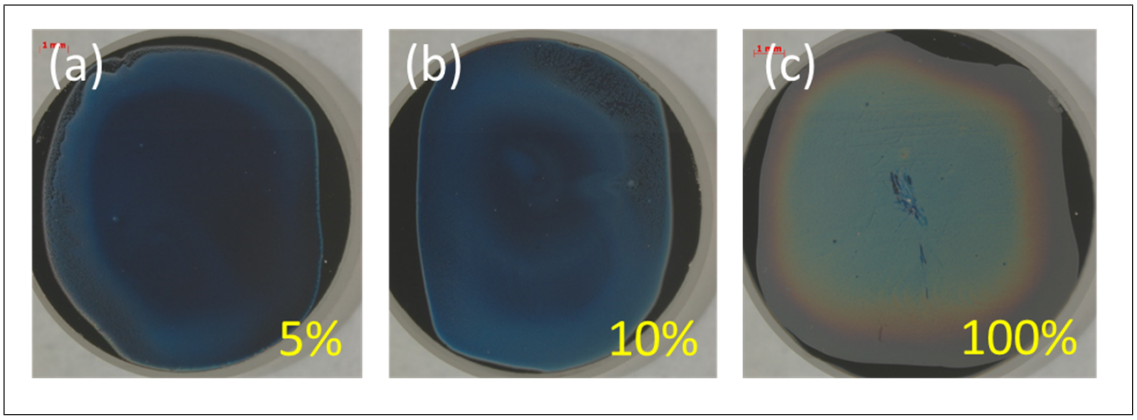

Figure 6.7: Graphene SAMs prepared via drop-casting of graphene/NMP dispersions

6.2.1.3 I-scan results of the BATOP SESAM

In order to evaluate the commercial potential of our graphene SAMs, comparisons were made with a SESAM purchased from BATOP (SAM-2000-44-10ps). The SESAM was tested with the same I-scan setup , parameters and steps described previously for the graphene SAMs. Figure 6.8 represents the typical curves of the SESAM nonlinear optical response at $2\mu m$ wavelength. All the tests were on the same sample, but at different points.

Similarly to our graphene SAMs, the SESAM exhibits strong saturable absorption when the laser intensity increased. However, the SESAM tests in Figure 6.8 were much more stable compared to that of the graphene SAM in Figure 6.4, implying that the SESAM chip has a very homogeneous structure. This advantage is likely due to the high-cost, but precise, control during chip growth process.

The linear reflectance of SESAM is around 64.6% and the saturated reflectance is close to 74.6%. Thus the modulation depth should be ∼10%, corresponding closely with the value from the factory data sheet. The Saturated Intensity (I_S) can be estimated to be 72 GW/cm^2. All the NLO parameters obtained from these tests are also presented in Table 6.1 for comparisons.

It should be mentioned that the response of the SESAM is very sensitive to the laser wavelength in our measurements. A small wavelength shift to even just 1.9 μm will result in no saturable absorption response from the SESAM chip. However, obvious saturable absorptions can still be observed from both of the graphene SAMs examined at the same 1.9 μm wavelength, highlighting the broadband response potential of graphene SAMs.

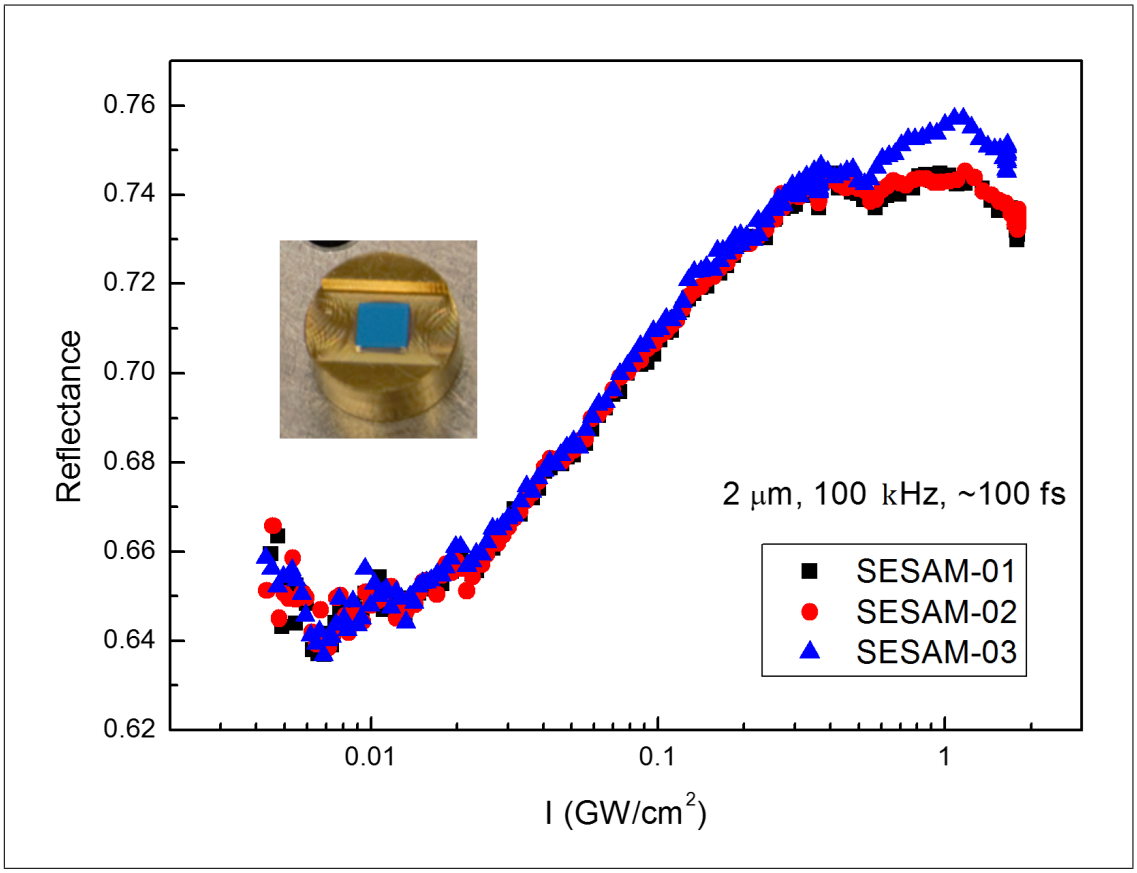

Figure 6.8: I-scan curves from the BATOP SESAM at $2\mu m$, ~100 fs laser with 100 kHz repetition rate. Inset: SESAM chip on copper substrate. 01, 02 and 03 indicate the different test point on the same chip

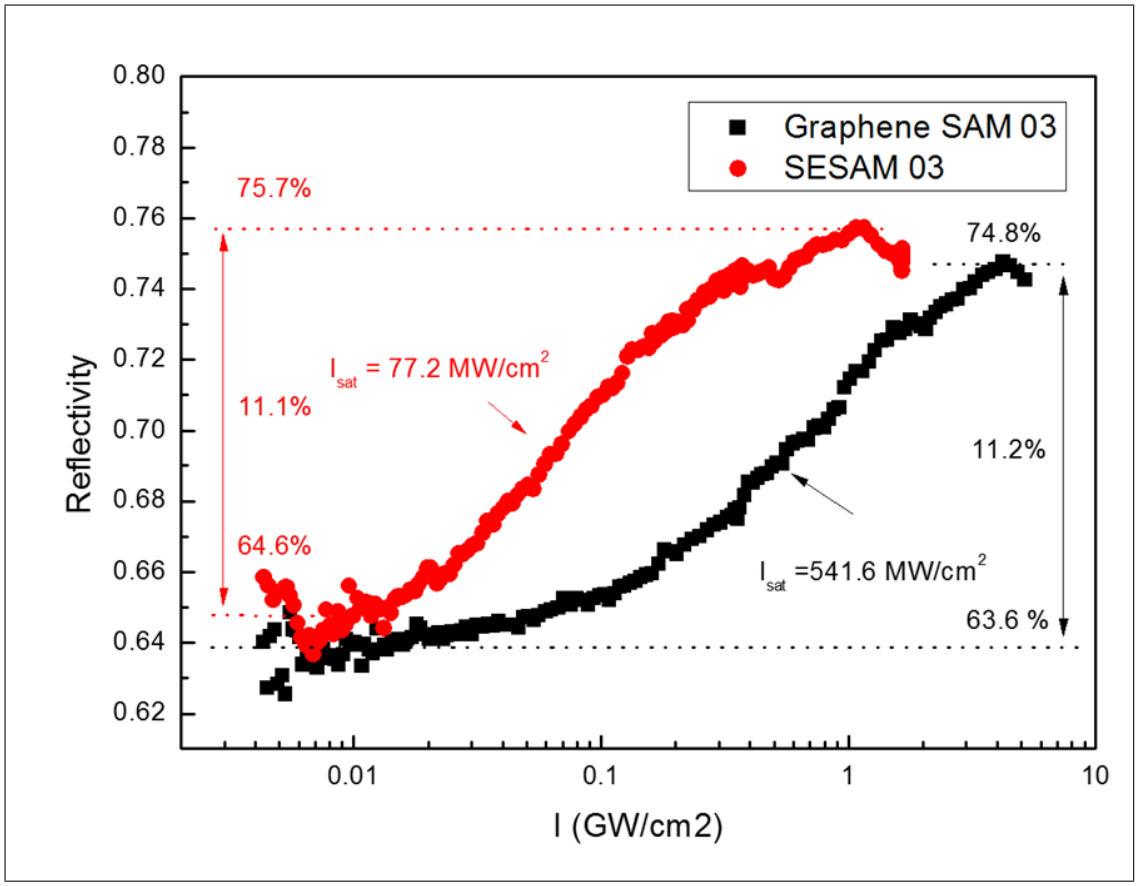

Figure 6.9: Direct Comparison Between Vacuum-Filtration Prepared Graphene SAM and BATOP SESAM at $2\mu m$. Both SAMs exhibit very similar saturable absorption behaviour except different saturated intensity I_s. The curves are picked from Figure 6.4 and Figure 6.8 respectively.

6.2.1.4 Comparison between the Graphene SAMs and the BATOP SESAM I-Scan results

Figure 6.9 presents a direct comparison between the vacuum-filtrated graphene SAM and the commercial BATOP SESAM for better clarity.

Figure 6.10 (b) presents the experimental I-scan curve of GSAM and SESAM. Both samples exhibited typical saturable absorption behaviour, i.e., reflectance increasing with incident laser power. To further analyse the NLO response of our samples, we employed a modified slow-absorber model to fit the results. (Eq. 6.2) The fitting curves are presented in solid lines in Figure 6.10 (b), displaying a favourable fit with experimental results. Both samples showed very similar linear reflectivity, R_0, of 64%, maximum reflectivity, R_{max}, of 76% and a modulation depth, ΔR, of 13%. Note that the R_0 value of our GSAM obtained via I-scan,

63.7%, approximates to the 65.3% we got from integrating sphere, which implies strong coherence of our measurements. The saturated fluence, F_s, is defined as the laser intensity when a saturable absorber reaches its half modulation depth. Our measurements revealed a saturated fluence at 52.4 and 6.9 $\mu J/cm^2$ for our GSAM and the commercial SESAM respectively. These correspond to saturated intensities, I_s, of 349.3 and 46.0 MW/cm^2 respectively. All parameters are summarised in Table 6.1. The I-scan results imply our GSAM has a comparable performance to the SESAM at 2 μm wavelength except for the F_s value. However, it should be noted that the GSAM has a much broader wavelength response. During measurements, it is observed that even a small wavelength drift to 1.9 μm eliminated the saturable absorption response of the commercial SESAM. Furthermore, if the surface roughness can be reduced for graphene films, then GSAMs have excellent potential to outperform standard SESAM designs.

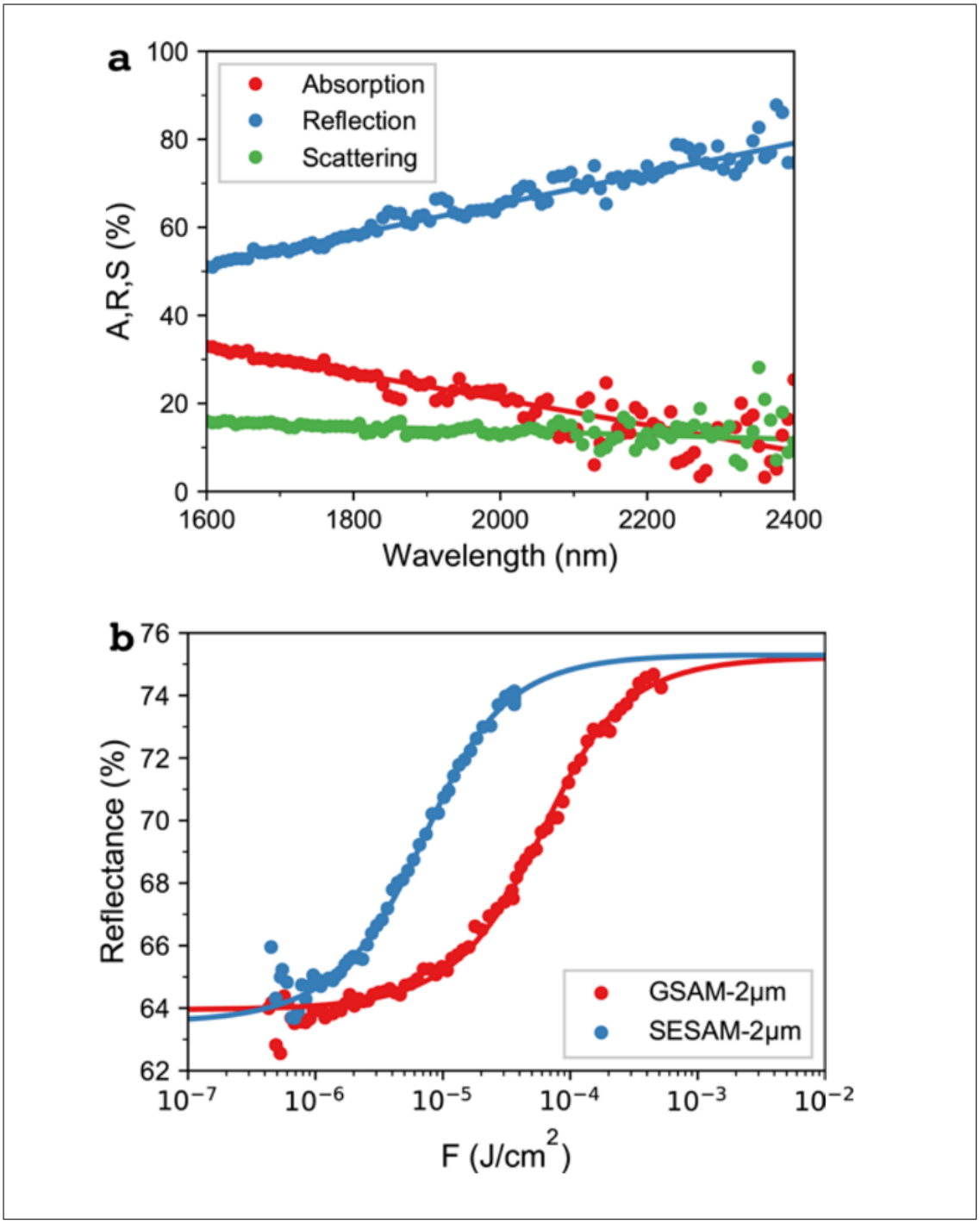

Figure 6.10: Optical responses of graphene saturable absorber mirror. (a) Absorption, reflection and scattering responses of our GSAM with a wavelength range from 1.6 to 2.4 μm using an integrating sphere. The scattering at 2 μm is shown be 13.8 % for GSAM. Solid lines are for visual guide. (b) Scatters represent the nonlinear reflectance of GSAM and SESAM as a function of laser fluence with 2 μm 100 fs pulses. Solid Lines show the fitting curves by a slow-absorber model with nonlinear regression algorithm

Table 6.1: Nonlinear saturable absorption parameters of graphene SAM and SESAM via I-scan measurements. R_0, R_{max} and ΔR denote for the linear reflectivity, maximum reflectivity and modulation depth respectively. A_0 and A_{ns} are the linear and non-saturable absorption respectively. S is the scattering loss caused by the surface roughness.

Sample	R_0	R_{max}	ΔR (%)	A_0 (%)	A_{ns} (%)	S (%)	F_s ($\mu J/cm^2$)	I_S (MW/cm^2)
Drop-cast GSAM-5%	79.6	85.8	6.2	20.4	14.2	-	-	1600
Drop-cast GSAM-10%	43.4	47.7	4.3	56.6	52.3	-	-	417
Drop-cast GSAM-100%	10.5	>27.7	>17.2	89.5	<72.3	-	-	>1400
vac.filtrated GSAM	63.7	76.3	12.6	20.9	9.9	13.8	52.4	536
SESAM	63.6	76.8	13.2	36.4	23.2	-	6.9	71

However, the graphene SAM needs a higher laser intensity to be saturated than the SESAM according to the larger I_S. It should be mentioned that considering one advantage of ultrafast lasers are there high intensity, the larger I_S is possibly acceptable in most practical applications.

Another issue that should be noted is that the real saturated intensity of the graphene SAM may not be so different than the SESAM due to fast response time of graphene. It is reported that the response time of graphene is extremely fast, with literature values as low as 100 fs (Bonaccorso *et al.*, 2010), which is of the same order of the excited laser pulse duration (100 fs). However, the SESAM used was a much slower absorber, with a response time of 10 ps. The fast response time of graphene may lead to a much larger saturated intensity with this particular laser set-up because some electrons fall back to the ground state during the pulse duration. This was explored via pump-probe measurements.

The drop-cast GSAMs showed that the various NLO parameters of the GSAM can be tweaked and tailored via the film thickness, which is controllable via the dispersion concentration. The 5% drop-cast GSAM performed comparably with both the vacuum-filtrated GSAM and the commercial SESAM. This device actually showed superior linear reflectivity, R_0, of 79.6% and maximum reflectivity, R_{max}, of 85.8% but had a lower modulation depth, ΔR, of 6%. Note that the non-saturable absorption (A_{ns}) is 14.2%, but does not take in to account the scattering losses due to surface roughness, which was done for the vacuum-filtrated

GSAM. As such, when also taking into account the higher R_0 and R_{max}, and lower ΔR, the actual A_{ns} is likely lower than the vacuum-filtrated GSAM. While the vacuum-filtrated device was estimated to be 5 graphene layers thick, this would indicate that the 5% drop-cast GSAM would consist of fewer layers. With further engineering of the fabrication process could improve the drop-cast devices further to be far superior to other mode-locking options. Such engineering could include higher temperature or lower vacuum during the curing process, or a post-curing treatment to ensure better homogeneity.

The other drop-cast GSAMs exhibited poor parameters in respect to the other devices examined in this chapter. However as stated previously, they highlight the possibilities to tailor SAM parameters to whatever is required for the particular situation. Such drastic increases in thickness are not required and a slight increase in concentration could tailor the modulation depth, ΔR, from 4% to 20% for example.

6.3 Carrier Dynamics

Carrier dynamics play a pivotal role in the NLO response of saturable absorbers. Degenerate pump-probe measurements were carried out on the vacuum-filtrated GSAM and the SESAM using reflection geometry. Both the pump and the probe pulses were at 2 μm or 800 μm with linear and horizontal polarisation. Figure 6.11 (a) and (b) present the GSAM differential reflectivity ΔR/R as a function of probe delayed time t with 2 μm and 800 nm wavelength pulses respectively. The variations around zero delay are believed to be due to the coherent artefact. (Vardeny & Tauc, 1981) As shown in Figure 6.11 (a) and (b), the GSAM exhibited typical saturable absorption from 800 nm to 2 μm, i.e., the reflectivity immediately increased after pump pulse excitations. We also measured the SESAM for comparison at 2 μm in Figure 6.11(c). To get the excited carrier lifetime, we employed a two-exponential model with autocorrelations to fit our results:(Prasankumar & Taylor, 2016)

$$\frac{\Delta R}{R} = \{D_1 exp(-\frac{t}{\tau_1}) erfc(\frac{\sigma}{\sqrt{2}\tau_1} - \frac{t}{\sqrt{2}\sigma}) + D_2 exp(-\frac{t}{\tau_2}) erfc(\frac{\sigma}{\sqrt{2}\tau_2} - \frac{t}{\sqrt{2}\sigma})\} \quad (6.1)$$

where t is delayed time, D_1 and D_2 are relative amplitudes, τ_1 and τ_2 are two relaxation times, erfc represents the integral error function and σ is the laser pulse duration. All fitted pump-probe curves are presented as the solid lines in Figure 6.11, displaying a favourable fit to the experimental results. The carrier lifetimes are summarized in Table 6.2.

From our measurements, the carrier relaxations of GSAM exhibit to be very fast, i.e., τ_2 is 1.15 ps for 800 nm and 1.19 ps for 2 μm. These agree well with previous reports in liquid-phase exfoliated dispersions.(Wang *et al.*, 2016a) However, the SESAM carrier relaxation, τ_2, is slower at 63 ps for 2 μm pulses, which is significantly longer than GSAM. This becomes more obvious when we compare the GSAM and the SESAM curves together in Figure 6.11 (d), where the GSAM recovered within 3 ps whereas the SESAM seemed to be unchanged even after 8 ps. Our results imply that our GSAM is significantly faster as a saturable absorber than the commercial SESAM at 2 μm wavelength.

In Table 6.2, the short part, τ_1, of our GSAM and SESAM was determined to be 168 fs and 1.109 ps respectively at 2 μm wavelength. This process may be explained by carrier-carrier scattering after laser excitation.(Breusing *et al.*, 2009; Kumar *et al.*, 2009b) The long part of SESAM carrier relaxation, τ_2, was measured to be 63.0 ps while that of GSAM was only 1.19 ps. This implies that our GSAM is a much faster saturable absorber than the commercial SESAM. We attribute the observed τ_2 values to carrier-photon scattering.(Breusing *et al.*, 2009; Kumar *et al.*, 2009b)

Faster carrier relaxation times means that the absorber can recover from bleached with less time. This recovery time is very important for determining the laser pulse-duration when it works as a mode-locker. It is known that the saturable absorber has two modes when they are used as passive mode-locker, i.e., fast and slow mode-locking.(Haus, 1975d) In fast-absorber mode locking, the absorber recover time is about equal to the output laser pulse duration. Even in a slow-absorber mode-locking, the minimum pulse duration is still limited to $\tau_p/30$, where τ_p is absorber recovery time.(Paschotta & Keller, 2001) Because the carrier-photon scattering process is strong and slow as shown in Figure 6.11, we take τ_2 as absorber recovery time τ_p. Thus, the pulse duration limit is 2 ps for SESAM and 37 fs for graphene, showcasing the advantage of utilising graphene in producing ultrafast pulses 100 fs.

Table 6.2: Fitting Parameters for time-dependant reflectivity measurements of the GSAM and SESAM using Eq.6.1. E is the laser pulse energy. D_1 and D_2 are relative amplitudes. τ_1 and τ_2 represent the carrier relaxation times. The long part of carrier relaxation τ_2 at 2 μm is measured to be 1.19 ps in the vacuum-filtrated GSAM, much faster than that 63 ps in the commercial SESAM

λ (nm)	Sample	E (nJ)	F (mJ/cm^2)	D_1	D_2	τ_1 (ps)	τ_2 (ps)	Pulse Width (ps)
800	GSAM	10	1.06	0.00188	0.000345	0.193	1.036	0.255
	GSAM	20	2.12	0.57	0.00072	0.093	1.063	0.288
	GSAM	30	3.18	0.545	0.00089	0.102	1.141	0.312
	GSAM	40	4.24	0.982	0.00116	0.115	1.224	0.367
	GSAM	60	6.36	1.007	0.00167	0.107	1.269	0.329
	Average					0.122	1.1466	0.31
2000	SESAM	10	0.12	0.001087	0.00268	1.083	67.14	0.259
	SESAM	20	0.24	0.000226	0.003105	1.011	64.02	0.104
	SESAM	30	0.36	0.0013	0.003405	1.233	57.85	0.11
	Average					1.109	63	0.158
2000	GSAM	10	0.12	1.397	0.00074	0.091	1.397	0.274
	GSAM	20	0.24	0.644	0.00156	0.159	0.996	0.155
	GSAM	30	0.36	4.333	0.00226	0.253	1.177	0.096
	Average					0.168	1.19	0.175

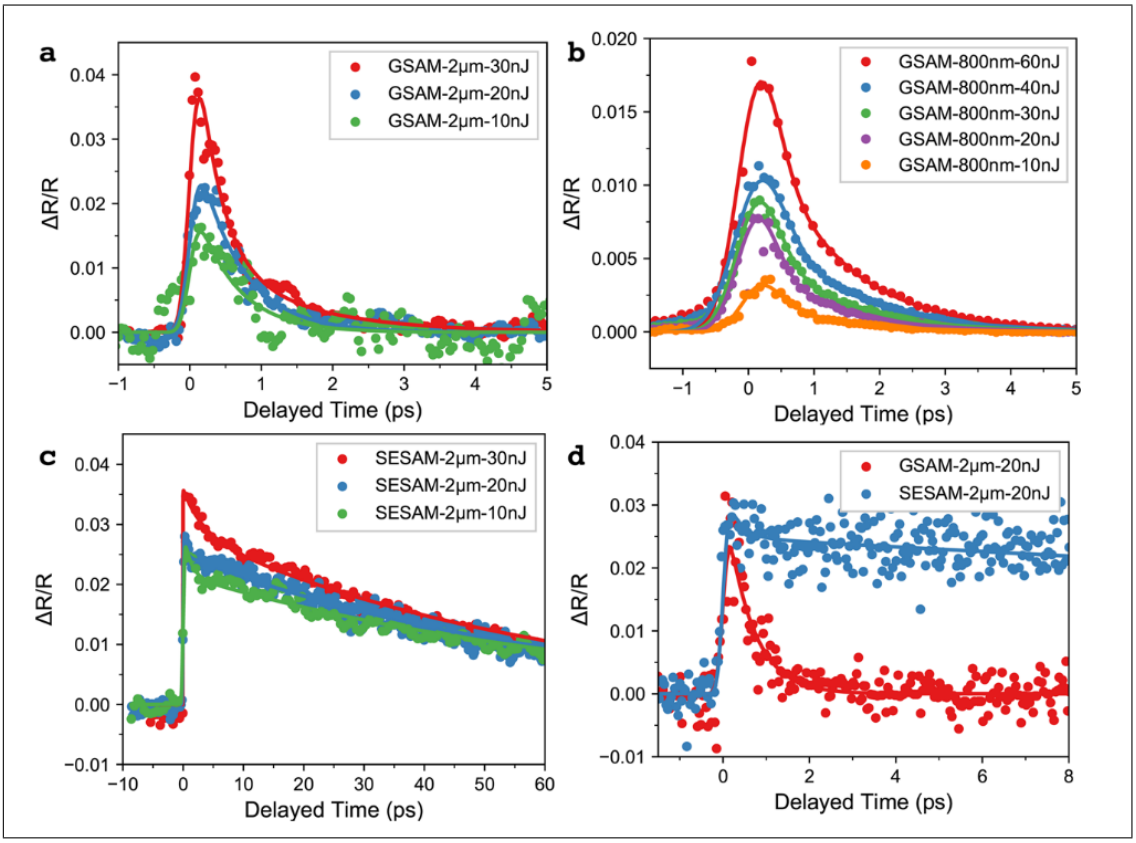

Figure 6.11: Time-dependant reflectivity of our GSAM and the commercial SESAM with fs pulses excitation (150 fs, 100 kHz). 1 nJ corresponds to the laser fluence of 0.106 mJ/cm^2 and 12.0 $\mu J/cm^2$ for 800 nm and 2 μm respectively. All scatters are from experiments while solid lines are fitting results using a two-exponential model. (a)-(b) GSAM differential reflectivity as a function of delayed time measured at 2 μm and 800 nm. (c) The same measurements from SESAM at 2 μm. (d) comparison of our GSAM and the SESAM up to 8 ps delay time, where the carrier life-time in GSAM and SESAM were measured to be 1.2 and 63 ps respectively. The polarization of the pump and probe are linear and in the same direction.

Table 6.3: NLO parameters of the graphene and SESAM derived from I-scan at 2 μm. The σ_g and σ_e are the cross-section of ground state and excited state respectively. The k represents the absorber density per area.

	SA	$Model$	$(Eq.6.2)$		SA	$Mirror$	$Model$	$(Eq.6.6)$
$Nano-structure$	σ_g (x10^{-15} cm^2)	σ_e (x10^{-15} cm^2)	σ_e/σ_g	k (x10^{13} cm^2)	σ_g (x10^{-15} cm^2)	σ_e (x10^{-15} cm^2)	σ_e/σ_g	k (x10^{13} cm^2)
$Graphene$	3.19	1.44	0.451	9.357	2.12	0.936	0.442	7.067
$SESAM$	29.9	18.7	0.625	1.517	20.04	12.32	0.615	1.14

Table 6.4: Saturated fluence and intensity with slow- and fast-absorber models. The I_s for the slow-absorber model and F_s for the fast-absorber model are calculated based on a pulse duration of 100 fs and 1 ns respectively.

	$Slow-absorber$ $(pulsewidth¡¡\tau_p)$		$Fast-absorber$ $(pulsewidth>>\tau_p)$	
$Nanostructure$	F$_s$ ($\mu J/cm^2$)	I$_s$ (MW/cm^2)	F$_s$ (mJ/cm^2)	I$_s$ (MW/cm^2)
$Graphene$	54.2	542	26.2	26.2
$SESAM$	6.9	69.2	0.527	0.527

6.4 Analysis

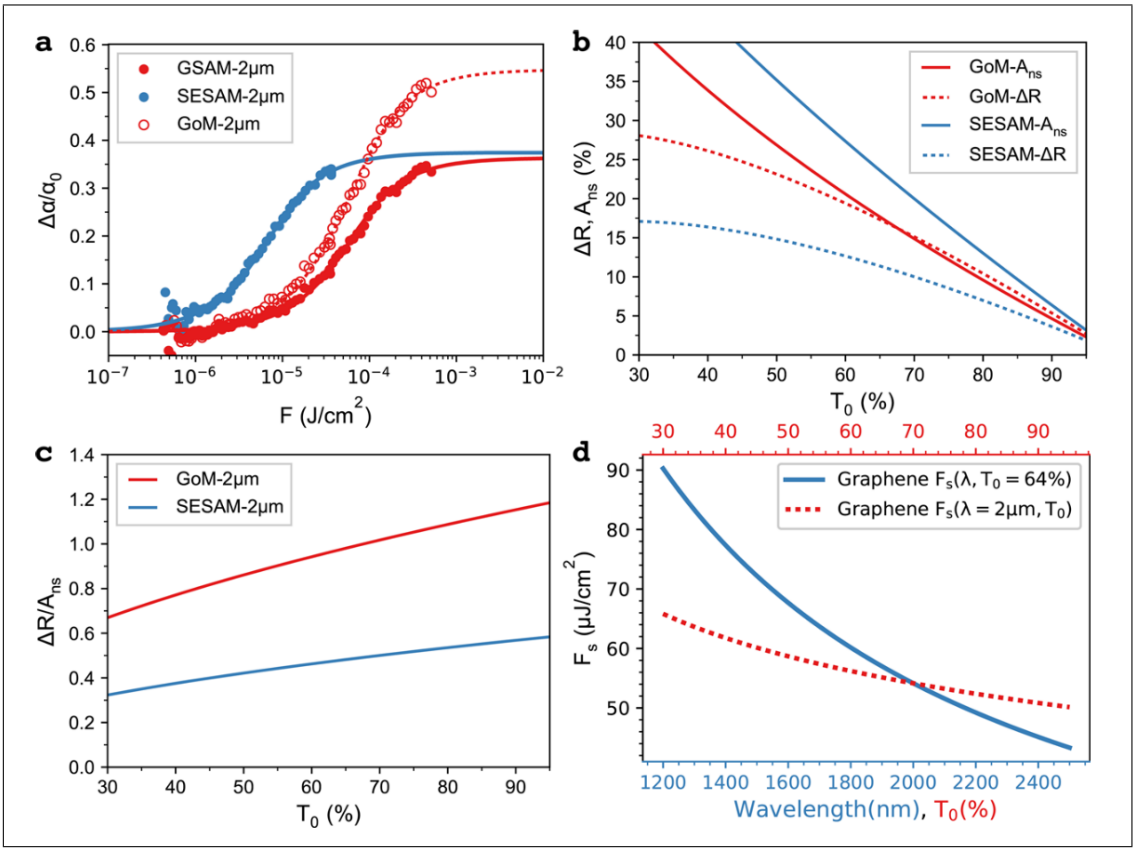

Figure 6.12: (a) Solid circles and lines: NLO performances of our GSAM and the commercial SESAM at 2 μm. Hollow circles: the response of graphene on mirror (GoM) after subtracted the 13.8% surface scattering from the GSAM. (b) Simulated modulation depth ΔR (dash lines) and non-saturated loss A_{ns} (solid lines) as a function of linear optical transmission at 2 μm for both saturable absorptive nanostructures. (c) The $\Delta R/A_{ns}$ ratio as a function of linear transmission calculated from (b), showing better performance of the graphene over SESAM. (d) Saturated laser fluence F_s of graphene as a function of wavelength (bottom axis, blue solid line) and linear optical transmission T_0 (top axis, red dashed line) respectively when a slow-absorber model is applied, i.e., pulse width $<<$ τ_2 (1.19 ps).

The carrier decay lifetimes of the vacuum-filtrated GSAM and the commercial SESAM (1.19 ps and 63 ps) are much longer than the laser pulse width (0.15 ps) in Figure 6.11 and as such both samples can be treated as slow-absorbers. Note that the slow-absorber model is still very useful for real mode-locking application, in which the saturable absorber interacts with several-hundred-fs pulses. The

response of a slow-absorber, achieved with a modified Frantz-Nodvik solution, is given by:(Burshtein *et al.*, 1998)

$$T(F) = T_0 + \frac{T_{FN} - T_0}{1 - T_0}(T_{max} - T_0) \tag{6.2}$$

Where

$$T_0 = e^{-\sigma_g NL} \tag{6.3}$$

$$T_{max} = e^{-\sigma_e NL} \tag{6.4}$$

and

$$T_{FN} = \frac{ln[1 + T_0(e^{\frac{\sigma_g F}{\hbar\omega}})]\hbar\omega}{\sigma_g F} \tag{6.5}$$

are the ground state and excited state cross-section respectively. N is the absorber atom density and L is the absorber length. F represents the laser energy fluence and ω is the photon angular frequency. Note that N always accompanies with L. To avoid the difficulty of getting the exact effective thickness of both saturable absorber mirrors, we employed the absorber density per area k instead of N and L, where k = NL. Eq. 6.2 describes the transmission when the absorber carriers are in an equilibrium state.

In these experiments, the laser is vertically incident onto the mirrors and actually passes the saturable absorber twice in a very short time in the saturable absorber mirror (SAM) configuration. On the first pass of photons through the saturable absorber, the light transmission can be described by the Eq. 6.2, i.e., T(F). Then the photons are reflected by the mirror and pass through the absorber for the second time. Because the time between the first and second pass is very short, the carriers do not recover from the first-pass excitation. In other words, the photons sense the as-bleached absorber on the second pass. Upon the approximation of slow absorber, the transmission sensed by the second-pass photons can be written as T(F+FT(F)). The F in the brackets is for the remaining effect of the first pass photons and the FT(F) is the second-pass light intensity. Therefore, the reflection of a SAM using a slow-absorber model can be derived as:

$$R = T(F) \cdot T(F + F \cdot T(F)) \tag{6.6}$$

We neglect the loss from mirror imperfection here. The modulation depth of SAM is then as follows:

$$\Delta R = R_{max} - R_0 = T_{max}^2 - T_0^2 \tag{6.7}$$

And the non-saturable loss of the SAM is:

$$A_{ns} = 1 - R_{max} = 1 - T_{max}^2 \tag{6.8}$$

Here the T_0 and T_{max} stand for the same expressions as in Eq. 6.2.

We employed both models mentioned previously to fit our I-scan results, i.e., Eq. 6.2 SA model and SA mirror model Eq. 6.6 for both SAMs. Both models show excellent fitting whereas Eq. 6.6 exhibited less errors than Eq. 6.2. The sum of squares due to error (SSE) using Eq. 6.6 was 1.1X10^{-3}, while SSE using Eq. 6.2 was 1.3 X10^{-3}. A lower SSE implies better fitting, indicating Eq. 6.6 is a better model than Eq. 6.2 for a SAM. To better show the nonlinear optical extinction, we present the Eq. 6.6 fitted curves in Figure 6.10 after converting the reflectance to normalized differential absorption $\Delta\alpha/\alpha_0$ [13] The representation by differential absorption $\Delta\alpha/\alpha_0$ has an advantage over reflectance because sample thickness has no effect on the differential absorption $\Delta\alpha/\alpha_0$. This can help us to better understand the pristine NLO properties of materials. The solid scatters are the original data while the red hollow data points are for the real NLO response excluding the 13.8% surface scattering effect showed in Figure 6.10. It is obvious that although the graphene has a larger saturated fluence F_s, it also has a larger $\Delta\alpha/\alpha_0$. This implies that graphene has a better modulation depth and non-saturable loss than the commercial SESAM used in this study.

The obtained NLO parameters of both nanostructures from fitting are summarized in Table 6.3. It can be seen that the cross-sections obtained from Eq. 6.6 are much smaller than that from Eq. 6.2. This is because the carriers absorb twice in the SA mirror model while only once in the SA model. The ground state cross-section, σ_g, and excited state cross-section, σ_e, of graphene were measured to be 2.12 $X10^{-15} cm^2$ and 0.936 $X10^{-15}$ cm^2 respectively. These are one-order smaller than that of SESAM, which are 20.04 $X10^{-15}$ cm^2 and 12.32 $X10^{-15}$ cm^2. Note that the cross-section ratio of the excited states to the ground state, σ_e/σ_g, are measured to be 0.442 and 0.615 for graphene and SESAM respectively. The graphene σ_e/σ_g at 2 μm is close to the previous reported 0.41-0.48 at 1030 nm. The smaller σ_e/σ_g in graphene implies that there are less non-saturable losses when compared with the SESAM.

As a design guideline for a practical SAM with varying linear optical trans-

mission, we calculated the theoretical performance of both nanostructures. Figure 6.12 (b) plotted theoretical modulation depth ΔR and non-saturable loss, A_{ns}, as a function of sample linear transmission T_0 from 30% to 95%. The calculation parameters are shown in Table 6.3. The solid lines are for the non-saturable absorption A_{ns} and the dashed lines are for the modulation depth, ΔR. From the Figure 6.12(b), for the same linear transmission, the commercial SESAM nanostructure always has a larger non-saturable absorption, A_{ns}, and less modulation depth, ΔR, comparing to those of graphene. Furthermore, the modulation depth, ΔR, of the SESAM nanostructure is always less than that of graphene. The ratio, $\Delta R/A_{ns}$, in Figure 6.12(c) display the advantage of graphene over the nanostructure of SESAMs more clearly, where graphene always has a higher $\Delta R/A_{ns}$, value. This means a well-designed GSAM may produce much less absorptive heat than SESAM if both operate at the same ΔR. This is quite important because light absorption is one of the main reasons for device failure as well as the limitation of laser output power. It should be noted that despite material properties playing an important role in the damage of SAM, its threshold also strongly depends on the device design. (Saraceno *et al.*, 2012; Zaugg *et al.*, 2013) However, with a better material like graphene, it is still possible to expect a mode-locker of higher damage threshold than that of traditional SESAMs in the mid-infrared.

The saturated fluence, F_s, and the saturable intensity, I_s, are key parameters for a mode locker. They are defined by the light fluence or intensity when the absorption coefficient decreased by a half. For slow-absorbers (pulse width $<< \tau_p$, where τ_p is the absorber recovery time), the F_s in the region $T_0 = [0.01, 0.99]$ can be expressed as an analytical form derived from Eq. 6.2:

$$F_s = (5.038T_0^{-0.08223} - 3.449)\hbar\omega/\sigma_g \tag{6.9}$$

Figure 6.12 (d) displays the calculated F_s from Eq. 6.9, where the blue dashed line is for the fixed 64% T_0 and the red solid line is for the constant 2 μm wavelength. The decreasing F_s implies an easier saturation of graphene as the wavelength goes to mid-infrared and the transmission increases. This explains wavelength-dependant results reported on graphene as well as other 2D materials such as MoS2 and black phosphorus in previous investigations.(Husaini *et al.*, 2013; Woodward *et al.*, 2015a; Zhang *et al.*, 2016b)

For fast-absorbers, the saturated intensity I_s can be derived from the steady-state solution of three-state rate equation (pulse width $>>\tau_p$):(Keller *et al.*, 1996)

$$I_s = (\hbar\omega))((\sigma_g\tau_p) \tag{6.10}$$

We use the saturated fluence, F_s, for slow-absorber and saturated intensity,

I_s, for fast-absorber because the laser pulse-width will not be effective and the whole expression can be simplified. However, the simple relationship of $F_s = I_s\delta$ is required if one wishes to convert saturated fluence/intensity to another in a slow-/fast- absorber model, where δ is laser pulse width. Table 6.4 presents the typical F_s and I_s for both materials in slow-/fast-absorber models at 2 μm. Note that we use a pulse width of $\delta = 100$ fs for slow-absorber and $\delta = 1$ ns to calculate the asterisked I_s and F_s respectively. The graphene value for I_s is 542 MW/cm2 for 100 fs pulses whereas it is 26.2 MW/cm^2 for 1 ns pulses. This has been observed in the group's previous investigations in MoS_2, $MoSe_2$ and black phosphorus.(Wang *et al.*, 2013b, 2014a, 2016a; Zhang *et al.*, 2016b,c) Similar effects on F_s were observed. Table 6.4 shows how much the laser pulse width can affect the NLO measurement results.

6.5 GSAM Conclusion

In this work, we systematically compared the performance of a multi-layered GSAM device with a commercial SESAM at a wavelength of 2 μm. The GSAM was fabricated via the transfer of a vacuum-filtrated graphene film onto a silver-coated mirror. The nonlinear optical performance and carrier dynamics at the 2 μm wavelength were investigated by I-scan and pump-probe techniques with mid-infrared 2 μm, 100 fs laser pulses. With a similar linear optical reflection of 64% our GSAM exhibited comparable modulation depth of 13% and non-saturable loss of 9.9%. Moreover, after subtracting the 13.8% surface scattering loss, the pristine graphene possesses much better NLO properties than the nanostructures in the comparing SESAM. The cross-section ratio of the excited-state over ground state, σ_e/σ_g, is fitted to be 0.442 and 0.615 for graphene and SESAM respectively, implying graphene based SAM may produce less loss and heat than SESAM when operating as a mode-locker in a laser cavity. Additionally, graphene has been shown to be a much faster saturable absorber than the commercial SESAM in our pump-probe experiment. The graphene displayed carrier relaxation times of 1.14 ps and 1.2 ps at 800 nm and 2 μm respectively, while the SESAM was slower at 63 ps at 2 μm. This advantage of graphene is very favourable for generating high repetition and short-pulse laser. These results imply that with proper design, graphene based saturable mirror can be superior than the current commercial SESAM in modulation depth, non-saturable loss and carrier relaxation for future mid-infrared lasers.

6.6 Integration Of Graphene SAM Into Mode-Locked Laser Systems

In this section, the tests integrating the graphene SAMs into 2μm lasers systems are discussed in more detail. While the lasers designed and tested at the ISLA facilities exhibited no stable mode-locking, a separate group achieved stable pulse generation at 1.5μm with a repetition rate of around 17MHz.

As mentioned in Section 1.3, the ISLA project aimed to make two pulsed lasers at 2 μm, one based on Q-switching (Demo Laser 2) and mode-locking (Demo Laser 3). It is for the development of mode-locked laser that the research laid out in this thesis was primarily undertaken, though graphene SAM samples were also briefly tested in Rofin's Q-switched design.

The actual mechanism to achieve the mode-locking of the system was the first issue to be tackled during the project, with many other methods aside from a graphene SAM were initially considered and investigated. Spliced fibre with graphene coated on the end was an early contender for the mode-locking system, but after initial testing, the graphene SAM method seemed to be a better choice.

6.6.1 1.5 Micron Mode-Locked Laser - Auckland Group

A collaboration with Prof. Neil Broderick's and Dr. Jianyong Jin's groups at The Auckland University in New Zealand was organised to test the practical mode-locking performance of the GSAM devices in a pulsed laser device. Samples identical to the graphene SAMs sent to the ISLA members were prepared and shipped to Prof. Broderick's group. This included several drop-cast samples and a CVD graphene SAM.

The laser was a simple ring laser configuration (shown in Figure 6.13), with a length of erbium (Er) doped fibre as the gain medium, an isolator, polarisation controller, the graphene SAM and an output coupler. This was finalised after discussions between the Prof. Blau and Prof Broderick groups.

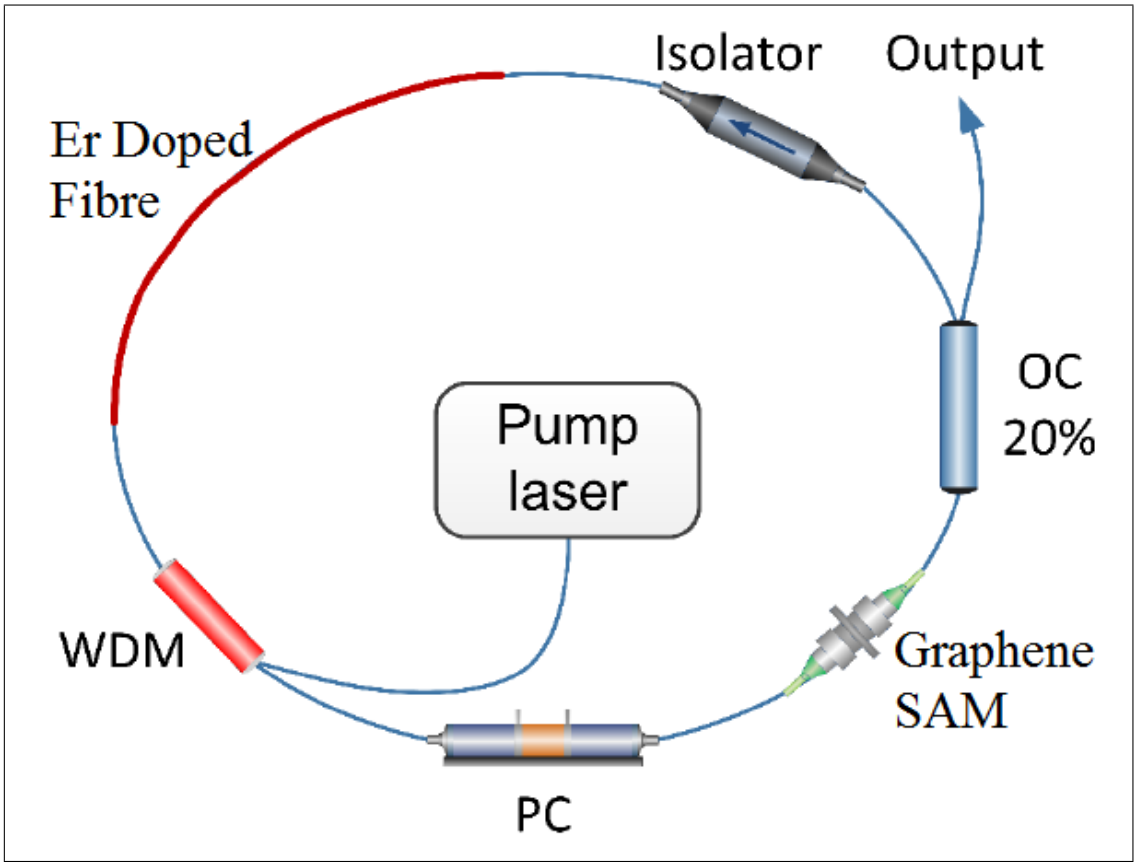

Figure 6.13: Basic schematic of the laser set up at Auckland University.

The output wavelength was around 1.5 μm, as shown in Figure 6.14

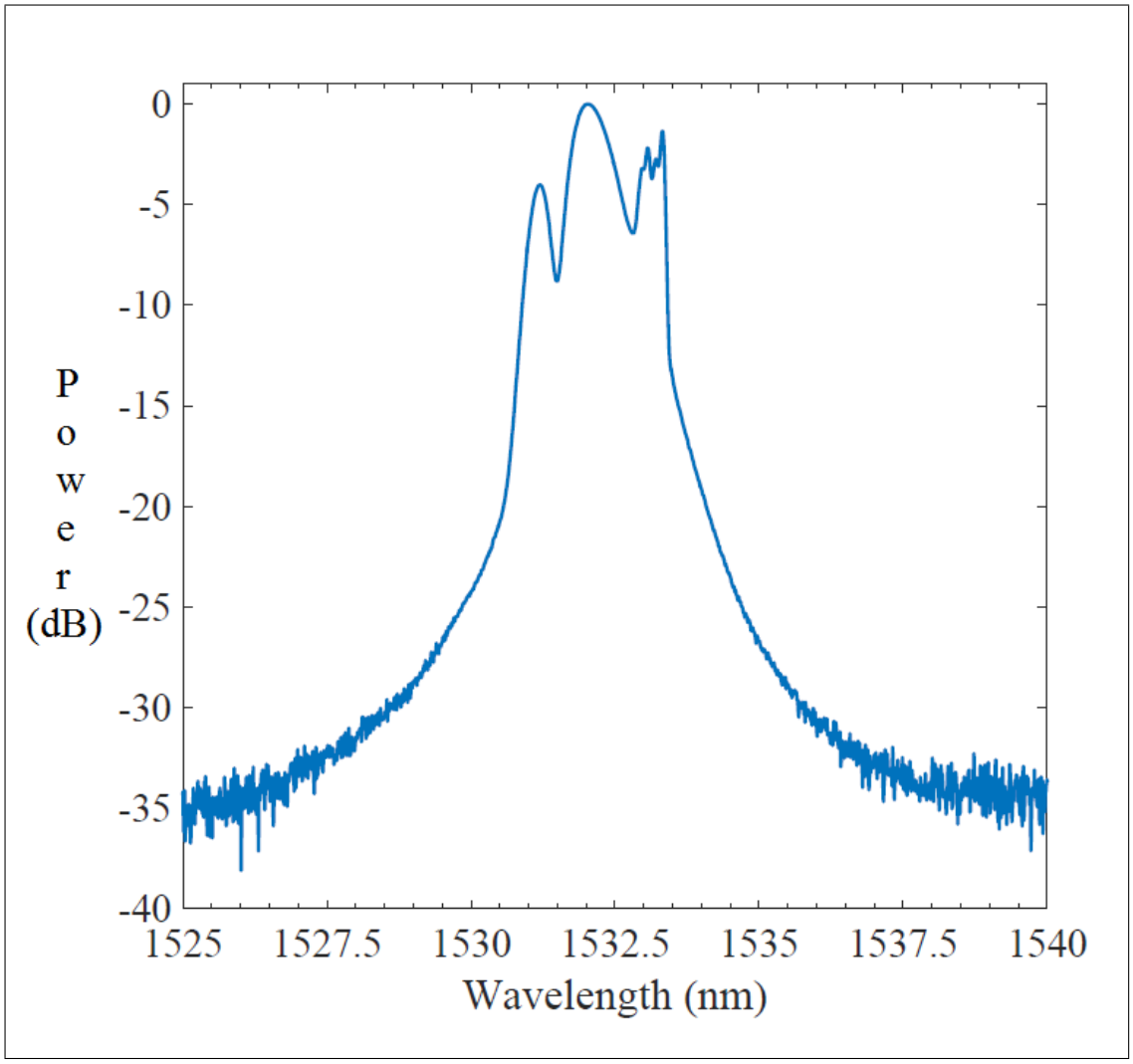

Figure 6.14: Wavelength of the laser pulses achieved, around 1.5μm.

The train of pulses is shown in Figure 6.15, with a pulse duration in the picosecond range and a demonstrated repetition rate of around 17 MHz. This was achieved utilising the graphene saturable absorber mirrors (G-SAM) to mode-lock the system.

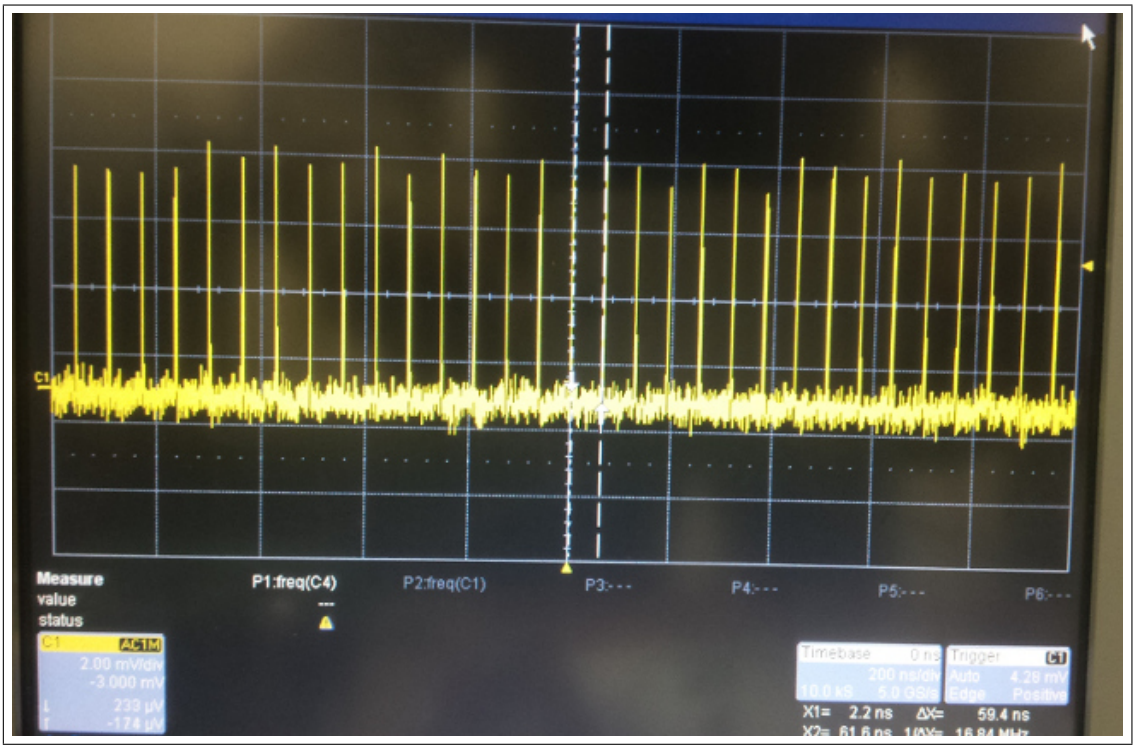

Figure 6.15: Train of pulses achieved with the graphene SAM, with a repetition rate of 17MHz and a pulse duration in the region of picoseconds.

These initial results were very promising, and work is ongoing to get more thorough data from the laser setup. While it is important to validate the performance of the graphene SAMs designed and produced during the time frame of the project, which these Auckland results displaying stable mode-locking at 1.5 μm begin to do.

6.6.2 2 Micron Mode-Locked Laser - ISLA Group

After several meetings and correspondences at the beginning of the project, the architecture of the mode-locked laser was agreed to be based on a typical 1 μm fibre-Master Oscillator Power Amplifier (MOPA) design, incorporating components specifically designed to operate at the 2μm regime:

- A Tm doped fibre oscillator generates picosecond pulses at a repetition rate of $\sim$ 50 MHz
- Two pre-amplifier stages follow
- Final power amplifier stage

The laser design used ISLA components almost exclusively:

- Couplers and combiners - Gooch and Housego (Torquay)
- Optical isolators - Gooch and Housego (Torquay)
- Single-mode (SM) and multi-mode (MM) pump diodes - II-VI
- Pulse picker AO modulator - Gooch and Housego (UK)
- Tm and Ho doped fibres - Optoelectronics Research Centre (ORC)
- graphene SAM modelockers - Trinity College Dublin

6.6.2.1 Schematic

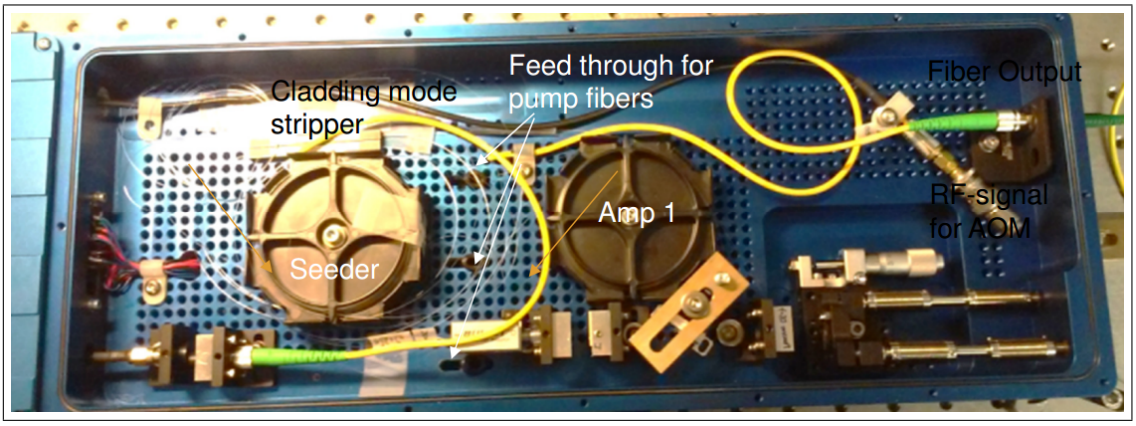

Figure 6.16: Photo of the laser head after modifications and tidying up, courtesy of Dr. Peter Hofmann

The schematic of the mode-locked laser is shown in Figures 6.17.

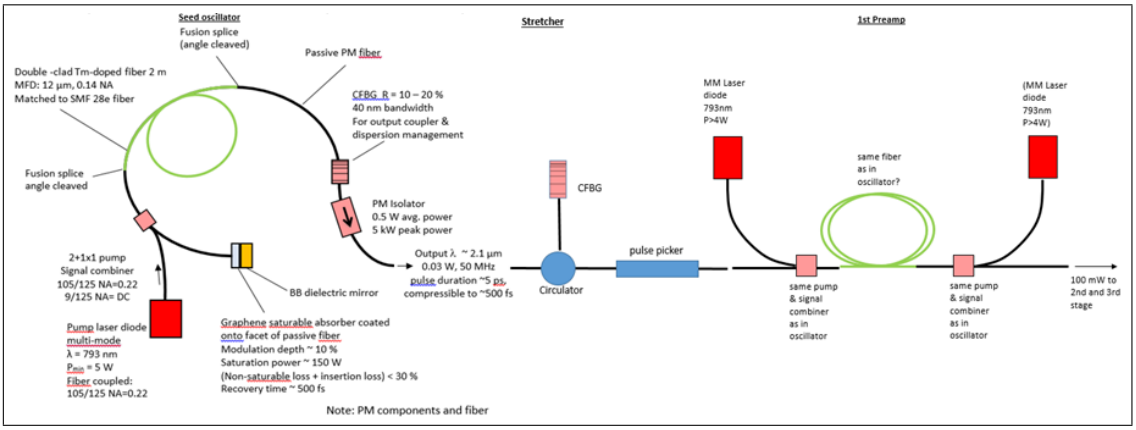

Figure 6.17: Front end of the mode-locked laser, courtesy of ISLA

6.6.3 Tests

A CW oscillator was implemented to successfully verify the functionality of the components. An industrial grade housing was customised, and the seeder and amplifier stages were built at JDSU.

This system was then shipped to ORC and commissioned, which included several visits from JDSU members to perform collaborative experimental work. The custom JDSU pulse picker driver was integrated with the Gooch and Housego AO pulse picker modulator.

When tested, Q-switched mode-locking burst behaviour was observed, but stable mode-locking was not achieved with either the graphene SAMs developed during this project, nor was mode-locking achieved with various purchased commercial SESAMs. These tests were performed at JDSU facilities, by JDSU researchers.

The mode-locked laser remained at ORC after the duration of the project, and development continued with assistance from JDSU.

Table 6.5 shows the results obtained when the graphene SAMs were tested in ISLA's mode-locked laser. Samples 1 and 2 shows CVD graphene SAMs, 3 through 10 show drop-cast graphene SAMs, samples 11 through 13 are filtration prepared graphene SAMs, and sample 14 and 15 are commercial SESAMs. The BATOP SESAM is the same type that was used in the I-scan experiments described in Chapter 6.

As shown in this table, while the various graphene SAMs, prepared with different methods, gave similar readings to the commercial BATOP SESAM, which is specifically designed to operate at $2\mu m$. While touting comparable characteristics, as shown in Table 6.5 and Chapter 6, during the time period of the ISLA project none of the graphene SAMs or purchased SESAMs managed to achieve stable mode-locking. As the commercial SESAMs also failed to produce stable mode-locking and the successful mode-locking achieved in collaboration with the Auckland group, this implies that there is likely an issue with the laser set-up or design and not with the actual mode-locking device.

Work and testing at ORC continued past the project end date, but as of writing no stable mode-locking was achieved with the graphene or commercial devices.

6.6.4 2 Micron Q-Switched Laser - ISLA Group

The design and construction of Q-switched laser was overseen by Rofin, and tests were performed by Rofin researchers. The aim for this laser was to utilise Q-switching to achieve pulsed operation at $2\mu m$. Using a commercial SESAM, pulses were generated for a short time in the 1-100 ns range before the SESAM was damaged.

Graphene SAM samples were sent and used in the system, with no observable stable Q-switching in the measured 1-100 ns region. It is possible pulses were produced in the μs region, as graphene Q-switching has been shown to occur in this region by groups such as Wang *et al.* (2012b) ($\sim 2.3\mu s$ pulses at 1,884 nm, with 70 nJ maximum pulse energy), but this is not suitable for the laser design.

Table 6.5: Results from graphene SAMs and commercial SESAMs used in mode-locked laser, courtesy of Dr. Peter Hofmann

#	Method	Source	I_{TH} (A)	P_{out} (mW)	I_{max} mod. (A)	Cavity Free Spectral Range (MHz)	Mod. Amp. (dBm)	Stable Mode-Locking Achieved
01	CVD	TCD	1.67 (bc)	80	2.7	20.8	-42	No
02	CVD	TCD	-	-	-	-	-	No
03	OVEN	TCD	1.69 (bc)	100	2.3	-	-55	No
04	OVEN	TCD	-	-	-	-	-	No
05	OVEN	TCD	-	-	-	-	-	No
06	OVEN	TCD	2.0 (img.)	-	2.7	-	-	No
07	VAC	TCD	-	-	-	-	-	No
08	VAC	TCD	1.8	-	2.7	20	-41.2	No
09	VAC	TCD	1.8	-	-	21	-45	No
10	VAC	TCD	1.7	100	2.5	21	-45	No
11	VAC filt.	TCD	1.75	70-100	2.6-2.8	21	-42	No
12	VAC filt.	TCD	-	-	-	-	-	No
13	VAC filt.	TCD	-	-	-	-	-	No
14	SESAM	Batop	1.74	60-70	2.5	26,21	-41	No
15	Dielectric	L-O	1.67	100	2.3	21	-41	No

6.6.5 Graphene SAM Integration into Laser System Conclusions

While both the mode-locked and Q-switch lasers designed and constructed by the ISLA group did not achieve stable mode-locking at 2 μm, Prof. Broderick's group managed to develop a laser system that successfully mode-locked using the drop-cast graphene SAM samples at 1.5 μm. A stable repetition rate of 17 MHz and a pulse duration in the realm of picoseconds was obtained.

As shown in the next chapter in Table 7.6, groups such as Zhang *et al.* (2012c), Jung *et al.* (2012), Jung *et al.* (2013) and Liu *et al.* (2012) have shown successful mode-locking in the 2 μm region.

7 Conclusion

7.1 Results

In this thesis, the potential of graphene SAMs for mode-locking ultrafast lasers has been demonstrated, in particular at 2 μm.

Graphene and other 2D materials were successfully dispersed via liquid-phase exfoliation methods in NMP. This were then utilised to manufacture optically thin films for nonlinear optical examination and for mode-locking device fabrication.

The saturable absorption of graphene thin films (prepared via drop-casting) was demonstrated in Chapter 5 at 1 μm (Section 5.2.1.3), 1.2 μm and 2 μm (Sections 5.2.2 and 5.2.3), utilising the Z-scan technique. The graphene also reacted favourably with the three different laser systems used, and in particular the different repetition rates (80 MHz, 25 kHz and 100 kHz).

The strong saturable absorption and Kerr nonlinearity was present for all the different graphene samples used (C_{CVD}, C_{5K} and C_{3K}) in Section 5.2.1.3. An example of the nonlinear optical properties is summarised below in Table 7.1, which itself is a summary of Tables 5.1, 5.3, 5.4 and 5.5. These exceptionally strong nonlinear properties at such relatively low intensities implies that graphene has excellent potential for various optical devices, and mode-lockers in particular. The simple drop-casting method produce high-quality samples which has great potential as a cheap and scalable production method that pairs perfectly with LPE 2D materials.

Table 7.1: Nonlinear optical properties of C_{CVD}, C_{5K} and C_{3K} from various z-scan experiments at different pulse energies at 200fs, 25 kHz, 1030 nm with the Pharos laser discussed in Section 5.2.1.3.

Sample	Pulse Energy (nJ)	I_0 (GW/cm^2)	Modulation Depth (%)	β ($X10^3$ cm/GW)	$Im(\chi^{(3)})$ ($-X10^{-8}$ esu)	n_2 ($-cm^2/GW$)	$Re(\chi^{(3)})$ ($X10^{-8}$ esu)	$\chi^{(3)}$ ($X10^{-8}$ esu)
C_{CVD}	1.7	3.9	0.45	3.4	0.52	0.11	2.1	2.1
C_{5K}	0.48	1.12	1.78	24	360	0.77	14	15
C_{5K}	1.5	4.5	2.9	9.8	1.5	0.28	5	5
C_{3K}	1.7	2	6	17.9	2.7	0.28	5.2	5.9

The response at 1.2 μm was more pronounced than at 2 μm. The successful demonstration of saturable absorption in graphene at 2 μm allowed the group to move on to the development of mode-locking devices for ultrafast pulsed lasers operating at the same wavelength.

The Kerr nonlinearity was explored via the closed aperture mode of the graphene-NMP dispersions. As shown in Figure 5.33, at an intensity of $2.7 * 10^{-2} GW/cm^2$ a value of $n_2 = 1.16 * 10^{-6} cm^2 W^{-1}$ is obtained by fitting. This agrees fairly well with the literature value of $10^{-7} cm^2 W^{-1}$ (Zhang *et al.*, 2012a). The order of magnitude difference between the two values may be due to the imperfect fit.

Graphene saturable absorption mirrors (G-SAM) were prepared via drop-casting, vacuum filtration and CVD prepared graphene, and their nonlinear optical properties were examined with the I-scan technique at 2 μm in Chapter 6. These were compared with a commercial SESAM from BATOP, and the graphene SAMs were proven to have similar characteristics, summarised in Table 6.1.

The vacuum-filtrated graphene SAM and the SESAM had very similar values for linear reflectance (63.6% to 64.6%), non-saturable losses (25% each) and modulation depth (∼11% each). However, the graphene SAM needs a higher laser intensity to be saturated than the SESAM according to the larger I_S. It should be mentioned that considering one advantage of ultrafast lasers are there high intensity, the larger I_S is possibly acceptable in most practical applications.

Another issue that should be noted is that the real saturated intensity of the graphene SAM may not be so different than the SESAM due to fast response time of graphene. It is reported that the response time of graphene is extremely fast, with literature values as low as 100 fs (Bonaccorso *et al.*, 2010), which is of the same order of the excited laser pulse duration (100 fs). However, the SESAM used was a much slower absorber, with a response time of 10 ps. The fast response time of graphene may lead to a much larger saturated intensity with this particular laser set-up because some electrons fall back to the ground state during the pulse duration.

It is important to note that the graphene SAMs not only performed almost identically to the BATOP commercial SESAM, which are specifically designed to operate at 2 μm, but also that the commercial SESAM is extremely sensitive to wavelength, and a small wavelength shift to 1.9 μm renders the commercial SESAM useless. This is not an issue for the graphene SAMs, which operate over a wide wavelength range.

The advantage of the drop-casting method of liquid-phase exfoliated graphene is that the NLO parameters can be somewhat tailored by altering the film thickness.

The graphene SAMs were tested in Demo Laser 3 at JDSU in Zurich, and was discussed in Chapter 6.6. The CVD, drop-cast and vacuum filtration prepared graphene SAMs performed similarly to the BATOP SESAM in the holmium laser, as displayed in Table 6.5. Despite the promising characteristic of the SAMs, no stable mode-locking was achieved as of the time of writing.

Drop-cast thin films of boron nitride (BN) and molybdenum disulphide (MoS_2) were examined via Z-scan technique at 2 μm. MoS_2 displayed clear saturable absorption, and BN exhibited an optical limiting response.

7.2 Comparisons

7.2.1 Nonlinear Optical Properties

The results obtained in Chapter 5, and summarised in Tables 5.9 and 5.10, are compared with published results from other groups in Tables 7.2, 7.3 and 7.4.

It should be noted that the measured beam waist of 95 μm (in Chapter 6) was initially assumed to be correct, but a more thorough consideration would imply that the actual beam waist should be smaller. Judging from the fittings of the z-scan results in Chapter 5, a beam waist of around 50 μm atleast (likely smaller still) helped with the numerical fitting greatly, compared with 95 μm. As such an actual beam waist of around 50 μm was assumed throughout the thesis, which in turn affected the quoted intensity values. While the beam waist was probably

even smaller than 50 μm, the actual intensity values may be closer to the published results. The difference in intensities may also account for the different β values.

In the thin film results (Table 7.2), the discrepancies in β may also be due to the differences in the pulse duration and repetition rate.

Whereas the published results of β seem to correlate much more closely with the graphene dispersion results, as shown in Table 7.4.

The graphene/polymer results from Chapter 5 seem to have much noise in the z-scan graphs, perhaps due strange interactions between the graphene filler in the polymer matrix. The graphene/PMMA (at $1.2\mu m$) results were too inconsistent to perform a numeric fitting on. While the fitting of the graphene/polystyrene (at $2\mu m$) results for β appear to be relatively close to the values reported by Demetriou *et al.* (2015).

Table 7.2: Comparison of the graphene thin film open aperture results with published results, including the nonlinear optical absorption coefficient

Sample	Wavelength (nm)	Pulse Duration	Repetition Rate (Hz)	Intensity (GW/cm^2)	β (cm/GW)	Reference
Graphene Thin Film	1,200	100 fs	(MHz) 80	0.0048	($\times 10^6$) -22.2	Thesis
Graphene Thin Film	1,200	100 fs	(MHz) 80	0.032	($\times 10^6$) -7.3	Thesis
Graphene Thin Film	1,200	100 fs	(MHz) 80	0.053	($\times 10^6$) -4.2	Thesis
Graphene Thin Film	1,200	100 fs	(MHz) 80	0.11	($\times 10^6$) -2.3	Thesis
Graphene Thin Film	1,200	100 fs	(MHz) 80	0.28	($\times 10^6$) -0.95	Thesis
Graphene Thin Film	2,000	100 fs	(MHz) 80	0.008	($\times 10^6$) -1.2	Thesis
Graphene Thin Film	2,000	100 fs	(MHz) 80	0.016	($\times 10^6$) -0.86	Thesis
Graphene Thin Film	2,000	100 fs	(MHz) 80	0.021	($\times 10^6$) -0.92	Thesis
Graphene Thin Film	2,000	100 fs	(MHz) 80	0.045	($\times 10^6$) -0.18	Thesis
Graphene Thin Film	2,000	100 fs	(MHz) 0.1	2.5	($\times 10^6$) -0.0037	Thesis
Graphene Thin Film	2,000	100 fs	(MHz) 0.1	5.1	($\times 10^6$) -0.0064	Thesis
Graphene Thin Film	2,000	100 fs	(MHz) 0.1	8.9	($\times 10^6$) -0.0051	Thesis
Graphene Oxide	532	4 ns	1	(μJ) 200	0.45	Zheng *et al.* (2016)
GO /Pt	532	4 ns	1	(μJ) 200	0.53	Zheng *et al.* (2016)
GO /Pt-Cu	532	4 ns	1	(μJ) 200	0.62	Zheng *et al.* (2016)
Graphene	1,064	40 ps	10	0.35	0.59	Zhang *et al.* (2016a)
Graphene	532	30 ps	10	0.87	0.40	Zhang *et al.* (2016a)
Graphene /Nitrogen	1,064	40 ps	10	0.35	0.76	Zhang *et al.* (2016a)
Graphene /Nitrogen	532	30 ps	10	0.87	0.46	Zhang *et al.* (2016a)

Table 7.3: Comparison of the graphene/polymer open aperture results with published results, including the nonlinear optical absorption coefficient

Sample	Wavelength (nm)	Pulse Duration (fs)	Repetition Rate (MHz)	Intensity (GW/cm^2)	β (cm/GW)	Reference
0wt% Graphene /Polystrene	2,000	100	80	0.045	-0.25	Thesis
1wt% Graphene /Polystrene	2,000	100	80	0.045	-0.2	Thesis
5wt% Graphene /Polystrene	2,000	100	80	0.045	-0.1	Thesis
Graphene in PVA	1,550	(ns) 4	-	0.55	2.7	Demetriou *et al.* (2015)
Graphene in PVA	2,000	(ns) 4	-	1.7	3.3	Demetriou *et al.* (2015)
Graphene in PVA	2,400	(ns) 4	-	1.95	4.9	Demetriou *et al.* (2015)

Table 7.4: Comparison of the graphene dispersion open aperture results with published results, including the nonlinear optical absorption coefficient

Sample	Wavelength (nm)	Pulse Duration (fs)	Repetition Rate (MHz)	Intensity (GW/cm^2)	β (cm/GW)	Reference
Graphene in NMP	1,200	100	80	0.0032	0.85	Thesis
Graphene in NMP	1,200	100	80	0.008	1.8	Thesis
Graphene in NMP	1,200	100	80	0.018	1700	Thesis
Graphene in NMP	2,000	100	80	0.0095	12.8	Thesis
Graphene in NMP	2,000	100	80	0.032	3.7	Thesis
Graphene in NMP	2,000	100	80	0.043	4.8	Thesis
Graphene in Alcohol	800	50	-	29	($\times 10^{-2}$) 2.76	Fan *et al.* (2012)
Graphene in Alcohol	800	50	-	46	($\times 10^{-2}$) 1.96	Fan *et al.* (2012)
Graphene in Alcohol	800	50	-	88	($\times 10^{-2}$) 1.14	Fan *et al.* (2012)
Graphene in Alcohol	800	50	-	117	($\times 10^{-2}$) 1.03	Fan *et al.* (2012)
Graphene in DMF	532	-	-	2.1	2.2	Liu *et al.* (2009)

7.2.2 Graphene Mode-Locked Lasers

Stable mode-locking was achieved during the tenure of the ISLA project, through the collaboration with the Prof. Broderick's and Prof Jin's groups at the Auckland University, which achieved picosecond pulses with a repetition rate of around 17MHz at 1.5μm using the graphene SAMs described in this text in an Erbium doped fibre laser, and is discussed in Section 6.6.1.

Other groups have also published about the mode-locking capabilities of graphene, as shown in Tables 7.5 (focusing on Erbium doped fibre lasers) and 7.6 (and solution processed fibre lasers). These tables are an expanded version of Table 1.2. In these tables, Wavelength (λ) is the wavelength, τ is the pulse duration, f is the repetition rate and P is the power.

Several groups have even shown successful mode-locking in the 2 μm region (Jung *et al.*, 2012, 2013; Liu *et al.*, 2012; Zhang *et al.*, 2012c). So it certainly feasible that the graphene SAM described in this report, in combination with the fibre laser designed by the ISLA consortium, can achieve stable mode-locking under favourable circumstances.

Table 7.5: Examples of Successful Graphene Mode-locking on Erbium Doped Fibre Lasers, Utilising Solution Processing

Coupling Method	Fabrication Method	Laser λ (nm)	Laser τ	Parameters f (MHz)	Parameters P (mW)	Reference
Sand	LPE	1557	800 fs	-	-	Hasan *et al.* (2009a)
-wiching		1559	464 fs	19.9	1	Sun *et al.* (2010b)
		1525 -1559	1 ps	8	1	Sun *et al.* (2010d)
		1560	174 fs	27.4	1.2	Popa *et al.* (2010)
		1560	630 fs	19.9	-	Hasan *et al.* (2010)
		1532	850 fs	5.27	-	Martinez *et al.* (2010b)
		1562	865 fs	9.67GHz	316	Martinez & Yamashita (2012)
		$\sim$ 1530	8.8 ps	8.03	3.56	Luo *et al.* (2012a)
		1560	1 ps	13.6	3.7	Luo *et al.* (2012b)
		1565	190 fs	42.8	0.4	Cunning *et al.* (2011)
		1530	900 fs	8.4	-	Lau *et al.* (2018)
		1550	0.6-1.17ps	60.6	3	Rosa *et al.* (2017)
		1559	464 fs	19.9	1	Sun *et al.* (2010d)
	FG	1570	1.08 ps	6.95	-	Bao *et al.* (2010)
	GO	1596	770 fs	21.79	0.85	Zhao *et al.* (2013)
	RGO	1590	694 fs	6.95	50	Zhang *et al.* (2009b)
		1560	18 ps	7.47	1.2	He *et al.* (2012)
		1562	938 fs	15.2	4.1	Gui *et al.* (2011)
		1562	950 fs	502.8	2.3	Fu *et al.* (2013b)
		1560 1560	1.64 ps 9.15 ps	2.57 7.05	- -	Cui & Liu (2013)
		1572	-	91.5	-	Kim *et al.* (2011)
		1576	415 fs	6.84	-	Lin *et al.* (2013b)
Evane	RGO	1561	1.3 ps	6.99	15.5	Song *et al.* (2010a)
-scent		1557	15.7 ps	3.33	4.2	Wang *et al.* (2012a)
Wave		1555	510 fs	506.9	80	Choi *et al.* (2012)
	GO	1561	4.85 ns	7.68	4.3	Liu *et al.* (2011b)
		1560	780 fs	14.64	0.36	Lee *et al.* (2013b)
	LPE	1567	650 fs	25	-	Lin *et al.* (2013a)
Free	RGO	1560	395 fs	58	1.96	Sobon *et al.* (2012)
-Space	GO	1561	400 fs	49.45	1	Paul *et al.* (2013)
		1560	0.2 - 3 ps	0.93 - 23	5.8	Xu *et al.* (2012a)
		1531	0.5 - 20 ns	0.5	19.5	Xu *et al.* (2012b)
	LPE	1558	3 - 20 ns	0.2 - 1.5	553	Xu *et al.* (2012c)
		1564	2.47 ps	1.21	-	Zheng *et al.* (2012b)
Reflective	LPE	1532	$\sim$ps	17MHz	-	Thesis

Table 7.6: Examples of Successful Graphene Mode-locking on Fibre Lasers, Utilising Solution Processing

Coupling Method	Fabrication Method	λ (nm)	Laser τ	Parameters f (MHz)	P (mW)	Reference
		Ytterbium	Doped			
Sand	GO	1029	191 ps	-	539	Li *et al.* (2013)
-wiching			1.68 ns			
		Thulium	Doped			
Sandwiching	LPE	1940	3.6 ns	6.46	2	Zhang *et al.* (2012c)
Evanescent Wave	GO	1910	1.3 ps	15.9	0.5	Jung *et al.* (2012)
		1950	0.59 ps	33.25	142	Jung *et al.* (2013)
		Raman	Laser			
Sandwiching	LPE	1180	200 ns	0.4	60	Zhang *et al.* (2012b)
		Nd:YAG	Laser			
Transmittive	RGO	1064	4 ps	88	100	Tan *et al.* (2010)
		Nd:YVO4	Laser			
Transmittive	GO	1064	-	75	1000	Sun *et al.* (2011)
		1064	-	88	1200	Zhang *et al.* (2011b)
Reflective		1064	8.8 ps	84	3060	Feng *et al.* (2013b)
		Nd:GdVO4	Laser			
Transmittive	GO	1064	4.5 ps	70	1100	Wang *et al.* (2012c)
Reflective		1341	11 ps	100	1290	Xu *et al.* (2012d)
		1065	16 ps	43	360	Xu *et al.* (2011f)
		1063	12 ps	-	680	Wang *et al.* (2013c)
		Yb:KGW	Laser			
Reflective	LPE	1031	428 fs	86	504	Xu *et al.* (2011b)
		Yb:LSO	Laser			
Reflective	GO	1058	9.8 ps	87	950	Feng *et al.* (2013a)
		Tm:YAP	Laser			
Transmittive	GO	2023	<10ps	71.8	268	Liu *et al.* (2012)
		Yb	Laser			
Butt-coupled	LPE	1039	1.06 ps	1.5GHz	202	Mary *et al.* (2013)
Reflective	LPE	1532	∼ps	17MHz	-	Thesis

7.3 Novelty

While there has now been several examples of graphene being used as a mode-locker for pulsed lasers, in particular at 2 μm (as shown in Table 2.4), when the project began this was a unique concept. While several research groups have shown stable mode-locking at 2 μm using graphene, there has yet to be a commercially mode-locked laser using graphene at this wavelength.

The Liquid Phase Exfoliated (LPE) 2D material production is a robust, flexible, scalable and cheap method. However, it is still a niche production method, that is used by a relatively small proportion of the research community. As such, the nonlinear optical study of the LPE graphene compared with the CVD samples is a unique study which has not been previously explored. The pulse duration measurements explored via z-scan on these samples is also an unusual aspect of the research presented in the thesis.

The scattering measurements of our GSAMs is a fairly unique avenue of research, and is not usually something that is included when examining SA devices.

7.4 Future Work

A potential continuation of this work is to continue the development of Demo Laser 3 and the utilisation of the graphene SAMs described previously. This work is ongoing, with the laser system having moved to ORC in Southampton. The graphene SAMs discussed in this thesis compared well with commercial devices, and further refinement could produce better GSAMs that far surpass current options.

Another approach would be to run computer simulations to estimate the performance of the graphene SAMs at 2 μm. This could help further differentiate the graphene SAM from the commercial SESAMs.

Improvements to the homogeneity of the drop-cast films is something that would greatly benefit the mode-locker device manufacturing process.

Improvements to drop-casting and film production can vastly improve the sample quality. With simple drop casting, high-quality samples around 20 nm thick were produced during this work. A more systematic approach to the reliance of film thickness and quality on dispersion concentration, oven temperature, vacuum level, substrate etc. would help improve devices produced with these methods.

A more thorough exploration of the nonlinear optical properties of graphene would be quite interesting. Different wavelengths, power, pulse durations and repetition rates are all potential parameters to vary.

Due to the similar preparation methods of other pseudo-2D materials, such as boron nitride (BN) and Transition Metal Dichalcogenides (TMDC), an equally more thorough explanation into these materials would be prudent. Similarly, it

would be interesting to examine samples prepared with blends of these materials, such as prepared and shown in Figure 4.5.

Liquid phase exfoliation is a powerful, flexible technique, that has the potential to prepare a large range of 2D materials in a medium that aligns well with various sample production methods. A selection of various 2D materials in dispersion was shown in Figure 5.3. These dispersion can be blended with other materials, such as polymers, and act as a filler in these materials, altering their parameters greatly.

There are many interesting and relevant directions research into 2D materials can explore, with liquid-phase exfoliated samples being an excellent tool in the nanoscientist's tool-box. As Richard Feynman said, "There's Plenty of Room at the Bottom".

A

Appendix

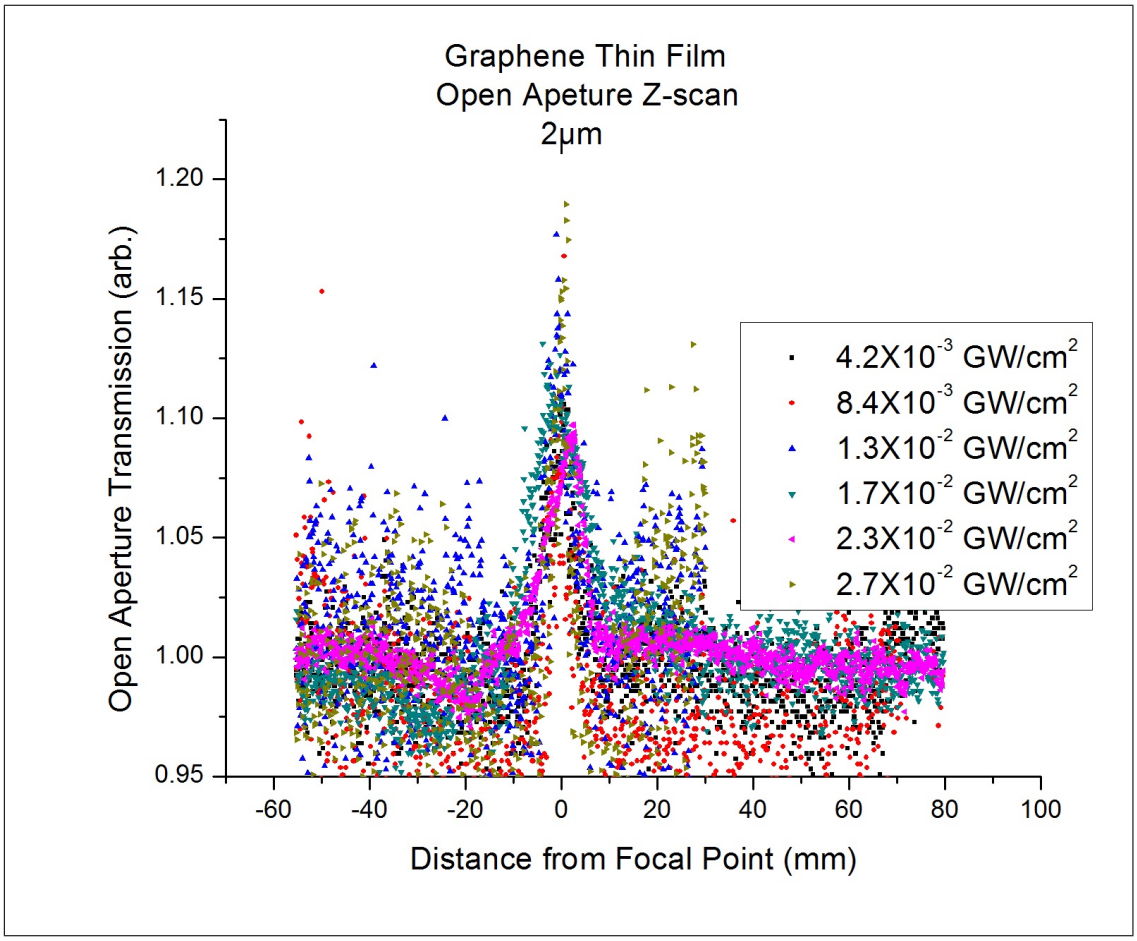

Figure A.1: Graphene thin film open aperture Z-scan at 2 μm.

A.1 Carbon Nanotubes

Single-walled carbon nanotube solutions were prepared by suspending the NTs in N-Cyclohexyl-2-pyrrolidone (CHP). A more localised sonication was employed, with the use of a sonic tip. Thin films were fabricated identically to the graphene films, described in Chapter 3. Nanotubes were purchased from cheaptubes.com, and the CHP was purchased from Sigma Aldrich.

While nanotube chirality was chosen to be operational at 2 μm, both the

NT/CHP dispersions (Figure A.2) and the NT thin film (Figure A.3) exhibit an optical limiting effect.

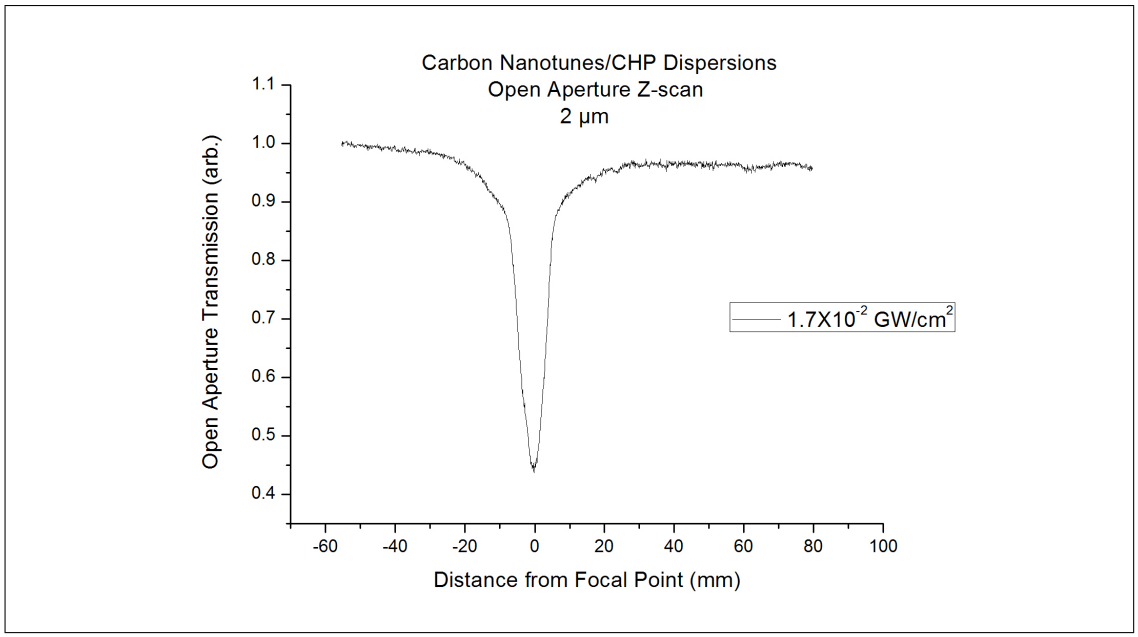

Figure A.2: Carbon nanotubes/CHP dispersion open aperture Z-scan at several intensities at 2 μm

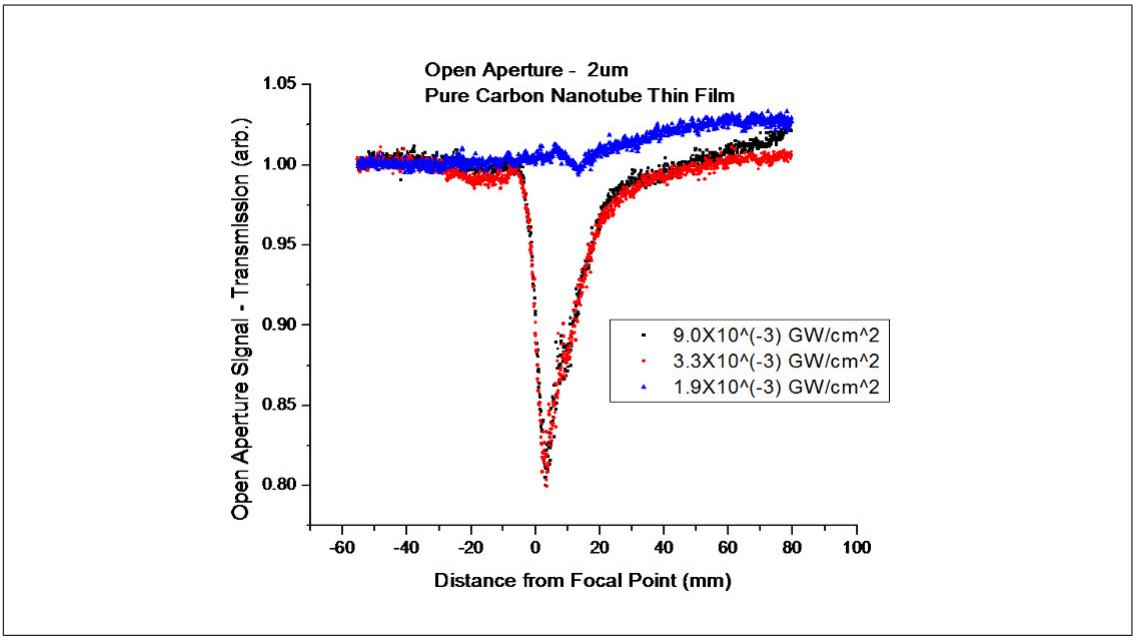

Figure A.3: Carbon nanotubes thin film open aperture Z-scan at several intensities at 2 μm

A.2 Boron Nitride

Boron Nitride (BN) samples were prepared by drop-casting 20 μL of the BN/NMP dispersion onto the borosilicate coverslips, and either dried in the oven or a vacuum desiccator, similar to the graphene samples described in Chapter 3. As can be seen in Figure A.4, BN displays an optical limiting response at 2 μm.

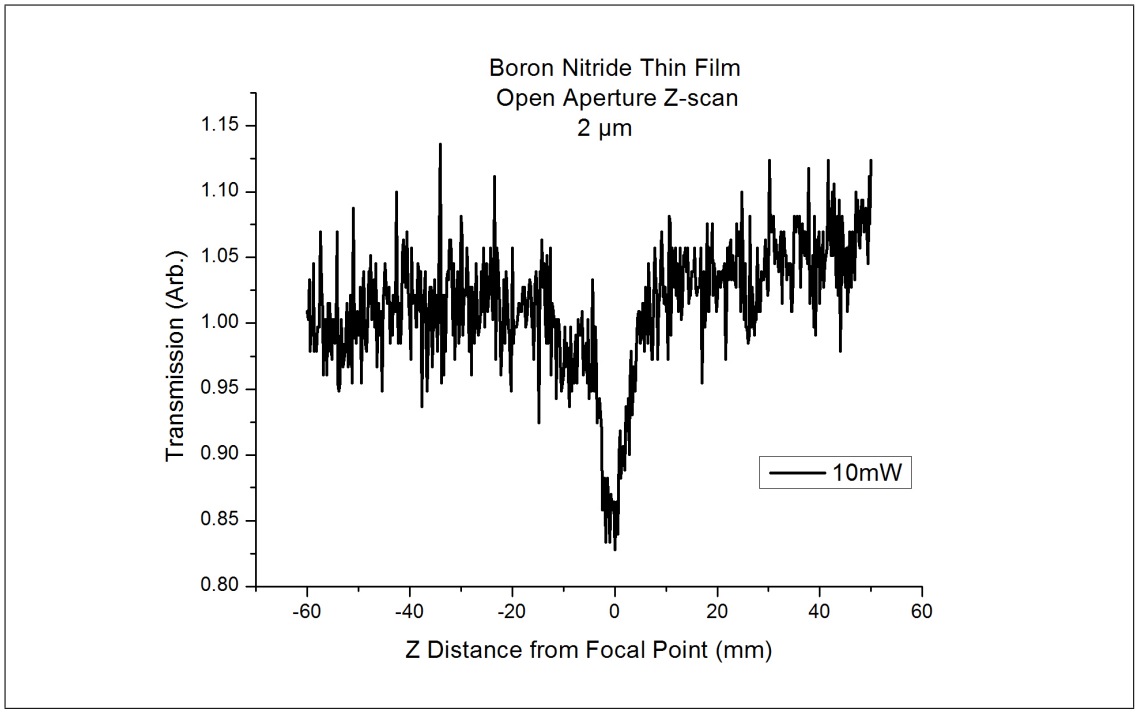

Figure A.4: Boron Nitride (BN) thin film open aperture Z-scan at several intensities at 2 μm

A.3 Molybdenum Disulphide

Molybdenum Disulphide (MoS_2) samples were prepared by drop-casting 20 μL of the MoS_2/NMP dispersion onto the borosilicate coverslips, and either dried in the oven or a vacuum desiccator, similar to the graphene samples described in Chapter 3 and the boron nitride samples outlined in Section A.2. As can be seen in Figure A.5, MoS_2 exhibits saturable absorption at 2 μm.

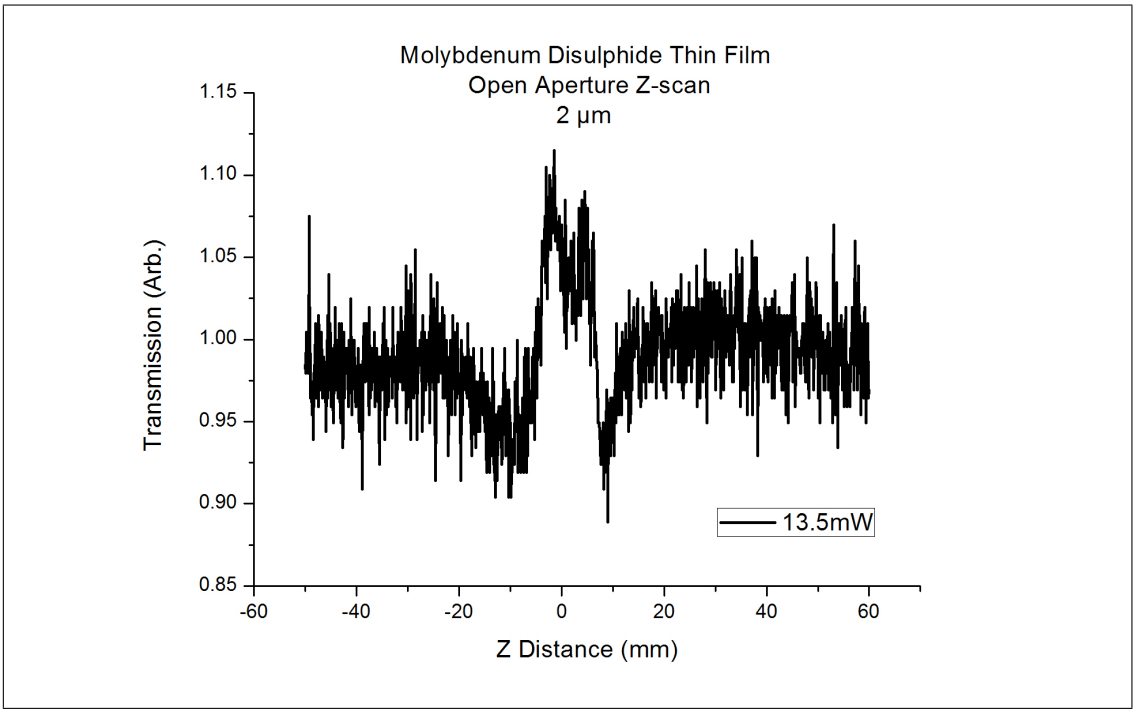

Figure A.5: Molybdenum Disulphide (MoS_2) thin film open aperture Z-scan at several intensities at 2 μm

References

Ahmad, H., Suthaskumar, M., Tiu, Z., Zarei, A. & Harun, S. (2016). Q-switched erbium-doped fiber laser using mose2 as saturable absorber. *Optics & Laser Technology*, **79**, 20 – 23. (Cited on page 77.)

Ando, T., Zheng, Y. & Suzuura, H. (2002). Dynamical conductivity and zero-mode anomaly in honeycomb lattices. *Journal of the Physical Society of Japan*, **71**, 1318–1324. (Cited on page 18.)

Bae, S., Kim, H., Lee, Y., Xu, X., Park, J.S., Zheng, Y., Balakrishnan, J., Lei, T., Kim, H.R., Song, Y.I. *et al.* (2010). Roll-to-roll production of 30-inch graphene films for transparent electrodes. *Nature nanotechnology*, **5**, 574–578. (Cited on page 1.)

Balandin, A.A., Ghosh, S., Bao, W., Calizo, I., Teweldebrhan, D., Miao, F. & Lau, C.N. (2008). Superior thermal conductivity of single-layer graphene. *Nano letters*, **8**, 902–907. (Cited on page 27.)

Baltuska, A., Wei, Z., Pshenichnikov, M.S. & Wiersma, D.A. (1997). Optical pulse compression to 5 fs at a 1-mhz repetition rate. *Optics letters*, **22**, 102–104. (Cited on page 41.)

Bao, Q., Zhang, H., Wang, Y., Ni, Z., Yan, Y., Shen, Z.X., Loh, K.P. & Tang, D.Y. (2009). Atomic-layer graphene as a saturable absorber for ultrafast pulsed lasers. *Advanced Functional Materials*, **19**, 3077–3083. (Cited on pages 1, 27, 29 and 197.)

Bao, Q., Zhang, H., Yang, J.x., Wang, S., Tang, D.Y., Jose, R., Ramakrishna, S., Lim, C.T. & Loh, K.P. (2010). Graphene–polymer nanofiber membrane for ultrafast photonics. *Advanced Functional Materials*, **20**, 782–791. (Cited on pages 27 and 233.)

Bao, Q., Zhang, H., Ni, Z., Wang, Y., Polavarapu, L., Shen, Z., Xu, Q.H., Tang, D. & Loh, K.P. (2011). Monolayer graphene as a saturable absorber in a mode-locked laser. *Nano Research*, **4**, 297–307. (Cited on pages 1 and 27.)

Barone, V., Hod, O. & Scuseria, G.E. (2006). Electronic structure and stability of semiconducting graphene nanoribbons. *Nano letters*, **6**, 2748–2754. (Cited on pages 1 and 27.)

Berger, C., Song, Z., Li, X., Wu, X., Brown, N., Naud, C., Mayou, D., Li, T., Hass, J., Marchenkov, A.N. *et al.* (2006). Electronic confinement and coherence in patterned epitaxial graphene. *Science*, **312**, 1191–1196. (Cited on page 3.)

Bethge, J., Steinmeyer, G., Stibenz, G., Staudt, P., Brée, C., Demircan, A., Redlin, H. & Düsterer, S. (????). Weierstraß-institut. (Cited on page 41.)

Bittner, S., Dietz, B., Miski-Oglu, M., Oria Iriarte, P., Richter, A. & Schäfer, F. (2010). Observation of a dirac point in microwave experiments with a photonic crystal modeling graphene. *Phys. Rev. B*, **82**, 014301. (Cited on page 55.)

Blake, P., Brimicombe, P.D., Nair, R.R., Booth, T.J., Jiang, D., Schedin, F., Ponomarenko, L.A., Morozov, S.V., Gleeson, H.F., Hill, E.W. *et al.* (2008). Graphene-based liquid crystal device. *Nano letters*, **8**, 1704–1708. (Cited on pages 7 and 9.)

Bonaccorso, F., Sun, Z., Hasan, T. & Ferrari, A. (2010). Graphene photonics and optoelectronics. *Nature photonics*, **4**, 611–622. (Cited on pages 1, 27, 45, 125, 204 and 227.)

Boyd, R.W. (2003). *Nonlinear optics*. Elsevier. (Cited on page 46.)

Breusing, M., Ropers, C. & Elsaesser, T. (2009). Ultrafast carrier dynamics in graphite. *Physical review letters*, **102**, 086809. (Cited on pages 27 and 206.)

Brovelli, L., Jung, I., Kopf, D., Kamp, M., Moser, M., Kärtner, F. & Keller, U. (1995). Self-starting soliton modelocked ti-sapphire laser using a thin semiconductor saturable absorber. *Electronics Letters*, **31**, 287–289. (Cited on page 43.)

Burshtein, Z., Blau, P., Kalisky, Y., Shimony, Y. & Kikta, M.R. (1998). Excited-state absorption studies of cr/sup 4+/ ions in several garnet host crystals. *IEEE Journal of Quantum Electronics*, **34**, 292–299. (Cited on pages 46, 64, 65, 67 and 211.)

Cerullo, G., De Silvestri, S. & Magni, V. (1994a). Self-starting kerr-lens mode locking of a ti: sapphire laser. *Optics letters*, **19**, 1040–1042. (Cited on page 41.)

Cerullo, G., De Silvestri, S., Magni, V. & Pallaro, L. (1994b). Resonators for kerr-lens mode-locked femtosecond ti: sapphire lasers. *Optics letters*, **19**, 807–809. (Cited on page 41.)

Chang, Y.M., Kim, H., Lee, J.H. & Song, Y.W. (2010a). Multilayered graphene efficiently formed by mechanical exfoliation for nonlinear saturable absorbers in fiber mode-locked lasers. *Applied Physics Letters*, **97**, 211102. (Cited on pages xvii, 57 and 88.)

Chang, Y.M., Kim, H., Lee, J.H. & Song, Y.W. (2010b). Multilayered graphene efficiently formed by mechanical exfoliation for nonlinear saturable absorbers in fiber mode-locked lasers. *Applied Physics Letters*, **97**, 211102. (Cited on page 88.)

Chapple, P., Staromlynska, J., Hermann, J., Mckay, T. & McDuff, R. (1997). Single-beam z-scan: measurement techniques and analysis. *Journal of Nonlinear Optical Physics & Materials*, **6**, 251–293. (Cited on page 126.)

Chen, B., Zhang, X., Wu, K., Wang, H., Wang, J. & Chen, J. (2015). Q-switched fiber laser based on transition metal dichalcogenides mos2, mose2, ws2, and wse2. *Opt. Express*, **23**, 26723–26737. (Cited on pages 77 and 87.)

Chen, H., Chen, Y., Yin, J., Zhang, X., Guo, T. & Yan, P. (2016). High-damage-resistant tungsten disulfide saturable absorber mirror for passively q-switched fiber laser. *Opt. Express*, **24**, 16287–16296. (Cited on pages 48, 71 and 72.)

Chen, Y., Zhao, C., Wang, Z., Song, J., Zhang, H. & Wen, S. (2012). Erbium-doped fiber laser passively mode-locked by a position-adjustable graphene saturable absorber. *Optical Engineering*, **51**, 084203–1. (Cited on pages 1 and 27.)

Chi, C., Lee, J., Koo, J. & Lee, J.H. (2014). All-normal-dispersion dissipative-soliton fiber laser at 1.06 μm using a bulk-structured bi2te3topological insulator-deposited side-polished fiber. *Laser Physics*, **24**, 105106. (Cited on page 88.)

Cho, W.B., Kim, J.W., Lee, H.W., Bae, S., Hong, B.H., Choi, S.Y., Baek, I.H., Kim, K., Yeom, D.I. & Rotermund, F. (2011). High-quality, large-area monolayer graphene for efficient bulk laser mode-locking near 1.25 μm. *Optics letters*, **36**, 4089–4091. (Cited on pages 27 and 28.)

Choi, H., Borondics, F., Siegel, D.A., Zhou, S.Y., Martin, M.C., Lanzara, A. & Kaindl, R.A. (2009). Broadband electromagnetic response and ultrafast dynamics of few-layer epitaxial graphene. *Applied Physics Letters*, **94**, 172102. (Cited on page 27.)

Choi, S.Y., Cho, D.K., Song, Y.W., Oh, K., Kim, K., Rotermund, F. & Yeom, D.I. (2012). Graphene-filled hollow optical fiber saturable absorber for efficient soliton fiber laser mode-locking. *Optics express*, **20**, 5652–5657. (Cited on pages 81 and 233.)

Christov, I.P., Kapteyn, H.C., Murnane, M.M., Huang, C.P. & Zhou, J. (1995). Space–time focusing of femtosecond pulses in a ti: sapphire laser. *Optics letters*, **20**, 309–311. (Cited on page 41.)

Coelho, R. (2012). *Physics of Dielectrics for the Engineer*, vol. 1. Elsevier. (Cited on page 31.)

Coleman, J.N., Lotya, M., O'Neill, A., Bergin, S.D., King, P.J., Khan, U., Young, K., Gaucher, A., De, S., Smith, R.J., Shvets, I.V., Arora, S.K., Stanton, G., Kim, H.Y., Lee, K., Kim, G.T., Duesberg, G.S., Hallam, T., Boland, J.J., Wang, J.J., Donegan, J.F., Grunlan, J.C., Moriarty, G., Shmeliov, A., Nicholls, R.J., Perkins, J.M., Grieveson, E.M., Theuwissen, K., McComb, D.W., Nellist, P.D. & Nicolosi, V. (2011a). Two-dimensional nanosheets produced by liquid exfoliation of layered materials. *Science*, **331**, 568–571. (Cited on page 190.)

Coleman, J.N., Lotya, M., ONeill, A., Bergin, S.D., King, P.J., Khan, U., Young, K., Gaucher, A., De, S., Smith, R.J. *et al.* (2011b). Two-dimensional nanosheets produced by liquid exfoliation of layered materials. *Science*, **331**, 568–571. (Cited on pages 55, 75 and 125.)

Cui, Y. & Liu, X. (2013). Graphene and nanotube mode-locked fiber laser emitting dissipative and conventional solitons. *Optics express*, **21**, 18969–18974. (Cited on pages 79, 81, 88 and 233.)

Cundiff, S., Ippen, E., Haus, H. & Knox, W. (1996). Frequency-dependent mode size in broadband kerr-lens mode locking. *Optics letters*, **21**, 662–664. (Cited on page 41.)

Cunning, B., Brown, C. & Kielpinski, D. (2011). Low-loss flake-graphene saturable absorber mirror for laser mode-locking at sub-200-fs pulse duration. *Applied Physics Letters*, **99**, 261109. (Cited on pages 27, 71, 75, 79, 83 and 233.)

Cunningham, G., Lotya, M., Cucinotta, C.S., Sanvito, S., Bergin, S.D., Menzel, R., Shaffer, M.S.P. & Coleman, J.N. (2012). Solvent exfoliation of transition metal dichalcogenides: Dispersibility of exfoliated nanosheets varies only weakly between compounds. *ACS Nano*, **6**, 3468–3480, pMID: 22394330. (Cited on page 55.)

Dal Conte, S., Bottegoni, F., Pogna, E.A.A., De Fazio, D., Ambrogio, S., Bargigia, I., D'Andrea, C., Lombardo, A., Bruna, M., Ciccacci, F., Ferrari, A.C., Cerullo, G. & Finazzi, M. (2015a). Ultrafast valley relaxation dynamics in monolayer mos_2 probed by nonequilibrium optical techniques. *Phys. Rev. B*, **92**, 235425. (Cited on pages xvii, 57 and 62.)

Dal Conte, S., Bottegoni, F., Pogna, E.A.A., De Fazio, D., Ambrogio, S., Bargigia, I., D'Andrea, C., Lombardo, A., Bruna, M., Ciccacci, F., Ferrari, A.C., Cerullo, G. & Finazzi, M. (2015b). Ultrafast valley relaxation dynamics in monolayer mos_2 probed by nonequilibrium optical techniques. *Phys. Rev. B*, **92**, 235425. (Cited on page 80.)

Dawlaty, J.M., Shivaraman, S., Chandrashekhar, M., Rana, F. & Spencer, M.G. (2008a). Measurement of ultrafast carrier dynamics in epitaxial graphene. *Applied Physics Letters*, **92**, 042116. (Cited on pages xvii, 57, 59 and 62.)

Dawlaty, J.M., Shivaraman, S., Chandrashekhar, M., Rana, F. & Spencer, M.G. (2008b). Measurement of ultrafast carrier dynamics in epitaxial graphene. *Applied Physics Letters*, **92**, 042116+. (Cited on pages 62 and 66.)

Dawlaty, J.M., Shivaraman, S., Strait, J., George, P., Chandrashekhar, M., Rana, F., Spencer, M.G., Veksler, D. & Chen, Y. (2008c). Measurement of the optical absorption spectra of epitaxial graphene from terahertz to visible. *Applied Physics Letters*, **93**, 131905. (Cited on page 193.)

Demetriou, G., Biancalana, F., Bookey, H.T. & Kar, A. (2015). Nonlinear optical properties of a graphene-polyvinyl alcohol composite from 1550 nm to 2400 nm. In *CLEO: QELS_Fundamental Science*, JTu5A–29, Optical Society of America. (Cited on pages 228 and 230.)

Demetriou, G., Bookey, H.T., Biancalana, F., Abraham, E., Wang, Y., Ji, W. & Kar, A.K. (2016). Nonlinear optical properties of multilayer graphene in the infrared. *Opt. Express*, **24**, 13033–13043. (Cited on page 142.)

Dhanabalan, S.C., Ponraj, J.S., Guo, Z., Li, S., Bao, Q. & Zhang, H. (2017). Emerging trends in phosphorene fabrication towards next generation devices. *Advanced Science*, **4**, 1600305. (Cited on page 48.)

Dong, N., Li, Y., Zhang, S., McEvoy, N., Zhang, X., Cui, Y., Zhang, L., Duesberg, G.S. & Wang, J. (2016a). Dispersion of nonlinear refractive index in layered ws 2 and wse 2 semiconductor films induced by two-photon absorption. *Optics letters*, **41**, 3936–3939. (Cited on pages 75 and 150.)

Dong, N., Li, Y., Zhang, S., McEvoy, N., Zhang, X., Cui, Y., Zhang, L., Duesberg, G.S. & Wang, J. (2016b). Dispersion of nonlinear refractive index in layered ws2 and wse2 semiconductor films induced by two-photon absorption. *Opt. Lett.*, **41**, 3936–3939. (Cited on pages 75 and 81.)

Dong, N., Li, Y., Zhang, S., Zhang, X. & Wang, J. (2017). Optically induced transparency and extinction in dispersed mos2, mose2, and graphene nanosheets. *Advanced Optical Materials*, **5**, 1700543. (Cited on page 46.)

Dong, N., Li, Y., Zhang, S., McEvoy, N., Gatensby, R., Duesberg, G.S. & Wang, J. (2018). Saturation of two-photon absorption in layered transition metal dichalcogenides: Experiment and theory. *ACS Photonics*, **5**, 1558–1565. (Cited on page 46.)

Dremetsika, E., Dlubak, B., Gorza, S.P., Ciret, C., Martin, M.B., Hofmann, S., Seneor, P., Dolfi, D., Massar, S., Emplit, P. & Kockaert, P. (2016). Measuring the nonlinear refractive index of graphene using the optical kerr effect method. *Opt. Lett.*, **41**, 3281–3284. (Cited on page 147.)

Du, J., Wang, Q., Jiang, G., Xu, C., Zhao, C., Xiang, Y., Chen, Y., Wen, S. & Zhang, H. (2014). Ytterbium-doped fiber laser passively mode locked by few-layer molybdenum disulfide (mos 2) saturable absorber functioned with evanescent field interaction. *Scientific reports*, **4**, 6346. (Cited on pages 48, 83 and 84.)

Du, X., Skachko, I., Duerr, F., Luican, A. & Andrei, E.Y. (2009). Fractional quantum hall effect and insulating phase of dirac electrons in graphene. *Nature*, **462**, 192–195. (Cited on pages 1 and 27.)

Eilers, H., Hoffman, K.R., Dennis, W.M., Jacobsen, S.M. & Yen, W.M. (1992). Saturation of 1.064 m absorption in cr,ca:y3al5o12 crystals. *Applied Physics Letters*, **61**, 2958–2960. (Cited on page 51.)

Eizenberg, M. & Blakely, J. (1979). Carbon interaction with nickel surfaces: Monolayer formation and structural stability. *The Journal of Chemical Physics*, **71**, 3467–3477. (Cited on page 10.)

Fan, Y., Jiang, Z. & Yao, L. (2012). Two-photon absorption of monolayer graphene suspensions in femtosecond regime. *Chinese Optics Letters*, **10**, 071901–071901. (Cited on pages 175 and 231.)

Feng, C., Liu, J., Wang, Y., Zheng, L., Su, L. & Xu, J. (2013a). An yb3+-doped lu2sio5 mode-locked laser using a reflective graphene oxide absorber. *Laser Physics*, **23**, 065802. (Cited on pages 81 and 234.)

Feng, C., Wang, Y., Liu, J., Tsang, Y.H., Song, Y. & Yu, Z. (2013b). 3w high-power laser passively mode-locked by graphene oxide saturable absorber. *Optics Communications*, **298**, 168–170. (Cited on pages 80 and 234.)

Feng, Y., Dong, N., Wang, G., Li, Y., Zhang, S., Wang, K., Zhang, L., Blau, W.J. & Wang, J. (2015a). Saturable absorption behavior of free-standing graphene polymer composite films over broad wavelength and time ranges. *Optics express*, **23**, 559–569. (Cited on pages xvii, xviii, xix, 47, 51, 52, 53, 55, 57, 58, 62, 64, 65, 68, 70, 76, 77 and 119.)

Feng, Y., Dong, N., Wang, G., Li, Y., Zhang, S., Wang, K., Zhang, L., Blau, W.J. & Wang, J. (2015b). Saturable absorption behavior of free-standing graphene polymer composite films over broad wavelength and time ranges. *Opt. Express*, **23**, 559–569. (Cited on page 52.)

Ferrari, A.C. & Basko, D.M. (2013). Raman spectroscopy as a versatile tool for studying the properties of graphene. *Nature nanotechnology*, **8**, 235. (Cited on page 191.)

Fork, R.L., Greene, B.I. & Shank, C.V. (1981). Generation of optical pulses shorter than 0.1 psec by colliding pulse mode locking. *Applied Physics Letters*, **38**, 671–672. (Cited on page 77.)

Fork, R.L., Brito Cruz, C.H., Becker, P. & Shank, C.V. (1987). Compression of optical pulses to six femtoseconds by using cubic phase compensation. *Optics letters*, **12**, 483–485. (Cited on page 40.)

Fu, B., Gui, L., Zhang, W., Xiao, X., Zhu, H. & Yang, C. (2013a). Passive harmonic mode locking in erbium-doped fiber laser with graphene saturable absorber. *Optics Communications*, **286**, 304 – 308. (Cited on pages 79, 81 and 88.)

Fu, B., Gui, L., Zhang, W., Xiao, X., Zhu, H. & Yang, C. (2013b). Passive harmonic mode locking in erbium-doped fiber laser with graphene saturable absorber. *Optics Communications*, **286**, 304–308. (Cited on pages 79, 80, 88 and 233.)

Gao, W., Huang, L., Xu, J., Chen, Y., Zhu, C., Nie, Z., Li, Y., Wang, X., Xie, Z., Zhu, S., Xu, J., Wan, X., Zhang, C., Xu, Y., Shi, Y. & Wang, F. (2018). Broadband photocarrier dynamics and nonlinear absorption of pld-grown wte2 semimetal films. *Applied Physics Letters*, **112**, 171112. (Cited on pages xvii and 57.)

Gates, D.M. (1966). Spectral distribution of solar radiation at the earth's surface. *Science*, **151**, 523–529. (Cited on page 28.)

Ge, S., Li, C., Zhang, Z., Zhang, C., Zhang, Y., Qiu, J., Wang, Q., Liu, J., Jia, S., Feng, J. & Sun, D. (2015). Dynamical evolution of anisotropic response in black phosphorus under ultrafast photoexcitation. *Nano Letters*, **15**, 4650–4656, pMID: 26039361. (Cited on page 80.)

Geim, A.K. & Novoselov, K.S. (2007). The rise of graphene. *Nature materials*, **6**, 183–191. (Cited on page 1.)

Geusic, J., Marcos, H. & Van Uitert, L. (1964). Laser oscillations in nd-doped yttrium aluminum, yttrium gallium and gadolinium garnets. *Applied Physics Letters*, **4**, 182. (Cited on page 19.)

Gordon, R.A., Yang, D., Crozier, E.D., Jiang, D.T. & Frindt, R.F. (2002). Structures of exfoliated single layers of ws_2, mos_2, and $mose_2$ in aqueous suspension. *Phys. Rev. B*, **65**, 125407. (Cited on page 55.)

Gould, R.G. (1959). The laser, light amplification by stimulated emission of radiation. In *The Ann Arbor conference on optical pumping, the University of Michigan*, vol. 15, 128. (Cited on page 19.)

Green, A.A. & Hersam, M.C. (2009). Solution phase production of graphene with controlled thickness via density differentiation. *Nano Letters*, **9**, 4031–4036. (Cited on page 7.)

Gui, L., Zhang, W., Li, X., Xiao, X., Zhu, H., Wang, K., Wu, D. & Yang, C. (2011). Self-assembled graphene membrane as an ultrafast mode-locker in an erbium fiber laser. *Photonics Technology Letters, IEEE*, **23**, 1790–1792. (Cited on pages 81 and 233.)

Guo, Z., Chen, S., Wang, Z., Yang, Z., Liu, F., Xu, Y., Wang, J., Yi, Y., Zhang, H., Liao, L., Chu, P.K. & Yu, X.F. (2017). Metal-ion-modified black phosphorus with enhanced stability and transistor performance. *Advanced Materials*, **29**, 1703811. (Cited on page 47.)

Gusynin, V., Sharapov, S. & Carbotte, J. (2006). Unusual microwave response of dirac quasiparticles in graphene. *Physical review letters*, **96**, 256802. (Cited on page 18.)

Haiml, M., Grange, R. & Keller, U. (2004). Optical characterization of semiconductor saturable absorbers. *Applied Physics B*, **79**, 331–339. (Not cited.)

Hanlon, D., Backes, C., Doherty, E., Cucinotta, C.S., Berner, N.C., Boland, C., Lee, K., Harvey, A., Lynch, P., Gholamvand, Z. *et al.* (2015). Liquid exfoliation of solvent-stabilized few-layer black phosphorus for applications beyond electronics. *Nature communications*, **6**, 8563. (Cited on page 55.)

Harter, D., Shand, M. & Band, Y. (1984). Power/energy limiter using reverse saturable absorption. *Journal of applied physics*, **56**, 865–868. (Cited on page 32.)

Hasan, T., Sun, Z., Wang, F., Bonaccorso, F., Tan, P.H., Rozhin, A.G. & Ferrari, A.C. (2009a). Nanotube-polymer composites for ultrafast photonics. *Adv. Mater*, **21**, 3874–3899. (Cited on pages 27 and 233.)

Hasan, T., Sun, Z., Wang, F., Bonaccorso, F., Tan, P.H., Rozhin, A.G. & Ferrari, A.C. (2009b). NanotubePolymer Composites for Ultrafast Photonics. *Adv. Mater.*, **21**, 3874–3899. (Cited on page 8.)

Hasan, T., Torrisi, F., Sun, Z., Popa, D., Nicolosi, V., Privitera, G., Bonaccorso, F. & Ferrari, A. (2010). Solution-phase exfoliation of graphite for ultrafast photonics. *physica status solidi (b)*, **247**, 2953–2957. (Cited on pages 7, 8 and 233.)

Haus, H. *et al.* (1975). Theory of mode locking with a slow saturable absorber. *Quantum Electronics, IEEE Journal of*, **11**, 736–746. (Cited on pages 39 and 40.)

Haus, H.A. (1975a). Theory of mode locking with a fast saturable absorber. *Journal of Applied Physics*, **46**, 3049–3058. (Cited on pages 39, 78, 81 and 190.)

Haus, H.A. (1975b). Theory of mode locking with a fast saturable absorber. *Journal of Applied Physics*, **46**, 3049–3058. (Cited on page 78.)

Haus, H.A. (1975c). Theory of mode locking with a fast saturable absorber. *Journal of Applied Physics*, **46**, 3049–3058. (Cited on page 81.)

Haus, H.A. (1975d). Theory of mode locking with a fast saturable absorber. *Journal of Applied Physics*, **46**, 3049–3058. (Cited on page 206.)

Haus, H.A. (2000). Mode-locking of lasers. *Selected Topics in Quantum Electronics, IEEE Journal of*, **6**, 1173–1185. (Cited on page 48.)

Haus, H.A., Fujimoto, J.G. & Ippen, E.P. (1991). Structures for additive pulse mode locking. *JOSA B*, **8**, 2068–2076. (Cited on pages 39 and 41.)

He, X., Liu, Z.B., Wang, D., Yang, M., Liao, C. & Zhao, X. (2012). Passively mode-locked fiber laser based on reduced graphene oxide on microfiber for ultra-wide-band doublet pulse generation. *Journal of Lightwave Technology*, **30**, 984–989. (Cited on pages 81 and 233.)

Hernandez, Y., Nicolosi, V., Lotya, M., Blighe, F.M., Sun, Z., De, S., McGovern, I., Holland, B., Byrne, M., Gun'Ko, Y.K. *et al.* (2008a). High-yield production of graphene by liquid-phase exfoliation of graphite. *Nature nanotechnology*, **3**, 563–568. (Cited on pages 6, 119 and 125.)

Hernandez, Y., Nicolosi, V., Lotya, M., Blighe, F.M., Sun, Z., De, S., McGovern, I.T., Holland, B., Byrne, M., Gun'Ko, Y.K., Boland, J.J., Niraj, P., Duesberg, G., Krishnamurthy, S., Goodhue, R., Hutchison, J., Scardaci, V., Ferrari, A.C. & Coleman, J.N. (2008b). High-yield production of graphene by liquid-phase exfoliation of graphite. *Nature Nanotechnology*, **3**, 563–568. (Cited on pages 6, 7, 8, 9, 131 and 190.)

Hill, E.W., Geim, A.K., Novoselov, K., Schedin, F. & Blake, P. (2006). Graphene spin valve devices. *Magnetics, IEEE Transactions on*, **42**, 2694–2696. (Cited on page 1.)

Holonyak Jr, N. & Bevacqua, S. (1962). Coherent (visible) light emission from ga (as1-xpx) junctions. *Applied Physics Letters*, **1**, 82–83. (Cited on page 19.)

Hönninger, C., Giesen, A., Zhang, G. & Keller, U. (1995). Femtosecond yb: Yag laser using semiconductor saturable absorbers. *Optics letters*, **20**, 2402–2404. (Cited on page 43.)

Hönninger, C., Paschotta, R., Morier-Genoud, F., Moser, M. & Keller, U. (1999). Q-switching stability limits of continuous-wave passive mode locking. *JOSA B*, **16**, 46–56. (Cited on page 34.)

Hou, J., Zhang, B., He, J., Wang, Z., Lou, F., Ning, J., Zhao, R. & Su, X. (2014). Passively q-switched 2 μm tm:yap laser based on graphene saturable absorber mirror. *Appl. Opt.*, **53**, 4968–4971. (Cited on pages 71, 75, 80 and 83.)

Huang, J., Dong, N., Zhang, S., Sun, Z., Zhang, W. & Wang, J. (2017). Nonlinear absorption induced transparency and optical limiting of black phosphorus nanosheets. *ACS Photonics*, **4**, 3063–3070. (Cited on pages 46 and 75.)

Huang, Y., Luo, Z., Li, Y., Zhong, M., Xu, B., Che, K., Xu, H., Cai, Z., Peng, J. & Weng, J. (2014). Widely-tunable, passively q-switched erbium-doped fiber laser with few-layer mos2 saturable absorber. *Opt. Express*, **22**, 25258–25266. (Cited on pages 77, 83 and 87.)

Husaini, S., Slagle, J.E., Murray, J.M., Guha, S., Gonzalez, L.P. & Bedford, R.G. (2013). Broadband saturable absorption and optical limiting in graphene-polymer composites. *Applied Physics Letters*, **102**, 191112. (Cited on page 213.)

Ippen, E., Eilenberger, D. & Dixon, R. (1980a). Picosecond pulse generation by passive mode locking of diode lasers. *Applied Physics Letters*, **37**, 267–269. (Cited on page 78.)

Ippen, E.P., Eilenberger, D.J. & Dixon, R.W. (1980b). Picosecond pulse generation by passive mode locking of diode lasers. *Applied Physics Letters*, **37**, 267–269. (Cited on pages 78 and 81.)

Javan, A., Bennett Jr, W.R. & Herriott, D.R. (1961). Population inversion and continuous optical maser oscillation in a gas discharge containing a he-ne mixture. *Physical Review Letters*, **6**, 106. (Cited on page 19.)

Jin, X., Hu, G., Zhang, M., Hu, Y., Albrow-Owen, T., Howe, R.C.T., Wu, T.C., Wu, Q., Zheng, Z. & Hasan, T. (2018a). 102 fs pulse generation from a long-term stable, inkjet-printed black phosphorus-mode-locked fiber laser. *Opt. Express*, **26**, 12506–12513. (Cited on pages 48 and 85.)

Jin, X., Hu, G., Zhang, M., Hu, Y., Albrow-Owen, T., Howe, R.C.T., Wu, T.C., Wu, Q., Zheng, Z. & Hasan, T. (2018b). 102 fs pulse generation from a long-term stable, inkjet-printed black phosphorus-mode-locked fiber laser. *Opt. Express*, **26**, 12506–12513. (Cited on page 84.)

Jung, I., Kärtner, F., Brovelli, L., Kamp, M. & Keller, U. (1995a). Experimental verification of soliton mode locking using only a slow saturable absorber. *Optics letters*, **20**, 1892–1894. (Cited on pages 39, 40, 41 and 42.)

Jung, I., Moser, M., Brovelli, L., Kamp, M. & Keller, U. (1995b). Scaling of the antiresonant fabry–perot saturable absorber design toward a thin saturable absorber. *Optics letters*, **20**, 1559–1561. (Cited on page 43.)

Jung, I., Kärtner, F., Henkmann, J., Zhang, G. & Keller, U. (1997a). High-dynamic-range characterization of ultrashort pulses. *Applied Physics B: Lasers and Optics*, **65**, 307–310. (Cited on page 42.)

Jung, I., Kärtner, F., Matuschek, N., Sutter, D., Morier-Genoud, F., Zhang, G., Keller, U., Scheuer, V., Tilsch, M. & Tschudi, T. (1997b). Self-starting 6.5-fs pulses from a ti: sapphire laser. *Optics letters*, **22**, 1009–1011. (Cited on page 41.)

Jung, M., Koo, J., Debnath, P., Song, Y.W. & Lee, J.H. (2012). A mode-locked 1.91? m fiber laser based on interaction between graphene oxide and evanescent field. *Applied Physics Express*, **5**, 112702. (Cited on pages 80, 223, 232 and 234.)

Jung, M., Koo, J., Park, J., Song, Y.W., Jhon, Y.M., Lee, K., Lee, S. & Lee, J.H. (2013). Mode-locked pulse generation from an all-fiberized, tm-ho-codoped fiber laser incorporating a graphene oxide-deposited side-polished fiber. *Optics express*, **21**, 20062–20072. (Cited on pages 80, 223, 232 and 234.)

Kajava, T.T. & Gaeta, A.L. (1996). Q switching of a diode-pumped nd:yag laser with gaas. *Opt. Lett.*, **21**, 1244–1246. (Cited on page 78.)

Kärtner, F. & Keller, U. (1995a). Stabilization of solitonlike pulses with a slow saturable absorber. *Optics letters*, **20**, 16–18. (Cited on pages 39, 42 and 77.)

Kärtner, F. & Keller, U. (1995b). Stabilization of solitonlike pulses with a slow saturable absorber. *Optics letters*, **20**, 16–18. (Cited on page 77.)

Kärtner, F., Kopf, D. & Keller, U. (1995). Solitary-pulse stabilization and shortening in actively mode-locked lasers. *JOSA B*, **12**, 486–496. (Cited on page 41.)

Kärtner, F., Jung, I. & Keller, U. (1996). Soliton mode-locking with saturable absorbers. *Selected Topics in Quantum Electronics, IEEE Journal of*, **2**, 540–556. (Cited on page 39.)

Kärtner, F., Matuschek, N., Schibli, T., Keller, U., Haus, H., Heine, C., Morf, R., Scheuer, V., Tilsch, M. & Tschudi, T. (1997). Design and fabrication of double-chirped mirrors. *Optics letters*, **22**, 831–833. (Cited on page 41.)

Kaup, D. (1990). Perturbation theory for solitons in optical fibers. *Physical Review A*, **42**, 5689. (Cited on page 41.)

Keller, U. (1996). Advances in all-solid-state ultrafast lasers. In *Ultrafast Phenomena X*, 3–5, Springer. (Cited on page 43.)

Keller, U. (2003). Recent developments in compact ultrafast lasers. *Nature*, **424**, 831–838. (Cited on pages xvi, 32, 33 and 42.)

Keller, U., Thooft, G., Knox, W., Cunningham, J. *et al.* (1991). Femtosecond pulses from a continuously self-starting passively mode-locked ti: sapphire laser. *Optics letters*, **16**, 1022–1024. (Cited on page 40.)

Keller, U., Miller, D., Boyd, G., Chiu, T., Ferguson, J. & Asom, M. (1992). Solid-state low-loss intracavity saturable absorber for nd: Ylf lasers: an antiresonant semiconductor fabry–perot saturable absorber. *Optics letters*, **17**, 505–507. (Cited on page 43.)

Keller, U., Weingarten, K.J., Kärtner, F.X., Kopf, D., Braun, B., Jung, I.D., Fluck, R., Hönninger, C., Matuschek, N. & Au, J.A.d. (1996). Semiconductor saturable absorber mirrors (sesam's) for femtosecond to nanosecond pulse generation in solid-state lasers. *Selected Topics in Quantum Electronics, IEEE Journal of*, **2**, 435–453. (Cited on pages xvi, 37, 38, 39, 46 and 213.)

Khan, U., O'Neill, A., Lotya, M., De, S. & Coleman, J.N. (2010). High-concentration solvent exfoliation of graphene. *Small*, **6**, 864–871. (Cited on pages 6 and 132.)

Khazaeinezhad, R., Kassani, S.H., Nazari, T., Jeong, H., Kim, J., Choi, K., Lee, J.U., Kim, J.H., Cheong, H., Yeom, D.I. & Oh, K. (2015). Saturable optical absorption in mos2 nano-sheet optically deposited on the optical fiber facet. *Optics Communications*, **335**, 224 – 230. (Cited on page 83.)

Khazaeizhad, R., Kassani, S.H., Jeong, H., Yeom, D.I. & Oh, K. (2014). Mode-locking of er-doped fiber laser using a multilayer mos2 thin film as a saturable absorber in both anomalous and normal dispersion regimes. *Opt. Express*, **22**, 23732–23742. (Cited on pages 83 and 84.)

Kim, H., Cho, J., Jang, S.Y. & Song, Y.W. (2011). Deformation-immunized optical deposition of graphene for ultrafast pulsed lasers. *Applied Physics Letters*, **98**, 021104. (Cited on pages 81 and 233.)

Kim, K.S., Zhao, Y., Jang, H., Lee, S.Y., Kim, J.M., Kim, K.S., Ahn, J.H., Kim, P., Choi, J.Y. & Hong, B.H. (2009). Large-scale pattern growth of graphene films for stretchable transparent electrodes. *Nature*, **457**, 706–710. (Cited on page 3.)

Kim, M.H., Calmano, T., Choi, S.Y., Lee, B.J., Baek, I.H., Ahn, K.J., Yeom, D.I., Kränkel, C. & Rotermund, F. (2016). Monolayer graphene coated yb:yag channel waveguides for q-switched laser operation. *Opt. Mater. Express*, **6**, 2468–2474. (Cited on page 88.)

Kim, S. & Drzal, L.T. (2009). High latent heat storage and high thermal conductive phase change materials using exfoliated graphite nanoplatelets. *Solar Energy Materials and Solar Cells*, **93**, 136–142. (Cited on page 6.)

Kong, L., Qin, Z., Xie, G., Guo, Z., Zhang, H., Yuan, P. & Qian, L. (2016). Black phosphorus as broadband saturable absorber for pulsed lasers from 1m to 2.7m wavelength. *Laser Physics Letters*, **13**, 045801. (Cited on pages 71, 72, 75 and 84.)

Kong, L.C., Xie, G.Q., Yuan, P., Qian, L.J., Wang, S.X., Yu, H.H. & Zhang, H.J. (2015). Passive q-switching and q-switched mode-locking operations of 2 μm tm:clngg laser with mos2 saturable absorber mirror. *Photon. Res.*, **3**, A47–A50. (Cited on pages 48, 72 and 84.)

Koo, J., Jhon, Y.I., Park, J., Lee, J., Jhon, Y.M. & Lee, J.H. (2016a). Near-infrared saturable absorption of defective bulk-structured wte2 for femtosecond laser mode-locking. *Advanced Functional Materials*, **26**, 7454–7461. (Cited on page 88.)

Koo, J., Park, J., Lee, J., Jhon, Y.M. & Lee, J.H. (2016b). Femtosecond harmonic mode-locking of a fiber laser at 3.27 ghz using a bulk-like, mose2-based saturable absorber. *Opt. Express*, **24**, 10575–10589. (Cited on pages 77 and 87.)

Kopf, D., Kärtner, F., Weingarten, K. & Keller, U. (1994). Pulse shortening in a nd: glass laser by gain reshaping and soliton formation. *Optics letters*, **19**, 2146–2148. (Cited on page 41.)

Kopf, D., Weingarten, K., Kärtner, F. & Keller, U. (1995). Diode-pumped mode-locked nd: glass lasers with an antiresonant fabry–perot saturable absorber. *Optics letters*, **20**, 1169–1171. (Cited on page 42.)

Kopf, D., Zhang, G., Fluck, R., Moser, M. & Keller, U. (1996). All-in-one dispersion-compensating saturable absorber mirror for compact femtosecond laser sources. *Optics letters*, **21**, 486–488. (Cited on page 43.)

Kubecek, V., Diels, J.C. & Stintz, A. (2004). Bidirectional operation of a ring diode-pumped mode-locked nd: Yvo4 laser. In *Photonics Europe*, 309–314, International Society for Optics and Photonics. (Not cited.)

Kumar, S., Anija, M., Kamaraju, N., Vasu, K., Subrahmanyam, K., Sood, A. & Rao, C. (2009a). Femtosecond carrier dynamics and saturable absorption in graphene suspensions. *Applied physics letters*, **95**, 191911. (Cited on pages 27, 47, 53 and 55.)

Kumar, S., Anija, M., Kamaraju, N., Vasu, K., Subrahmanyam, K., Sood, A. & Rao, C. (2009b). Femtosecond carrier dynamics and saturable absorption in graphene suspensions. *Applied physics letters*, **95**, 191911. (Cited on page 206.)

Kuzmenko, A., Van Heumen, E., Carbone, F. & Van Der Marel, D. (2008). Universal optical conductance of graphite. *Physical review letters*, **100**, 117401. (Cited on page 18.)

Lang, B. (1975). A leed study of the deposition of carbon on platinum crystal surfaces. *Surface Science*, **53**, 317–329. (Cited on page 9.)

Lau, K.Y., Bakar, M.H.A., Muhammad, F.D., Latif, A.A., Omar, M.F., Yusoff, Z. & Mahdi, M.A. (2018). Dual-wavelength, mode-locked erbium-doped fiber laser employing a graphene/polymethyl-methacrylate saturable absorber. *Opt. Express*, **26**, 12790–12800. (Cited on pages 81 and 233.)

Lazzeri, M., Piscanec, S., Mauri, F., Ferrari, A. & Robertson, J. (2006). Phonon linewidths and electron-phonon coupling in graphite and nanotubes. *Physical review B*, **73**, 155426. (Cited on page 27.)

Lee, J., Koo, J., Debnath, P., Song, Y.W. & Lee, J.H. (2013a). AQ-switched, mode-locked fiber laser using a graphene oxide-based polarization sensitive saturable absorber. *Laser Physics Letters*, **10**, 035103. (Cited on page 81.)

Lee, J., Koo, J., Debnath, P., Song, Y.W. & Lee, J.H. (2013b). A q-switched, mode-locked fiber laser using a graphene oxide-based polarization sensitive saturable absorber. *Laser Physics Letters*, **10**, 035103. (Cited on page 233.)

Lee, J., Koo, J., Jhon, Y.M. & Lee, J.H. (2014). A femtosecond pulse erbium fiber laser incorporating a saturable absorber based on bulk-structured bi2te3 topological insulator. *Opt. Express*, **22**, 6165–6173. (Cited on page 88.)

Li, D., Mueller, M.B., Gilje, S., Kaner, R.B. & Wallace, G.G. (2008). Processable aqueous dispersions of graphene nanosheets. *Nature nanotechnology*, **3**, 101–105. (Cited on page 9.)

Li, H., Xia, H., Lan, C., Li, C., Zhang, X., Li, J. & Liu, Y. (2015). Passively*q*-switched erbium-doped fiber laser based on few-layer mos2saturable absorber. *IEEE Photonics Technology Letters*, **27**, 69–72. (Cited on page 83.)

Li, J., Luo, H., Zhai, B., Lu, R., Guo, Z., Zhang, H. & Liu, Y. (2016). Black phosphorus: a two-dimension saturable absorption material for mid-infrared q-switched and mode-locked fiber lasers. *Scientific reports*, **6**, 30361. (Cited on page 47.)

Li, X., Wang, Y., Wang, Y., Zhang, Y., Wu, K., Shum, P.P., Yu, X., Zhang, Y. & Wang, Q. (2013). All-normal-dispersion passively mode-locked yb-doped fiber ring laser based on a graphene oxide saturable absorber. *Laser Physics Letters*, **10**, 075108. (Cited on pages 80 and 234.)

Lin, K.H., Chern, G.W., Yu, C.T., Liu, T.M., Pan, C.C., Chen, G.T., Chyi, J.I., Huang, S.H., Li, P.C. & Sun, C.K. (2005). Optical piezoelectric transducer for nano-ultrasonics. *IEEE transactions on ultrasonics, ferroelectrics, and frequency control*, **52**, 1404–14. (Cited on pages xix and 100.)

Lin, Y.H., Yang, C.Y., Liou, J.H., Yu, C.P. & Lin, G.R. (2013a). Using graphene nanoparticle embedded in photonic crystal fiber for evanescent wave mode-locking of fiber laser. *Optics express*, **21**, 16763–16776. (Cited on pages 81 and 233.)

Lin, Y.H., Yang, C.Y., Liou, J.H., Yu, C.P. & Lin, G.R. (2013b). Using graphene nanoparticle embedded in photonic crystal fiber for evanescent wave mode-locking of fiber laser. *Opt. Express*, **21**, 16763–16776. (Cited on page 233.)

Lin, Y.M., Dimitrakopoulos, C., Jenkins, K.A., Farmer, D.B., Chiu, H.Y., Grill, A. & Avouris, P. (2010). 100-ghz transistors from wafer-scale epitaxial graphene. *Science*, **327**, 662–662. (Cited on page 1.)

Liu, H., Luo, A.P., Wang, F.Z., Tang, R., Liu, M., Luo, Z.C., Xu, W.C., Zhao, C.J. & Zhang, H. (2014a). Femtosecond pulse erbium-doped fiber laser by a few-layer mos2 saturable absorber. *Opt. Lett.*, **39**, 4591–4594. (Cited on pages 83 and 87.)

Liu, J., Wu, S., Yang, Q., Song, Y., Wang, Z. & Wang, P. (2011a). 163 nj graphene mode-locked yb-doped fiber laser. In *CLEO: Science and Innovations*, JWA23, Optical Society of America. (Cited on page 28.)

Liu, J., Wang, Y., Qu, Z., Zheng, L., Su, L. & Xu, J. (2012). Graphene oxide absorber for 2 μm passive mode-locking tm: Yalo3 laser. *Laser Physics Letters*, **9**, 15–19. (Cited on pages 27, 79, 223, 232 and 234.)

Liu, M., Zheng, X.W., Qi, Y.L., Liu, H., Luo, A.P., Luo, Z.C., Xu, W.C., Zhao, C.J. & Zhang, H. (2014b). Microfiber-based few-layer mos2 saturable absorber for 2.5 ghz passively harmonic mode-locked fiber laser. *Opt. Express*, **22**, 22841–22846. (Cited on page 84.)

Liu, M., Zheng, X.W., Qi, Y.L., Liu, H., Luo, A.P., Luo, Z.C., Xu, W.C., Zhao, C.J. & Zhang, H. (2014c). Microfiber-based few-layer mos2 saturable absorber for 2.5 ghz passively harmonic mode-locked fiber laser. *Opt. Express*, **22**, 22841–22846. (Cited on page 84.)

Liu, W., Liu, M., Lei, M., Fang, S. & Wei, Z. (2018). Titanium selenide saturable absorber mirror for passive q-switched er-doped fiber laser. *IEEE Journal of Selected Topics in Quantum Electronics*, **24**, 1–5. (Cited on page 72.)

Liu, Z., Wang, Y., Zhang, X., Xu, Y., Chen, Y. & Tian, J. (2009). Nonlinear optical properties of graphene oxide in nanosecond and picosecond regimes. *Applied Physics Letters*, **94**, 021902. (Cited on page 231.)

Liu, Z.B., He, X. & Wang, D. (2011b). Passively mode-locked fiber laser based on a hollow-core photonic crystal fiber filled with few-layered graphene oxide solution. *Optics letters*, **36**, 3024–3026. (Cited on pages 81 and 233.)

Lotya, M., Hernandez, Y., King, P.J., Smith, R.J., Nicolosi, V., Karlsson, L.S., Blighe, F.M., De, S., Wang, Z., McGovern, I.T., Duesberg, G.S. & Coleman, J.N. (2009). Liquid Phase Production of Graphene by Exfoliation of Graphite in Surfactant/Water Solutions. *J. Am. Chem. Soc.*, **131**, 3611–3620. (Cited on pages 6, 7 and 8.)

Lotya, M., King, P.J., Khan, U., De, S. & Coleman, J.N. (2010). High-concentration, surfactant-stabilized graphene dispersions. *ACS nano*, **4**, 3155–3162. (Cited on pages 6 and 7.)

Lu, L., Wang, W., Wu, L., Jiang, X., Xiang, Y., Li, J., Fan, D. & Zhang, H. (2017a). All-optical switching of two continuous waves in few layer bismuthene based on spatial cross-phase modulation. *ACS Photonics*, **4**, 2852–2861. (Cited on pages xvii, 57 and 58.)

Lu, L., Wang, W., Wu, L., Jiang, X., Xiang, Y., Li, J., Fan, D. & Zhang, H. (2017b). All-optical switching of two continuous waves in few layer bismuthene based on spatial cross-phase modulation. *Acs Photonics*, **4**, 2852–2861. (Cited on page 56.)

Lu, S.B., Miao, L.L., Guo, Z.N., Qi, X., Zhao, C.J., Zhang, H., Wen, S.C., Tang, D.Y. & Fan, D.Y. (2015). Broadband nonlinear optical response in multi-layer black phosphorus: an emerging infrared and mid-infrared optical material. *Opt. Express*, **23**, 11183–11194. (Cited on pages xvii and 57.)

Lu, X., Yu, M., Huang, H. & Ruoff, R.S. (1999). Tailoring graphite with the goal of achieving single sheets. *Nanotechnology*, **10**, 269. (Cited on page 4.)

Lukatskaya, M.R., Mashtalir, O., Ren, C.E., Dall'Agnese, Y., Rozier, P., Taberna, P.L., Naguib, M., Simon, P., Barsoum, M.W. & Gogotsi, Y. (2013). Cation intercalation and high volumetric capacitance of two-dimensional titanium carbide. *Science*, **341**, 1502–1505. (Cited on page 56.)

Luo, Z., Wang, J., Zhou, M., Xu, H., Cai, Z. & Ye, C. (2012a). Multiwavelength mode-locked erbium-doped fiber laser based on the interaction of graphene and fiber-taper evanescent field. *Laser Physics Letters*, **9**, 229. (Cited on pages 79, 80, 88 and 233.)

Luo, Z., Huang, Y., Weng, J., Cheng, H., Lin, Z., Xu, B., Cai, Z. & Xu, H. (2013). 1.06μm q-switched ytterbium-doped fiber laser using few-layer topological insulator bi2se3 as a saturable absorber. *Opt. Express*, **21**, 29516–29522. (Cited on page 86.)

Luo, Z., Huang, Y., Zhong, M., Li, Y., Wu, J., Xu, B., Xu, H., Cai, Z., Peng, J. & Weng, J. (2014). 1-, 1.5-, and 2-μm fiber lasers q-switched by a broadband few-layer mos2 saturable absorber. *J. Lightwave Technol.*, **32**, 4077–4084. (Cited on pages 83, 84 and 87.)

Luo, Z., Li, Y., Zhong, M., Huang, Y., Wan, X., Peng, J. & Weng, J. (2015). Nonlinear optical absorption of few-layer molybdenum diselenide (mose2) for passively mode-locked soliton fiber laser

invited

. *Photon. Res.*, **3**, A79–A86. (Cited on pages 77 and 87.)

Luo, Z., Wu, D., Xu, B., Xu, H., Cai, Z., Peng, J., Weng, J., Xu, S., Zhu, C., Wang, F. *et al.* (2016). Two-dimensional material-based saturable absorbers: towards compact visible-wavelength all-fiber pulsed lasers. *Nanoscale*, **8**, 1066–1072. (Cited on page 48.)

Luo, Z.C., Cao, W.J., Luo, A.P. & Xu, W.C. (2012b). Optical deposition of graphene saturable absorber integrated in a fiber laser using a slot collimator for passive mode-locking. *Applied Physics Express*, **5**, 055103. (Cited on pages 81 and 233.)

Ma, J., Lu, S., Guo, Z., Xu, X., Zhang, H., Tang, D. & Fan, D. (2015). Few-layer black phosphorus based saturable absorber mirror for pulsed solid-state lasers. *Opt. Express*, **23**, 22643–22648. (Cited on pages 71 and 75.)

Maiman, T.H. (1960). Stimulated optical radiation in ruby. (Cited on page 19.)

Maiman, T.H. (1967). Ruby laser systems. US Patent 3,353,115. (Not cited.)

Maldonado, E.P., Barbosa, E.A., Wetter, N.U., Courrol, L.C., Ranieri, I.M., Morato, S.P. & Vieira, N.D. (2001). Mode-locking operation of nd: Luylf. *Optical Engineering*, **40**, 1573–1578. (Cited on page 40.)

Mao, D., Du, B., Yang, D., Zhang, S., Wang, Y., Zhang, W., She, X., Cheng, H., Zeng, H. & Zhao, J. (2016). Nonlinear saturable absorption of liquid-exfoliated molybdenum/tungsten ditelluride nanosheets. *Small*, **12**, 1489–1497. (Cited on pages xvii and 54.)

Maragó, O.M., Bonaccorso, F., Saija, R., Privitera, G., Gucciardi, P.G., Iatì, M.A., Calogero, G., Jones, P.H., Borghese, F., Denti, P. *et al.* (2010). Brownian motion of graphene. *ACS nano*, **4**, 7515–7523. (Cited on page 7.)

Martinez, A. & Sun, Z. (2013). Nanotube and graphene saturable absorbers for fibre lasers. *Nature Photonics*, **7**, 842–845. (Cited on page 125.)

Martinez, A. & Yamashita, S.a. (2012). 10 ghz fundamental mode fiber laser using a graphene saturable absorber. *Applied Physics Letters*, **101**, 041118. (Cited on page 233.)

Martinez, A., Fuse, K., Xu, B. & Yamashita, S. (2010a). Optical deposition of graphene and carbon nanotubes in a fiber ferrule for passive mode-locked lasing. *Opt. Express*, **18**, 23054–23061. (Cited on page 81.)

Martinez, A., Fuse, K., Xu, B. & Yamashita, S. (2010b). Optical deposition of graphene and carbon nanotubes in a fiber ferrule for passive mode-locked lasing. *Optics express*, **18**, 23054–23061. (Cited on pages 81 and 233.)

Martinez, A., Fuse, K. & Yamashita, S. (2011). Mechanical exfoliation of graphene for the passive mode-locking of fiber lasers. *Applied Physics Letters*, **99**, 121107. (Cited on pages 29 and 81.)

Mary, R., Brown, G., Beecher, S.J., Torrisi, F., Milana, S., Popa, D., Hasan, T., Sun, Z., Lidorikis, E., Ohara, S. *et al.* (2013). 1.5 ghz picosecond pulse generation from a monolithic waveguide laser with a graphene-film saturable output coupler. *Optics express*, **21**, 7943–7950. (Cited on pages 81 and 234.)

Meyer, J., Geim, A., Katsnelson, M., Novoselov, K., Obergfell, D., Roth, S., Girit, C. & Zettl, A. (2007). On the roughness of single-and bi-layer graphene membranes. *Solid State Communications*, **143**, 101–109. (Cited on pages 1 and 27.)

Moulton, P.F. (1986). Spectroscopic and laser characteristics of ti: Al 2 o 3. *JOSA B*, **3**, 125–133. (Cited on page 40.)

Nair, R., Blake, P., Grigorenko, A., Novoselov, K., Booth, T., Stauber, T., Peres, N. & Geim, A. (2008). Fine structure constant defines visual transparency of graphene. *Science*, **320**, 1308–1308. (Cited on pages xv, xvi, 16, 17 and 18.)

New, G. (1972). Mode-locking of quasi-continuous lasers. *Optics Communications*, **6**, 188–192. (Cited on pages 39 and 40.)

Novoselov, K., Geim, A.K., Morozov, S., Jiang, D., Katsnelson, M., Grigorieva, I., Dubonos, S. & Firsov, A. (2005a). Two-dimensional gas of massless dirac fermions in graphene. *nature*, **438**, 197–200. (Cited on page 10.)

Novoselov, K., Jiang, D., Schedin, F., Booth, T., Khotkevich, V., Morozov, S. & Geim, A. (2005b). Two-dimensional atomic crystals. *Proceedings of the National Academy of Sciences of the United States of America*, **102**, 10451–10453. (Cited on page 7.)

Novoselov, K.S., Geim, A.K., Morozov, S.V., Jiang, D., Zhang, Y., Dubonos, S.V., Grigorieva, I.V. & Firsov, A.A. (2004a). Electric Field Effect in Atomically Thin Carbon Films. (Cited on page 3.)

Novoselov, K.S., Geim, A.K., Morozov, S.V., Jiang, D., Zhang, Y., Dubonos, S.V., Grigorieva, I.V. & Firsov, A.A. (2004b). Electric Field Effect in Atomically Thin Carbon Films. *Science*, **306**, 666–669. (Cited on page 55.)

Paschotta, R. & Keller, U. (2001). Passive mode locking with slow saturable absorbers. *Applied Physics B*, **73**, 653–662. (Cited on page 206.)

Paul, M.C., Sobon, G., Sotor, J., Abramski, K., Jagiello, J., Kozinski, R., Lipinska, L. & Pal, M. (2013). A graphene-based mode-locked nano-engineered zirconia–yttria–aluminosilicate glass-based erbium-doped fiber laser. *Laser Physics*, **23**, 035110. (Cited on pages 81 and 233.)

Pawliszewska, M., Martynkien, T., Przewłoka, A. & Sotor, J. (2018). Dispersion-managed ho-doped fiber laser mode-locked with a graphene saturable absorber. *Opt. Lett.*, **43**, 38–41. (Cited on page 79.)

Podila, R., Anand, B., Spear, J.T., Puneet, P., Philip, R., Siva Sankara Sai, S. & Rao, A.M. (2012). Effects of disorder on the optical properties of cvd grown polycrystalline graphene. *Nanoscale*, **4**, 1770–1775. (Cited on page 53.)

Pokrass, M., Burshtein, Z., Gvishi, R. & Nathan, M. (2012). Saturable absorption of multi-walled carbon nanotubes/hybrid-glass composites. *Opt. Mater. Express*, **2**, 825–838. (Cited on page 46.)

Popa, D., Sun, Z., Torrisi, F., Hasan, T., Wang, F. & Ferrari, A. (2010). Sub 200 fs pulse generation from a graphene mode-locked fiber laser. *Applied Physics Letters*, **97**, 203106. (Cited on pages 28, 29, 79 and 233.)

Prasankumar, R.P. & Taylor, A.J. (2016). *Optical techniques for solid-state materials characterization*. CRC Press. (Cited on page 205.)

Qiaoliang Bao, Y.W.Z.N.Y.Y.Z.X.S.K.P.L.D.Y.T., Han Zhang (2009). Atomiclayer graphene as a saturable absorber for ultrafast pulsed lasers. *Advanced Functional Materials*, **19**, 3077–3083. (Cited on pages 48 and 55.)

Qin, Z., Xie, G., Zhang, H., Zhao, C., Yuan, P., Wen, S. & Qian, L. (2015). Black phosphorus as saturable absorber for the q-switched er:zblan fiber laser at 2.8 μm. *Opt. Express*, **23**, 24713–24718. (Cited on pages 48, 71, 75, 84 and 85.)

Qin, Z., Xie, G., Zhao, C., Wen, S., Yuan, P. & Qian, L. (2016). Mid-infrared mode-locked pulse generation with multilayer black phosphorus as saturable absorber. *Opt. Lett.*, **41**, 56–59. (Cited on pages 71, 75 and 81.)

Qin, Z., Hai, T., Xie, G., Ma, J., Yuan, P., Qian, L., Li, L., Zhao, L. & Shen, D. (2018). Black phosphorus q-switched and mode-locked mid-infrared er:zblan fiber laser at 3.5 μm wavelength. *Opt. Express*, **26**, 8224–8231. (Cited on pages 71, 75 and 85.)

Rosa, H.G., neda, J.A.C., Cruz, C.H.B., Padilha, L.A., Gomes, J.C.V., de Souza, E.A.T. & Fragnito, H.L. (2017). Controlled stacking of graphene monolayer saturable absorbers for ultrashort pulse generation in erbium-doped fiber lasers. *Opt. Mater. Express*, **7**, 2528–2537. (Cited on pages 81 and 233.)

Rusdi, M.F.M., Latiff, A.A., Paul, M.C., Das, S., Dhar, A., Ahmad, H. & Harun, S.W. (2017). Titanium dioxide (tio2) film as a new saturable absorber for generating mode-locked thulium-holmium doped all-fiber laser. *Optics & Laser Technology*, **89**, 16 – 20. (Cited on pages 84 and 85.)

Said, A., Sheik-Bahae, M., Hagan, D.J., Wei, T., Wang, J., Young, J. & Van Stryland, E.W. (1992). Determination of bound-electronic and free-carrier nonlinearities in znse, gaas, cdte, and znte. *JOSA B*, **9**, 405–414. (Cited on pages 126 and 194.)

Salin, F., Piché, M. & Squier, J. (1991). Mode locking of ti: Al 2 o 3 lasers and self-focusing: a gaussian approximation. *Optics letters*, **16**, 1674–1676. (Cited on page 40.)

Samuel, E., Tuan, T.H., Asano, K., Suzuki, T. & Ohishi, Y. (2013). Optical parametric gain of tellutire/phosphate highly nonlinear optical fiber. In *Optical Communication Systems (OPTICS), 2013 International Conference on*, 1–5, IEEE. (Cited on page 194.)

Saraceno, C.J., Schriber, C., Mangold, M., Hoffmann, M., Heckl, O.H., Baer, C.R.E., Golling, M., Sdmeyer, T. & Keller, U. (2012). Sesams for high-power oscillators: Design guidelines and damage thresholds. *IEEE Journal of Selected Topics in Quantum Electronics*, **18**, 29–41. (Cited on page 213.)

Schedin, F., Geim, A., Morozov, S., Hill, E., Blake, P., Katsnelson, M. & Novoselov, K. (2007). Detection of individual gas molecules adsorbed on graphene. *Nature materials*, **6**, 652–655. (Cited on page 16.)

Schröder, W.U., Birkelund, J.R., Huizenga, J.R., Wilcke, W.W. & Randrup, J. (1980). Effect of pauli blocking on exchange and dissipation mechanisms operating in heavy-ion reactions. *Phys. Rev. Lett.*, **44**, 308–312. (Cited on page 49.)

Seo, J.W.T., Green, A.A., Antaris, A.L. & Hersam, M.C. (2011). High-concentration aqueous dispersions of graphene using nonionic, biocompatible block copolymers. *The Journal of Physical Chemistry Letters*, **2**, 1004–1008. (Cited on page 8.)

Sheik-Bahae, M., Said, A.A. & Van Stryland, E.W. (1989a). High-sensitivity, single-beam n 2 measurements. *Optics letters*, **14**, 955–957. (Cited on page 49.)

Sheik-Bahae, M., Said, A.A. & Van Stryland, E.W. (1989b). High-sensitivity, single-beam n 2 measurements. *Optics letters*, **14**, 955–957. (Cited on page 194.)

Sheik-Bahae, M., Said, A.A., Wei, T.., Hagan, D.J. & Van Stryland, E.W. (1990). Sensitive measurement of optical nonlinearities using a single beam. *IEEE Journal of Quantum Electronics*, **26**, 760–769. (Cited on page 51.)

Shi, H., Yan, R., Bertolazzi, S., Brivio, J., Gao, B., Kis, A., Jena, D., Xing, H.G. & Huang, L. (2013a). Exciton dynamics in suspended monolayer and few-layer mos2 2d crystals. *ACS nano*, **7**, 1072–1080. (Cited on page 58.)

Shi, H., Yan, R., Bertolazzi, S., Brivio, J., Gao, B., Kis, A., Jena, D., Xing, H.G. & Huang, L. (2013b). Exciton dynamics in suspended monolayer and few-layer mos2 2d crystals. *ACS Nano*, **7**, 1072–1080, pMID: 23273148. (Cited on pages 62, 63 and 70.)

Shih, C.J., Vijayaraghavan, A., Krishnan, R., Sharma, R., Han, J.H., Ham, M.H., Jin, Z., Lin, S., Paulus, G.L., Reuel, N.F. *et al.* (2011). Bi-and trilayer graphene solutions. *Nature nanotechnology*, **6**, 439–445. (Cited on page 3.)

Silfvast, W.T. (1996). *Laser fundamentals*, vol. 459. Cambridge University Press New York. (Cited on page 18.)

Sobon, G., Sotor, J., Jagiello, J., Kozinski, R., Zdrojek, M., Holdynski, M., Paletko, P., Boguslawski, J., Lipinska, L. & Abramski, K.M. (2012). Graphene oxide vs. reduced graphene oxide as saturable absorbers for er-doped passively mode-locked fiber laser. *Optics express*, **20**, 19463–19473. (Cited on pages 81 and 233.)

Song, Y., Liang, Z., Jiang, X., Chen, Y., Li, Z., Lu, L., Ge, Y., Wang, K., Zheng, J., Lu, S., Ji, J. & Zhang, H. (2017a). Few-layer antimonene decorated microfiber: ultra-short pulse generation and all-optical thresholding with enhanced long term stability. *2D Materials*, **4**, 045010. (Cited on pages xvii, 57 and 84.)

Song, Y., Liang, Z., Jiang, X., Chen, Y., Li, Z., Lu, L., Ge, Y., Wang, K., Zheng, J., Lu, S., Ji, J. & Zhang, H. (2017b). Few-layer antimonene decorated microfiber: ultra-short pulse generation and all-optical thresholding with enhanced long term stability. *2D Materials*, **4**, 045010. (Cited on pages xvii and 57.)

Song, Y.W., Jang, S.Y., Han, W.S. & Bae, M.K. (2010a). Graphene mode-lockers for fiber lasers functioned with evanescent field interaction. *Applied Physics Letters*, **96**, 051122. (Cited on pages 1, 27, 81 and 233.)

Song, Y.W., Jang, S.Y., Han, W.S. & Bae, M.K. (2010b). Graphene mode-lockers for fiber lasers functioned with evanescent field interaction. *Applied Physics Letters*, **96**, 051122. (Cited on page 81.)

Sotor, J., Sobon, G., Macherzynski, W., Paletko, P., Grodecki, K. & Abramski, K.M. (2014a). Mode-locking in er-doped fiber laser based on mechanically exfoliated sb2te3 saturable absorber. *Opt. Mater. Express*, **4**, 1–6. (Cited on pages 84 and 85.)

Sotor, J., Sobon, G., Macherzynski, W., Paletko, P., Grodecki, K. & Abramski, K.M. (2014b). Mode-locking in er-doped fiber laser based on mechanically exfoliated sb2te3 saturable absorber. *Opt. Mater. Express*, **4**, 1–6. (Cited on page 86.)

Sotor, J., Sobon, G., Kowalczyk, M., Macherzynski, W., Paletko, P. & Abramski, K.M. (2015a). Ultrafast thulium-doped fiber laser mode locked with black phosphorus. *Opt. Lett.*, **40**, 3885–3888. (Cited on pages 84 and 85.)

Sotor, J., Sobon, G., Macherzynski, W., Paletko, P. & Abramski, K.M. (2015b). Black phosphorus saturable absorber for ultrashort pulse generation. *Applied Physics Letters*, **107**, 051108. (Cited on page 48.)

Spence, D.E., Kean, P.N. & Sibbett, W. (1991). 60-fsec pulse generation from a self-mode-locked ti: sapphire laser. *Optics letters*, **16**, 42–44. (Cited on page 40.)

Stingl, A., Szipöcs, R., Lenzner, M., Spielmann, C. & Krausz, F. (1995). Sub-10-fs mirror-dispersion-controlled ti: sapphire laser. *Optics letters*, **20**, 602–604. (Cited on page 41.)

Suess, R.J., Jadidi, M.M., Murphy, T.E. & Mittendorff, M. (2015). Carrier dynamics and transient photobleaching in thin layers of black phosphorus. *Applied Physics Letters*, **107**, 081103. (Cited on page 67.)

Sun, D., Wu, Z.K., Divin, C., Li, X., Berger, C., de Heer, W.A., First, P.N. & Norris, T.B. (2008). Ultrafast Relaxation of Excited Dirac Fermions in Epitaxial Graphene Using Optical Differential Transmission Spectroscopy. *Physical Review Letters*, **101**. (Cited on pages 62 and 66.)

Sun, X., Nie, H., He, J., Zhao, R., Su, X., Wang, Y., Zhang, B., Wang, R. & Yang, K. (2017). Passively mode-locked 1.34 μm bulk laser based on few-layer black phosphorus saturable absorber. *Opt. Express*, **25**, 20025–20032. (Cited on pages 71, 75 and 83.)

Sun, Z., Hasan, T., Torrisi, F., Popa, D., Privitera, G., Wang, F., Bonaccorso, F., Basko, D.M. & Ferrari, A.C. (2009). Graphene Mode-Locked Ultrafast Laser. *ACS nano*. (Cited on page 27.)

Sun, Z., Hasan, T., Torrisi, F., Popa, D., Privitera, G., Wang, F., Bonaccorso, F., Basko, D.M. & Ferrari, A.C. (2010a). Graphene Mode-Locked Ultrafast Laser. *ACS Nano*, **4**, 803–810. (Cited on pages 6, 77, 86 and 87.)

Sun, Z., Hasan, T., Torrisi, F., Popa, D., Privitera, G., Wang, F., Bonaccorso, F., Basko, D.M. & Ferrari, A.C. (2010b). Graphene mode-locked ultrafast laser. *ACS nano*, **4**, 803–810. (Cited on pages 29 and 233.)

Sun, Z., Hasan, T., Wang, F., Rozhin, A.G., White, I.H. & Ferrari, A.C. (2010c). Ultrafast stretched-pulse fiber laser mode-locked by carbon nanotubes. *Nano Research*, **3**, 404–411. (Cited on page 27.)

Sun, Z., Popa, D., Hasan, T., Torrisi, F., Wang, F., Kelleher, E.J., Travers, J.C., Nicolosi, V. & Ferrari, A.C. (2010d). A stable, wideband tunable, near transform-limited, graphene-mode-locked, ultrafast laser. *Nano Research*, **3**, 653–660. (Cited on pages 6, 27, 28, 77, 87 and 233.)

Sun, Z., Popa, D., Hasan, T., Torrisi, F., Wang, F., Kelleher, E.J., Travers, J.C., Nicolosi, V. & Ferrari, A.C. (2010e). A stable, wideband tunable, near transform-limited, graphene-mode-locked, ultrafast laser. *Nano Research*, **3**, 653–660. (Cited on page 81.)

Sun, Z., Popa, D., Hasan, T., Torrisi, F., Wang, F., Kelleher, E.J.R., Travers, J.C., Nicolosi, V. & Ferrari, A.C. (2010f). A stable, wideband tunable, near transform-limited, graphene-mode-locked, ultrafast laser. *Nano Research*, **3**, 653–660. (Cited on page 75.)

Sun, Z., Lin, X., Yu, H., Hasan, T., Torrisi, F., Zhang, L., Sun, L., Guo, L., Hou, W., Li, J. *et al.* (2011). High-power ultrafast solid-state laser using graphene based saturable absorber. In *CLEO: Science and Innovations*, JWA79, Optical Society of America. (Cited on page 234.)

Szipöcs, R., Spielmann, C., Krausz, F. & Ferencz, K. (1994). Chirped multilayer coatings for broadband dispersion control in femtosecond lasers. *Optics Letters*, **19**, 201–203. (Cited on page 41.)

Tan, W., Su, C., Knize, R., Xie, G., Li, L. & Tang, D. (2010). Mode locking of ceramic nd: yttrium aluminum garnet with graphene as a saturable absorber. *Applied Physics Letters*, **96**, 031106. (Cited on pages 27, 80 and 234.)

Tang, X., Liang, W., Zhao, J., Li, Z., Qiu, M., Fan, T., Luo, C.S., Zhou, Y., Li, Y., Guo, Z., Fan, D. & Zhang, H. (2017). Fluorinated phosphorene: Electrochemical synthesis, atomistic fluorination, and enhanced stability. *Small*, **13**, 1702739. (Cited on page 47.)

Tao, L., Huang, X., He, J., Lou, Y., Zeng, L., Li, Y., Long, H., Li, J., Zhang, L. & Tsang, Y.H. (2018). Vertically standing ptse2 film: a saturable absorber for a passively mode-locked nd:luvo4 laser. *Photon. Res.*, **6**, 750–755. (Cited on page 82.)

Thoen, E., Koontz, E., Joschko, M., Langlois, P., Schibli, T., Kärtner, F., Ippen, E. & Kolodziejski, L. (1999). Two-photon absorption in semiconductor saturable absorber mirrors. *Applied physics letters*, **74**, 3927–3929. (Not cited.)

Tongay, S., Zhou, J., Ataca, C., Lo, K., Matthews, T.S., Li, J., Grossman, J.C. & Wu, J. (2012a). Thermally driven crossover from indirect toward direct bandgap in 2d semiconductors: Mose2 versus mos2. *Nano letters*, **12**, 5576–5580. (Cited on pages xvii, 54 and 55.)

Tongay, S., Zhou, J., Ataca, C., Lo, K., Matthews, T.S., Li, J., Grossman, J.C. & Wu, J. (2012b). Thermally driven crossover from indirect toward direct bandgap in 2d semiconductors: Mose2 versus mos2. *Nano Letters*, **12**, 5576–5580, pMID: 23098085. (Cited on page 55.)

Torrisi, F., Hasan, T., Wu, W., Sun, Z., Lombardo, A., Kulmala, T.S., Hsieh, G.W., Jung, S., Bonaccorso, F., Paul, P.J. *et al.* (2012). Inkjet-printed graphene electronics. *Acs Nano*, **6**, 2992–3006. (Cited on pages 8 and 9.)

Tsuda, S., Knox, W., De Souza, E., Jan, W. & Cunningham, J. (1995). Low-loss intracavity alas/algaas saturable bragg reflector for femtosecond mode locking in solid-state lasers. *Optics letters*, **20**, 1406–1408. (Cited on page 43.)

Valdmanis, J.A. & Fork, R. (1986). Design consideration for a femtosecond pulse laser balancing self phase modulation, group velocity dispersion, saturable absorption, and saturable gain. Tech. rep., AT and T Bell Lab., Murray Hill, NJ 07974. (Cited on page 40.)

Valles, C., Drummond, C., Saadaoui, H., Furtado, C.A., He, M., Roubeau, O., Ortolani, L., Monthioux, M. & Penicaud, A. (2008). Solutions of negatively charged graphene sheets and ribbons. *Journal of the American Chemical Society*, **130**, 15802–15804. (Cited on pages 6 and 7.)

Vardeny, Z. & Tauc, J. (1981). Picosecond coherence coupling in the pump and probe technique. *Optics Communications*, **39**, 396–400. (Cited on page 205.)

Wan, H., Cai, W., Wang, F., Jiang, S., Xu, S. & Liu, J. (2016). High-quality monolayer graphene for bulk laser mode-locking near 2 μm. *Optical and Quantum Electronics*, **48**, 1–8. (Cited on page 36.)

Wang, G., Wang, K., Szydowska, B.M., Baker-Murray, A.A., Wang, J.J., Feng, Y., Zhang, X., Wang, J. & Blau, W.J. (2017a). Ultrafast nonlinear optical properties of a graphene saturable mirror in the 2 m wavelength region. *Laser & Photonics Reviews*, **11**, 1700166. (Cited on pages viii, xix, xxvi, 46, 47, 53, 55, 59, 72, 74, 75, 82 and 192.)

Wang, G., Liang, G., Baker-Murray, A.A., Wang, K., Wang, J.J., Zhang, X., Bennett, D., Luo, J.T., Wang, J., Fan, P. & Blau, W.J. (2018a). Nonlinear optical performance of few-layer molybdenum diselenide as a slow-saturable absorber. *Photon. Res.*, **6**, 674–680. (Cited on pages xvii, xviii, 58, 60, 62, 69 and 188.)

Wang, G., Liang, G., Baker-Murray, A.A., Wang, K., Wang, J.J., Zhang, X., Bennett, D., Luo, J.T., Wang, J., Fan, P. & Blau, W.J. (2018b). Nonlinear optical performance of few-layer molybdenum diselenide as a slow-saturable absorber. *Photon. Res.*, **6**, 674–680. (Cited on pages 46, 53, 58, 63, 66 and 70.)

Wang, J., Luo, Z., Zhou, M., Ye, C., Fu, H., Cai, Z., Cheng, H., Xu, H. & Qi, W. (2012a). Evanescent-light deposition of graphene onto tapered fibers for passive q-switch and mode-locker. *Photonics Journal, IEEE*, **4**, 1295–1305. (Cited on pages 79, 81, 88 and 233.)

Wang, K., Wang, J., Fan, J., Lotya, M., ONeill, A., Fox, D., Feng, Y., Zhang, X., Jiang, B., Zhao, Q., Zhang, H., Coleman, J.N., Zhang, L. & Blau, W.J. (2013a). Ultrafast saturable absorption of two-dimensional mos2 nanosheets. *ACS Nano*, **7**, 9260–9267, pMID: 24090402. (Cited on pages xvii, 46, 47, 51, 52, 53, 54 and 82.)

Wang, K., Wang, J., Fan, J., Lotya, M., ONeill, A., Fox, D., Feng, Y., Zhang, X., Jiang, B., Zhao, Q. *et al.* (2013b). Ultrafast saturable absorption of two-dimensional mos2 nanosheets. *ACS nano*, **7**, 9260–9267. (Cited on page 214.)

Wang, K., Feng, Y., Chang, C., Zhan, J., Wang, C., Zhao, Q., Coleman, J.N., Zhang, L., Blau, W.J. & Wang, J. (2014a). Broadband ultrafast nonlinear absorption and nonlinear refraction of layered molybdenum dichalcogenide semiconductors. *Nanoscale*, **6**, 10530–10535. (Cited on pages xviii, 58, 69, 70 and 214.)

Wang, K., Szydłowska, B.M., Wang, G., Zhang, X., Wang, J.J., Magan, J.J., Zhang, L., Coleman, J.N., Wang, J. & Blau, W.J. (2016a). Ultrafast nonlinear excitation dynamics of black phosphorus nanosheets from visible to mid-infrared. *ACS nano*, **10**, 6923–6932. (Cited on pages 206 and 214.)

Wang, K., Szydowska, B.M., Wang, G., Zhang, X., Wang, J.J., Magan, J.J., Zhang, L., Coleman, J.N., Wang, J. & Blau, W.J. (2016b). Ultrafast nonlinear excitation dynamics of black phosphorus nanosheets from visible to mid-infrared. *ACS Nano*, **10**, 6923–6932, pMID: 27281449. (Cited on pages xvii, xviii, 46, 47, 51, 53, 55, 57, 58, 62, 63, 66 and 69.)

Wang, Q., Teng, H., Zou, Y., Zhang, Z., Li, D., Wang, R., Gao, C., Lin, J., Guo, L. & Wei, Z. (2012b). Graphene on sic as a q-switcher for a 2 μm laser. *Optics letters*, **37**, 395–397. (Cited on page 221.)

Wang, S., Ang, P.K., Wang, Z., Tang, A.L.L., Thong, J.T. & Loh, K.P. (2009a). High mobility, printable, and solution-processed graphene electronics. *Nano letters*, **10**, 92–98. (Cited on page 3.)

Wang, S., Zhang, Y., Abidi, N. & Cabrales, L. (2009b). Wettability and surface free energy of graphene films. *Langmuir*, **25**, 11078–11081. (Cited on page 8.)

Wang, S., Yu, H., Zhang, H., Wang, A., Zhao, M., Chen, Y., Mei, L. & Wang, J. (2014b). Broadband few-layer mos2 saturable absorbers. *Advanced Materials*, **26**, 3538–3544. (Cited on pages 82 and 84.)

Wang, X., Zhi, L. & Müllen, K. (2008). Transparent, conductive graphene electrodes for dye-sensitized solar cells. *Nano letters*, **8**, 323–327. (Cited on pages 1 and 9.)

Wang, Y., Qu, Z., Liu, J. & Tsang, Y.H. (2012c). Graphene oxide absorbers for watt-level high-power passive mode-locked nd: Gdvo 4 laser operating at 1 μm. *Journal of Lightwave Technology*, **30**, 3259–3262. (Cited on pages 79, 80 and 234.)

Wang, Y., Chen, H., Hsieh, W. & Tsang, Y. (2013c). Mode-locked nd: Gdvo 4 laser with graphene oxide/polyvinyl alcohol composite material absorber as well as an output coupler. *Optics Communications*, **289**, 119–122. (Cited on page 234.)

Wang, Y., Huang, G., Mu, H., Lin, S., Chen, J., Xiao, S., Bao, Q. & He, J. (2015). Ultrafast recovery time and broadband saturable absorption properties of black phosphorus suspension. *Applied Physics Letters*, **107**, 091905. (Cited on pages xvii, 47, 53, 57, 62 and 67.)

Wang, Y., Chen, W., Mero, M., Zhang, L., Lin, H., Lin, Z., Zhang, G., Rotermund, F., Cho, Y.J., Loiko, P., Mateos, X., Griebner, U. & Petrov, V. (2017b). Sub-100 fs tm:mgwo4 laser at 2017 nm mode locked by a graphene saturable absorber. *Opt. Lett.*, **42**, 3076–3079. (Cited on pages 79 and 81.)

Wang, Z., Zhao, R., He, J., Zhang, B., Ning, J., Wang, Y., Su, X., Hou, J., Lou, F., Yang, K. *et al.* (2016c). Multi-layered black phosphorus as saturable absorber for pulsed cr: Znse laser at 2.4 μm. *Optics Express*, **24**, 1598–1603. (Cited on pages 48, 71, 72 and 75.)

Weinberger, P. (2008). John kerr and his effects found in 1877 and 1878. *Philosophical Magazine Letters*, **88**, 897–907. (Cited on page 30.)

Winnerl, S., Orlita, M., Plochocka, P., Kossacki, P., Potemski, M., Winzer, T., Malic, E., Knorr, A., Sprinkle, M., Berger, C. *et al.* (2011). Carrier relaxation in epitaxial graphene photoexcited near the dirac point. *Physical review letters*, **107**, 237401. (Cited on page 27.)

Woodward, R., Howe, R., Hu, G., Torrisi, F., Zhang, M., Hasan, T. & Kelleher, E. (2015a). Few-layer mos 2 saturable absorbers for short-pulse laser technology: current status and future perspectives. *Photonics Research*, **3**, A30–A42. (Cited on page 213.)

Woodward, R.I., Kelleher, E.J.R., Howe, R.C.T., Hu, G., Torrisi, F., Hasan, T., Popov, S.V. & Taylor, J.R. (2014). Tunable q-switched fiber laser based on saturable edge-state absorption in few-layer molybdenum disulfide (mos2). *Opt. Express*, **22**, 31113–31122. (Cited on page 87.)

Woodward, R.I., Howe, R.C.T., Hu, G., Torrisi, F., Zhang, M., Hasan, T. & Kelleher, E.J.R. (2015b). Few-layer mos2 saturable absorbers for short-pulse laser technology: current status and future perspectives

invited

. *Photon. Res.*, **3**, A30–A42. (Cited on page 83.)

Woodward, R.I., Howe, R.C.T., Hu, G., Torrisi, F., Zhang, M., Hasan, T. & Kelleher, E.J.R. (2015c). Few-layer mos2 saturable absorbers for short-pulse laser technology: current status and future perspectives

invited

. *Photon. Res.*, **3**, A30–A42. (Cited on page 84.)

Woodward, R.I., Howe, R.C.T., Runcorn, T.H., Hu, G., Torrisi, F., Kelleher, E.J.R. & Hasan, T. (2015d). Wideband saturable absorption in few-layer molybdenum diselenide (mose2) for q-switching yb-, er- and tm-doped fiber lasers. *Opt. Express*, **23**, 20051–20061. (Cited on page 77.)

Wu, K., Chen, B., Zhang, X., Zhang, S., Guo, C., Li, C., Xiao, P., Wang, J., Zhou, L., Zou, W. & Chen, J. (2018). High-performance mode-locked and q-switched fiber lasers based on novel 2d materials of topological insulators, transition metal dichalcogenides and black phosphorus: review and perspective (invited). *Optics Communications*, **406**, 214 – 229, optoelectronics and Photonics Based on Two-dimensional Materials. (Cited on page 48.)

Xia, F., Mueller, T., Lin, Y.m., Valdes-Garcia, A. & Avouris, P. (2009). Ultrafast graphene photodetector. *Nature nanotechnology*, **4**, 839–843. (Cited on page 1.)

Xia, F., Wang, H., Xiao, D., Dubey, M. & Ramasubramaniam, A. (2014a). Two-dimensional material nanophotonics. *Nature Photonics*, **8**, 899. (Cited on page 55.)

Xia, H., Li, H., Lan, C., Li, C., Zhang, X., Zhang, S. & Liu, Y. (2014b). Ultrafast erbium-doped fiber laser mode-locked by a cvd-grown molybdenum disulfide (mos2) saturable absorber. *Opt. Express*, **22**, 17341–17348. (Cited on pages 83 and 84.)

Xie, G.Q., Ma, J., Lv, P., Gao, W.L., Yuan, P., Qian, L.J., Yu, H.H., Zhang, H.J., Wang, J.Y. & Tang, D.Y. (2012). Graphene saturable absorber for q-switching and mode locking at 2 μm wavelength

invited

. *Opt. Mater. Express*, **2**, 878–883. (Cited on pages 72, 75 and 87.)

Xing, C., Jing, G., Liang, X., Qiu, M., Li, Z., Cao, R., Li, X., Fan, D. & Zhang, H. (2017). Graphene oxide/black phosphorus nanoflake aerogels with robust thermo-stability and significantly enhanced photothermal properties in air. *Nanoscale*, **9**, 8096–8101. (Cited on page 47.)

Xing, G., Guo, H., Zhang, X., Sum, T.C. & Huan, C.H.A. (2010). The physics of ultrafast saturable absorption in graphene. *Opt. Express*, **18**, 4564–4573. (Cited on page 55.)

Xu, B., Cheng, Y., Wang, Y., Huang, Y., Peng, J., Luo, Z., Xu, H., Cai, Z., Weng, J. & Moncorgé, R. (2014a). Passively q-switched nd:yalo3 nanosecond laser using mos2 as saturable absorber. *Opt. Express*, **22**, 28934–28940. (Cited on pages 82, 83 and 84.)

Xu, B., Cheng, Y., Wang, Y., Huang, Y., Peng, J., Luo, Z., Xu, H., Cai, Z., Weng, J. & Moncorgé, R. (2014b). Passively q-switched nd:yalo3 nanosecond laser using mos2 as saturable absorber. *Opt. Express*, **22**, 28934–28940. (Cited on page 83.)

Xu, J., Liu, J., Wu, S., Yang, Q.H. & Wang, P. (2012a). Graphene oxide mode-locked femtosecond erbium-doped fiber lasers. *Optics express*, **20**, 15474–15480. (Cited on page 233.)

Xu, J., Wu, S., Li, H., Liu, J., Sun, R., Tan, F., Yang, Q.H. & Wang, P. (2012b). Dissipative soliton generation from a graphene oxide mode-locked er-doped fiber laser. *Optics express*, **20**, 23653–23658. (Cited on pages 84 and 233.)

Xu, J., Wu, S., Liu, J., Wang, Q., Yang, Q.H. & Wang, P. (2012c). Nanosecond-pulsed erbium-doped fiber lasers with graphene saturable absorber. *Optics Communications*, **285**, 4466–4469. (Cited on pages 81 and 233.)

Xu, J.L., Li, X.L., He, J.L., Hao, X.P., Wu, Y.Z., Yang, Y. & Yang, K.J. (2011a). Performance of large-area few-layer graphene saturable absorber in femtosecond bulk laser. *Applied Physics Letters*, **99**, 261107. (Cited on page 80.)

Xu, J.L., Li, X.L., He, J.L., Hao, X.P., Wu, Y.Z., Yang, Y. & Yang, K.J. (2011b). Performance of large-area few-layer graphene saturable absorber in femtosecond bulk laser. *Applied Physics Letters*, **99**, 261107. (Cited on pages 80 and 234.)

Xu, J.L., Li, X.L., Wu, Y.Z., Hao, X.P., He, J.L. & Yang, K.J. (2011c). Graphene saturable absorber mirror for ultra-fast-pulse solid-state laser. *Optics letters*, **36**, 1948–1950. (Cited on page 29.)

Xu, J.L., Li, X.L., Wu, Y.Z., Hao, X.P., He, J.L. & Yang, K.J. (2011d). Graphene saturable absorber mirror for ultra-fast-pulse solid-state laser. *Opt. Lett.*, **36**, 1948–1950. (Cited on pages 72, 75 and 83.)

Xu, J.L., Li, X.L., Wu, Y.Z., Hao, X.P., He, J.L. & Yang, K.J. (2011e). Graphene saturable absorber mirror for ultra-fast-pulse solid-state laser. *Opt. Lett.*, **36**, 1948–1950. (Cited on pages 72, 75 and 82.)

Xu, J.L., Li, X.L., Wu, Y.Z., Hao, X.P., He, J.L. & Yang, K.J. (2011f). Graphene saturable absorber mirror for ultra-fast-pulse solid-state laser. *Optics letters*, **36**, 1948–1950. (Cited on page 234.)

Xu, J.L., Li, X.L., He, J.L., Hao, X.P., Yang, Y., Wu, Y.Z., Liu, S.D. & Zhang, B.T. (2012d). Efficient graphene q switching and mode locking of 1.34 μm neodymium lasers. *Optics letters*, **37**, 2652–2654. (Cited on pages 80 and 234.)

Xu, L., Szipöcs, R., Spielmann, C. & Krausz, F. (1996). Ultrabroadband ring oscillator for sub-10-fs pulse generation. *Optics letters*, **21**, 1259–1261. (Cited on page 41.)

Xu, Y., Wang, Z., Guo, Z., Huang, H., Xiao, Q., Zhang, H. & Yu, X.F. (2016). Solvothermal synthesis and ultrafast photonics of black phosphorus quantum dots. *Advanced Optical Materials*, **4**, 1223–1229. (Cited on page 47.)

Yang, H., Feng, X., Wang, Q., Huang, H., Chen, W., Wee, A.T. & Ji, W. (2011a). Giant two-photon absorption in bilayer graphene. *Nano letters*, **11**, 2622–2627. (Cited on page 51.)

Yang, H., Feng, X., Wang, Q., Huang, H., Chen, W., Wee, A.T.S. & Ji, W. (2011b). Giant two-photon absorption in bilayer graphene. *Nano Letters*, **11**, 2622–2627, pMID: 21650165. (Cited on page 52.)

Yang, L., Deslippe, J., Park, C.H., Cohen, M.L. & Louie, S.G. (2009). Excitonic effects on the optical response of graphene and bilayer graphene. *Phys. Rev. Lett.*, **103**, 186802. (Cited on page 62.)

Young, H.D., Freedman, R.A. & Ford, L. (2007). *University Physics Vol 2 (Chapters 21-37)*, vol. 2. Pearson education. (Cited on page 30.)

Yu, H., Chen, X., Zhang, H., Xu, X., Hu, X., Wang, Z., Wang, J., Zhuang, S. & Jiang, M. (2010). Large energy pulse generation modulated by graphene epitaxially grown on silicon carbide. *ACS nano*, **4**, 7582–7586. (Cited on page 27.)

Zaugg, C., Sun, Z., Wittwer, V., Popa, D., Milana, S., Kulmala, T., Sundaram, R., Mangold, M., Sieber, O., Golling, M. *et al.* (2013). Ultrafast and widely tuneable vertical-external-cavity surface-emitting laser, mode-locked by a graphene-integrated distributed bragg reflector. *Optics express*, **21**, 31548–31559. (Cited on page 213.)

Zhan, Y., Wang, L., Wang, J.Y., Li, H.W. & Yu, Z.H. (2015). Yb:YAG thin disk laser passively q-switched by a hydro-thermal grown molybdenum disulfide saturable absorber. *Laser Physics*, **25**, 025901. (Cited on pages 83, 84 and 87.)

Zhang, F., Wang, Z., Wang, D., Wu, Z., Wang, S. & Xu, X. (2016a). Nonlinear optical effects in nitrogen-doped graphene. *RSC Advances*, **6**, 3526–3531. (Cited on page 229.)

Zhang, H., Liu, C.X., Qi, X.L., Dai, X., Fang, Z. & Zhang, S.C. (2009a). Topological insulators in bi 2 se 3, bi 2 te 3 and sb 2 te 3 with a single dirac cone on the surface. *Nature physics*, **5**, 438. (Cited on page 85.)

Zhang, H., Tang, D., Zhao, L., Bao, Q. & Loh, K. (2009b). Large energy mode locking of an erbium-doped fiber laser with atomic layer graphene. *Optics Express*, **17**, 17630–17635. (Cited on pages 27, 81 and 233.)

Zhang, H., Tang, D., Zhao, L., Bao, Q., Loh, K., Lin, B. & Tjin, S. (2010). Compact graphene mode-locked wavelength-tunable erbium-doped fiber lasers: from all anomalous dispersion to all normal dispersion. *Laser Physics Letters*, **7**, 591–596. (Cited on page 28.)

Zhang, H., Virally, S., Bao, Q., Ping, L.K., Massar, S., Godbout, N. & Kockaert, P. (2012a). Z-scan measurement of the nonlinear refractive index of graphene. *Optics letters*, **37**, 1856–1858. (Cited on pages 163 and 226.)

Zhang, H., Lu, S., Zheng, J., Du, J., Wen, S., Tang, D. & Loh, K. (2014a). Molybdenum disulfide (mos 2) as a broadband saturable absorber for ultra-fast photonics. *Optics express*, **22**, 7249–7260. (Cited on pages 82 and 83.)

Zhang, H., Lu, S.B., Zheng, J., Du, J., Wen, S.C., Tang, D.Y. & Loh, K.P. (2014b). Molybdenum disulfide (mos2) as a broadband saturable absorber for ultra-fast photonics. *Opt. Express*, **22**, 7249–7260. (Cited on pages xvii, 53, 55, 57 and 84.)

Zhang, H., Lu, S.B., Zheng, J., Du, J., Wen, S.C., Tang, D.Y. & Loh, K.P. (2014c). Molybdenum disulfide (mos2) as a broadband saturable absorber for ultra-fast photonics. *Opt. Express*, **22**, 7249–7260. (Cited on pages 53, 82, 83 and 84.)

Zhang, J., Ouyang, H., Zheng, X., You, J., Chen, R., Zhou, T., Sui, Y., Liu, Y., Cheng, X. & Jiang, T. (2018). Ultrafast saturable absorption of $mos_2 nanosheets under different pulse-width excitation conditions. Optics Letters$, **43**, 243. (*Cited on pages* 68 *and* 70.)

Zhang, L., Wang, Y., Yu, H., Zhang, S., Hou, W., Lin, X. & Li, J. (2011a). High power passively mode-locked nd: Yvo4 laser using graphene oxide as a saturable absorber. *Laser Physics*, **21**, 2072–2075. (Cited on page 28.)

Zhang, L., Wang, Y., Yu, H., Zhang, S., Hou, W., Lin, X. & Li, J. (2011b). High power passively mode-locked nd: Yvo4 laser using graphene oxide as a saturable absorber. *Laser Physics*, **21**, 2072–2075. (Cited on pages 79, 80 and 234.)

Zhang, L., Wang, G., Hu, J., Wang, J., Fan, J., Wang, J. & Feng, Y. (2012b). Linearly polarized 1180-nm raman fiber laser mode locked by graphene. *Photonics Journal, IEEE*, **4**, 1809–1815. (Cited on pages 80 and 234.)

Zhang, M., Kelleher, E., Torrisi, F., Sun, Z., Hasan, T., Popa, D., Wang, F., Ferrari, A., Popov, S. & Taylor, J. (2012c). Tm-doped fiber laser mode-locked by graphene-polymer composite. *Optics express*, **20**, 25077–25084. (Cited on pages 80, 223, 232 and 234.)

Zhang, M., Howe, R.C.T., Woodward, R.I., Kelleher, E.J.R., Torrisi, F., Hu, G., Popov, S.V., Taylor, J.R. & Hasan, T. (2015a). Solution processed mos2-pva composite for sub-bandgap mode-locking of a wideband tunable ultrafast er:fiber laser. *Nano Research*, **8**, 1522–1534. (Cited on page 87.)

Zhang, R.W., Zhang, C.W., Ji, W.X., Yan, S.S. & Yao, Y.G. (2017a). First-principles prediction on bismuthylene monolayer as a promising quantum spin hall insulator. *Nanoscale*, **9**, 8207–8212. (Cited on page 55.)

Zhang, S., Yan, Z., Li, Y., Chen, Z. & Zeng, H. (2015b). Atomically thin arsenene and antimonene: semimetal–semiconductor and indirect–direct band-gap transitions. *Angewandte Chemie International Edition*, **54**, 3112–3115. (Cited on page 55.)

Zhang, S., Li, Y., Zhang, X., Dong, N., Wang, K., Hanlon, D., Coleman, J.N., Zhang, L. & Wang, J. (2016b). Slow and fast absorption saturation of black phosphorus: experiment and modelling. *Nanoscale*, **8**, 17374–17382. (Cited on pages 66, 67, 213 and 214.)

Zhang, S., Zhang, X., Wang, H., Chen, B., Wu, K., Wang, K., Hanlon, D., Coleman, J.N., Chen, J., Zhang, L. & Wang, J. (2016c). Size-dependent saturable absorption and mode-locking of dispersed black phosphorus nanosheets. *Opt. Mater. Express*, **6**, 3159–3168. (Cited on pages 75 and 214.)

Zhang, S., Zhang, X., Wang, H., Chen, B., Wu, K., Wang, K., Hanlon, D., Coleman, J.N., Chen, J., Zhang, L. *et al.* (2016d). Size-dependent saturable absorption and mode-locking of dispersed black phosphorus nanosheets. *Optical Materials Express*, **6**, 3159–3168. (Cited on page 73.)

Zhang, X., Selkirk, A., Zhang, S., Huang, J., Li, Y., Xie, Y., Dong, N., Cui, Y., Zhang, L., Blau, W.J. & Wang, J. (2017b). Mos2/carbon nanotube coreshell nanocomposites for enhanced nonlinear optical performance. *Chemistry A European Journal*, **23**, 3321–3327. (Cited on page 46.)

Zhang, Y., Tan, Y.W., Stormer, H.L. & Kim, P. (2005). Experimental observation of the quantum hall effect and berry's phase in graphene. *Nature*, **438**, 201–204. (Cited on pages 1, 4 and 9.)

Zhao, J., Wang, Y., Yan, P., Ruan, S., Zhang, G., Li, H. & Tsang, Y. (2013). An l-band graphene-oxide mode-locked fiber laser delivering bright and dark pulses. *Laser Physics*, **23**, 075105. (Cited on pages 81 and 233.)

Zheng, C., Li, W., Xiao, X., Ye, X. & Chen, W. (2016). Synthesis and optical limiting properties of graphene oxide/bimetallic nanoparticles. *Optik-International Journal for Light and Electron Optics*, **127**, 1792–1796. (Cited on page 229.)

Zheng, J., Tang, X., Yang, Z., Liang, Z., Chen, Y., Wang, K., Song, Y., Zhang, Y., Ji, J., Liu, Y., Fan, D. & Zhang, H. (2017a). Few-layer phosphorene-decorated microfiber for all-optical thresholding and optical modulation. *Advanced Optical Materials*, **5**, 1700026. (Cited on page 47.)

Zheng, J., Yang, Z., Si, C., Liang, Z., Chen, X., Cao, R., Guo, Z., Wang, K., Zhang, Y., Ji, J., Zhang, M., Fan, D. & Zhang, H. (2017b). Black phosphorus based all-optical-signal-processing: Toward high performances and enhanced stability. *ACS Photonics*, **4**, 1466–1476. (Cited on page 47.)

Zheng, Z., Zhao, C., Lu, S., Chen, Y., Li, Y., Zhang, H. & Wen, S. (2012a). Microwave and optical saturable absorption in graphene. *Opt. Express*, **20**, 23201–23214. (Cited on pages 52, 55 and 81.)

Zheng, Z., Zhao, C., Lu, S., Chen, Y., Li, Y., Zhang, H. & Wen, S. (2012b). Microwave and optical saturable absorption in graphene. *Optics express*, **20**, 23201–23214. (Cited on page 233.)

Zhou, J., Christov, I.P., Taft, G., Huang, C.P., Murnane, M.M. & Kapteyn, H.C. (1994). Pulse evolution in a broad-bandwidth ti: sapphire laser. *Optics letters*, **19**, 1149–1151. (Cited on page 41.)

Zhou, Y., Zhang, M., Guo, Z., Miao, L., Han, S.T., Wang, Z., Zhang, X., Zhang, H. & Peng, Z. (2017). Recent advances in black phosphorus-based photonics, electronics, sensors and energy devices. *Mater. Horiz.*, **4**, 997–1019. (Cited on page 48.)